

The Pennsylvania State University
The Graduate School
Department of Mechanical and Nuclear Engineering

**SCALED EXPERIMENTS ON AIR INGRESS
IN THE VERY HIGH TEMPERATURE REACTOR (VHTR)**

A Thesis in
Nuclear Engineering
by
Jenna J. Baird

© 2010 Jenna J. Baird

Submitted in Partial Fulfillment
of the Requirements
for the Degree of

Master of Science

December 2010

The thesis of Jenna J. Baird was reviewed and approved* by the following:

Seungjin Kim
Assistant Professor of Mechanical and Nuclear Engineering
Thesis Advisor

Fan-Bill Cheung
Professor of Mechanical and Nuclear Engineering

Arthur Motta
Professor of Nuclear Engineering and Materials Science and Engineering
Chair of Nuclear Engineering

*Signatures are on file in the Graduate School

ABSTRACT

In the postulated Depressurized Loss of Forced Convection (D-LOFC) for the Very High Temperature Reactor (VHTR), the gravity driven air ingress phenomenon is of particular interest. This accident scenario involves depressurization of helium from the reactor vessel due to a rupture in the primary coolant pipe, followed by the exchange of the helium with the air driven by the density difference. This ingress of air could potentially lead to oxidation of graphite structure in the reactor and ultimately to a release of radioactive fission products. The present study performs scaled adiabatic separate-effects experiments using air and helium as working fluids to highlight the hydrodynamic effects in the process of air ingress. A scaling analysis is performed to design a test apparatus using the Gas Turbine Modular Helium Reactor (GT-MHR) as the reference prototypic reactor. The scaling is performed to preserve the exchange time ratio between the scaled and prototypic case to be close to unity. The test vessel is made of a carbon steel cylinder with 60.96 cm (24 in) in diameter and 182.88 cm (72 in) in length. It is sealed at the top and bottom with flat plates via flanges. It is designed to accommodate three break locations, namely, two horizontal breaks on the side and one vertical break on the top of the vessel. These represent the horizontal primary coolant pipe and the vertical refueling standpipe, respectively. To investigate the geometric effects on the ingress phenomenon, the break locations are designed to accommodate pipe breaks of various length-to-diameter ratios (L/D) and break angles. In the present study, the air ingress via two horizontal side breaks is investigated with a pipe break of $L/D = 3$. The oxygen concentration is measured with an oxygen analyzer at several axial and radial locations within the test apparatus. It is found that the majority of the local data follows the same general trend. Oscillations are observed in the data for locations within close proximity as a result of the helium-air interface. The transient behaviors of both the local and the averaged oxygen concentration data show characteristics of hydrodynamic effects on the air ingress.

TABLE OF CONTENTS

LIST OF FIGURES	vi
LIST OF TABLES	xv
NOMENCLATURE	xvi
ACKNOWLEDGEMENTS	xviii
Chapter 1 Introduction	1
1.1 Research Background and Objectives.....	1
1.2 Literature Review	3
1.3 Water-Brine Scoping Experiments	18
Chapter 2 Scaling Analysis	20
2.1 Scaling Parameters	20
2.2 Scaling Approach and Results.....	28
Chapter 3 Experimental Facility	31
3.1 Engineering Design of Test Apparatus	32
3.2 Test Facility and Instrumentation.....	35
3.3 Experimental Approach.....	55
3.4 Experimental Procedure	61
Chapter 4 Experimental Results and Discussion	61
4.1 Data Verification and Repeatability	63
4.2 Local Data	69
4.3 Area Average Scheme and Planar Data	77
4.4 Volume Average Scheme and Global Data.....	82
4.5 Discussion	87
Chapter 5 Conclusions and Future Work	88
5.1 Conclusions	88
5.2 Future Work	89
References.....	90
Appendix A Exchange Volume Calculation for GT-MHR (Kim and Talley, 2009)	94
Appendix B Engineering Drawings	100
Appendix C Nansulate EPX Product Data Sheet.....	128

Appendix D Air Ingress Data Collection Sheet	130
Appendix E Data Repeatability Plots with Error Bars	131
Appendix F Lower Side Break Data	135
Appendix G Lower Side Break MATLAB Plots	163
Appendix H Higher Side Break Data	166

LIST OF FIGURES

Figure 1-1: Reference Frame Moving with Heavier Fluid (von Karman, 1940)	3
Figure 1-2: Reference Frame for Flow Past a Cavity (Benjamin, 1968)	5
Figure 1-3: Data Plotted as q^* with respect to Inclination Angle (Mercer and Thompson, 1975)	8
Figure 1-4: Data Plotted as Froude Number with respect to L/D (Epstein, 1988).....	10
Figure 1-5: Gravity Currents for Small Density Differences (Keller and Chyou, 1991).....	11
Figure 1-6: Gravity Currents for Large Density Differences (Keller and Chyou, 1991).....	12
Figure 1-7: Data Plotted as Froude Number with respect to H/D (Hishida et al., 1993)	14
Figure 1-8: Data Plotted as Froude Number with respect to Inclination Angle (Hishida et al., 1993)	14
Figure 1-9: Data Plotted as Exchange Flow Rate with respect to Inclination Angle	16
Figure 1-10: Schematic of Two Categories of Lock-exchange Flows (Lowe et al., 2005)	17
Figure 2-1: Schematic of VHTR (MacDonald et al., 2003).....	21
Figure 3-1: Photograph of Test Apparatus.....	35
Figure 3-2: Photograph of Plug in Higher Side Break.....	36
Figure 3-3: Photograph of Nansulate EPX Applied to Top Plate	37
Figure 3-4: Photograph of Quincy Compressor Model QV-1.5 HP Rotary Vane Vacuum Pump	38
Figure 3-5: Photograph of AMETEK Thermox CEM O2/TM Trace Oxygen Analyzer	39
Figure 3-6: Oxygen Analyzer Accuracy Applied to a Data Set.....	40
Figure 3-7: Initial 200 s of Oxygen Analyzer Accuracy Applied to a Data Set	40
Figure 3-8: Photograph of Dwyer Flowmeter and Aspirator	41
Figure 3-9: Confirmation of Oxygen Analyzer Measurement	43
Figure 3-10: Test Facility Response Time	44
Figure 3-11: Photograph of OMEGA GCHAI Circulation Heater	45

Figure 3-12: Schematic of Test Facility (not to scale).....	46
Figure 3-13: Photograph of Experimental Test Facility	47
Figure 3-14: Photograph of Type T Thermocouple Bead Diameter	48
Figure 3-15: Measured Temperature with respect to Reference Temperature for Thermocouple Calibration	49
Figure 3-16: Region 20 to 25°C of Measured Temperature with respect to Reference Temperature for Thermocouple Calibration	49
Figure 3-17: Thermocouple Response Time.....	50
Figure 3-18: Photograph of Thermocouple Assembly Seal Plug.....	51
Figure 3-19: NI SCXI-1102 Input Module	53
Figure 3-20: NI SCXI-1600 USB Module.....	53
Figure 3-21: NI SCXI-1001 Slot Chassis	54
Figure 3-22: NI TC-2095 Thermocouple Connector	54
Figure 3-23: NI SH96-96 Shielded Cable.....	55
Figure 3-24: Schematic of Angular Port Locations	56
Figure 3-25: Schematic of Break Locations and Axial Port Locations	57
Figure 3-26: Schematic of Radial Location Color Code for Lower Side Break.....	58
Figure 3-27: Schematic of Radial Location Color Code for Higher Side Break	60
Figure 4-1: Comparison of Data for Continuous and Non-continuous Sampling.....	64
Figure 4-2: Oxygen Content Data for CPort2.....	65
Figure 4-3: Normalized Oxygen Content Data for CPort2	66
Figure 4-4: Comparison of Data at APort1 43.18 cm (17 in) to Verify Repeatability.....	67
Figure 4-5: Radial Locations for Symmetry Verification	68
Figure 4-6: Comparison of Data for Symmetry Verification.....	68
Figure 4-7: Local Data for APort1 along Radial Direction.....	70
Figure 4-8: Initial 120 s of Local Data for APort1 along Radial Direction	71

Figure 4-9: Local Data for APort2 along Radial Direction.....	71
Figure 4-10: Local Data for APort3 along Radial Direction.....	72
Figure 4-11: Variation of Air Content along Vessel Diameter for APort1	72
Figure 4-12: Local Data for Radial Location 30.48 cm (12 in) along Axial Direction for APort	73
Figure 4-13: Initial 150 s of Local Data for Radial Location 30.48 cm (12 in) along Axial Direction for APort	74
Figure 4-14: Local Data for APort4 along Radial Direction.....	75
Figure 4-15: Local Data for APort5 along Radial Direction.....	75
Figure 4-16: Local Data for Radial Location 30.48 cm (12 in) along Axial Direction for APort	76
Figure 4-17: Area Average Scheme for Lower Side Break	77
Figure 4-18: Planar Data for the Lower Side Break	79
Figure 4-19: Initial 150 s of Planar Data for the Lower Side Break	79
Figure 4-20: Area Average Scheme for Higher Side Break	80
Figure 4-21: Planar Data for the Higher Side Break.....	81
Figure 4-22: Initial 200 s of Planar Data for the Higher Side Break	82
Figure 4-23: Air Content Plotted along Axial Direction for Several Times for Lower Side Break	83
Figure 4-24: Planar Data Plotted with Global Data for Lower Side Break.....	84
Figure 4-25: Initial 150 s of Planar Data Plotted with Global Data for Lower Side Break	84
Figure 4-26: Air Content Plotted along Axial Direction for Several Times for Higher Side Break	85
Figure 4-27: Global Data Plotted with Planar Data for Higher Side Break.....	86
Figure 4-28: Initial 200 s of Global Data Plotted with Planar Data for Higher Side Break	86
Figure A-1: GT-MHR Schematics.....	94
Figure A-2: Cross-sectional view of core layout	96

Figure A-3: Fuel Block (dimensions are in Inches).....	97
Figure E-1: Comparison of Data at APort1 17 in to Verify Repeatability.....	131
Figure E-2: Initial 50 s of APort1 17in Data (Error Bars: $\pm 10\%$).....	132
Figure E-3: Region 50 s to 100 s of APort1 17in Data (Error Bars: $\pm 10\%$)	132
Figure E-4: Region 100 s to 140 s of APort1 17in Data (Error Bars: $\pm 10\%$)	133
Figure E-5: Region 140 s to 300 s of APort1 17in Data (Error Bars: $\pm 2\%$)	133
Figure E-6: Region 300 s to 2700 s of APort1 17in Data (Error Bars: $\pm 2\%$)	134
Figure F-1: Local Data for APort1 along Radial Direction	136
Figure F-2: Initial 120 s of Local Data for APort1 along Radial Direction	136
Figure F-3: Local Data for BPort1 along Radial Direction.....	137
Figure F-4: Initial 120 s of Local Data for BPort1 along Radial Direction	137
Figure F-5: Local Data for CPort1 along Radial Direction.....	138
Figure F-6: Initial 120 s of Local Data for CPort1 along Radial Direction	138
Figure F-7: Local Data for APort2 along Radial Direction	139
Figure F-8: Initial 150 s of Local Data for APort2 along Radial Direction	139
Figure F-9: Local Data for BPort2 along Radial Direction.....	140
Figure F-10: Initial 150 s of Local Data for BPort2 along Radial Direction	140
Figure F-11: Local Data for CPort2 along Radial Direction.....	141
Figure F-12: Initial 150 s of Local Data for CPort2 along Radial Direction	141
Figure F-13: Local Data for APort3 along Radial Direction	142
Figure F-14: Initial 200 s of Local Data for APort3 along Radial Direction	142
Figure F-15: Local Data for BPort3 along Radial Direction.....	143
Figure F-16: Initial 200 s of Local Data for BPort3 along Radial Direction	143
Figure F-17: Local Data for CPort3 along Radial Direction.....	144
Figure F-18: Initial 200 s of Local Data for CPort3 along Radial Direction	144

Figure F-19: Variation of Air Content along Vessel Diameter for APort1	145
Figure F-20: Variation of Air Content along Vessel Diameter for APort2	145
Figure F-21: Variation of Air Content along Vessel Diameter for APort3	146
Figure F-22: Local Data for Radial Location 0.5 in along Axial Direction for APort	147
Figure F-23: Initial 150 s of Local Data for Radial Location 0.5 in along Axial Direction for APort	147
Figure F-24: Local Data for Radial Location 2 in along Axial Direction for APort	148
Figure F-25: Initial 150 s of Local Data for Radial Location 2 in along Axial Direction for APort	148
Figure F-26: Local Data for Radial Location 7 in along Axial Direction for APort	149
Figure F-27: Initial 150 s of Local Data for Radial Location 7 in along Axial Direction for APort	149
Figure F-28: Local Data for Radial Location 12 in along Axial Direction for APort	150
Figure F-29: Initial 150 s of Local Data for Radial Location 12 in along Axial Direction for APort	150
Figure F-30: Local Data for Radial Location 17 in along Axial Direction for APort	151
Figure F-31: Initial 150 s of Local Data for Radial Location 17 in along Axial Direction for APort	151
Figure F-32: Local Data for Radial Location 22 in along Axial Direction for APort	152
Figure F-33: Initial 150 s of Local Data for Radial Location 22 in along Axial Direction for APort	152
Figure F-34: Local Data for Radial Location 23.5 in along Axial Direction for APort	153
Figure F-35: Initial 150 s of Local Data for Radial Location 23.5 in along Axial Direction for APort	153
Figure F-36: Local Data for Radial Location 0.5 in along Axial Direction for BPort	154
Figure F-37: Initial 150 s of Local Data for Radial Location 0.5 in along Axial Direction for BPort	154
Figure F-38: Local Data for Radial Location 2 in along Axial Direction for BPort	155

Figure F-39: Initial 150 s of Local Data for Radial Location 2 in along Axial Direction for BPort.....	155
Figure F-40: Local Data for Radial Location 7 in along Axial Direction for BPort.....	156
Figure F-41: Initial 150 s of Local Data for Radial Location 7 in along Axial Direction for BPort.....	156
Figure F-42: Local Data for Radial Location 17 in along Axial Direction for BPort.....	157
Figure F-43: Initial 150 s of Local Data for Radial Location 17 in along Axial Direction for BPort.....	157
Figure F-44: Local Data for Radial Location 22 in along Axial Direction for BPort.....	158
Figure F-45: Initial 150 s of Local Data for Radial Location 22 in along Axial Direction for BPort.....	158
Figure F-46: Local Data for Radial Location 23.5 in along Axial Direction for BPort.....	159
Figure F-47: Initial 150s of Local Data for Radial Location 23.5 in along Axial Direction for BPort.....	159
Figure F-48: Local Data for Radial Location 17 in along Axial Direction for CPort.....	160
Figure F-49: Initial 150s of Local Data for Radial Location 17 in along Axial Direction for CPort.....	160
Figure F-50: Local Data for Radial Location 22 in along Axial Direction for CPort.....	161
Figure F-51: Initial 150s of Local Data for Radial Location 22 in along Axial Direction for CPort.....	161
Figure F-52: Local Data for Radial Location 23.5 in along Axial Direction for CPort.....	162
Figure F-53: Initial 150 s of Local Data for Radial Location 23.5 in along Axial Direction for CPort.....	162
Figure G-1: Initial Oxygen Content at (a) Port1, (b) Port2, and (c) Port3	163
Figure G-2: Oxygen Content 100 s after Initiation at (a) Port1, (b) Port2, and (c) Port3	163
Figure G-3: Oxygen Content 200 s after Initiation at (a) Port1, (b) Port2, and (c) Port3	164
Figure G-4: Oxygen Content 300 s after Initiation at (a) Port1, (b) Port2, and (c) Port3	164
Figure G-5: Oxygen Content 500 s after Initiation at (a) Port1, (b) Port2, and (c) Port3	164
Figure G-6: Oxygen Content 700 s after Initiation at (a) Port1, (b) Port2, and (c) Port3	165

Figure G-7: Oxygen Content 1,000 s after Initiation at (a) Port1, (b) Port2, and (c) Port3	165
Figure H-1: Local Data for APort1 along Radial Direction.....	167
Figure H-2: Initial 150 s of Local Data for APort1 along Radial Direction	167
Figure H-3: Local Data for BPort1 along Radial Direction.....	168
Figure H-4: Initial 150 s of Local Data for BPort1 along Radial Direction.....	168
Figure H-5: Local Data for CPort1 along Radial Direction.....	169
Figure H-6: Initial 150 s of Local Data for CPort1 along Radial Direction.....	169
Figure H-7: Local Data for APort4 along Radial Direction.....	170
Figure H-8: Initial 200 s of Local Data for APort4 along Radial Direction	170
Figure H-9: Local Data for BPort4 along Radial Direction.....	171
Figure H-10: Initial 200 s of Local Data for BPort4 along Radial Direction	171
Figure H-11: Local Data for CPort4 along Radial Direction.....	172
Figure H-12: Initial 200 s of Local Data for CPort4 along Radial Direction	172
Figure H-13: Local Data for APort5 along Radial Direction.....	173
Figure H-14: Initial 250 s of Local Data for APort5 along Radial Direction	173
Figure H-15: Local Data for BPort5 along Radial Direction.....	174
Figure H-16: Initial 250 s of Local Data for BPort5 along Radial Direction	174
Figure H-17: Local Data for CPort5 along Radial Direction.....	175
Figure H-18: Initial 250 s of Local Data for CPort5 along Radial Direction	175
Figure H-19: Local Data for APort6 along Radial Direction.....	176
Figure H-20: Initial 300 s of Local Data for APort6 along Radial Direction	176
Figure H-21: Local Data for BPort6 along Radial Direction.....	177
Figure H-22: Initial 300 s of Local Data for BPort6 along Radial Direction	177
Figure H-23: Local Data for CPort6 along Radial Direction.....	178
Figure H-24: Initial 300 s of Local Data for CPort6 along Radial Direction	178

Figure H-25: Local Data for APort7 along Radial Direction.....	179
Figure H-26: Initial 400 s of Local Data for APort7 along Radial Direction	179
Figure H-27: Local Data for BPort7 along Radial Direction.....	180
Figure H-28: Initial 400 s of Local Data for BPort7 along Radial Direction	180
Figure H-29: Local Data for CPort7 along Radial Direction.....	181
Figure H-30: Initial 400 s of Local Data for CPort7 along Radial Direction	181
Figure H-31: Variation of Air Content along Vessel Diameter for APort1	182
Figure H-32: Variation of Air Content along Vessel Diameter for APort4	182
Figure H-33: Variation of Air Content along Vessel Diameter for APort5	183
Figure H-34: Variation of Air Content along Vessel Diameter for APort6	183
Figure H-35: Variation of Air Content along Vessel Diameter for APort7	184
Figure H-36: Local Data for Radial Location 0.5 in along Axial Direction for APort.....	185
Figure H-37: Initial 200 s of Local Data for Radial Location 0.5 in along Axial Direction for APort	185
Figure H-38: Local Data for Radial Location 7 in along Axial Direction for APort.....	186
Figure H-39: Initial 200 s of Local Data for Radial Location 7 in along Axial Direction for APort	186
Figure H-40: Local Data for Radial Location 12 in along Axial Direction for APort.....	187
Figure H-41: Initial 200 s of Local Data for Radial Location 12 in along Axial Direction for APort	187
Figure H-42: Local Data for Radial Location 17 in along Axial Direction for APort.....	188
Figure H-43: Initial 200 s of Local Data for Radial Location 17 in along Axial Direction for APort	188
Figure H-44: Local Data for Radial Location 23.5 in along Axial Direction for APort.....	189
Figure H-45: Initial 200 s of Local Data for Radial Location 23.5 in along Axial Direction for APort	189
Figure H-46: Local Data for Radial Location 0.5 in along Axial Direction for BPort	190

Figure H-47: Initial 200 s of Local Data for Radial Location 0.5 in along Axial Direction for BPort.....	190
Figure H-48: Local Data for Radial Location 7 in along Axial Direction for BPort	191
Figure H-49: Initial 200 s of Local Data for Radial Location 7 in along Axial Direction for BPort.....	191
Figure H-50: Local Data for Radial Location 17 in along Axial Direction for BPort	192
Figure H-51: Initial 200 s of Local Data for Radial Location 17 in along Axial Direction for BPort.....	192
Figure H-52: Local Data for Radial Location 23.5 in along Axial Direction for BPort	193
Figure H-53: Initial 200 s of Local Data for Radial Location 23.5 in along Axial Direction for BPort.....	193
Figure H-54: Local Data for Radial Location 17 in along Axial Direction for CPort	194
Figure H-55: Initial 200 s of Local Data for Radial Location 17 in along Axial Direction for CPort.....	194
Figure H-56: Local Data for Radial Location 23.5 in along Axial Direction for CPort	195
Figure H-57: Initial 200 s of Local Data for Radial Location 23.5 in along Axial Direction for CPort.....	195

LIST OF TABLES

Table 2-1: Froude Numbers for Angle Variation (Horizontal Break)	28
Table 2-2: Froude Numbers for L/D Variation (Vertical Break)	29
Table 2-3: Scaling Parameter Ratios for Angle Variation (Horizontal Break)	31
Table 2-4: Scaling Parameter Ratios for L/D Variation (Vertical Break).....	31
Table 2-5: Reynolds Number Ratios for Scaled Design	31
Table 3-1: Engineering Design Parameter Ratios for Angle Variation (Lower Side Break)...	33
Table 3-2: Engineering Design Parameter Ratios for Angle Variation (Higher Side Break) ..	33
Table 3-3: Engineering Design Parameter Ratios for L/D Variation (Top Break)	34
Table 3-4: Reynolds Number Ratios for Engineering Design	34
Table 3-5: Oxygen Analyzer Accuracy for Oxygen Content Range	39
Table 3-6: Flowmeter Adjustments with Actual Flow Rate Range	42
Table 3-7: Data Acquisition System Components	52
Table 3-8: Axial Locations for Lower Side Break.....	58
Table 3-9: Radial Locations for Lower Side Break	59
Table 3-10: Axial Locations for Higher Side Break	60
Table 3-11: Radial Locations for Higher Side Break	61
Table 4-1: Room Oxygen Content for Normalization of Data	66
Table 4-2: Cut-off Times for the Lower Side Break.....	69
Table 4-3: Cut-off Times for the Higher Side Break	69
Table 4-4: Areas for Enclosed Regions for Lower Side Break.....	78
Table 4-5: Areas for Enclosed Regions for Higher Side Break	81

NOMENCLATURE

A = area of cross section of break pipe

D = diameter of break pipe

D_h = hydraulic diameter of pipe

Fr = Froude number

g = gravitational constant

L = length of break pipe

Pe = Peclet number

Q = volumetric flow rate

r = radius

Re = Reynolds number

Sc = Schmidt number

t = time

j = local superficial exchange velocity

V = Mixing volume

Greek Letters

ρ = density of fluid

μ = dynamic viscosity of fluid

θ = angle

ν = kinematic viscosity

Δ = difference

Subscripts/Superscripts

H = Higher density fluid (air)

k = fluid

L = Lower density fluid (helium)

HA = Helium-Air

P,HA = Prototypic Helium-Air

R = Ratio

S,HA = Scaled Helium-Air

WB = Water-brine

Units

C = Celcius

cm = centimeters

F = Fahrenheit

in = inches

K = Kelvin

kg = kilograms

L = liters

m = meter

min = minutes

mm = millimeters

kPa = kilopascals

psi = pounds per square inch

s = seconds

scfh = standard cubic feet per hour

W = watts

ACKNOWLEDGEMENTS

First and foremost, I would like to thank my mother, Patricia Baird, my father, Robert Baird, and my family in its entirety for their love, support, and encouragement throughout my graduate studies at the Pennsylvania State University.

I would like to express much gratitude to my advisor, Professor Seungjin Kim, for the opportunity to be part of this research project. His guidance and expertise have been extremely valuable throughout the duration of my graduate education. I would also like to acknowledge Dr. Cheung and Dr. Motta for reviewing this manuscript.

Special thanks are due to the students in the Advanced Multiphase Flow Laboratory (Frank Nedwidek, James Spring, Justin Talley and Mohan Yadev) for their help and support. I would like to thank my roommates Eric So and Flavio Griggio who kept me motivated throughout my graduate studies. My appreciation goes out to Jackie Grandel, my friend and sister that I never had, who has been there to support me since the beginning of my educational career at Penn State.

The success of this project could not have been accomplished without the financial support from the U.S. Nuclear Regulatory Commission.

Chapter 1

Introduction

1.1 Research Background and Objectives

A Loss-of-Coolant Accident (LOCA) of particular interest when considering the design of a Very High Temperature Reactor (VHTR) is the Depressurized Loss of Forced Convection (D-LOFC). This type of scenario may be caused by a large crack or double-ended guillotine break to either the horizontal primary core inlet and outlet flow duct or the vertical refueling standpipe at the top of the vessel. When depressurization of the reactor vessel occurs, helium is blown down into the reactor containment and mixes with air. Once pressure between the reactor vessel and containment equalizes, the air-helium mixture inside reactor containment will begin to flow into the vessel at the rupture location with a simultaneous outflow of helium. The density difference between the two fluids is the primary reason for this gravity driven exchange flow. This postulated scenario was first identified by Schultz (1996) and it was noted that the ingress rate may vary depending on the rupture location.

As ingress progresses air mixes with helium inside the vessel, the density difference between the containment and vessel fluids decreases and ingress slows. The ingress of air into the reactor vessel may lead to oxidation of the in-core graphite structure. Ultimately, this could lead to a release of radioactive material to the environment in an extreme case.

It is the conventional idea that there exist two stages of ingress after depressurization and gravity driven exchange namely, molecular diffusion and natural circulation. As time progresses and the gravity driven exchange slows, molecular diffusion and natural circulation become more important. While some previous studies (Takeda, 1997, Takeda and Hishida, 1996, Oh et al.,

2006, and No et al., 2007) focused mainly on diffusion, Oh et al. (2008) described gravity driven exchange as an important stage of ingress and further confirmed this idea in Oh et al. (2009). The present study focuses primarily on the gravity driven exchange as it is the initial stage to determine the exchange rate and degree of ingress. This will allow for the evaluation of the time required for mitigation when such an event should occur.

Currently, there are no predictive models for postulated LOCA scenarios in the VHTR. Also, the database for air ingress to establish models is limited. For this reason, the main objectives of this research are to perform scaled adiabatic and heated experiments with helium and air as working fluids to provide a more extensive understanding of the gravity driven exchange flow phenomena and also to establish a database for systems analysis code development and validation. This study aims to achieve the following:

- To design a test facility capable of performing adiabatic and heated experiments with helium and air as the working fluids. The facility is designed to perform separate-effects experiments on pipe breaks including (1) break location i.e., primary pipe (horizontal) and standpipe (vertical), (2) pipe break Length-to-Diameter ratio (L/D) and (3) break orientation i.e., angle of inclination.
- To perform scaled adiabatic helium-air experiments using the horizontal side breaks and break length $L/D = 3$. Oxygen concentration is monitored during the experiments with an oxygen analyzer at various radial locations and several axial locations within the test apparatus.

1.2 Literature Review

Gravity driven exchange flows have been studied extensively in the past due to its relevance to ventilation and air handling, the management of waste water, and accident scenarios throughout numerous disciplines. These studies investigated factors such as the speed and shape of the front, characteristics of the interface, and the exchange flow rate. This section will discuss the previous works both theoretical and experimental for gravity driven exchange flow which may be valuable background for this study.

One of the first to consider a heavy fluid moving with constant velocity intruding into a light fluid was von Karman (1940). An intrusion of muddy water into a clear reservoir or salt water into fresh water was considered for this analysis. The front of the heavier fluid travels at about a constant speed and maintains a consist shape. So, the flow was considered relative to a reference frame moving with the heavier fluid as shown in Figure 1-1.

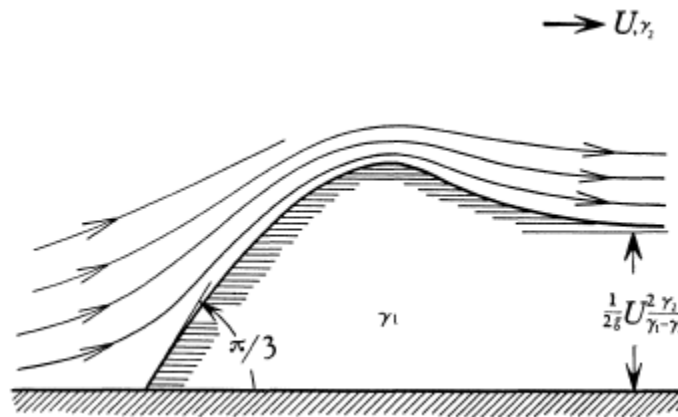


Figure 1-1: Reference Frame Moving with Heavier Fluid (von Karman, 1940)

It can also be seen from the figure that the slope at the head is determined to be approximately $\pi/3$ or 60 degrees. In this work, energy conservation was considered and an equation for the thickness of the heavy fluid layer, y , was developed and is given by:

$$y = \frac{\gamma_2}{\gamma_1 - \gamma_2} \frac{U^2}{2g} \quad (1-1)$$

where γ_1 is the specific gravity of the heavier fluid, γ_2 is the specific gravity of the lighter fluid, U is the velocity of the front and g is the gravitational constant.

Yih and Guha (1955) developed a mathematical formulation to predict the interface between the two fluid layers of stratified flow. It was shown that a hydraulic jump which can be described by a change in depth of the propagating front is formed. Conservation of momentum was used to develop the formulation for the two fluid layers to determine the jump conditions and the depth downstream of the jump. In order to model the change in depth of each layer due to the occurrence of the hydraulic jump, interfacial shear was neglected and a hydrostatic pressure distribution was assumed. An oil and water mixing experiment was used to verify the predictions of this formulation.

Benjamin (1968) considered two approaches for flow-force balance or momentum flux with pressure force, an analysis of energy-conserving flow and flow with energy loss. For this theory, the problem of flow past a cavity represented by Figure 1-2 was considered.

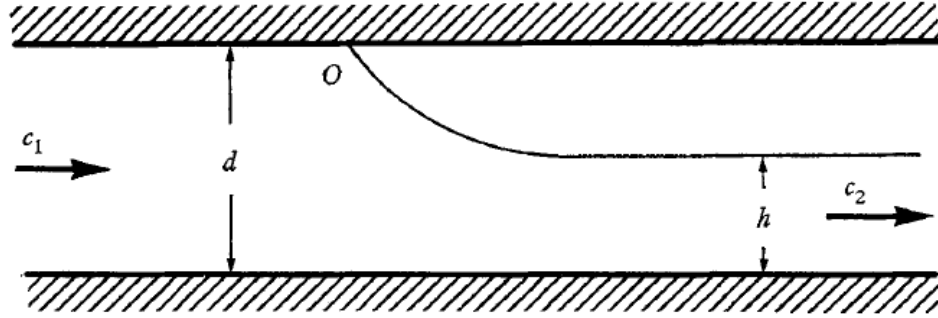


Figure 1-2: Reference Frame for Flow Past a Cavity (Benjamin, 1968)

In the analysis for no energy loss, an equation was deduced for the velocity far downstream, c_2 given by:

$$c_2^2 = \frac{g(d^2 - h^2)d}{(2d - h)h} \quad (1-2)$$

where g is the gravitational constant, d is the space between the planes, and h is the depth far downstream.

This equation corresponds to that derived by von Karman (1940). It was also determined that the solutions for this equation are given by:

$$h = d \text{ or } h = \frac{1}{2}d \quad (1-3)$$

For the analysis of flow with energy loss, it was found that the other possible solution is given by:

$$\frac{c_1}{(gd)^{1/2}} = \left[\frac{h(d^2 - h^2)}{d^2(2d - h)} \right]^{1/2} \quad (1-4)$$

It was determined that it is possible for the receding stream to fill more than half the depth ($h > \frac{1}{2}d$) if there is energy loss and it is impossible to have $h < \frac{1}{2}d$ as an external energy supply would be necessary to maintain the flow. Here, the maximum energy flux is obtained at $h/d = 0.6527$.

Experiments were performed by Leach and Thompson (1975) to investigate a depressurization accident in a Magnox reactor. For these experiments, water and brine and carbon dioxide and air were used as simulant fluid pairs. The horizontal pipe was considered with a length-to-diameter ratio range from 0.5 to 20. A sealed box of brine connected to a tank filled with water by a pipe was the apparatus used for these experiments. The weight of the brine container was recorded with respect to time using a force transducer. For the carbon dioxide and air experiments a pipe with a quick release valve was connected to a box filled with carbon dioxide. The quick release valve was initiated to allow the ingress of air and the concentration change in the box was measured with respect to time. In order to estimate the volumetric flow rate, a dimensional analysis was performed using the measured parameters from the experiments. A preventative action of purging the reactor vessel with carbon dioxide was suggested to prevent further ingress of air. The flow rate at which the carbon dioxide needed to be supplied to displace the air was also determined. A non-dimensional number identified as the discharge coefficient was used to express the results of the experiments. This discharge coefficient scales the inertia force with respect to the buoyancy force and is given by:

$$C_D = \frac{Q}{\sqrt{gD^5\Delta\rho/\rho}} \quad (1-5)$$

where Q is the measured volumetric exchange rate, g is the gravitational constant, D is the diameter of the pipe, $\Delta\rho$ is the density difference between the fluids and ρ is taken to be the density of either fluid as the density difference is small.

From the results, it was determined that the discharge coefficient is constant and the L/D ratio does not significantly affect the exchange flow.

Mercer and Thompson (1975) investigated buoyancy-driven exchange flows in inclined and vertical ducts. The experimental setup consisted of a 455 dm³ tank of brine connected to a duct which was submerged in a 1364 dm³ tank of water. The ducts investigated in this study covered a L/D range from 3.5 to 18 and inclination angle 0 to 90 degrees. A quick-release seal is removed from the end of the duct in order to initiate the experiment. For this study, two experiments were performed; first, the entire system was tilted with the duct connected normal to the compartments and second, only the break was tilted with the duct connected to the compartments at the angle of inclination. In order to determine the exchange flow rate, the weight of one compartment was measured with respect to time. A non-dimensional parameter similar to the discharge coefficient used by Leach and Thompson (1975) was used to express the results. This parameter is non-dimensional flow rate, q^* and is given by:

$$q^* = \frac{Q}{\sqrt{D^5g\Delta\rho/\rho}} \quad (1-6)$$

It was determined that q^* was not dependent on the L/D ratio and the results were found to agree with Leach and Thompson (1975). The results were plotted as q^* with respect to inclination angle. The value of q^* was observed to increase until an inclination angle between 0 and 15 degrees and decrease for any further increase in angle as shown in Figure 1-3. This graph also shows that the value of q^* is greater for smaller L/D ratios.

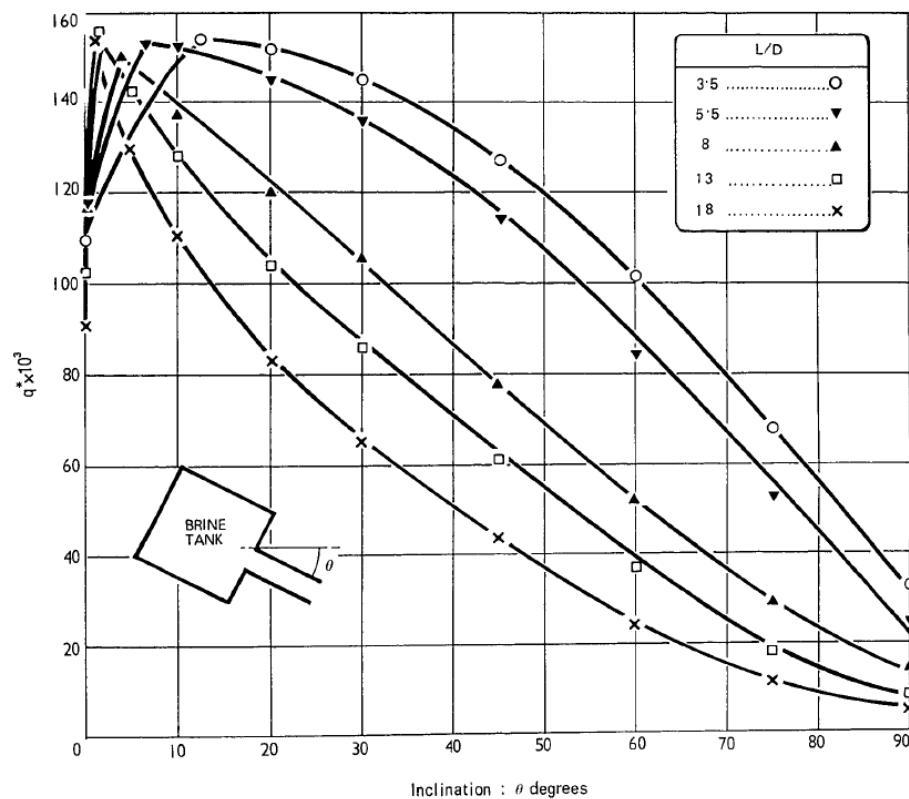


Figure 1-3: Data Plotted as q^* with respect to Inclination Angle (Mercer and Thompson, 1975)

Epstein (1988) investigated buoyancy-driven exchange flow through openings in a horizontal partition. The apparatus used for these experiments was a rectangular plexiglass tank 0.55 m square with a depth of 0.762 m. In order to divide the tank into an upper and lower compartment, a horizontal partition was implemented 0.33 m from the bottom. There was an

opening in the partition to mount either a simple orifice cut in a thin metal plate or a plexiglass tube. The tests were performed with water and brine with the density of brine ranging from 1028 to 1188 kg/m³. The length-to-diameter ratios considered in this study varied from 0.015 to 10. To perform the experiment, the lower tank was filled with water and the upper tank was filled with brine. A rubber stopper was used to initiate the countercurrent flow of water and brine through the opening. A hydrometer was used to measure the density in the upper tank at 2 minute intervals. The volume rate of flow for this study is given by the following equation:

$$Q = \frac{-V_H(d\rho_H/dt)}{(\rho_H - \rho_{L,0}) - \frac{V_H}{V_L}(\rho_{H,0} - \rho_H)} \quad (1-7)$$

where V_H and V_L are the volume of the heavy and light (brine and water) fluid, respectively, ρ_H is the density of brine at time t , and $\rho_{L,0}$ and $\rho_{H,0}$ are the density of water and brine, respectively at time equal to zero.

It was observed that the density change in the upper tank decreased linearly with time. The volumetric exchange rate is plotted as Froude number with respect to L/D shown in Figure 1-4. Here, Froude number is defined by the following:

$$Fr = \frac{Q}{\sqrt{D^5 g \Delta \rho / \bar{\rho}}} \quad (1-8)$$

where $\bar{\rho}$ is the mean density of the two fluids given by:

$$\bar{\rho} = \frac{\rho_H + \rho_L}{2} \quad (1-9)$$

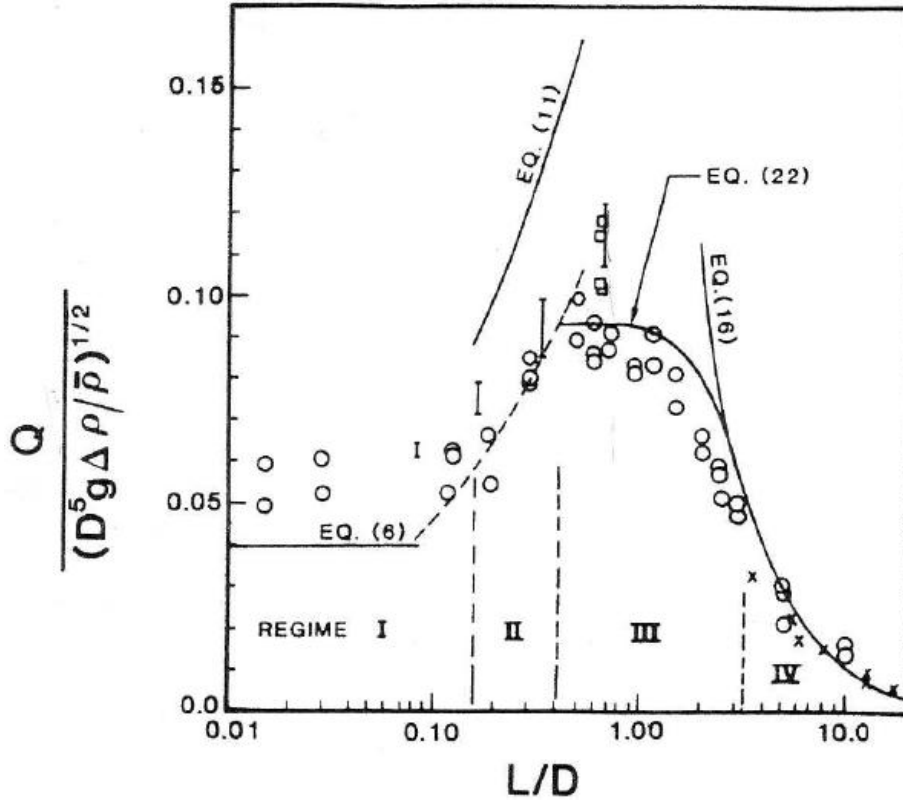


Figure 1-4: Data Plotted as Froude Number with respect to L/D (Epstein, 1988)

It can be seen from the figure that the Froude number increases until L/D is approximately equal to 0.6 at which point any further increase in L/D leads to a decrease in the Froude number. The data presented in the figure was divided into the following four exchange regimes: (I) an oscillatory exchange flow regime for small L/D described by Taylor wave theory, (II) a countercurrent Bernoulli flow regime described by an inviscid exchange flow model by the applying Bernoulli's equation (Brown, 1962), (III) a combined turbulent binary diffusion and Bernoulli flow regime the intermediate flow regime between II and IV described by Bernoulli type flow at the ends of the tube and turbulent diffusion at the center of the tube and (IV) a pure turbulent binary diffusion regime for large L/D described by chaotic mixing of the two fluids

leading to slower exchange between the compartments. An empirical correlation was developed and it was found to correspond quite well to the experimental data.

Another study by Keller and Chyou (1991) investigated the problem of hydraulic lock-exchange. Conservation of mass and momentum were used to formulate the hydraulic theory for this study. Here, gravity currents are studied for small density differences, $r \geq 0.281$, and large density differences, $0 < r \leq 0.281$, where r is the density ratio. It was assumed that both gravity currents were energy conserving and that the currents were connected by a long expansion wave and an internal hydraulic jump for small density difference as shown in Figure 1-5.

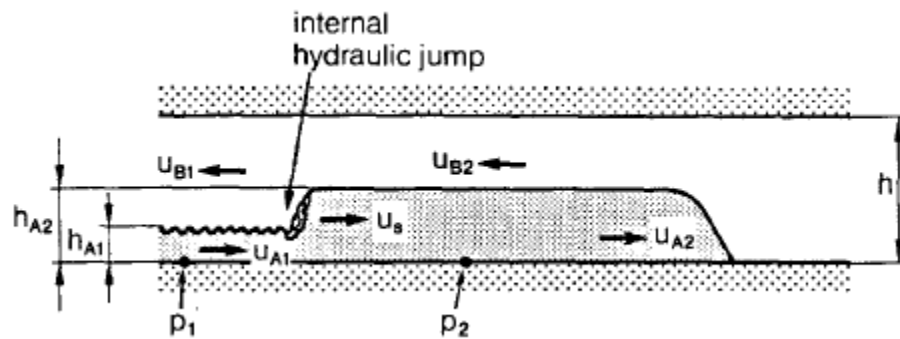


Figure 1-5: Gravity Currents for Small Density Differences (Keller and Chyou, 1991)

For large density differences, it was assumed that the heavier current was dissipative and that the currents were connected only by a long expansion wave as shown in Figure 1-6.

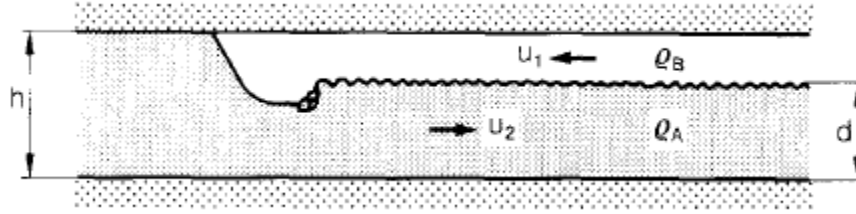


Figure 1-6: Gravity Currents for Large Density Differences (Keller and Chyou, 1991)

Aside from the theory, experiments were also performed. The test apparatus used for these experiments was a plexiglass channel 40 mm square with a length of 500 mm. A sliding gate driven by compressed air was installed to divide the channel. Various fluid pairs were considered in these experiments covering the entire density range from 0 to 1. It is found that the results are generally consistent with the proposed theory, but there was some influence by the viscous or wall friction effect.

In a study by Fumizawa (1992), helium air exchange flow was investigated through horizontal, vertical and inclined openings. The experimental test apparatus was a cylinder with a 194 mm diameter and 400 mm height which had an opening diameter of 20 mm and a height range of 0.5 to 200 mm. The height to diameter H/D range was from 3.5 to 18 and the apparatus was able to be tilted to inclination angles of 0 to 90 degrees. Three types of openings were examined including orifice, round, and long tube. Orifice implying a disregarded height effect as compared to the diameter, round indicating a comparable height and diameter, and long tube in which there was a disregarded diameter as compared to the height. An electronic balance was used to measure the change in mass throughout the experiments. The Mach-Zehnder interferometer, an optical system was used to visualize the helium-air exchange flow pattern. It was deduced that flow rate decreases with time as there is a simultaneous decrease in the density difference with time. The flow rate through round openings was found to be greater as compared

to orifices and tubes. The densimetric Froude number was constant with change in time, but was found to be larger for round openings than for orifices and tubes. Froude with respect to increasing H/D was constant for orifice, increased to reach a maximum for round, and decreased for tubes. The data from this experiment compared well to previous water brine results from Epstein and Mercer. For horizontal openings, the results from the interferometry showed an upward plume of helium and a downward plume of air that had a lateral swing with a 10s period. In this case there was no boundary and there was strong interaction between the helium and air indicating that the flow is very unstable. The helium traveled along the top and air along the bottom portion of the passage with a smooth interface between the fluids as shown from the interferometry for inclined openings. Here, the exchange flow rate and densimetric Froude number were the largest at 30 degrees.

Gröbelbauer et al. (1993) investigated lock-exchange flow with gases of different densities. The experiments were performed in a channel with a cross-section of $0.3 \times 0.3 \text{ m}^2$ and total length of 3.8 or 4.5 m. The channel is separated by a quick-opening gate which is used to initiate the experiments. The following fluid pairs were considered: CO_2/Argon , Argon/Air , $\text{R22}/\text{Argon}$, $\text{R22}/\text{Air}$, Air/Helium , $\text{Argon}/\text{Helium}$ and $\text{R22}/\text{Helium}$. From the results, it was concluded that gravity fronts of high density ratio are significantly different in propagation speed and shape from low density ratios gravity fronts (Boussinesq).

A three-stage process was identified by Hishida et al. (1993) for a stand pipe rupture accident. These are depressurization, air ingress by exchange flow, and air ingress by natural convection. The test apparatus and results for the air ingress exchange flow stage is the same as that described in Fumizawa (1992) as shown in Figure 1-7 and Figure 1-8.

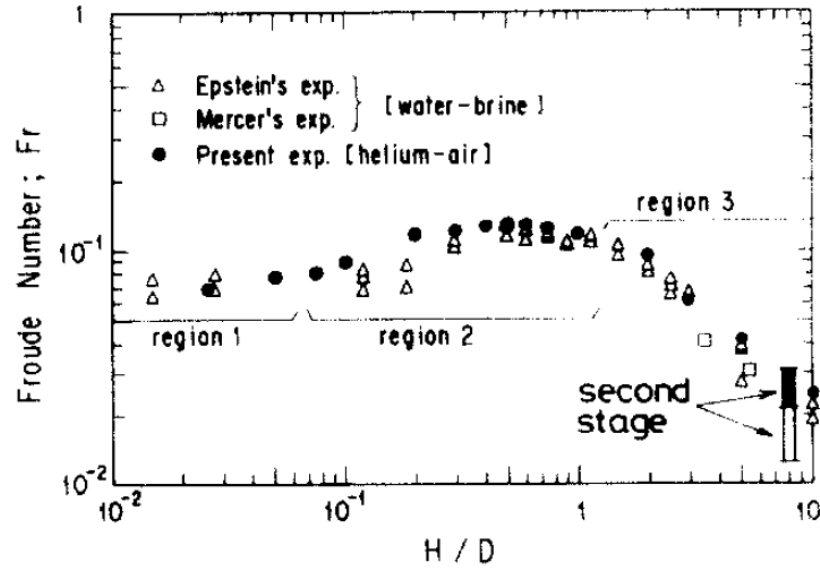


Figure 1-7: Data Plotted as Froude Number with respect to H/D (Hishida et al., 1993)

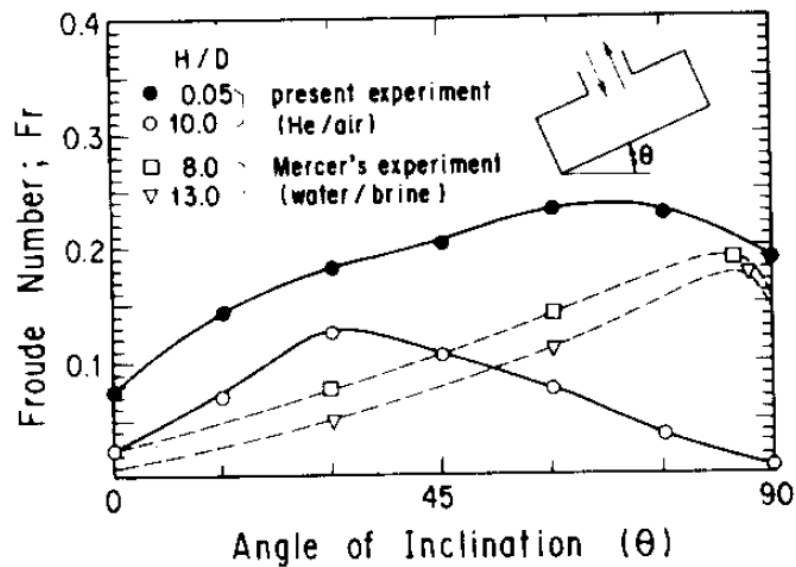


Figure 1-8: Data Plotted as Froude Number with respect to Inclination Angle (Hishida et al., 1993)

The test apparatus used for the natural convection stage was two hemispheres connected by a vertical pipe. The lower hemisphere simulated the top cover of the reactor vessel and the bottom plate of the hemisphere which is capable of being heated simulated the top surface of the

reactor core. The environment outside of the reactor or the reactor containment was simulated by the upper hemisphere. The vertical pipe that connected the lower and upper hemispheres simulated the stand pipe. The fluids used for these experiments were He, O₂, N₂, and CO₂. A laser-Doppler anemometer was used to measure the flow rate of the counter-flow in the replicated stand pipe and the smoke method was used to visualize the flow behavior. It was determined from the flow visualization and velocity measurements that the flow pattern was extremely complicated and the fluids within the pipe interacted strongly with each other.

A study performed by Tanaka et al. (2002) focused on the effects of the physical properties of gases and inclination angle on buoyancy driven exchange flow of two different gases. Three simulant fluid pairs were investigated, Helium-air, Argon-air, and SF₆-air, and the inclination angle was varied from 15 degrees to 90 degrees in 15 degree intervals. The test apparatus used in these experiments was a cylindrical tank of dimensions, 350 mm inner diameter, 350 mm length that was connected to a rectangular channel of dimensions, 5 mm width, 50 mm height, and 100 mm length. Net exchange flow rate was measured by an electronic mass and a laser-Doppler anemometer was used to measure the velocity profile. It was noted that molecular diffusion plays a significant role in gas-gas exchange as compared to liquid-liquid exchange. Through these experiments, it was found that there were two counterflow streams with a vortical circulation layer at the interface between the counterflow streams for each of the exchange flow pairs. An increase in inclination angle caused an increase in the cross-channel height of the vortical circulation flow layer. It was also concluded that with no increase in inclination angle the Grashof number and Schmidt number in the range of 1,000 to 10,000 and 0.22 to 1.4 respectively, did not affect the exchange flow pattern. Although, there was an increase in the non-dimensional net exchange flow rates with an increase in the Grashof and Schmidt number. It was observed that the axial velocity profiles of the inward and outward flow were

practically symmetrical. As the inclination angle was increased, the location of the peak inward and outward velocities moved toward the channel wall causing a decrease in the peak velocities. The results are plotted as exchange flow rate, q with respect to inclination angle as shown in Figure 1-9. It can be seen that q increases with an increase in the angle until reaching a maximum around $5\pi/12$ (75°) and decreases with any further increase in angle.

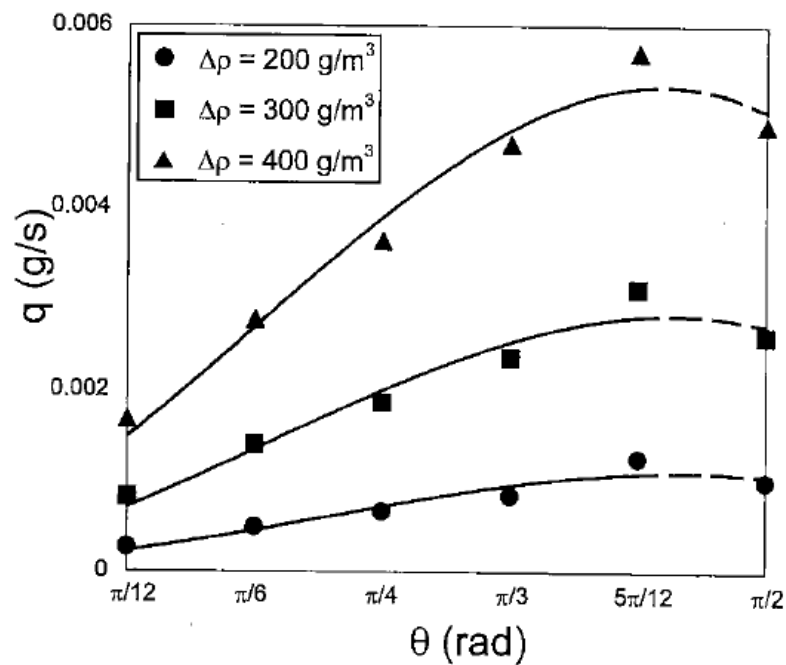


Figure 1-9: Data Plotted as Exchange Flow Rate with respect to Inclination Angle

(Tanaka et al., 2002)

Lowe et al. 2005 performed experiments on both fluids having small density differences (Boussinesq lock exchange) and large density differences (non-Boussinesq lock exchange). The test apparatus used to investigate the lock exchange was a rectangular channel with a removable lock gate. The tank had length of 182 cm, a width of 23 cm, and a depth of 20 cm. A shadowgraph was used to visualize the flow and video and photographs were used to measure the

depth and the front positions of the flow interface. Density ratios between 0.6 and 1 were studied in these experiments. For Boussinesq lock exchange, it was found that the speeds were constant for both currents and almost equal. The flow was identified to be symmetrical about the centerline meaning that each current occupies half the depth of the channel just as in previous studies. It was seen that the heavier current traveled at a faster but constant speed as compared to the lighter current in non-Boussinesq lock exchange. For this case, the heavier current was found to occupy less than half the depth of the channel. The theory proposed by Keller and Chyou (1991) was derived again in this study. The two categories of lock-exchange flow proposed are presented in Figure 1-10, (a) a left-propagating energy-conserving light current and a right-propagating energy-conserving heavy current, connected by a long wave of expansion and a bore, and (b) a left-propagating energy-conserving light current and a right-propagating dissipative heavy current, connected by an expansion wave.

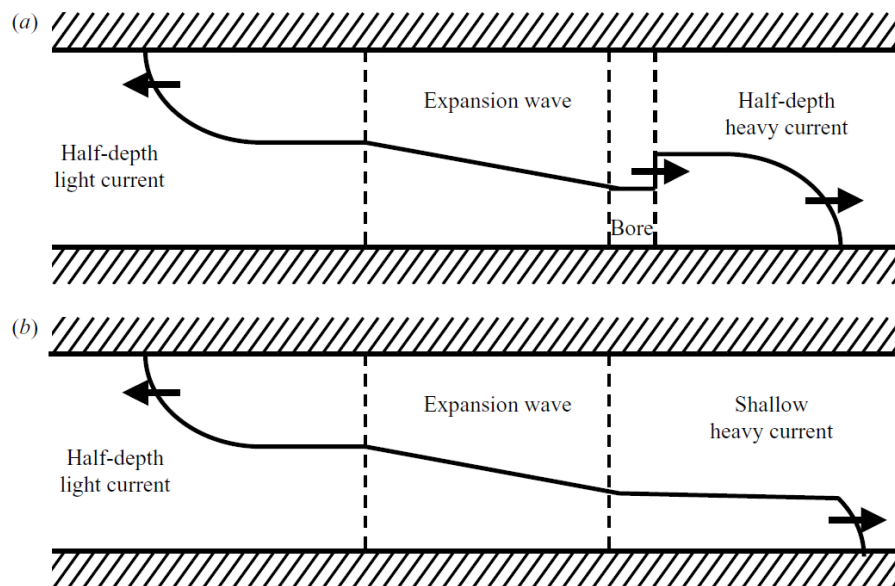


Figure 1-10: Schematic of Two Categories of Lock-exchange Flows (Lowe et al., 2005)

This study by Lowe et al. (2005) was extended to consider the lock-exchange category with only an expansion wave connecting the gravity currents as shown in Figure 1-10 (*b*). This non-Boussinesq exchange flow was considered for the complete range of density ratios. The experimental results were compared to computational simulations by Birman et al. (2005). A left-propagating energy-conserving light current and a right-propagating dissipative heavy current, connected by an expansion wave was found to be most representative of the non-Boussinesq lock exchange flow. This outcome was in disagreement with the theory proposed by Keller & Chyou (1991) which assumed both the currents to be energy conserving and connected by an expansion wave and an internal hydraulic jump.

1.3 Water-Brine Scoping Experiments

A previous study by Sarangi (2010) performed scoping experiments using water and brine as the working fluids to investigate the effects of geometric parameters on gravity driven exchange. The test apparatus used for the scoping experiments was scaled based on the Gas Turbine Modular Helium Reactor (GT-MHR) and consisted of two narrow rectangular acrylic compartments connected by pipes of varying lengths. The apparatus was mounted on a rail system in order to position it at various inclination angles. The length-to-diameter ratios and inclination angles investigated in this study were 0.63, 3.0 and 5.0 and 0, 15, 30, 45, 60, 75 and 90 degrees, respectively. A hydrometer was used to measure the time rate of change of the mixture density, which was used to obtain the volumetric exchange rate. From this flow visualization study, it was found that the mixture density changed linearly with time during the initial stage of ingress and as the ingress progressed, the mixture density began to change non-linearly with time. The results of the initial stage compared well to that of previous studies, but the results as the ingress progressed did not. The average Froude number followed a similar trend

as compared to that of previous studies, but the angle at which the peak Froude number occurred was higher. The Froude numbers of the initial stage were found to compare more with previous data than the average Froude number of the complete exchange. The overall exchange rate was found to be of the order of 70% lower than the exchange rate obtained by considering only the initial linear region of the exchange. It was determined from these experiments that the geometry of the compartment and angle of inclination have significant impacts on the ingress rate.

These scoping experiments using water and brine provided a basic understanding of gravity driven exchange that is expected in the helium-air experiments. However, there may be various differences due to the fluid properties and compartment geometry. The flow pattern may be different as the lock exchange in this study is considered to be Boussinesq as the density difference is small, but the helium-air density difference is much larger and the lock exchange is considered to be non-Boussinesq (Lowe et al., 2005). Molecular diffusion may play a more significant role because the diffusivity between helium and air is approximately 10^4 times greater than that for water and brine. Moreover, the ingress rate may differ from water and brine as the dynamic viscosity is about 10^2 times greater for helium-air (Fumizawa, 1992).

Chapter 2

Scaling Analysis

2.1 Scaling Parameters

In the present study, the experiments are performed using helium and air as working fluids in a scaled test apparatus. The scaling analysis used to design the helium-air test apparatus is based on the approach described in previous work by Kim and Talley (2009). The reference VHTR used for the scaling of the helium-air test apparatus is the Gas Turbine Modular Helium Reactor (GT-MHR) designed by General Atomics provided in MacDonald et al. (2003). The locations of importance for the air ingress scenario are identified as the two pipelines that connect to the vessel as shown by the schematic of the GT-MHR in Figure 2-1. These pipelines are the horizontal primary core inlet and outlet flow duct and the vertical refueling standpipe. In the present scaling analysis, the scaling parameters with and without temperature effects are considered. It is noted, however, that the present study focuses on the hydrodynamic effects in the gravity driven air ingress phenomenon. As such, the temperature effects are not considered.

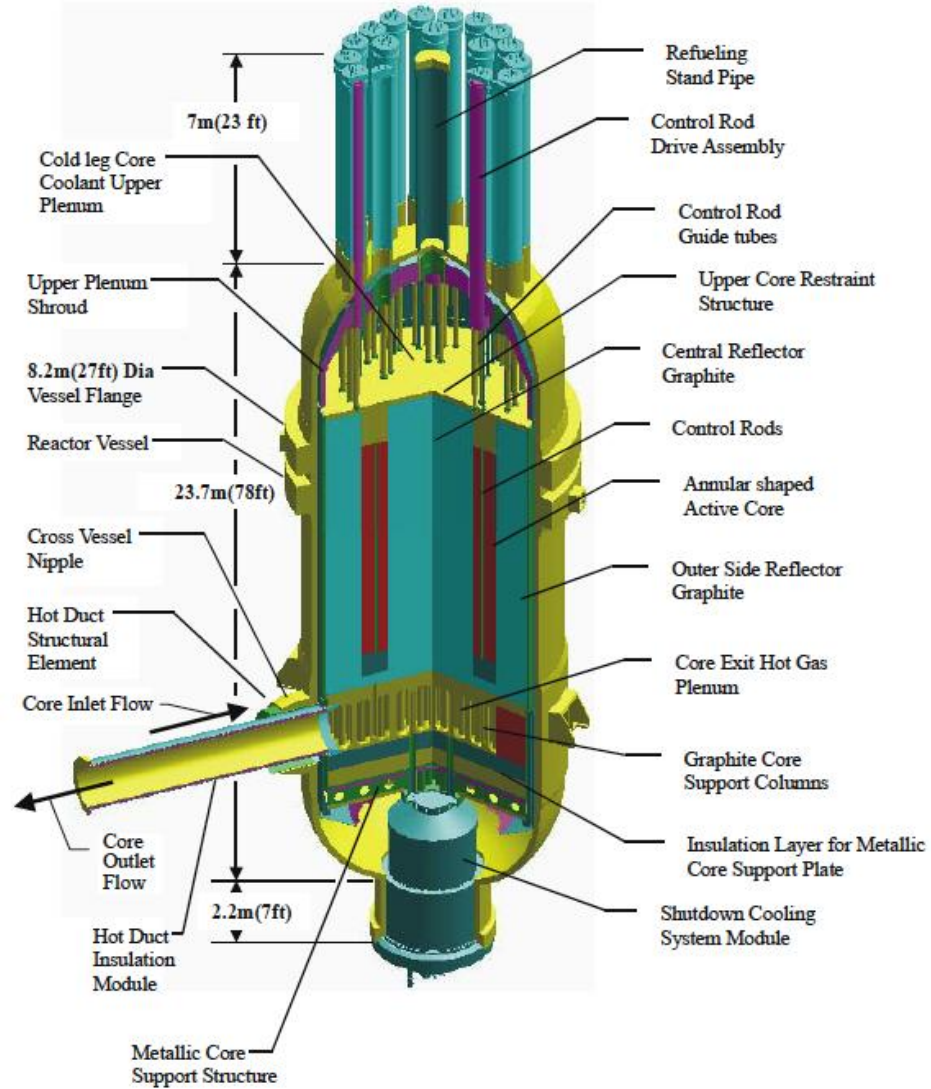


Figure 2-1: Schematic of VHTR (MacDonald et al., 2003)

Based on previous adiabatic studies by Mercer (1975) and Epstein (1988), Froude number is identified as the main non-dimensional number that accounts for geometric effects on gravity driven exchange. The Froude number is defined as the ratio of inertia force with respect to the buoyancy force and is given by:

$$Fr = \frac{j_k}{\sqrt{Dg\Delta\rho/\bar{\rho}}} \quad (2-1)$$

where k denotes the fluid (k is given as H or L indicating the heavier or lighter fluid, respectively), D denotes the diameter of the break, g is the gravitational constant, $\Delta\rho$ represents the density difference between the two fluids and $\bar{\rho}$ is the mean density of the two fluids. In this equation, j_k is the superficial fluid exchange velocity given by:

$$j_k = \alpha_k u_k \quad (2-2)$$

where u is the fluid exchange velocity and α denotes the area occupied by fluid k with respect to the total cross-sectional area of the pipe break given by:

$$\alpha_k = \frac{A_k}{A} \quad (2-3)$$

As the exchange rate is the major variable of significance for the air-ingress phenomena, it is important to note that the Froude number can be written in terms of the volumetric exchange rate given by:

$$Fr = \frac{Q}{A\sqrt{Dg\Delta\rho/\bar{\rho}}} \quad (2-4)$$

where Q denotes the volumetric exchange rate and A denotes the area of the break. The volumetric flow rate can be measured by observing the density change throughout the duration of the experiment. The equation from Epstein (1988) used for the water-brine scaling has been modified using mass balance for helium-air and is given by:

$$Q = \frac{V_L \frac{d\rho_L}{dt}}{(\rho_{H,0} - \rho_L)} \quad (2-5)$$

where V_L is the volume of the light fluid, ρ_L denotes the mixture density at time, t and $\rho_{H,0}$ is the initial density of the heavy fluid.

The major scaling parameter ratios (ratio between scaled helium-air and prototypic helium-air cases) for the design of the helium-air test apparatus are identified in previous work by Kim and Talley (2009) and are indicated by the following:

Froude Number Ratio:

$$Fr]_R = Fr_{S,HA} / Fr_{P,HA} \quad (2-6)$$

Global Exchange Rate Ratio:

$$Q]_R = Q_{S,HA} / Q_{P,HA} \quad (2-7)$$

Local Exchange Rate Ratio:

$$j]_R = j_{S,HA} / j_{P,HA} \quad (2-8)$$

Exchange Time Ratio:

$$t_G]_R = t_{G,S,HA} / t_{G,P,HA} \quad (2-9)$$

where S,HA and P,HA represent scaled helium-air and prototypic helium-air, respectively.

There are two different exchange ratios to consider for the fluid exchange rate, the global exchange rate ratio and the local exchange rate ratio. The global exchange rate ratio considers the entire volumetric fluid exchange, while the local exchange rate ratio considers the local fluid exchange velocity within the break alone. The volumetric exchange rate ratios can be deduced by the Froude number equation and are given by:

$$Q]_R = \frac{Fr_{S,HA}(\sqrt{D^5 g \Delta \rho / \bar{\rho}})_{S,HA}}{Fr_{P,HA}(\sqrt{D^5 g \Delta \rho / \bar{\rho}})_{P,HA}} \quad (2-10)$$

and

$$j]_R = \frac{Fr_{S,HA}(\sqrt{D g \Delta \rho / \bar{\rho}})_{S,HA}}{Fr_{P,HA}(\sqrt{D g \Delta \rho / \bar{\rho}})_{P,HA}} \quad (2-11)$$

Here, the Froude number ratio between the scaled and prototypic facility is equal to one because the two systems consider the same fluid pair. For this reason, these equations reduce to the following:

$$Q]_R = \frac{(\sqrt{D^5 g \Delta \rho / \bar{\rho}})_{S,HA}}{(\sqrt{D^5 g \Delta \rho / \bar{\rho}})_{P,HA}} \quad (2-12)$$

and

$$j]_R = \frac{(\sqrt{Dg\Delta\rho/\bar{\rho}})_{S,HA}}{(\sqrt{Dg\Delta\rho/\bar{\rho}})_{P,HA}} \quad (2-13)$$

These equations show that the exchange rate ratios are dependent on the break diameter and fluid properties.

The time ratio scales the total time required for complete exchange of the fluids for a given exchange volume and is given by:

$$t_G]_R = \frac{(V/Q)_{S,HA}}{(V/Q)_{P,HA}} \quad (2-14)$$

where V and Q are the volume and the volumetric exchange rate, respectively.

The Reynolds number is also investigated in order to scale the ratio of inertial forces to viscous forces of the fluid for the horizontal breaks.

$$Re_k = \frac{\rho_k j_k D_{h,k}}{\mu_k} \quad (2-15)$$

where ρ_k is the density of the fluid, j_k is the superficial fluid exchange velocity, D_h is the hydraulic diameter and μ_k is the viscosity of the fluid.

It is assumed that each fluid occupies half the depth of the pipe break diameter. Hence, the hydraulic diameter is given by:

$$D_h = \frac{4 \times (Area)}{Perimeter} = \frac{4 \left(\frac{1}{2} \pi \frac{D^2}{4} \right)}{\left(\frac{1}{2} \pi D + D \right)} = \frac{\pi D}{\pi + 2} \quad (2-16)$$

The superficial fluid exchange velocity can be calculated using the Froude numbers deduced from the previous studies. Thus, the Reynolds number can be rewritten by:

$$Re = \frac{\rho D_h (Fr \sqrt{Dg\Delta\rho/\bar{\rho}})}{2\mu} \quad (2-17)$$

Before performing heated experiments, several other non-dimensional numbers should be considered in order to investigate the effects of temperature and the other stages of air ingress, molecular diffusion and natural circulation. These are the Schmidt and Peclet and are described below.

Schmidt number is calculated to investigate viscous diffusion with respect to molecular diffusion and is given by:

$$Sc = \frac{\nu}{D} \quad (2-18)$$

where ν is the kinematic viscosity and D is the mass diffusivity.

The mass diffusivity, D_{ab} is calculated using an equation from Poling et al. (2001) given by:

$$D_{ab} = \frac{0.00266 \times T^{3/2}}{P M_{ab}^{1/2} \sigma_{ab}^2 \Omega_D} \quad (2-19)$$

where T is the temperature (K), P is the pressure (bar), σ_{ab} denotes the characteristic length (Å) and Ω_D represents the diffusion collision integral. Here, M_{ab} is given by:

$$M_{ab} = 2[(1/M_a) + (1/M_b)]^{-1} \quad (2-20)$$

where M_a and M_b are the molecular weights of gas a and b .

The characteristic length, σ_{ab} is given by:

$$\sigma_{ab} = \frac{\sigma_a + \sigma_b}{2} \quad (2-21)$$

In this equation, Ω_D is solely a function of kT/ε_{ab} where ε_{ab} is the characteristic energy given by:

$$\varepsilon_{ab} = (\varepsilon_a \varepsilon_b)^{1/2} \quad (2-22)$$

The values for Ω_D are tabulated as a function of kT/ε in Hirschfelder et al. (1954) and are used in this calculation of mass diffusivity of helium and air.

Peclet number scales the ratio of convective diffusion to molecular diffusion and is given by Reynolds number multiplied by Schmidt number:

$$Pe = Re \cdot Sc \quad (2-23)$$

2.2 Scaling Approach and Results

The scaling parameter ratios discussed are calculated based on the approach described in this section. For this approach, the Froude number, break pipe size, global and local exchange rate ratios, and exchange time ratio are determined.

Froude number:

The Froude numbers for a given angle and length-to-diameter ratio are estimated by using Figure 1-7 and Figure 1-8 from Hishida et al. (1993). It is important to note that these Froude numbers are obtained under adiabatic conditions and temperature effects are not considered. Table 2-1 and Table 2-2 show the Froude numbers that are used from Hishida et al. (1993).

Table 2-1: Froude Numbers for Angle Variation (Horizontal Break)

Angle (degrees)	Fr (L/D = 10, He-Air)
0 (vertical)	0.03
15	0.07
30	0.13
45	0.11
60	0.08
90 (horizontal)	0.01

Table 2-2: Froude Numbers for L/D Variation (Vertical Break)

L/D	Fr (Angle = 0°, He-Air)
0.06	0.0800
0.13	0.1000
0.5	0.1300
0.75	0.1200
1	0.1100
5	0.0400
10	0.0200

In order to be consistent with Hishida et al. (1993), the break inclination angles and length-to-diameter ratios used in this scaling analysis are chosen to be those from the tables above.

Pipe break size:

In order to determine the pipe break diameter for the scaled helium-air design, the size is varied from 0.635 cm (0.25 in) to 7.62 cm (3 in) for the coaxial primary core inlet/exit duct (horizontal break) and 2.54 cm (1 in) to 15.24 cm (6 in) for the refueling standpipe (vertical break). The pipe dimensions used for the prototypic case are taken to be the diameter of the VHTR hot-leg of approximately 1.5 m for the break angle effect and standpipe diameter of approximately 0.75 m for the L/D effect (Richards et al., 2006).

Global and local exchange rate ratios:

The scaling analysis is performed for both the adiabatic (unheated) and heated conditions. So, the global and local exchange rate ratios are obtained by using equations 2-12 and 2-13 and the fluid properties of helium and air for each condition. For the unheated condition, the fluid temperatures for both helium and air are chosen to be 20°C. The fluid temperatures for the prototypic condition are chosen to be 950°C for helium and 43°C for air. For the scaled heated

condition, the fluid temperatures are chosen to be 200°C and 20°C for helium and air, respectively.

Exchange time ratio:

The height to diameter ratio for the prototypic case is approximately equal to three. In order to be consistent with this ratio of three, the scaled design is determined to have a height of 182.88 cm (72 in) and a nominal diameter of 60.96 cm (24 in). For the scaled design, the horizontal break is based on a pipe break on the side of the test apparatus that is aligned with bottom of the vessel and the vertical break is based on a pipe break on the top of the vessel. In regard to these break locations, the exchange volume for the horizontal break is defined by the diameter of the pipe break and a complete volume exchange is assumed for the vertical break. The dimensions for the GT-MHR are used to estimate the volume exchange for the prototypic helium-air case for both the horizontal and vertical breaks. For the primary break, it is assumed that air will displace helium up to the line parallel to the top of the break. This volume is calculated to be approximately 94,000 liters (24,770 gallons), which is about 27% of the total volume within the reactor vessel. Since a complete volume exchange is assumed for the standpipe break, the entire volume of helium will be exchanged for air in containment. The total volume of helium in the GT-MHR is approximately 351,000 liters (92,600 gallons). The exchange volumes are calculated in Kim and Talley (2009) and are provided in Appendix A.

Based on an exchange time ratio closest to unity, the scaled pipe break diameter is determined to be 4.45 cm (1.75 in) for the horizontal break and 5.72 cm (2.25 in) for the vertical break. The scaling parameter ratios calculated for the unheated and heated helium-air conditions based on these pipe break diameters are shown in Table 2-3 for the horizontal break and Table 2-4 for the vertical break.

Table 2-3: Scaling Parameter Ratios for Angle Variation (Horizontal Break)

	$Fr]_R$	$Q]_R$	$j]_R$	$t_G]_R$	diameter, cm (in)
Unheated Helium-Air	1	1.363×10^{-4}	0.155	1.015	4.45 (1.75)
Heated Helium-Air	1	1.438×10^{-4}	0.164	0.962	4.45 (1.75)

Table 2-4: Scaling Parameter Ratios for L/D Variation (Vertical Break)

	$Fr]_R$	$Q]_R$	$j]_R$	$t_G]_R$	diameter, cm (in)
Unheated Helium-Air	1	1.446×10^{-3}	0.249	1.053	5.72 (2.25)
Heated Helium-Air	1	1.525×10^{-3}	0.263	0.998	5.72 (2.25)

The Reynolds number ratio is calculated for the horizontal breaks considering both fluids.

Table 2-5 provides the Reynolds number ratios for helium and air for the scaled design.

Table 2-5: Reynolds Number Ratios for Scaled Design

	$Re]_{R, \text{helium}}$	$Re]_{R, \text{air}}$	diameter, cm (in)
Unheated Helium-Air	0.0521	5.372×10^{-3}	4.45 (1.75)
Heated Helium-Air	0.0245	5.666×10^{-3}	4.45 (1.75)

Chapter 3

Experimental Facility

3.1 Engineering Design of Test Apparatus

The dimensions of the helium-air test apparatus are slightly modified from the scaling analysis results determined in the previous section due to practical engineering design considerations, simplicity, and machining capabilities.

A carbon steel pipe with a nominal diameter of 60.96 cm (24 in) and a height of 182.88 cm (72 in) is chosen to simulate the test apparatus. In order to compare the experimental data to computational results in the future, the design is simplified to incorporate flat plates rather than hemispheres at the top and bottom of the vessel. There are flanges at the top and bottom of the vessel to attach the plates. The top plate has two holes to implement a pressure gauge and a recirculation line to more quickly reach a desired temperature for the heated experiments. There are 13 holes in the bottom plate, one for the helium supply, one for the vacuum pump, and the remaining holes are instrumentation ports. The engineering drawings of the vessel, top plate, and bottom plate are in Appendix B.

There are three break locations, two on the side of the vessel and one on the top of the vessel. In order to investigate pipe breaks of various lengths, a flange design is implemented. Due to machining restrictions caused by this flange design, the side break could not be located at the very bottom of the vessel. Therefore, the center of the lower side break is oriented 11.43 cm (4.5 in) above the bottom of the vessel. A second side break is incorporated into the design and the

center of the pipe is located 34.29 cm (13.5 in) above the bottom. The second side break is to compare the helium-air data with the water-brine data, which accounts for the geometry effect. The top vertical break is located at the center of the vessel top. In order to simplify the design of the pipe break, an inner diameter of 5.08 cm (2 in) is chosen for both the horizontal and vertical break. This is between the two values of 4.45 cm (1.75 in) and 5.72 cm (2.25 in) determined in the scaling. As the pipe break diameter is modified from the scaling results, the parameter ratios are recalculated for the 5.08 cm (2 in) pipe break diameter and are shown in Table 3-1, Table 3-2 and Table 3-3. The pipe breaks are connected to a base flange, which can be attached to the vessel flange. The length-to-diameter ratios for the pipe breaks are chosen to be 1.0, 3.0, and 5.0. A L/D ratio of essentially zero can also be obtained at the vessel flange with a 7.62 cm (3 in) diameter break. There is also a unique flange that will be used to attach glass pipes at the break which will be used to obtain velocity information by Laser Doppler Anemometry (LDA) in future experiments. The engineering drawings of the pipe breaks are shown in Appendix B.

Table 3-1: Engineering Design Parameter Ratios for Angle Variation (Lower Side Break)

	$Fr]_R$	$Q]_R$	$j]_R$	$t_G]_R$	diameter, cm (in)
Unheated Helium-Air	1	1.904×10^{-4}	0.166	2.285	5.08 (2)
Heated Helium-Air	1	2.008×10^{-4}	0.175	2.166	5.08 (2)

Table 3-2: Engineering Design Parameter Ratios for Angle Variation (Higher Side Break)

	$Fr]_R$	$Q]_R$	$j]_R$	$t_G]_R$	diameter, cm (in)
Unheated Helium-Air	1	1.904×10^{-4}	0.166	6.023	5.08 (2)
Heated Helium-Air	1	2.008×10^{-4}	0.175	5.711	5.08 (2)

Table 3-3: Engineering Design Parameter Ratios for L/D Variation (Top Break)

	$Fr]_R$	$Q]_R$	$j]_R$	$t_G]_R$	diameter, cm (in)
Unheated Helium-Air	1	1.077×10^{-3}	0.235	1.414	5.08 (2)
Heated Helium-Air	1	1.136×10^{-3}	0.248	1.340	5.08 (2)

The Reynolds number ratios are also reevaluated for the engineering design for the horizontal breaks and are shown in Table 3-4.

Table 3-4: Reynolds Number Ratios for Engineering Design

	$Re]_{R, \text{helium}}$	$Re]_{R, \text{air}}$	diameter, cm (in)
Unheated Helium-Air	0.0636	6.564×10^{-3}	5.08 (2)
Heated Helium-Air	0.0299	6.922×10^{-3}	5.08 (2)

There are 68 individual instrumentation ports at four angular locations (A through D) each with 17 axial locations (1 through 17) on the side of the vessel. The ports are spaced evenly every 15.24 cm (6 in) along the entire height of the vessel and some are spaced more closely at the break locations. The port dimensions and locations on the vessel can be seen in the drawings in Appendix B. A photograph of the test apparatus is shown in Figure 3-1.

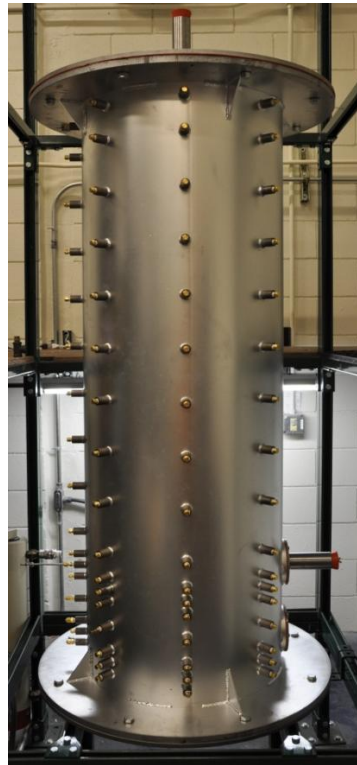


Figure 3-1: Photograph of Test Apparatus

3.2 Test Facility and Instrumentation

The gasket used to seal the top and bottom plates and pipe break components to the vessel flanges is made of an extreme-temperature silicone rubber. It has a thickness of 3.18 mm (1/8 in), and can be used in the temperature range of -51.1°C to 260°C (-60°F to 500°F) with a durometer hardness of 50 scale A (medium). A high temperature push-in tapered expandable round silicone rubber plug is used to seal the pipe break before initiation of the experiments. These plugs are capable of withstanding temperatures up to 287.78 °C (550°F) and have a durometer hardness of 55 scale A. In order to fit into the pipe inner diameter of 5.08 cm (2 in), the tapered plug that is used for $L/D = 1.0$, 3.0, and 5.0 has ends of 5 cm (1-31/32 in) and 6.27 cm (2-15/32 in) with a thickness of 2.54 cm (1 in). An L/D of essentially zero can also be achieved by fitting the vessel flange with a tapered plug of 7.46 cm (2-15/16 in) and 8.97 cm (3-17/32 in)

with a thickness of 3.89 cm (1-17/32 in). Figure 3-2 below shows one of the smaller plugs inserted into the higher side pipe break.

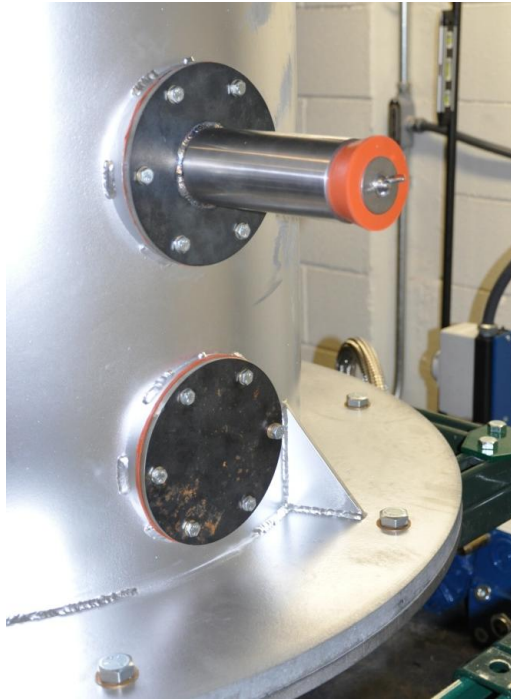


Figure 3-2: Photograph of Plug in Higher Side Break

In consideration of the future heated experiments, a water-based epoxy called Nansulate EPX provided by INDUSTRIAL NANOTECH Inc. is used as a thermal insulation coating. It has a thermal conductivity of 0.027 W/mK at 20°C and 3.18 mm (1/8 in) thickness as documented in Appendix C. This coating is applied on the top and bottom plates of the vessel to minimize the heat loss during the heated experiments as shown in Figure 3-3. The inside of the vessel is sprayed with specialty high heat paint for temperatures rated up to 600°C.



Figure 3-3: Photograph of Nansulate EPX Applied to Top Plate

A Quincy Compressor Model QV-1.5 HP Rotary Vane Vacuum Pump rated at ACFM at 759 mm HgV (29.9 in HgV) is used to evacuate the vessel before filling it with helium. The vacuum pump is direct driven by a flange-mounted motor and it has an inlet check valve mounted internally. The system is air-cooled with a high-efficiency multi-stage exhaust filter with fluid mist removal. The vacuum pump is connected to the test apparatus by 1.91 cm (0.75 in) stainless steel flexible tubing and is shown in Figure 3-4.



Figure 3-4: Photograph of Quincy Compressor Model QV-1.5 HP Rotary Vane Vacuum Pump

The oxygen concentration is measured during the experiments using an AMETEK Thermox CEM O₂/TM Trace Oxygen Analyzer shown in Figure 3-5. The operating range of the analyzer is 1 ppm to 100% O₂ with an accuracy of $\pm 2\%$ of the reading or 0.5 ppm O₂, whichever value is greater and $\pm 0.75\%$ of the reading or 0.05% O₂, whichever value is greater. Table 3-5 shows the accuracy for a given oxygen content with upper and lower boundaries. These accuracies are applied to a particular data set as shown in Figure 3-6 with a zoomed in version of the initial region in Figure 3-7. The repeatability is $\pm 0.5\%$ of reading or 0.1 ppm, whichever value is greater and $\pm 0.5\%$ of the reading or 0.1% O₂, whichever value is greater. A response time of less than 10 seconds at 1.0 L/min (2.12 scfh) to 90% of a 2-decade step change is documented in the manual (AMETEK, PDF). The analyzer is capable of sampling a flow up to a maximum inlet temperature of 204°C.



Figure 3-5: Photograph of AMETEK Thermox CEM O₂/TM Trace Oxygen Analyzer

Table 3-5: Oxygen Analyzer Accuracy for Oxygen Content Range

Oxygen Content Range	Accuracy	Upper Bound	Lower Bound
1600 ppm - 4999 ppm	$\pm 2\%$ of reading	reading $\times 1.02$	reading $\times 0.98$
0.5% - 6.66%	0.05% O ₂	reading + 0.05%	reading - 0.05%
6.67% - 21%	$\pm 0.75\%$ of reading	reading $\times 1.0075$	reading $\times 0.9925$

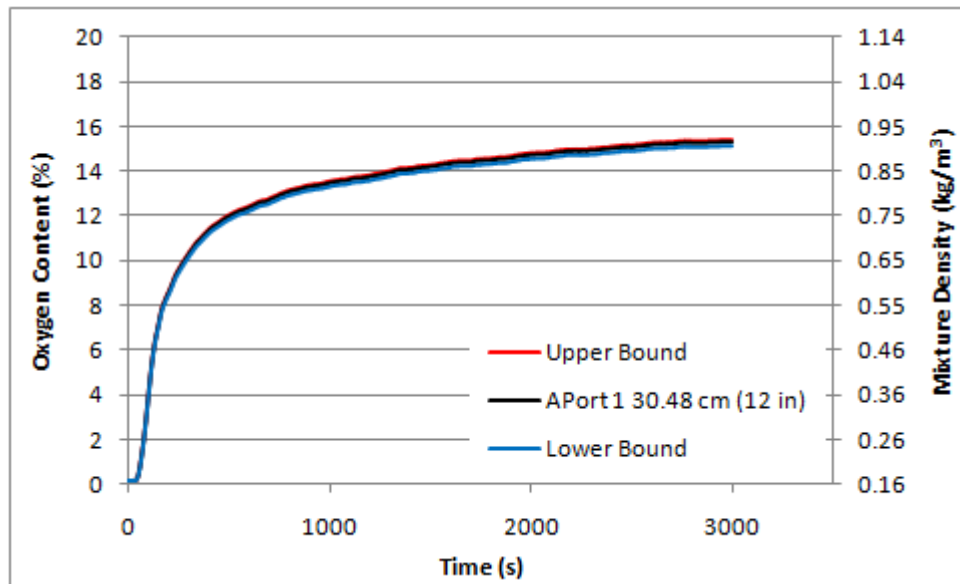


Figure 3-6: Oxygen Analyzer Accuracy Applied to a Data Set

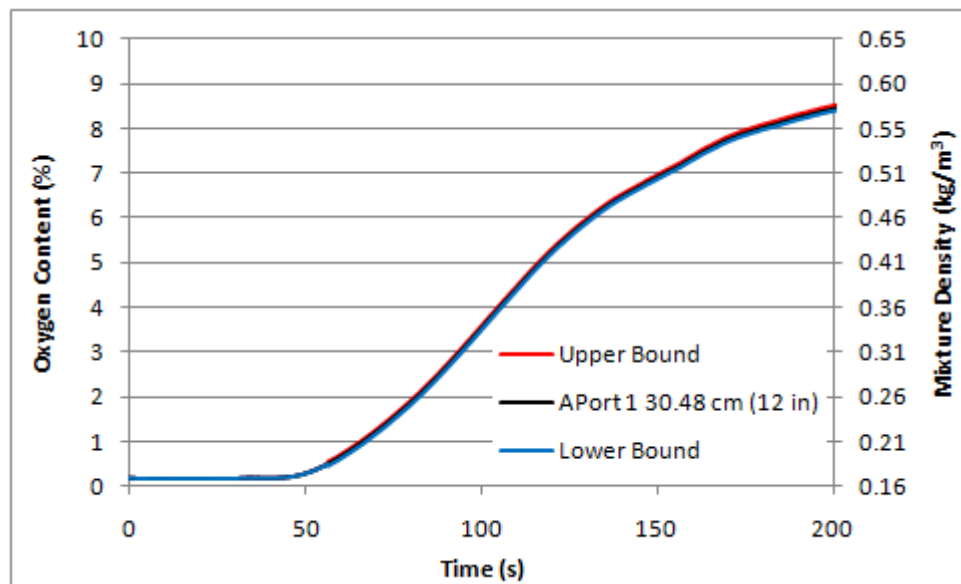


Figure 3-7: Initial 200 s of Oxygen Analyzer Accuracy Applied to a Data Set

The manufacturer supplied an aspirator for the oxygen analyzer outlet to induce a flow throughout the system. The engineering drawings for the system recommend an air supply in gauge pressure of 103.42 to 137.90 kPa (15 to 20 psig) to the aspirator regulator. The aspirator

regulator reduces this to a gauge pressure of approximately 34.47 kPa (5 psig) which induces a flow rate of about 4.72 L/min (10 scfh). A sampling rate of approximately 1.0 L/min (2.12 scfh) is suggested by the manual. In order to reduce the flow rate, a Dwyer air flowmeter is installed between the oxygen analyzer outlet and the aspirator as illustrated in Figure 3-8. The Dwyer air flowmeter (RMB-49-SSV) has a range of 0.24 to 2.36 L/min (0.5 to 5 scfh) with an accuracy of $\pm 5\%$.

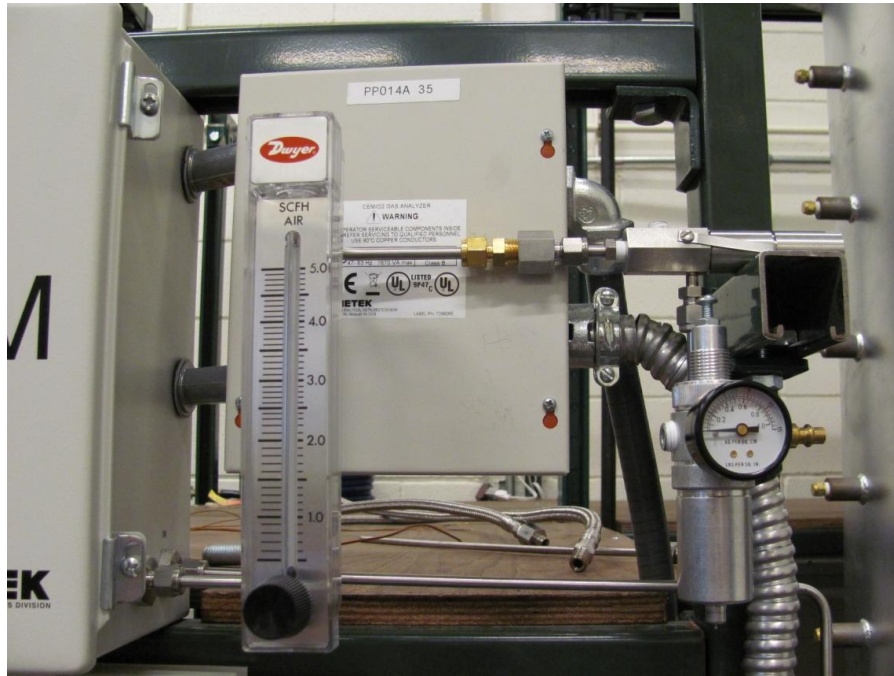


Figure 3-8: Photograph of Dwyer Flowmeter and Aspirator

While the flowmeter is calibrated for air, the flowmeter reading can be converted to a flow rate for other gases using equation 3-1 provided in the Dwyer catalog (Dwyer, Web 2009).

$$Q_{corr} = Q_{obs} \times \sqrt{\frac{1}{SG_x}} \quad (3-1)$$

where Q_{corr} is the corrected flow for specific gravity of gas x , Q_{obs} is the observed flowmeter reading, I is the specific gravity of air, and SG_x is the specific gravity of gas x being used in the flowmeter.

Since the specific gravity of the fluid mixture changes during the transient, the actual flow rate as indicated by the flowmeter also changes. For this reason, the experiments are performed by changing the regulated flow rate at several points during the transient. This is done to preserve a constant mixture flow rate at around 0.94 L/min (2 scfh). At the beginning of the experiment when the oxygen concentration is approximately zero, the flowmeter reading is set to 0.38 L/min (0.8 scfh) which corresponds to about 1 L/min (2.15 scfh) for helium. Since the flow rate decreases below 0.94 L/min (2 scfh) as the density of the sample increases, the flowmeter reading is increased by 0.09 L/min (0.2 scfh) at oxygen concentrations of 1.9%, 4.2%, 6.9%, 10.0% and 13.6% all of which correspond to about 1 L/min (2.15 scfh). The flowmeter adjustments are summarized in Table 3-6 below.

Table 3-6: Flowmeter Adjustments with Actual Flow Rate Range
(flow rate provided in liters per minute, L/min and standard cubic feet per hour, scfh)

Oxygen Concentration (%)	Flowmeter Adjustment, L/min (scfh)	Flow Rate Range, L/min (scfh)
0.0	0.38 (0.8)	1 - 0.81 (2.15 - 1.72)
1.9	0.47 (1)	1 - 0.84 (2.15 - 1.79)
4.2	0.57 (1.2)	1 - 0.87 (2.15 - 1.84)
6.9	0.66 (1.4)	1 - 0.89 (2.15 - 1.88)
10.0	0.76 (1.6)	1 - 0.90 (2.15 - 1.91)
13.6	0.85 (1.8)	1 - 0.92 (2.15 - 1.94)
17.5	0.94 (2)	1 - 0.94 (2.15 - 2.00)

A simple test was performed to ensure that the oxygen analyzer is operating properly. The gases used for this test are helium at approximately 3 ppm O₂ and compressed air at

approximately 21.7% O₂. These gases are each supplied through 6.35 mm (0.25 in) polyethylene flexible tubing which connect at a t-fitting that leads to the inlet of the oxygen analyzer. There is a valve on the compressed air line in order to control which fluid is supplied to the analyzer. First, the compressed air is supplied at a gauge pressure of about 34.37 kPa (5 psig) until a stable reading is observed on the analyzer. Next, the supply is switched to helium supplied at a gauge pressure of about 34.37 kPa (5 psig) until a stable reading is observed. Then, the supply is switched back to compressed air until the original oxygen content is reached. From Figure 3-9, it can be seen that the proper readings are observed for helium and air.

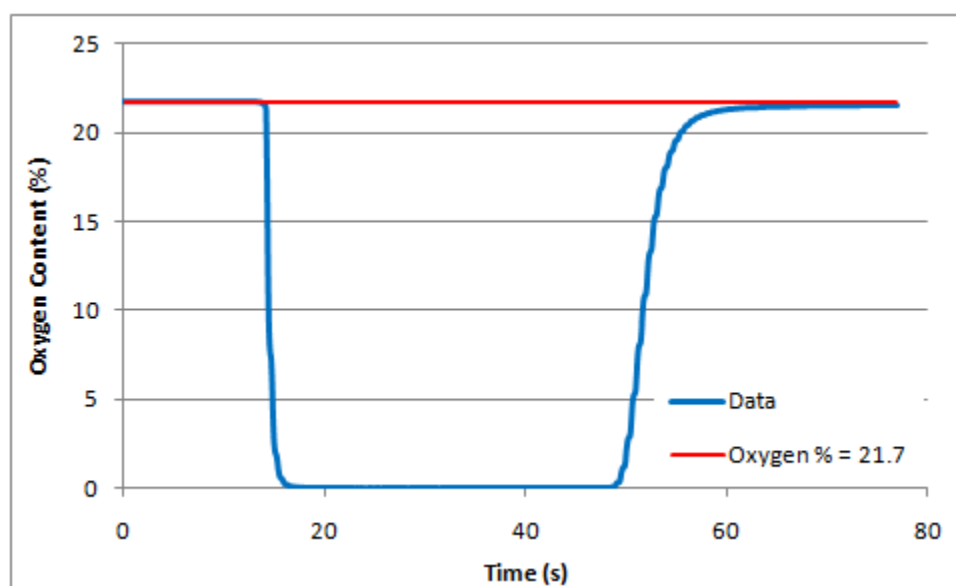


Figure 3-9: Confirmation of Oxygen Analyzer Measurement

The oxygen analyzer sample is collected through a combination of 6.35 mm (0.25 in) stainless steel tubing (hardline) and 6.35 mm (0.25 in) inner diameter stainless steel flexible tubing (flexline). The sampling probe that collects the sample within the vessel is 6.35 mm (0.25 in) stainless steel tubing with a wall thickness of 0.89 mm (0.035 in) that has a length of about 76.2 cm (30 in). The probe is connected to the 6.35 mm (0.25 in) inner diameter stainless steel

182.88 cm (72 in) flexible tubing using a Swagelok fitting with a Teflon ferrule set. The flexible tubing connects back to about 76.2 cm (30 in) of hardline which leads to the inlet of the oxygen analyzer. Based on a flow rate of about 0.94 L/min (2 scfh) and the volume of gas within the tubing, the time for the sample to travel from the vessel to the oxygen analyzer inlet is approximately 5.3 seconds.

A simple experiment to check the response time is performed for the test facility setup. The vessel is evacuated with the vacuum pump and backfilled with helium. Here, the sampling rate is based on a flowmeter setting of 0.94 L/min (2 scfh) for air. The sampling probe collects the helium from inside the vessel until a constant reading is observed on the oxygen analyzer. The probe is removed from the vessel and exposed to air until a stable reading is reached. A value in the ppm range is displayed on the analyzer when introducing helium to the system and a value of 20.8% is displayed on the analyzer when introducing air. It can be seen from Figure 3-10 that it takes approximately 75 seconds for the analyzer to read pure helium to air for the test facility setup.

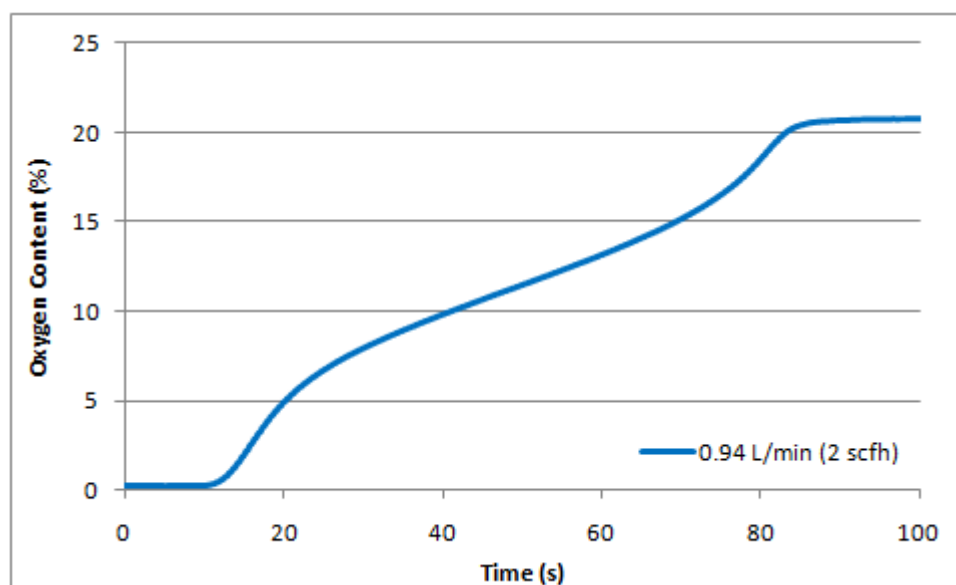


Figure 3-10: Test Facility Response Time

An OMEGA GCHAI series medium temperature steam, air, and gas circulation heater shown in Figure 3-11 will be used to heat the helium for the heated experiments. It is a 1.5 kW unit with a thermostat ranging from 93°C to 287°C. This heater is connected on the recirculation line which will be used to heat the helium for the heated experiments.



Figure 3-11: Photograph of OMEGA GCHAI Circulation Heater

A simple pressure gauge and a Rosemount 3051S Scalable Coplanar Pressure Transmitter (Model: 3051S1CD2A2F12A2AB1E5L4) are attached to the vessel to monitor the pressure. The pressure gauge is dial type with an operating pressure range of 0 to 103.42 kPa (0 to 15 psi) and 0 to -762 mm Hg (0 to -30 in Hg). It has an accuracy of $\pm 1\%$ full-scale and has a temperature range up to 232.22°C (450°F). The pressure transmitter has a range of 0 to 1269 mm H₂O (0 to 50 in H₂O) and has a 0.025% span accuracy (Rosemount, Web 2010).

A simplified line diagram is provided below in Figure 3-12 to show the connection of all components that make up the test facility. The hardline used for both the recirculation line and the line that connects the helium tank to the heater inlet is 1.91 cm (0.75 in) carbon steel pipe. There is a regulator on the helium tank to control the pressure supplied to the vessel. Valves are also included in various locations to manipulate the flow through the system. A photograph of the overall test facility is also provided in Figure 3-13.

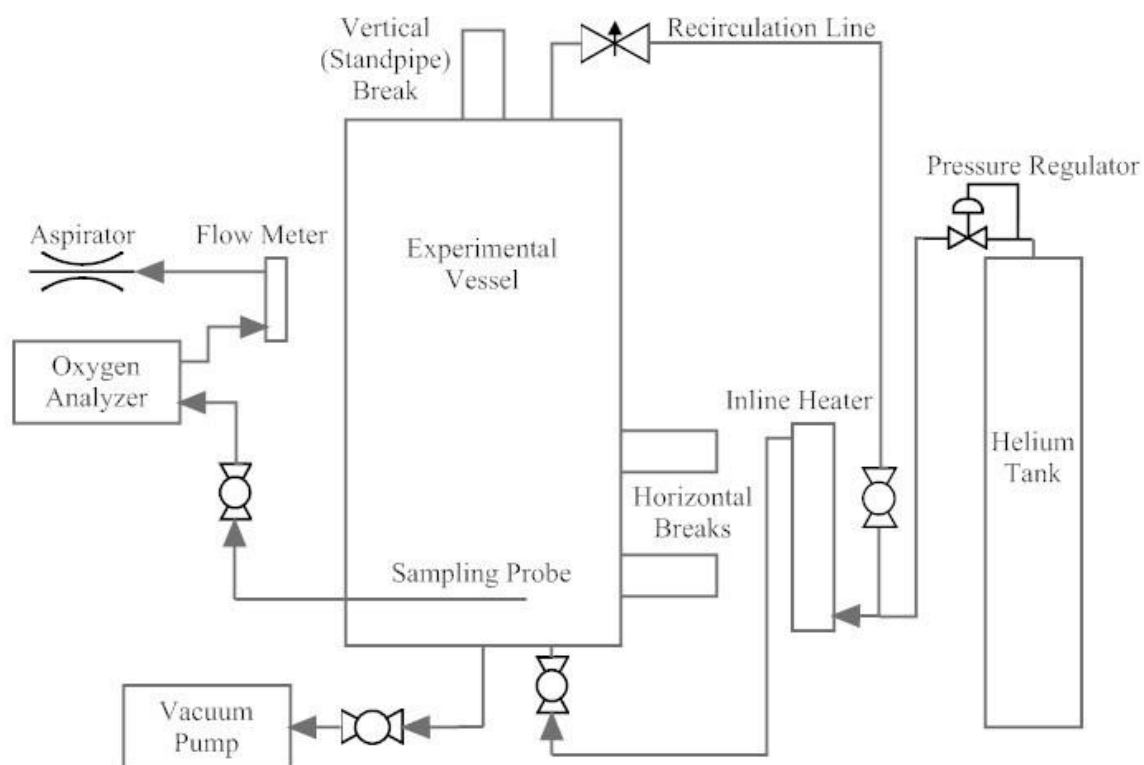


Figure 3-12: Schematic of Test Facility (not to scale)



Figure 3-13: Photograph of Experimental Test Facility

Thermocouples will be used to obtain temperature data at various radial and axial locations within the vessel for the heated experiments. The thermocouple wire is 24 gauge type T with special limits of error of $\pm 0.5^{\circ}\text{C}$ (0.4%) and a temperature range of 0°C to 350°C (TT-T-24-SLE). They are insulated with PFA Teflon or Neoflon rated from -267°C to 260°C .

An assembly of seven thermocouples is made for the calibration and response time experiment and heated shakedown tests. The TT-T-24-SLE thermocouple wire is arc welded at the end forming a bead diameter between 2.03 mm and 2.18 mm (0.080 in and 0.086 in) as shown in Figure 3-14. The time constant for the thermocouple wire is defined by OMEGA as the time required to reach 63.2% of an instantaneous temperature change in air. Based on the bead diameter, it is recognized that the time constant is approximately 5.8 seconds (OMEGA, Web). It

is also noted that for beaded-type thermocouples, the time constant should be multiplied by 1.5. Therefore, the time constant based on the documentation is about 8.7 seconds. A calibration of the thermocouples is performed as well as a response time experiment.

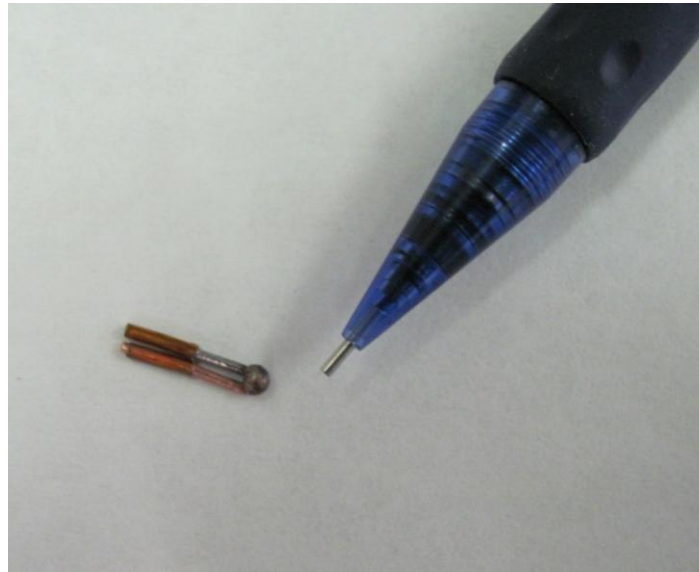


Figure 3-14: Photograph of Type T Thermocouple Bead Diameter

A precalibrated OMEGA thermocouple is used for the reference temperature for the calibration. The thermocouples are calibrated based on three point calibration using the test facility data acquisition system. The temperatures used for the three point calibration are 0°C, 23°C, and 100°C. The measured temperature is plotted versus the reference temperature for the seven thermocouples in Figure 3-15 with a zoomed in version in Figure 3-16.

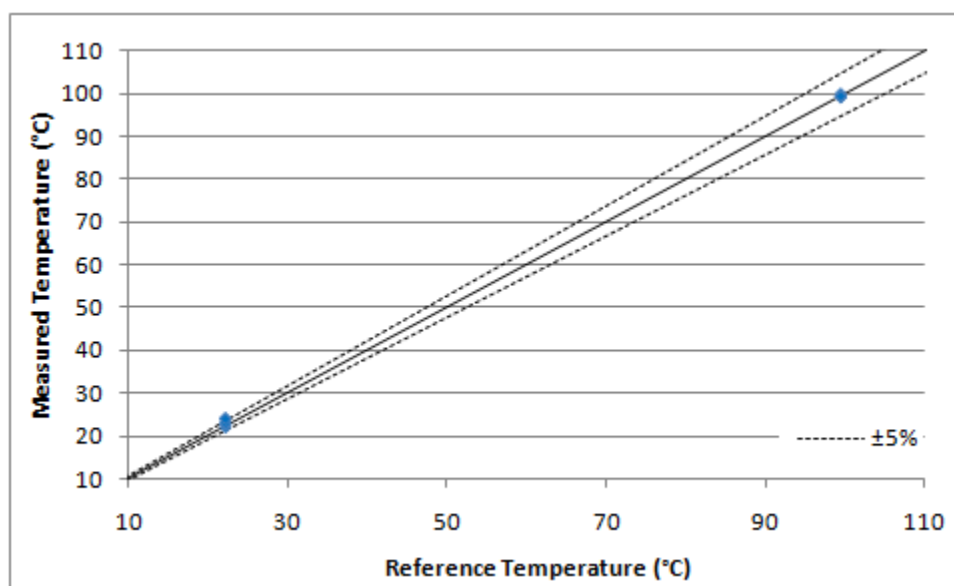


Figure 3-15: Measured Temperature with respect to Reference Temperature for Thermocouple Calibration

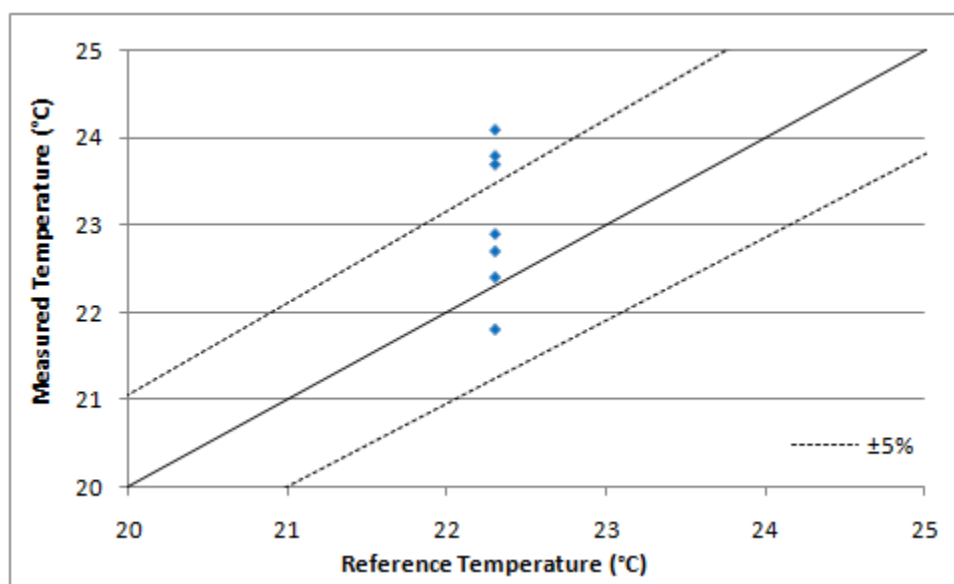


Figure 3-16: Region 20 to 25°C of Measured Temperature with respect to Reference Temperature for Thermocouple Calibration

For the response time experiment, the thermocouples are exposed to room temperature at about 23°C, submerged into boiling water at about 100°C, and returned to room temperature until a stable reading is observed. The thermocouple response plot is provided in Figure 3-17.

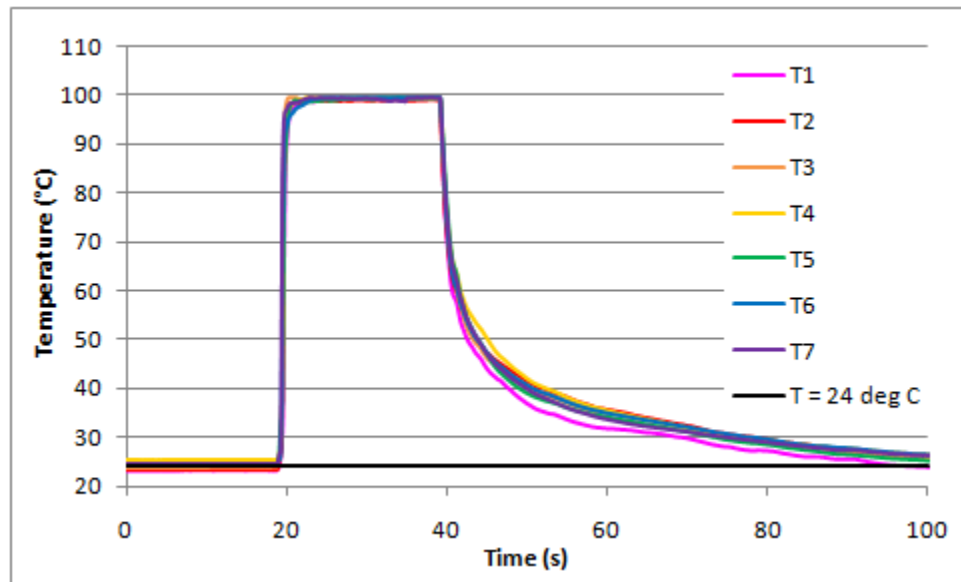


Figure 3-17: Thermocouple Response Time

Once the thermocouples are calibrated, it is necessary to find a way to bring them from the inside of the vessel to the data acquisition system in a sealed manner. In order to accomplish this, the thermocouples are fed through a short piece of 1.91 cm (0.75 in) tubing. The tubing is filled with Duralco 4461, a low viscosity epoxy rated at 260°C (500°F), encasing the thermocouples. The epoxy is allowed to set and a plug is formed around the thermocouple assembly as illustrated in Figure 3-18.

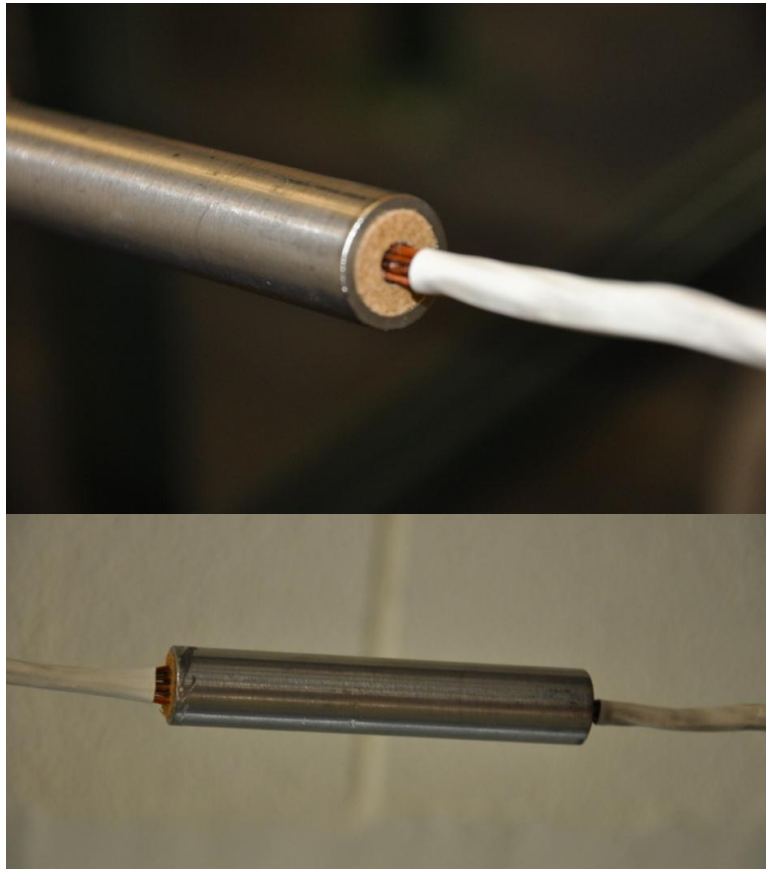


Figure 3-18: Photograph of Thermocouple Assembly Seal Plug

The tube used for the plug will be inserted into a 1.91 cm (0.75 in) Swagelok fitting that is threaded into one of the instrumentation ports in the bottom plate. One end of the TT-T-24-SLE thermocouples will be used for the temperature measurements and the other is connected to Kapton insulated type T thermocouple wire of 20 gauge with a temperature range of -267°C to 316°C (KK-T-20-SLE) which will be used to connect to the data acquisition system.

The Data Acquisition System (DAS) hardware was supplied by National Instruments (NI) and utilizes a USB control module to create a complete plug-and-play system (National Instruments, Web 2010). The components consist of slot chassis to house the modules, a USB control module that communicates with the computer, 4 32-channel input modules to produce a

128-channel system, four corresponding thermocouple connectors and the required cabling to connect the thermocouple connector accessories to the input modules. Table 3-7 shows the NI model numbers for each component and the DAS uncertainty is $\pm 1^{\circ}\text{C}$ (1.8°F) which includes lead wire uncertainties.

Table 3-7: Data Acquisition System Components

Hardware Description	Model Number
Input Module	NI SCXI-1102
USB Control Module	NI SCXI-1600
Slot Chassis	NI SCXI-1001
Thermocouple Connector	NI TC-2095
Cabling	NI SH96-96
Computer	Dell OptiPlex 360
Software Description	Version
Operating System	Windows XP Professional 2002 SP3
NI LabVIEW	8.2

Table 3-7 also shows the computer model number as well as the version of the windows operating system and LabVIEW.

The SCXI-1102 input module, shown in Figure 3-19, is specifically designed for thermocouple voltage signals and features a built-in signal amplifier as well as a 2 Hz lowpass filter to reduce signal noise.



Figure 3-19: NI SCXI-1102 Input Module

The SCXI-1600 control module, shown in Figure 3-20, is a 16-bit USB data acquisition and control module for the SCXI input module series. The NI SCXI-1600 plugs into an SCXI chassis and provides data acquisition and control capabilities for all modules in the chassis, communicating with a PC via a USB 2.0 connection.



Figure 3-20: NI SCXI-1600 USB Module

The SCXI-1001, shown in Figure 3-21, is a rugged, low-noise chassis that can hold up to 12 SCXI modules. This chassis powers SCXI modules as well as handles all timing, trigger, and signal routing between your digitizer and SCXI modules.

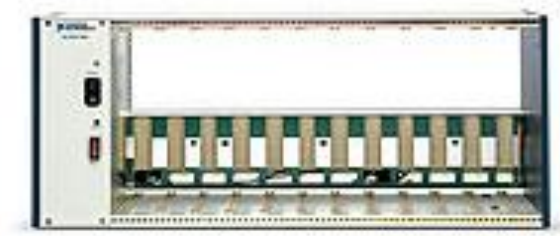


Figure 3-21: NI SCXI-1001 Slot Chassis

The TC-2095, shown in Figure 3-22, is a shielded, rack-mountable terminal accessory for SCXI input modules. The TC-2095 accepts mini thermocouple connectors and includes Cold-Junction Compensation (CJC) circuitry that can be applied on a channel by channel basis. This capability allows the DAS to not only make highly accurate temperature measurements but also voltage measurements from instruments that do not require CJC. The TC-2095 cables directly to the SCXI-1102 32-channel input module using SH96-96 shielded cable shown in Figure 3-23.



Figure 3-22: NI TC-2095 Thermocouple Connector



Figure 3-23: NI SH96-96 Shielded Cable

The DAS computer is a Dell OptiPlex 360 desktop and the operating system is Microsoft Windows XP Professional Version 2002 Service Pack 3. NI LabVIEW Version 8.2 was installed on the machine and was used to monitor and record data collected during the experiments.

3.3 Experimental Approach

In order to identify a measurement location, the following convention is used. The ports in the angular direction are labeled A through D (0° , 45° , 90° and 135°) starting at the port opposite the break location and rotating in the counterclockwise direction. Figure 3-24 below is a schematic demonstrating this convention.

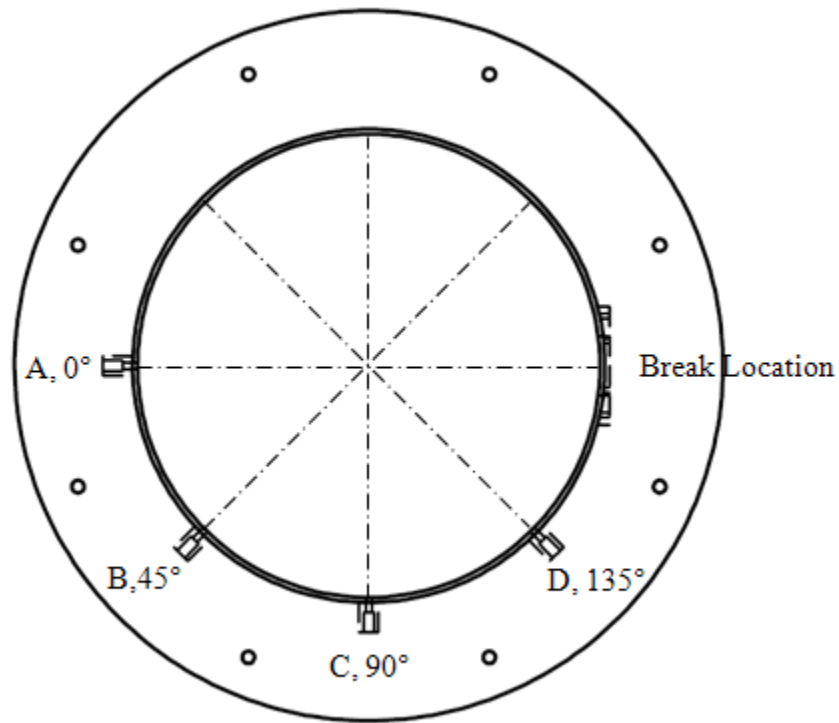


Figure 3-24: Schematic of Angular Port Locations

There are three break locations; one top break and two side breaks namely the higher side break and lower side break. The ports in the axial direction are labeled from 1 through 17, starting from the bottom. The axial ports are labeled in the schematic below in Figure 3-25.

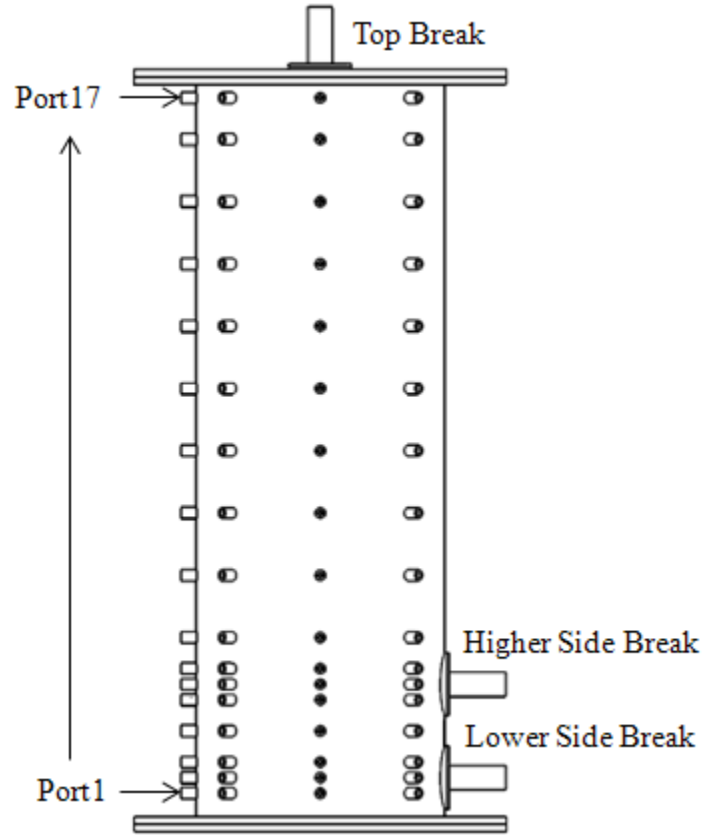


Figure 3-25: Schematic of Break Locations and Axial Port Locations

The experiments performed for this study are for the lower side break and the higher side break with a pipe break of $L/D = 3$. Half-symmetry about the vessel centerline is assumed and the majority of measurements are only taken for half of vessel cross sectional area for each axial location. Several measurements are made to verify symmetry and are presented in a following section. The radial locations are the measured distance from the opposite wall of the insertion port. The axial locations are identified by the distance above the bottom of the vessel.

For the lower side break, three axial measurement locations and 16 radial measurement locations are considered at each axial location. The radial measurement locations for the lower side break are labeled and color coded as shown in Figure 3-26. Here it can be seen that there are

more measurement locations within close proximity to the break and near the wall because of the helium-air interface and wall effect. As such, a total of 48 experiments are performed for the lower side break. The measurement locations for the lower side break are summarized in

Table 3-8 and Table 3-9. It should be noted that Port1 is 1.27 cm (0.5 in) below the break, Port2 is along the centerline of the break and Port3 is 1.27 cm (0.5 in) above the break.

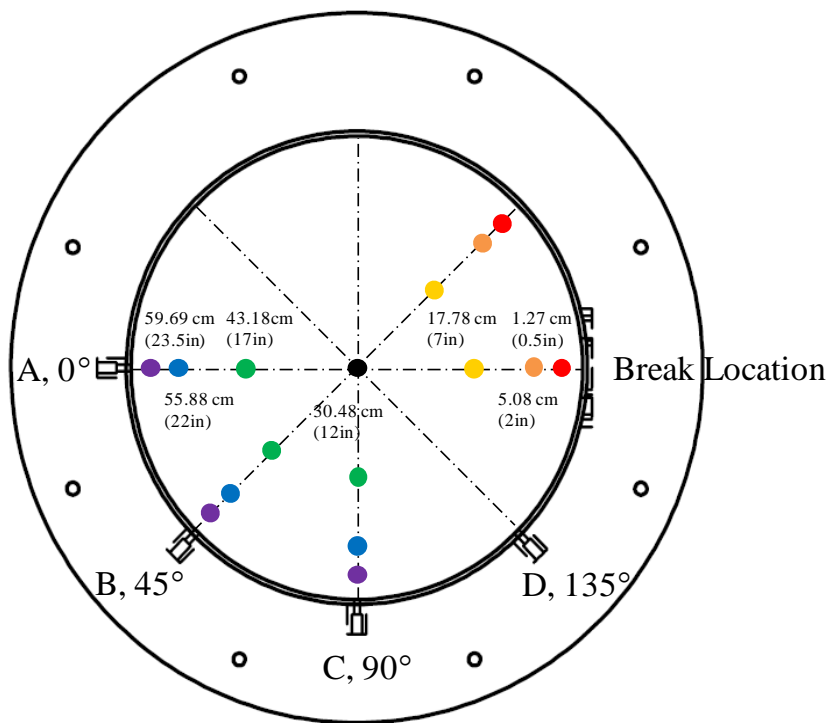


Figure 3-26: Schematic of Radial Location Color Code for Lower Side Break

Table 3-8: Axial Locations for Lower Side Break

	Axial Location, cm (in)
Port1	7.62 (3)
Port2	11.43 (4.5)
Port3	15.24 (6)

Table 3-9: Radial Locations for Lower Side Break

	Radial Location, cm (in)						
	1.27 (0.5)	5.08 (2)	17.78 (7)	30.48 (12)	43.18 (17)	55.88 (22)	59.69 (23.5)
APort	X	X	X	X	X	X	X
BPort	X	X	X		X	X	X
CPort					X	X	X

Five axial measurement locations and 11 radial measurement locations are considered at each axial location for the higher side break. The radial measurement locations for the higher side break are provided and color coded as shown in Figure 3-27. Here, data is not collected at radial distances of 5.08 cm (2 in) and 55.88 (22 in) because as shown from the lower side break experiments, the data follows the same general trend from 5.08 cm (2 in) through 59.69 cm (23.5 in). This also reduces the total number of experiments from 80 to 55 for the higher side break. Table 3-10 and Table 3-11 summarize the measurement locations for the higher side break. It should be noted that Port5 is 1.27 cm (0.5 in) below the break, Port6 is along the centerline of the break and Port7 is 1.27 cm (0.5 in) above the break.

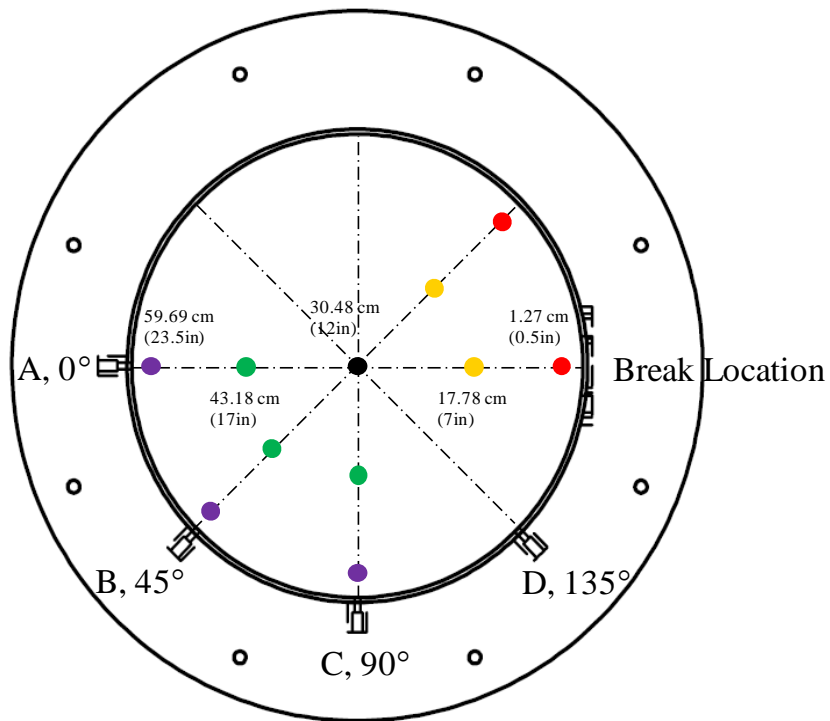


Figure 3-27: Schematic of Radial Location Color Code for Higher Side Break

Table 3-10: Axial Locations for Higher Side Break

	Axial Location, cm (in)
Port1	7.62 (3)
Port4	22.86 (9)
Port5	30.48 (12)
Port6	34.29 (13.5)
Port7	38.1 (15)

Table 3-11: Radial Locations for Higher Side Break

	Radial Location, cm (in)				
	1.27 (0.5)	17.78 (7)	30.48 (12)	43.18 (17)	59.69 (23.5)
APort	X	X	X	X	X
BPort	X	X		X	X
CPort				X	X

3.4 Experimental Procedure

Before the start of an experiment, the oxygen analyzer, vacuum pump, pressure transmitter, and data acquisition system are turned on and LabVIEW is opened and set to record the data at 5Hz. The oxygen concentration in the room is recorded before and after each experiment. The procedure used to perform the experiments for the present study is as follows:

- 1) Close all valves
- 2) Open helium regulator and set gauge backpressure of about 68.95 kPa (10 psig)
- 3) Open valve between vacuum pump and vessel
- 4) Turn on vacuum pump to evacuate vessel
- 5) Turn off vacuum pump once vessel is evacuated
- 6) Close valve between vacuum pump and vessel
- 7) Open valve between helium tank and vessel
- 8) Supply helium at gauge pressure of about 13.79 kPa (2 psig)
- 9) Open valve between vessel and oxygen analyzer once pressure in vessel becomes positive
- 10) Repeat steps 1 through 9 until oxygen concentration in vessel is below 2090 ppm (less than one percent air)

- 11) Increase pressure in vessel to a gauge pressure of about 13.79 kPa (2 psig)
- 12) Close valve between helium tank and vessel
- 13) Remove plug from break once gauge pressure decreases to about 6.89 kPa
(1psig) (pressure reduces as oxygen analyzer samples fluid in vessel)

The end of blowdown is simulated once step 13 has been performed and air ingress begins.

During each experiment, oxygen concentration, oxygen analyzer cell temperature, pressure, and room temperature is collected in LabVIEW. The data collection sheet that is used for the air ingress experiments is provided in Appendix D.

Chapter 4

Experimental Results and Discussion

4.1 Data Verification and Repeatability

In order to verify that continuous measurements during the experiments do not affect the data, continuous and non-continuous sampling of data is compared. This is also done for the axial location 1.27 cm (0.5 in) above the break to ensure the repeatability of the data. To perform a non-continuous measurement, the valve between the oxygen analyzer and vessel is opened and closed several times throughout the duration of an experiment. It can be seen from Figure 4-1 that the data is comparable for the continuous and non-continuous measurements.

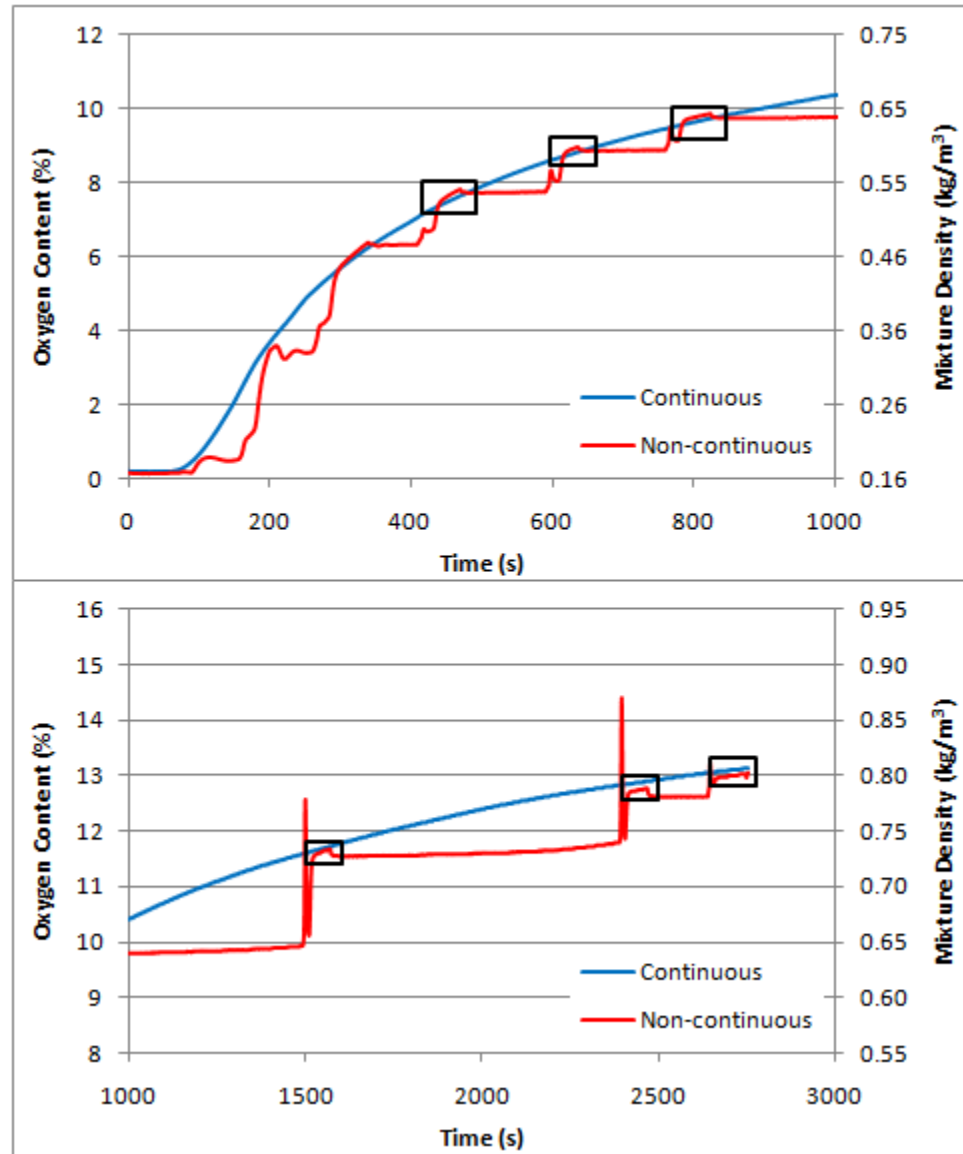


Figure 4-1: Comparison of Data for Continuous and Non-continuous Sampling

Because the oxygen concentration within the room varies, the oxygen concentration measurements, $C_{oxy,m}$ are normalized by the average oxygen concentration in the room, $\bar{C}_{oxy,r}$ before and after the experiment. This is done so that the data is comparable. For example, Figure 4-2 shows the oxygen concentration collected for radial locations at CPort2, where the data is collected on two different dates. It can be seen from the figure that the oxygen concentration

toward the end of the experiment does not compare well due to the change in oxygen concentration in the room. Therefore, the data is converted to obtain air content based on the average room oxygen content by:

$$C_{air} = \frac{C_{oxy,m}}{\bar{C}_{oxy,r}} \times 100\% \quad (4-1)$$

Table 4-1 summarizes the normalized air content percent for the measurements made at three different radial locations at CPort2. Figure 4-3 shows the results after the conversion, where the data at the end point compares better.

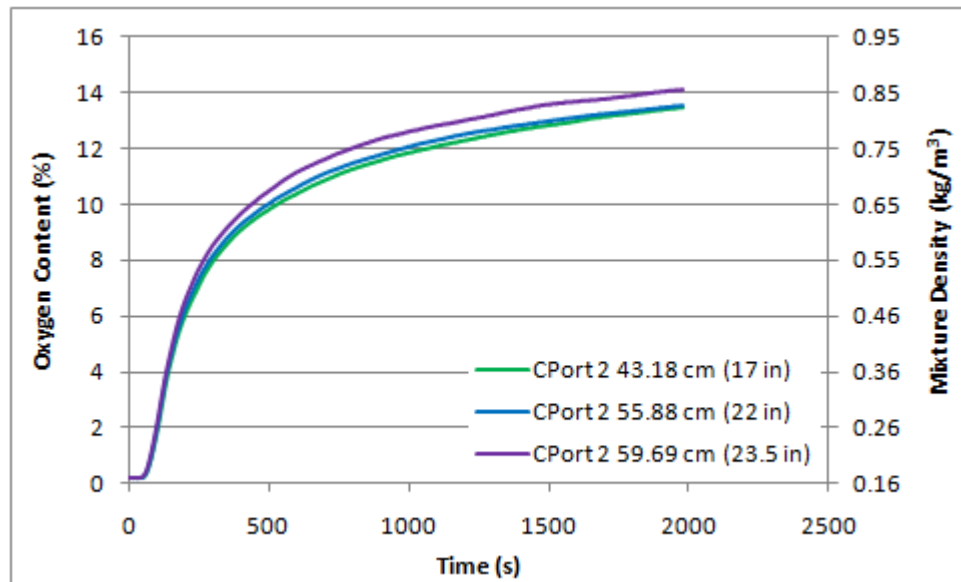


Figure 4-2: Oxygen Content Data for CPort2

Table 4-1: Room Oxygen Content for Normalization of Data

	CPort2 43.18cm (17in)	CPort2 55.88cm (22in)	CPort2 59.69cm (23.5in)
Initial Room Oxygen Content (%)	20.8	20.7	21.3
Final Room Oxygen Content (%)	20.7	20.8	21.1
Average Room Oxygen Content (%)	20.75	20.75	21.2

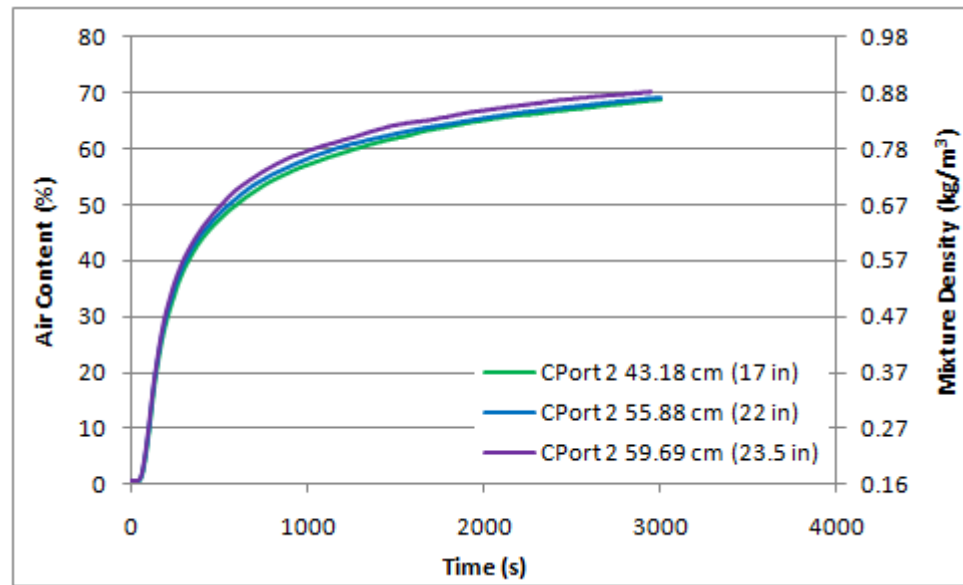


Figure 4-3: Normalized Oxygen Content Data for CPort2

In view of these, all data presented hereafter is converted to air content with respect to time using equation 4-1. A dual axis is included to provide the density of the helium-air mixture which is important for calculating volumetric flow rate. The calculation to convert from air content, C_{air} to mixture density, ρ_{mix} is shown in equation 4-2. The density of air and helium are 1.186 kg/m^3 and 0.1635 kg/m^3 , respectively.

$$\rho_{mix} = \frac{C_{air}}{100} \times 1.186 \frac{\text{kg}}{\text{m}^3} + \frac{1-C_{air}}{100} \times 0.1635 \frac{\text{kg}}{\text{m}^3} \quad (4-2)$$

Some experiments are repeated at the same position to check that the oxygen concentration measurements are repeatable. Data is collected multiple times at APort1 43.18 cm (17 in) to check the repeatability of the experiments. Figure 4-4 shows that the experiments are quite repeatable. The data fits within $\pm 10\%$ error bars for the first 140 seconds of the experiment and from 140 seconds through the end of the experiment the data fits within $\pm 2\%$ error bars. The percent error at the beginning of the experiment is greater because the oxygen content values are so small. Zoomed in versions of Figure 4-4 with error bars are provided in Appendix E.

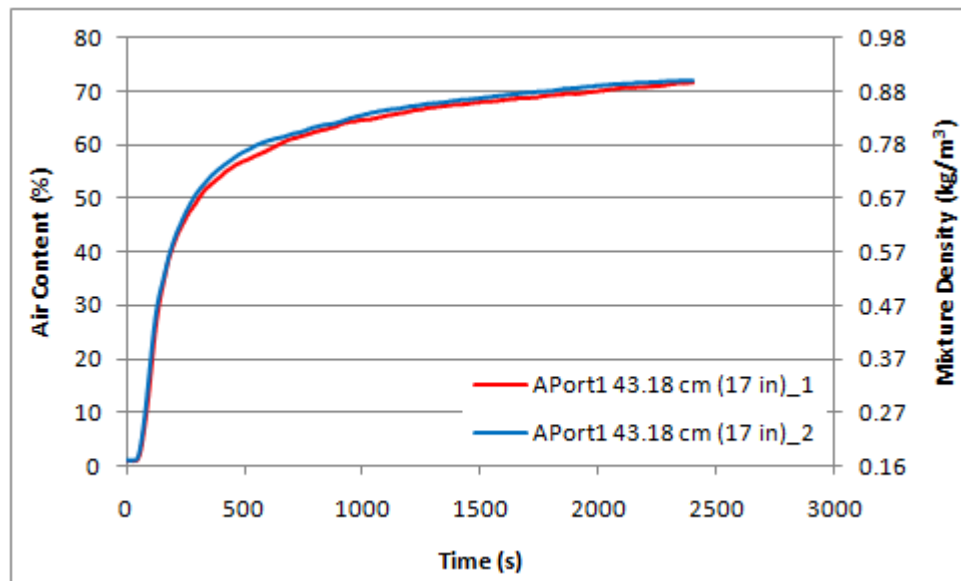


Figure 4-4: Comparison of Data at APort1 43.18 cm (17 in) to Verify Repeatability

As half-symmetry is assumed, experiments are performed to verify this assumption. The flow rate is regulated during the experiments in order to preserve a flow rate of approximately 0.94 L/min (2 scfh). Oxygen concentration measurements are collected at axisymmetric radial locations BPort1 5.08 cm (2 in) and DPort1 55.88 cm (22 in) shown in Figure 4-5. The data is compared in Figure 4-6 and indicates symmetry across the vessel centerline.

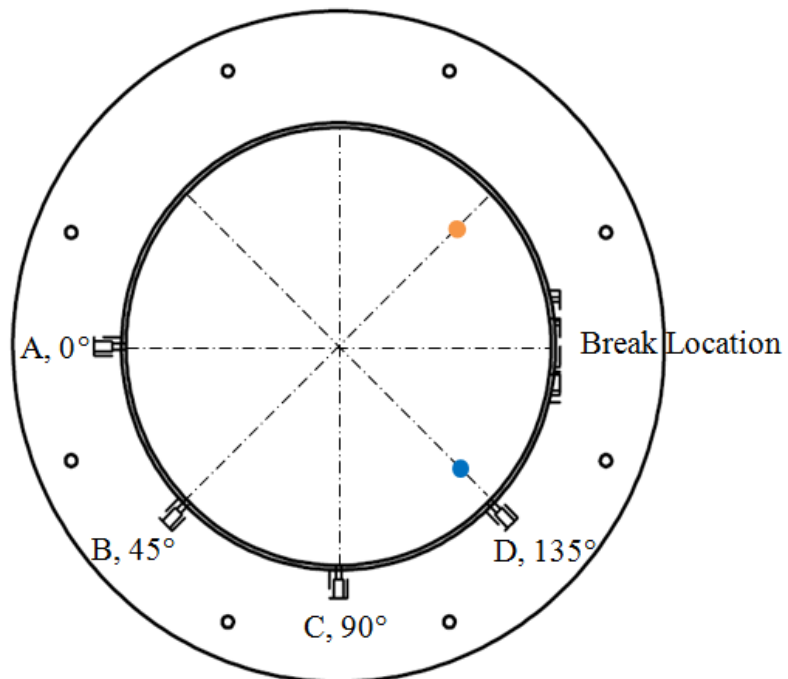


Figure 4-5: Radial Locations for Symmetry Verification

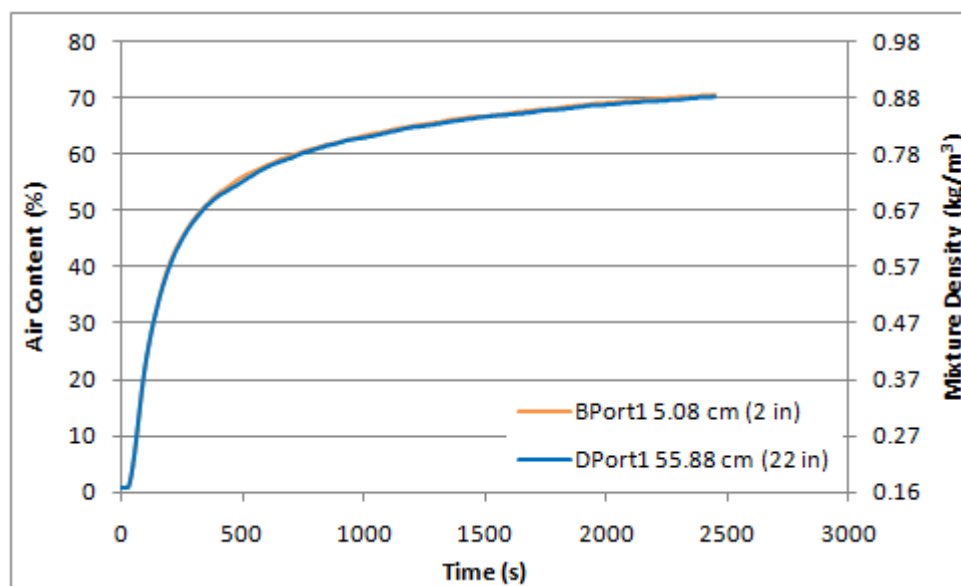


Figure 4-6: Comparison of Data for Symmetry Verification

4.2 Local Data

The local data presented in this section is cut-off once it takes 100 seconds for a measurement to change with the accuracy of the oxygen analyzer. This time changes for each data set, so the longest time for this to occur for a given axial location is used for the cut-off time. Table 4-2 and Table 4-3 summarize the cut-off times for each axial location for the lower side break and higher side break, respectively. All of the local data for the lower side break is presented in the form of an overall view and zoomed in view of the initial region for each data set in Appendix F. The comprehensive local data for the higher side break is provided in the same manner in Appendix H.

Table 4-2: Cut-off Times for the Lower Side Break

	Cut-off Time (s)
Port1	1631.4
Port2	1977.8
Port3	2391
Average	2000.07

Table 4-3: Cut-off Times for the Higher Side Break

	Cut-off Time (s)
Port1	1853
Port4	1853
Port5	2239.8
Port6	2510.2
Port7	2903.8
Average	2271.96

The local data is compared at the axial locations along the radial direction for the lower side break. It can be seen from Figure 4-7 that the local data for APort1 at radial locations 5.08 cm (2 in) through 59.69 cm (23.5 in) follow the same general trend. After a steep increase at the beginning of the experiment, data from APort1 1.27 cm (0.5 in) shows oscillations in the measurement. The APort1 1.27 cm (0.5 in) location is 1.27 cm (0.5 in) below the break and 1.27 cm (0.5 in) away from the break wall. This oscillation in the data at this location clearly reflects the unstable flow pattern of the helium-air interface at the entrance.

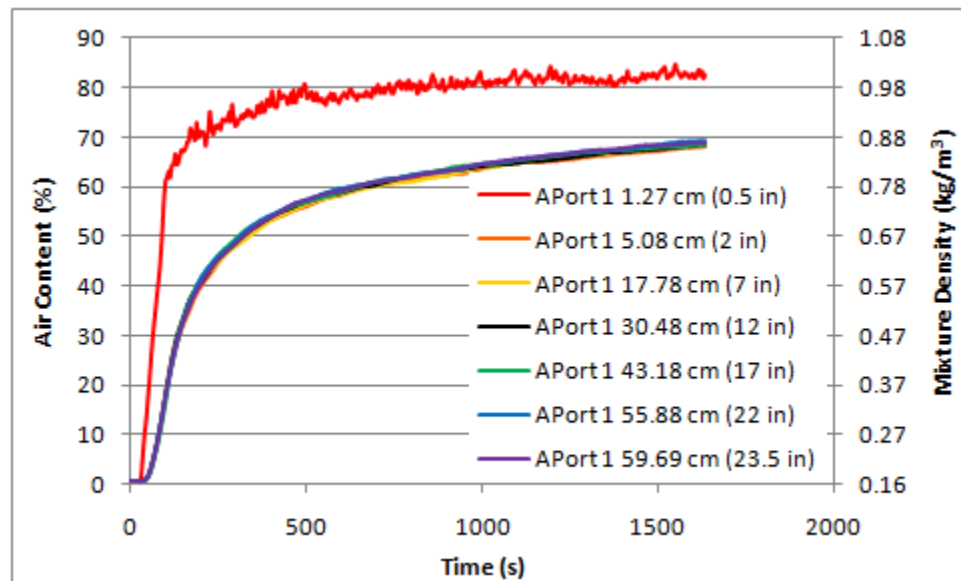


Figure 4-7: Local Data for APort1 along Radial Direction

From the zoomed in view of the initial region of Figure 4-7 shown in Figure 4-8, it can be seen that there is no evident time delay in the radial direction. It is speculated that the progression of ingress in the radial direction across the vessel diameter occurs lower than the lowest axial measurement location.

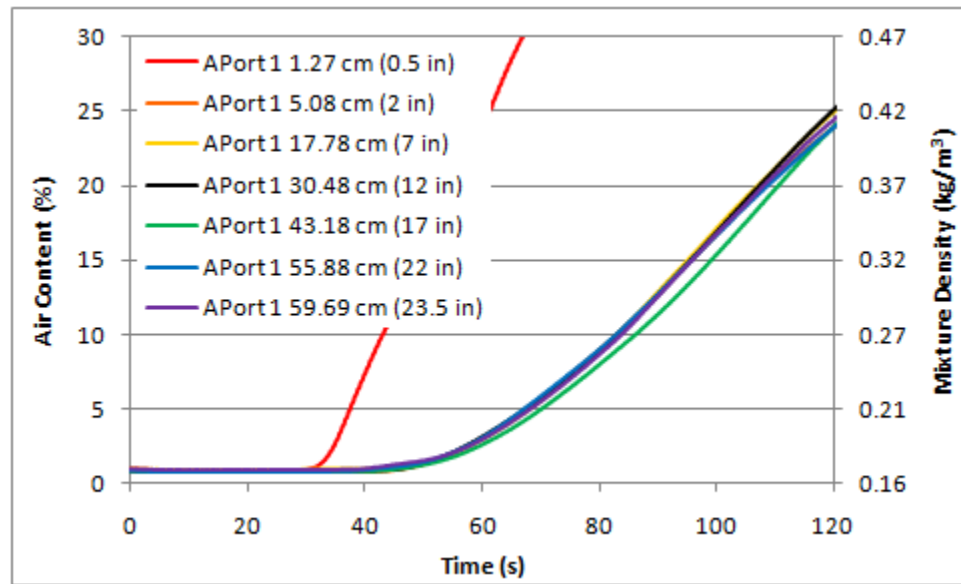


Figure 4-8: Initial 120 s of Local Data for APort1 along Radial Direction

Figure 4-9 and Figure 4-10 show that the local data follows the same general trend for APort2 and APort3.

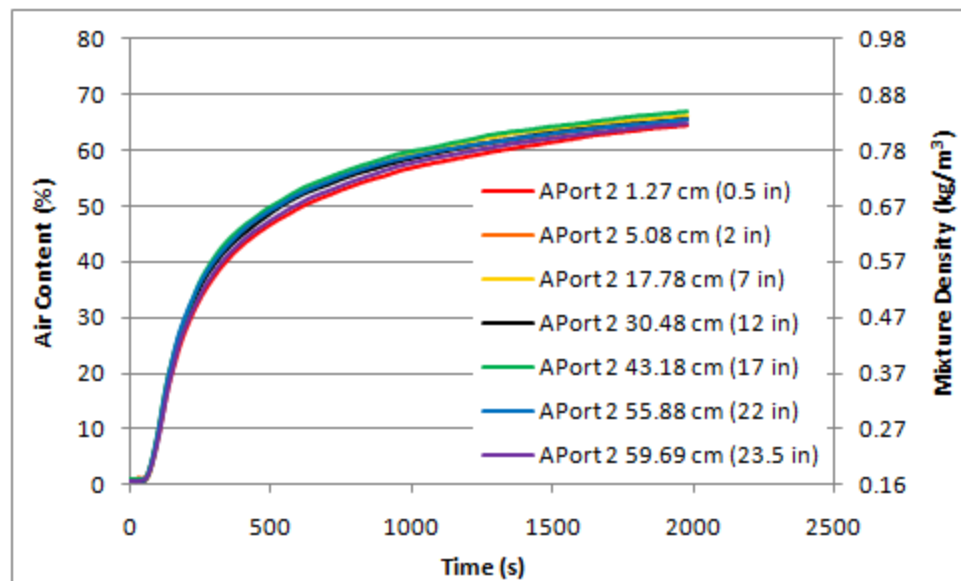


Figure 4-9: Local Data for APort2 along Radial Direction

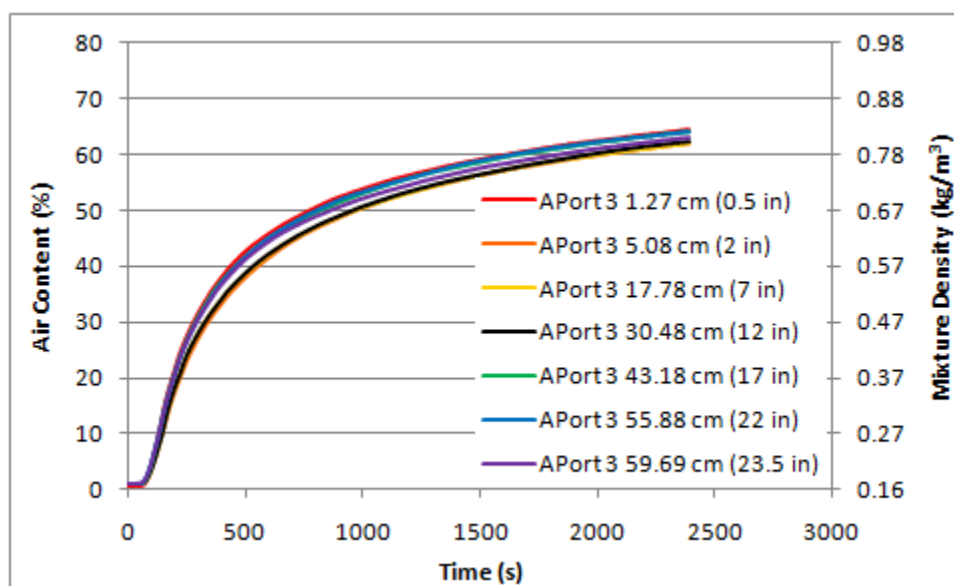


Figure 4-10: Local Data for APort3 along Radial Direction

To further show that the air content does not vary much along the diameter of the vessel, local air content measured at different times of ingress are plotted with respect to non-dimensional radius (r/R). It can be seen from Figure 4-11 that the only measurement location that has a different air content value is that closest to the break (APort1 1.27 cm (0.5 in)).

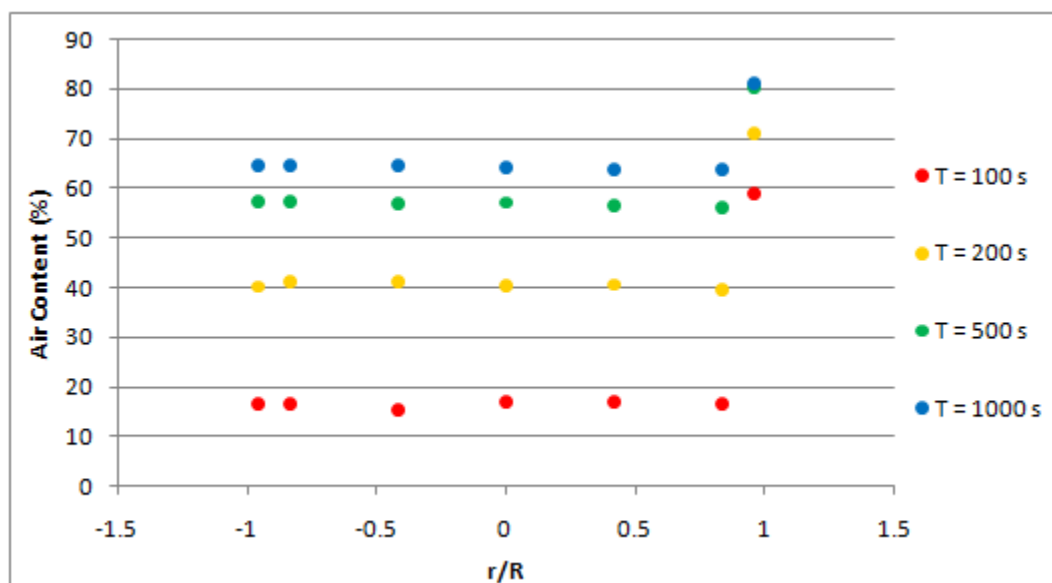


Figure 4-11: Variation of Air Content along Vessel Diameter for APort1

Plots of air content versus r/R for all other axial locations along the vessel diameter are provided in Appendix F for the lower side break. From these plots, it can be seen that the air content percent does not vary significantly for any other measurement location.

The local data measured at the same radial location is also compared for three different axial locations. The local data at the centerline of the vessel (APort) is presented in Figure 4-12 for the lower side break. It can be seen that the time rate of change in air content is greater for the lower elevations, which leads to a higher air content percent for a lower elevation at a given time of ingress. By zooming in on the initial 150 seconds of ingress, Figure 4-13 shows how air ingress progresses in time from the bottom of the vessel.

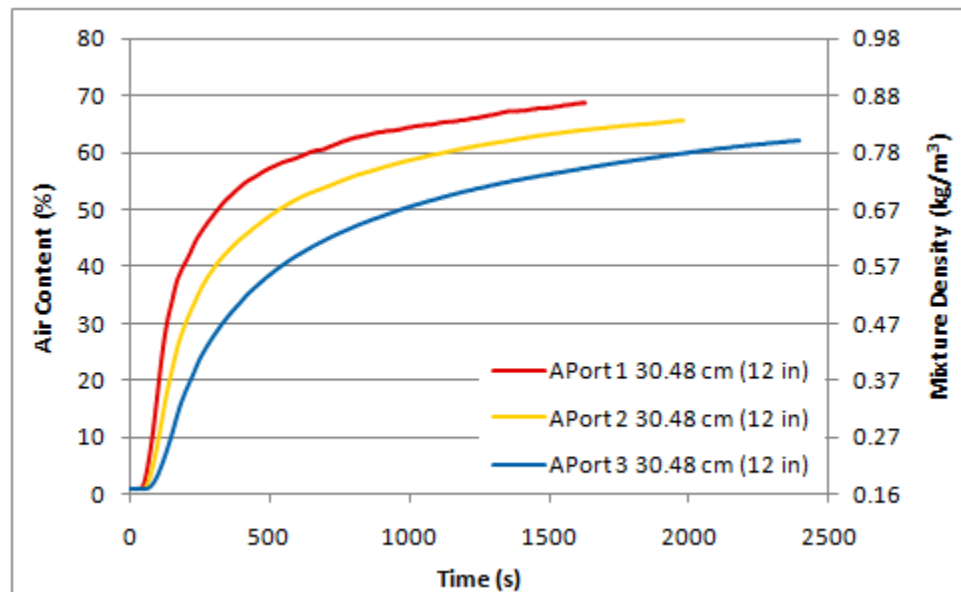


Figure 4-12: Local Data for Radial Location 30.48 cm (12 in) along Axial Direction for APort

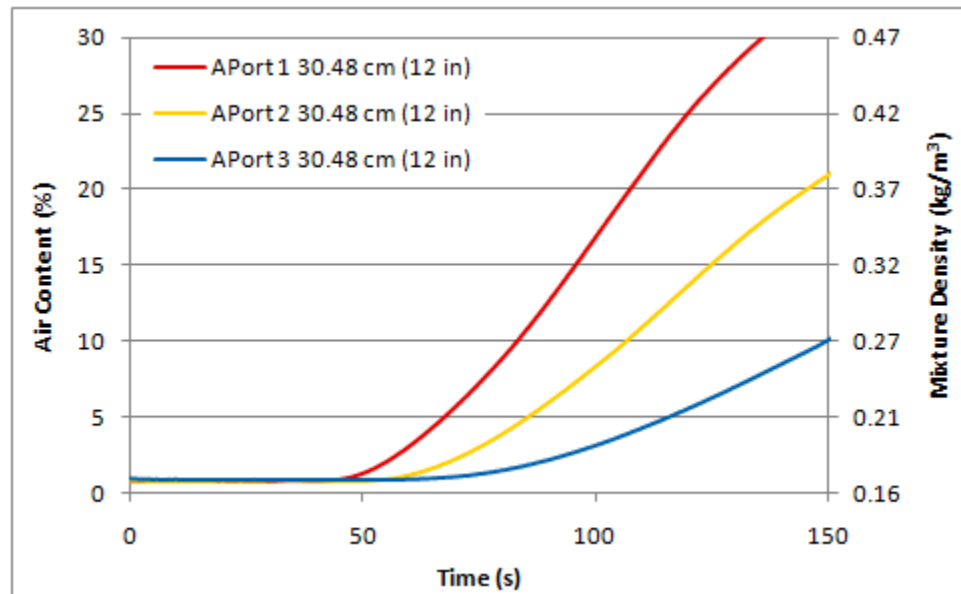


Figure 4-13: Initial 150 s of Local Data for Radial Location 30.48 cm (12 in) along Axial Direction for APort

The local data for the lower side break is input into MATLAB to generate planar plots of oxygen content at each axial location (Port1, Port2, and Port3). These planar plots are provided in Appendix G for various times through the transient.

For the higher side break, it can be seen from Figure 4-14 that the local data begins to have oscillations in the measurement at APort4 1.27 cm (0.5 in). Here, the end air content percent matches that of the other radial locations.

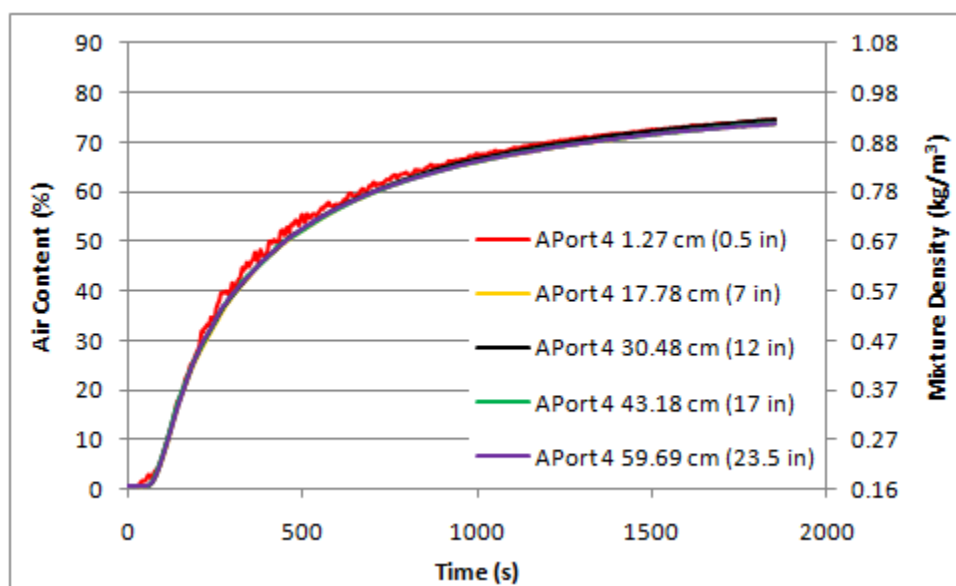


Figure 4-14: Local Data for APort4 along Radial Direction

The oscillations in the measurement become more prevalent at APort5 as shown in Figure 4-15. The APort5 1.27 cm (0.5 in) data compares to the APort1 1.27 cm (0.5 in) data for the lower side break which is expected because the axial orientation in relation to the break is the same (1.27 cm (0.5 in) below).

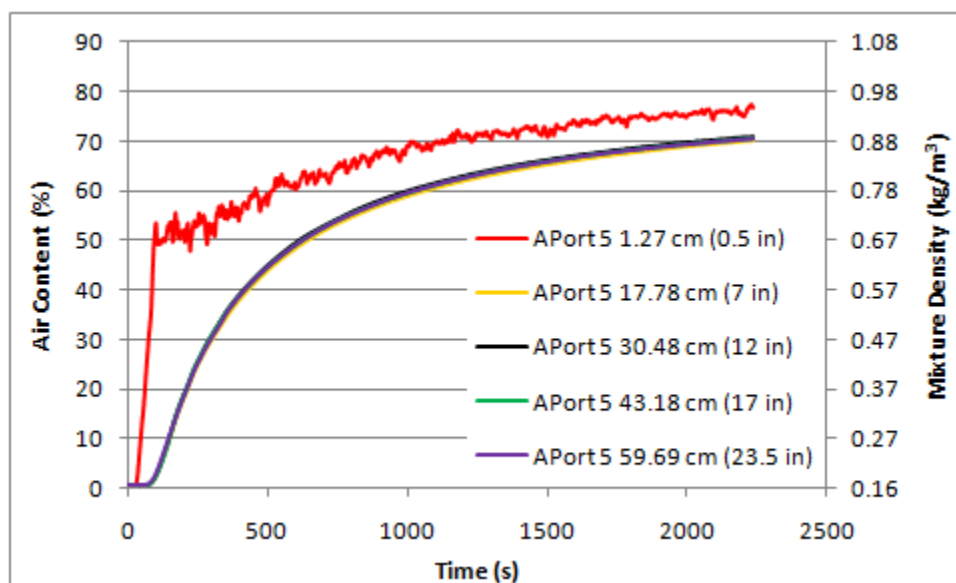


Figure 4-15: Local Data for APort5 along Radial Direction

Plots of air content versus r/R for the higher side break are provided in Appendix H.

These plots show that the only measurement location that has variation in the air content percent across the diameter is APort5 1.27 cm (0.5 in).

The local data at the vessel centerline is presented in Figure 4-16 for the higher side break. Similar to the lower side break, the air content percent at the same time for each axial location is higher for the lower oriented axial locations. Here, the time delay for an increase in the air content at the higher axial locations is still observed, but the end air content percent is similar for APort1 and APort4.

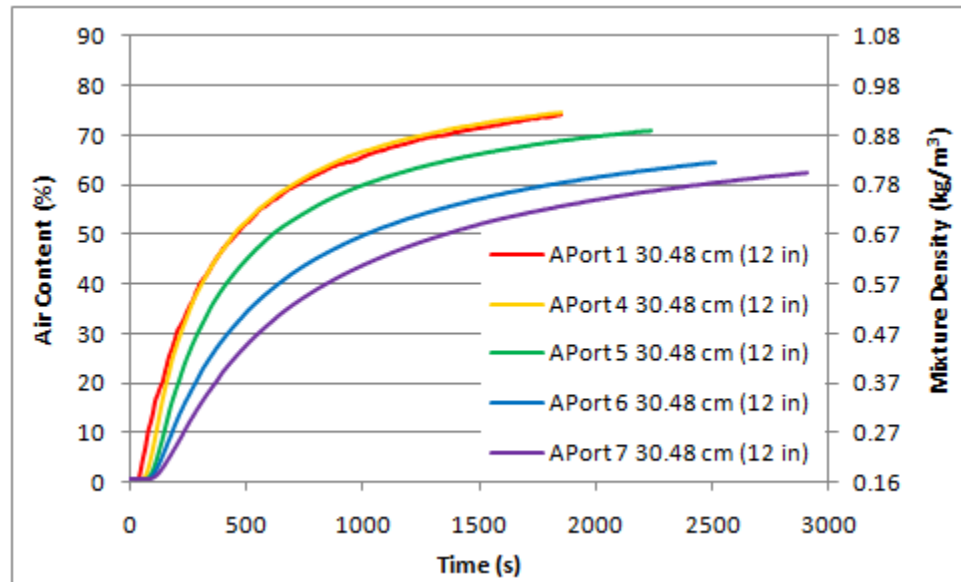


Figure 4-16: Local Data for Radial Location 30.48 cm (12 in) along Axial Direction for APort

4.3 Area Average Scheme and Planar Data

The local data for each axial location for the lower side break is area averaged based on the regions around each data point enclosed in dotted lines as shown in Figure 4-17. A constant air content percent is assumed across these enclosed regions. The areas for the enclosed regions are provided in Table 4-4.

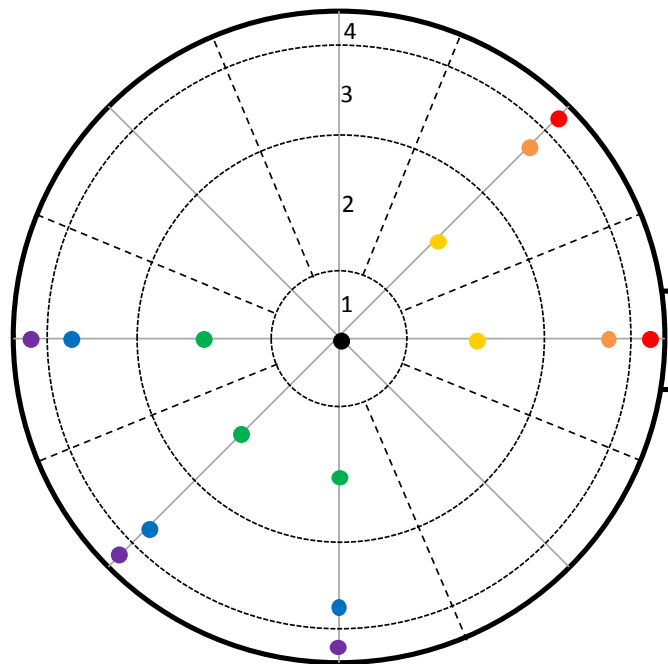


Figure 4-17: Area Average Scheme for Lower Side Break

Table 4-4: Areas for Enclosed Regions for Lower Side Break

	# Slices	Slice Area	Area
A Port1 1.27 cm (0.5 in)	1	11.17	11.17
A Port1 5.08 cm (2 in)	1	23.29	23.29
A Port1 17.78 cm (7 in)	1	19.63	19.63
A Port1 30.48 cm (12 in)	1	19.63	19.63
A Port1 43.18 cm (17 in)	1	19.63	19.63
A Port1 55.88 cm (22 in)	1	23.29	23.29
A Port1 59.69 cm (23.5 in)	1	11.17	11.17
B Port1 1.27 cm (0.5 in)	2	11.17	22.33
B Port1 5.08 cm (2 in)	2	23.29	46.58
B Port1 17.78 cm (7 in)	2	19.63	39.27
B Port1 43.18 cm (17 in)	2	19.63	39.27
B Port1 55.88 cm (22 in)	2	23.29	46.58
B Port1 59.69 cm (23.5 in)	2	11.17	22.33
C Port1 43.18 cm (17 in)	2	19.63	39.27
C Port1 55.88 cm (22 in)	2	23.29	46.58
C Port1 59.69 cm (23.5 in)	2	11.17	22.33
			Total Area
			452.39

All of the data for each axial location is input into equation 4-3 and 4-4 to obtain the planar data. The planar data for the lower side break is presented in Figure 4-18. Here, it can be seen that the planar data follows the same general trend as the local data in the axial direction.

$$\bar{\rho}_A = \frac{1}{A_{tot}} \int \rho(r, \theta) dA \quad (4-3)$$

$$\int \rho(r, \theta) dA \cong \sum_{n=1}^N A_n \rho_n(r, \theta) \quad (4-4)$$

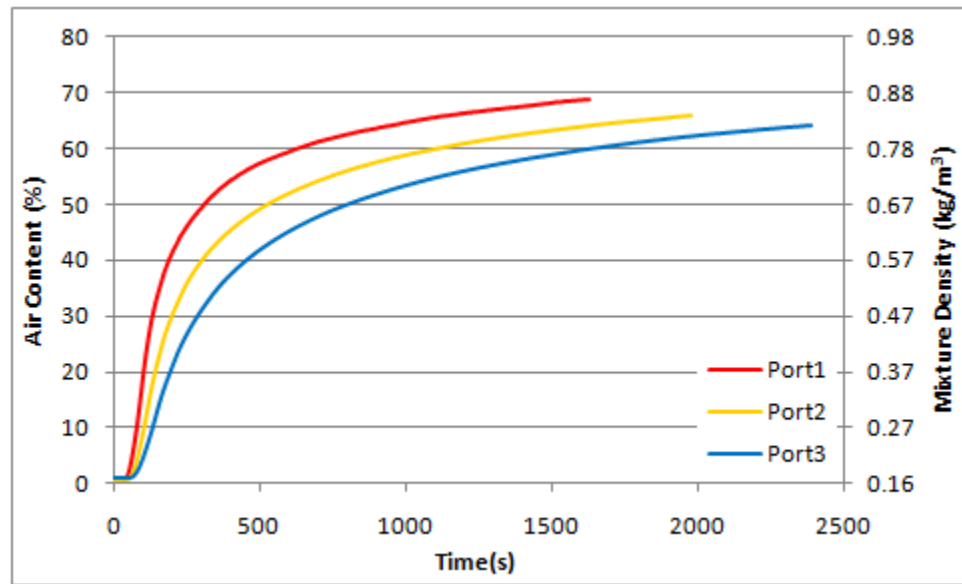


Figure 4-18: Planar Data for the Lower Side Break

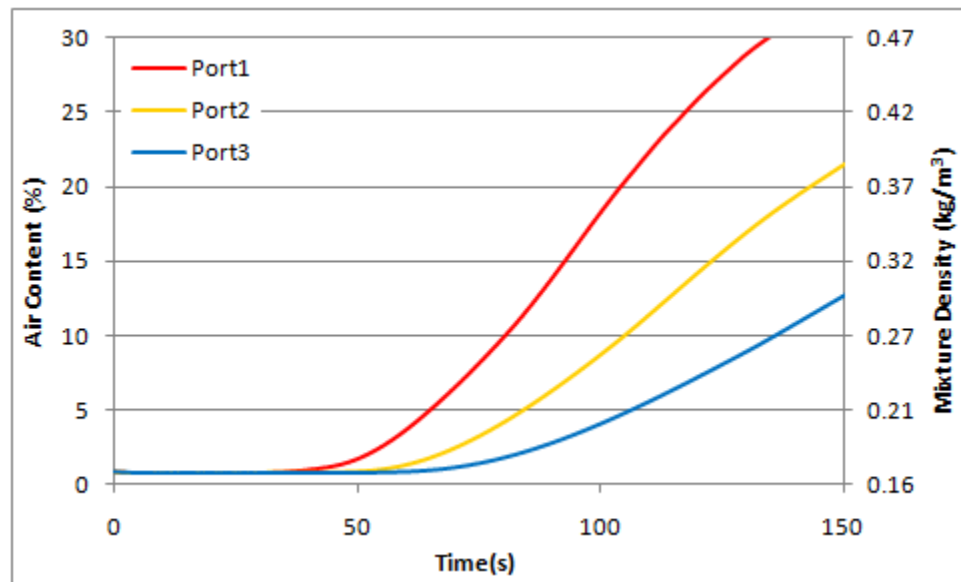


Figure 4-19: Initial 150 s of Planar Data for the Lower Side Break

The area averaging scheme for the higher side break is basically the same as that for the lower side break. Although there is no data for radial location 5.08 cm (2 in) and 55.88 cm (22 in), it is assumed that the data for 5.08 cm (2 in) through 59.69 cm (23.5 in) follows the same

general trend just as for the lower side break. It can be seen that region 2 and 3 from Figure 4-17 have been combined to be a single region as shown in Figure 4-20. Table 4-5 provides the areas for the enclosed regions.

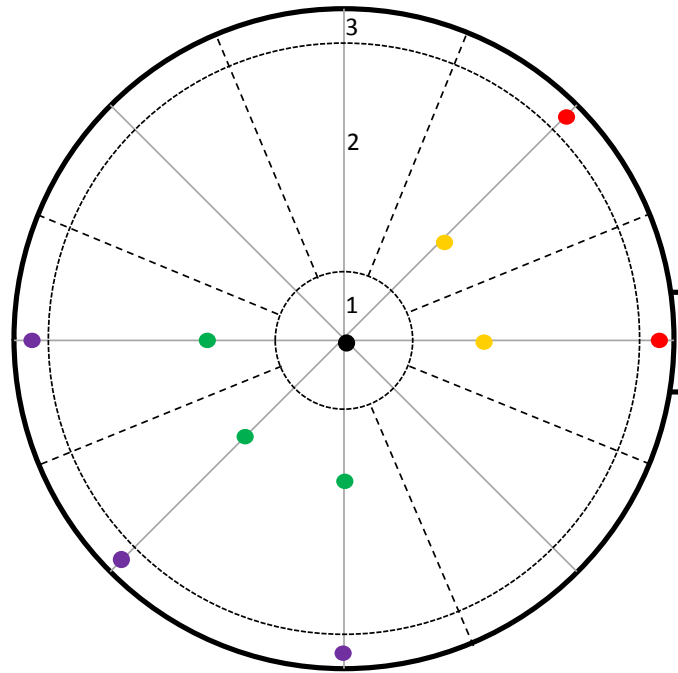


Figure 4-20: Area Average Scheme for Higher Side Break

Table 4-5: Areas for Enclosed Regions for Higher Side Break

	# Slices	Slice Area	Area
A Port1 1.27 cm (0.5 in)	1	11.17	11.17
A Port1 17.78 cm (7 in)	1	42.93	42.93
A Port1 30.48 cm (12 in)	1	19.63	19.63
A Port1 43.18 cm (17 in)	1	42.93	42.93
A Port1 59.69 cm (23.5 in)	1	11.17	11.17
B Port1 1.27 cm (0.5 in)	2	11.17	22.33
B Port1 17.78 cm (7 in)	2	42.93	85.85
B Port1 43.18 cm (17 in)	2	42.93	85.85
B Port1 59.69 cm (23.5 in)	2	11.17	22.33
C Port1 43.18 cm (17 in)	2	42.93	85.85
C Port1 59.69 cm (23.5 in)	2	11.17	22.33
			Total Area
			452.39

For the higher side break, equation 4-3 is used to obtain the planar data. Again, the planar data follows the same general trend as the local data in the axial direction.

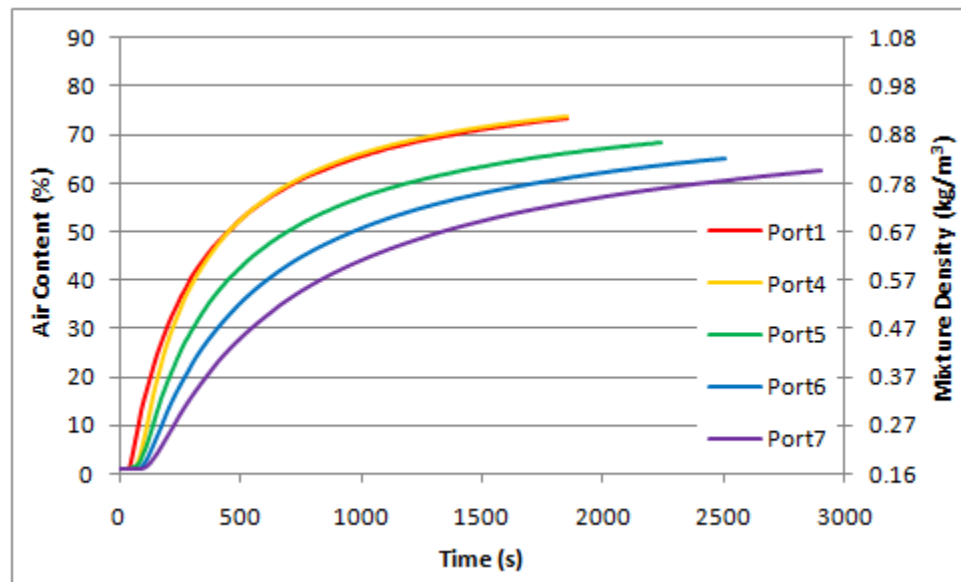


Figure 4-21: Planar Data for the Higher Side Break

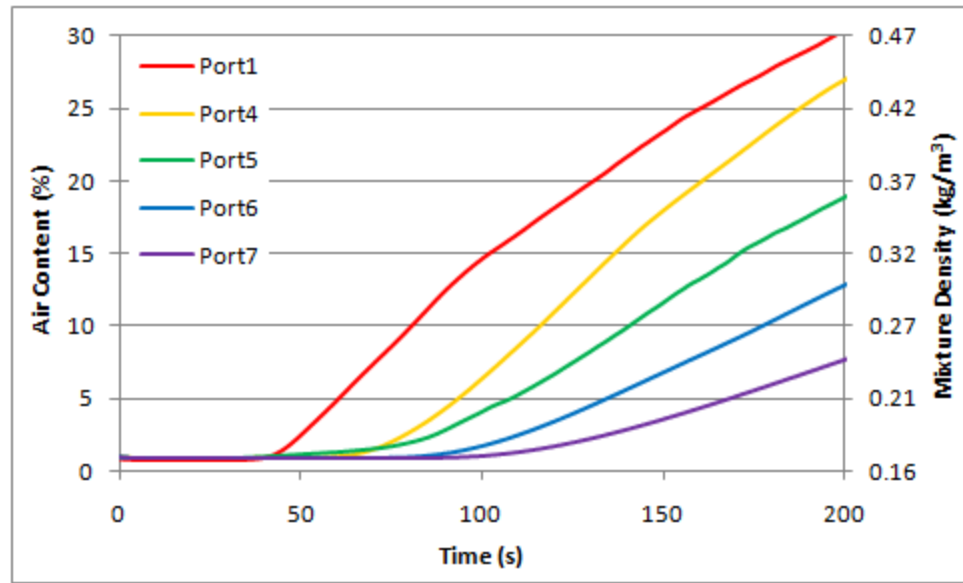


Figure 4-22: Initial 200 s of Planar Data for the Higher Side Break

4.4 Volume Average Scheme and Global Data

The planar data is volume averaged in order to obtain global data. The planar data is plotted as air content with respect to axial location (height) for several times as shown in Figure 4-23. It is assumed that the data along the bottom will be the same as that obtained at Port1 as indicated by the dotted line in the figure.

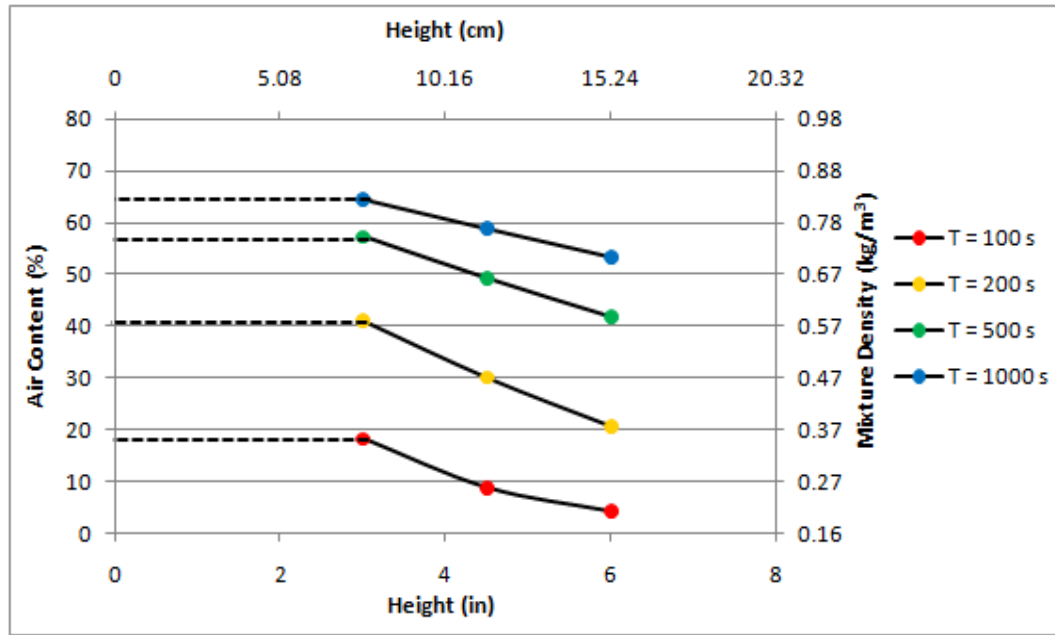


Figure 4-23: Air Content Plotted along Axial Direction for Several Times for Lower Side Break

Here, the area under the curve in combination with the planar data is used to obtain the volume average as given by the following equations.

$$\bar{\rho}_V = \frac{1}{H} \int \bar{\rho}_A(z) dz \quad (4-5)$$

$$\int \bar{\rho}_A(z) dz \cong \sum_{n=1}^N \frac{\Delta z_n}{2} (\bar{\rho}_{An} + \bar{\rho}_{An+1}) \quad (4-6)$$

By inputting the planar data into equations 4-5 and 4-6, the global data is obtained and is shown with the planar data in Figure 4-24 and Figure 4-25. It can be seen that the global data follows the same general trend as the local data and falls between the Port1 and Port2 local data.

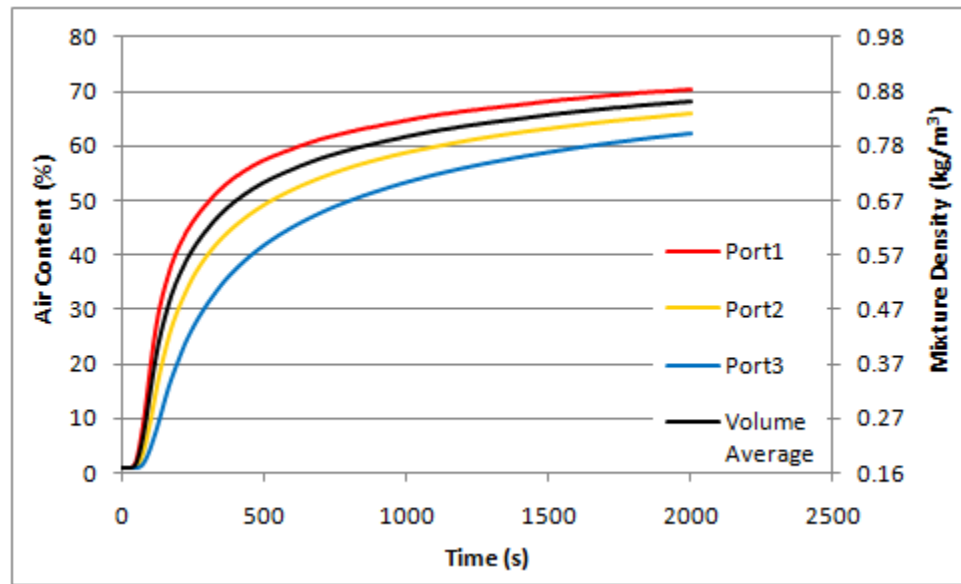


Figure 4-24: Planar Data Plotted with Global Data for Lower Side Break

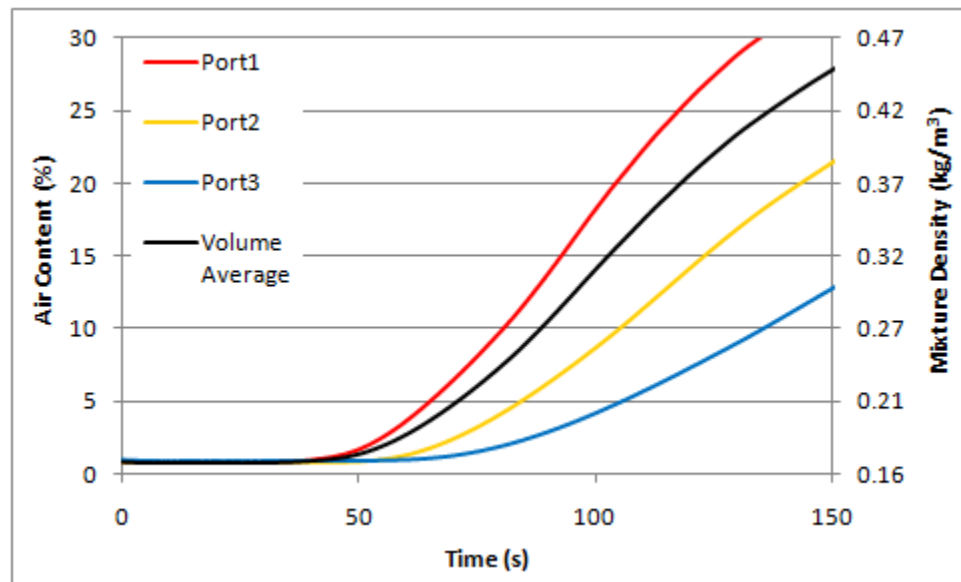


Figure 4-25: Initial 150 s of Planar Data Plotted with Global Data for Lower Side Break

Again, the planar data is input in equations 4-5 and 4-6 to obtain the global data for the higher side break. Figure 4-26 shows air content plotted with respect to height for several times.

Since the lowest port (Port1) is 7.62 cm (3 in) above the bottom of the vessel, there is no local data set for the very bottom of the vessel. For this reason, a probe is implemented through the bottom plate to obtain local data at the bottom centerline of the vessel. This local data at the centerline is used to confirm the data along the bottom of the vessel is the same as that of Port1 is a reasonable assumption as also shown in the figure.

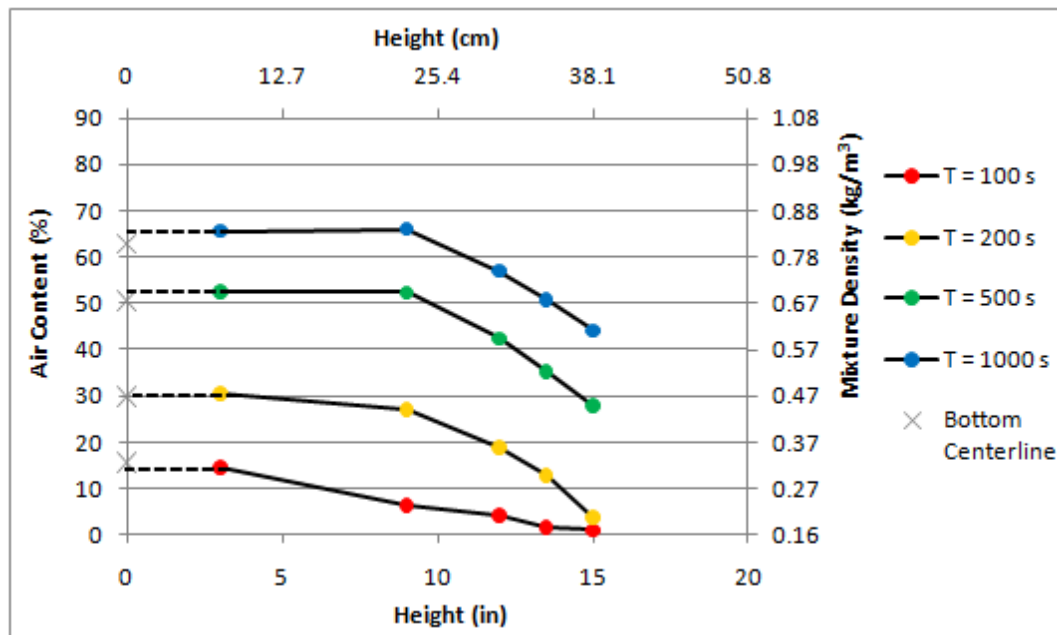


Figure 4-26: Air Content Plotted along Axial Direction for Several Times for Higher Side Break

The global data for the higher side break is also plotted with the planar data as shown in Figure 4-27 and Figure 4-28. It is shown that the global data resides between the planar data for Port1/Port4 and Port5.

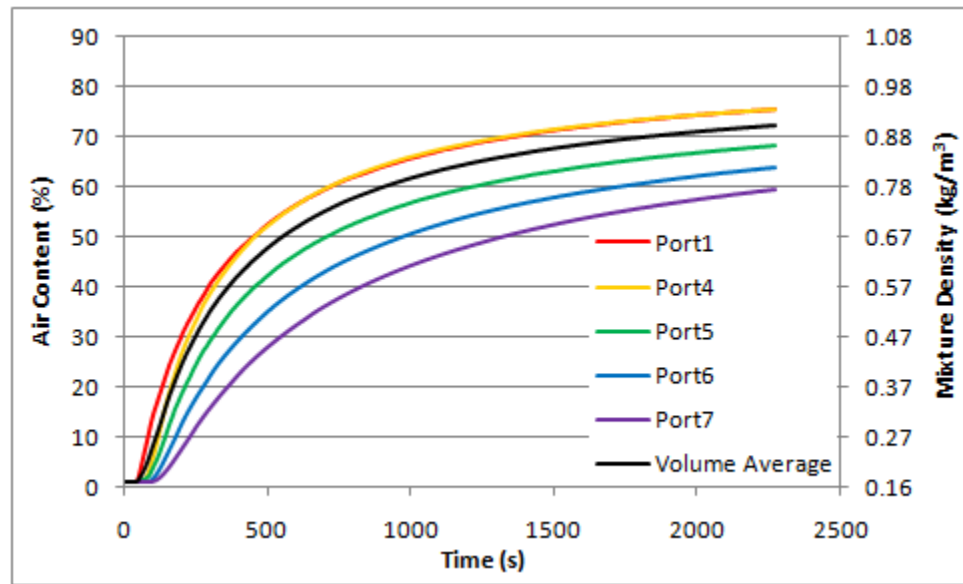


Figure 4-27: Global Data Plotted with Planar Data for Higher Side Break

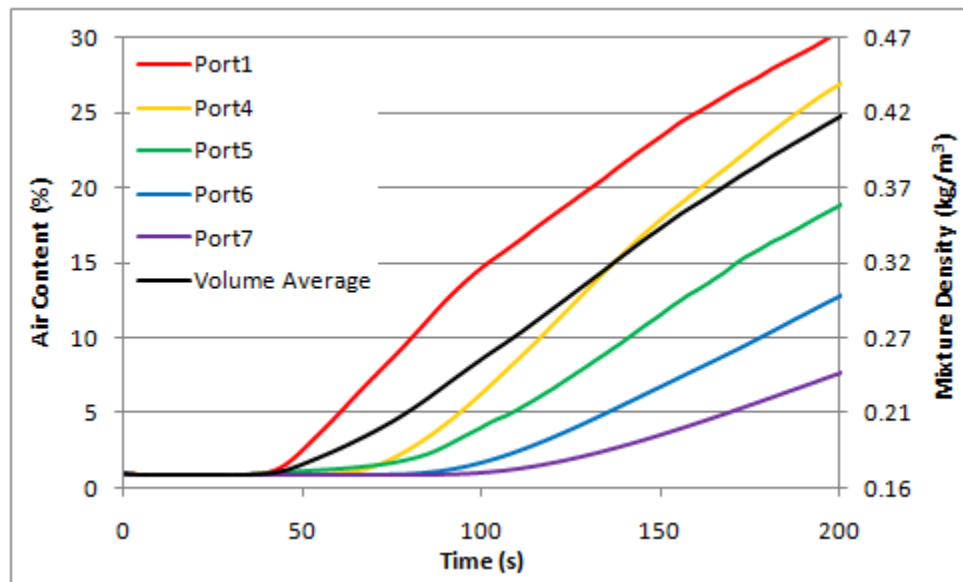


Figure 4-28: Initial 200 s of Global Data Plotted with Planar Data for Higher Side Break

4.5 Discussion

The local data presented for the lower and higher side break is compared along the radial direction as well as the axial direction. It is found that the local data for each axial location follows the same general trend along the radial direction except for the APort1 1.27 cm (0.5 in) measurement location for the lower side break and the APort4 1.27 cm (0.5 in) and APort5 1.27 cm (0.5 in) measurement locations for the higher side break. Here, APort1 1.27 cm (0.5 in) and APort5 1.27 cm (0.5 in) have the same axial and radial orientation in relation to the break (1.27 cm (0.5 in) below and 1.27 cm (0.5 in) away from the break wall). APort4 1.27 cm (0.5 in) has the same radial location, but an axial location 7.62 cm (3 in) below the break. These measurement locations are in such close proximity to the break that they see the helium-air interface. For this reason, the local data for these locations experience oscillations in the measurement. It is speculated that this oscillation in the data is due to the unstable flow pattern at the helium-air interface. For the data compared at a particular radial location along the axial direction, the time rate of change in air content is found to be greater for a lower oriented axial location. Hence, a higher air content percent is observed for a lower oriented axial location at the same time. There is also a time delay for an increase in the air content at the higher axial locations. This time delay indicates the progression of ingress in the axial direction as the air piles up from the bottom of the vessel. The air content percentage is relatively uniform across the vessel diameter. For this reason, the local data is area averaged using a basic scheme to obtain planar data for each axial location. This planar data is volume averaged considering the axial distance from the bottom of the vessel to obtain global data. It is found that the planar and global data follow the same general trend as the local data.

Chapter 5

Conclusions and Future Work

5.1 Conclusions

The present study aims to perform scaled adiabatic experiments to investigate the hydrodynamic effects of air ingress which are important in the postulated D-LOFC accident scenario in the VHTR. A test facility is designed in order gain a more extensive understanding of the air ingress phenomena. The experiment is performed using helium and air as the working fluids with a density ratio of approximately 0.14. The length-to-diameter ratio considered is $L/D = 3$ for the lower and higher side break locations. The transient local oxygen concentration is measured at various axial and radial locations with respect to time using an oxygen analyzer. These adiabatic experiments establish a database (the first of its kind) of local oxygen concentration/mixture density with respect to time for gravity driven exchange. The local data provides some general characteristics of the ingress. It is found that the majority of the local data follows the same general trend. The data for the locations within close proximity to the break are found to have oscillations in the measurement as a result of the helium-air interface. It is also shown that there is a time delay for an increase in air content for a higher oriented location. This indicates that the incoming air piles up from the bottom of the vessel. The global data for each side break is obtained by averaging the local data with respect to the vessel volume. The global data is found to follow the same general trend as the local data.

5.2 Future Work

As a continuation of this study, it is recommended to use the global data in the form of density change with respect to time in order to calculate the volumetric exchange rate, as done with the previous water-brine tests by Sarangi (2010).

Further experiments are recommended for this test facility. Experiments should be performed for the top break location. The geometric effects of length-to-diameter ratio and angle of inclination of the break should be investigated for all break locations. The other length-to-diameter ratios that can be considered based on the pipe breaks fabricated for this study are $L/D = 1$ and 5 . Temperature effects on ingress should also be investigated. Insulation should be applied to the test vessel in preparation for heated experiments. An internal structure could be put within the test vessel to perform experiments more comparable to the prototypic accident scenario. Laser Doppler Anemometry can be used in combination with glass pipe breaks to estimate a front velocity as well as a velocity profile within the break. The experimental results obtained could be compared to computational fluid dynamics analysis.

REFERENCES

- Benjamin, T. B., 1968, Gravity currents and related phenomena, *J. Fluid Mech*, **31** (2), pp. 209-248.
- Birman, V., Martin, J. E. & Meiburg, E., 2005, The non-Boussinesq lock-exchange problem. Part 2. High-resolution simulations. *J. Fluid Mech.* **537**, 125–144.
- Epstein, M., 1988, Buoyancy-driven exchange flow through small openings in horizontal partitions, *J. of Heat Transfer*, **110**, pp. 885-893.
- "Flow." *Dwyer Instruments, Inc. Online Catalog*. Sept. 2009. Web.
<<http://dwyerinstruments.dirxion.com>>.
- Fumizawa, M., 1992, Experimental study of helium-air exchange flow through a small opening, *Kerntechnik*, **57** (3), pp. 156-160.
- Gröbelbauer, H. P., Fanneløp, T. K. & Britter, R. E. 1993 The propagation of intrusion fronts of high density ratios. *J. Fluid Mech.* **250**, 669–687.
- Hirschfelder, J. O., C. E Curtiss, and R. B. Bird: *Molecular Theory of Gases and Liquids*, Wiley, New York, 1954.
- Hishida, M., Fumizawa, M., Takeda, T., Ogawa, M., and Takenaka, S., 1993, Researches on air ingress accidents of the HTTR, *Nuc. Eng. Des.*, **144**, pp. 317-325.
- Karman, T. von, 1940, The engineer grapples with non-linear problems, *Bull. Am. Math. Soc.*, **46**, pp. 615-683.

Keller, J. J., and Chyou, Y.-P., 1991, On the hydraulic lock-exchange problem. *J. Appl. Math. Phys.*, **42**, pp. 874-909.

Kim, S. and Talley, J.D., 2009, Quick Look Report Task 5: Air exchange and air ingress experimental data, Scaling analysis and test apparatus design for water-brine scoping experiments, prepared for the U.S Nuclear Regulatory Commission.

Leach, S.J., and Thompson, H., 1975, An investigation of some aspects of flow into gas cooled nuclear reactors following an accidental depressurization, *J. Br. Nucl. Energy Soc.*, **14** (3), pp. 243-250.

Lowe, R. J., Rottman, J. W. and Linden, P. F., 2005, The non-Boussinesq lock-exchange problem. Part 1. Theory and Experiments, *J. Fluid Mech.*, **537**, pp. 101-124.

MacDonald P. E. et al., September 2003, NGNP Point Design – Results of the Initial Neutronics and Thermal Hydraulic Assessments during FY-03, Idaho National Engineering and Environmental Laboratory, INEEL/EXT-03-00870 Rev. 1.

Mercer, A., and Thompson, H., 1975, An experimental investigation of some further aspects of the buoyancy-driven exchange flow between carbon dioxide and air following a depressurization accident in a Magnox Reactor, Part I: The exchange flow in inclined ducts, *J. Br. Nucl. Soc.*, **14**, pp. 327-334.

No, H. C. et al., 2007. Multicomponent Diffusion Analysis and Assessment of GAMMA Code and Improved RELAP 5 Code, *Nuclear Engineering and Design*, **237**, 997–1008.

Oh, C. H., Kim, E. S., Kang, H. S., No, H. C., and Cho, N. Z., December 2009, Experimental validation of stratified flow phenomena, graphite oxidation and mitigation strategies of air ingress accidents, FY-09. Idaho National Laboratory INL/EXT-09-16465 Rev. 1.

Oh, C. H., Kim, E. S., NO, H. C., and Cho, N. Z., December 2008, Experimental Validation of Stratified Flow Phenomena, Graphite Oxidation, and Mitigation Strategies of Air Ingress Accident, INL/EXT-08-14840.

Oh, C.H., et al., March 2006, Development of Safety Analysis Code and Experimental Validation for a Very High Temperature Gas-Cooled Reactor, INL/EXT-06-01362.

Poling, Bruce E., J. M. Prausnitz, and John P. O'Connell. *The Properties of Gases and Liquids*. New York: McGraw-Hill, 2001.

Product Data Sheet - Nansulate EPX. Industrial Nanotech. Print.

Products and Services. National Instruments, 2010. Web. <<http://www.ni.com/products/>>.

Richards, M. B., et al, April 2006, H2-MHR Pro-Conceptual Design Report: SI-Based Plant, General Atomics, GA-A25401.

"Rosemount 3051S Series of Instrumentation Scalable Pressure, Flow, and Level Solutions." *Product Data Sheet*. EMERSON Process Management, Aug. 2010. Web. <[http://www2.emersonprocess.com/siteadmincenter/PM Rosemount Documents/00813-0100-4801.pdf](http://www2.emersonprocess.com/siteadmincenter/PM%20Rosemount%20Documents/00813-0100-4801.pdf)>.

Sarangi, Suchismita. *Scaled Experiment on Gravity Driven Exchange Flow for the Very High Temperature Reactor*. Thesis. The Pennsylvania State University, 2010. Print.

Schultz, R. et al., *Next Generation Nuclear Plant Methods Technical Program Plan*, INL/EXT-06-11804, Rev 0.26, September 2006.

Takeda, T., 1997, Air Ingress Behavior during a Primary-pipe Rupture Accident of HTGR, JAERI-1338, Japan Atomic Energy Research Institute.

Takeda, T., and Hishida, M., 1996, Studies on Molecular Diffusion and Natural Convection in a Multicomponent Gas System, *International Journal of Heat and Mass Transfer*, 39 (3), 527-536.

Takeda, T., and Hishida, M., 1992, Studies on diffusion and natural convection of two component gases, *Nucl Eng Des*, 135, 341-354.

Tanaka, G., Zhang, B., and Hishida, M., 2002, Effects of Gas Properties and Inclination Angle on Exchange Flow through a Rectangular Channel, *JSME Int. J. Ser. B*, **45** (4), pp. 901-909.

Thermocouple Response Time. OMEGA Engineering, Inc. Web.

<<http://www.omega.com/temperature/Z/ThermocoupleResponseTime.html>>.

Thermox® CEM O2/TM Oxygen Analyzer User Manual. Pittsburgh: AMETEK. PDF.

Yih, C.S., and Guha, C.R., 1955. Hydraulic jump in a fluid system of two layers. *Tellus* 7 (3), 358-366.

Appendix A

Exchange Volume Calculation for GT-MHR (Kim and Talley, 2009)

In order to calculate the global exchange time ratio, a simple calculation is performed using the reference GT-MHR (Richards et al., 2006) to determine the volume to be exchanged. The reactor vessel schematics are given in Figures A-1 (a) and A-1 (b). As shown in Figure A-1, the lower hemisphere includes the shutdown cooling system and this volume is neglected in calculating the open volume of the vessel. Also, the support structures under the core are neglected, as well as any internals in the upper hemisphere (controls rods, etc).

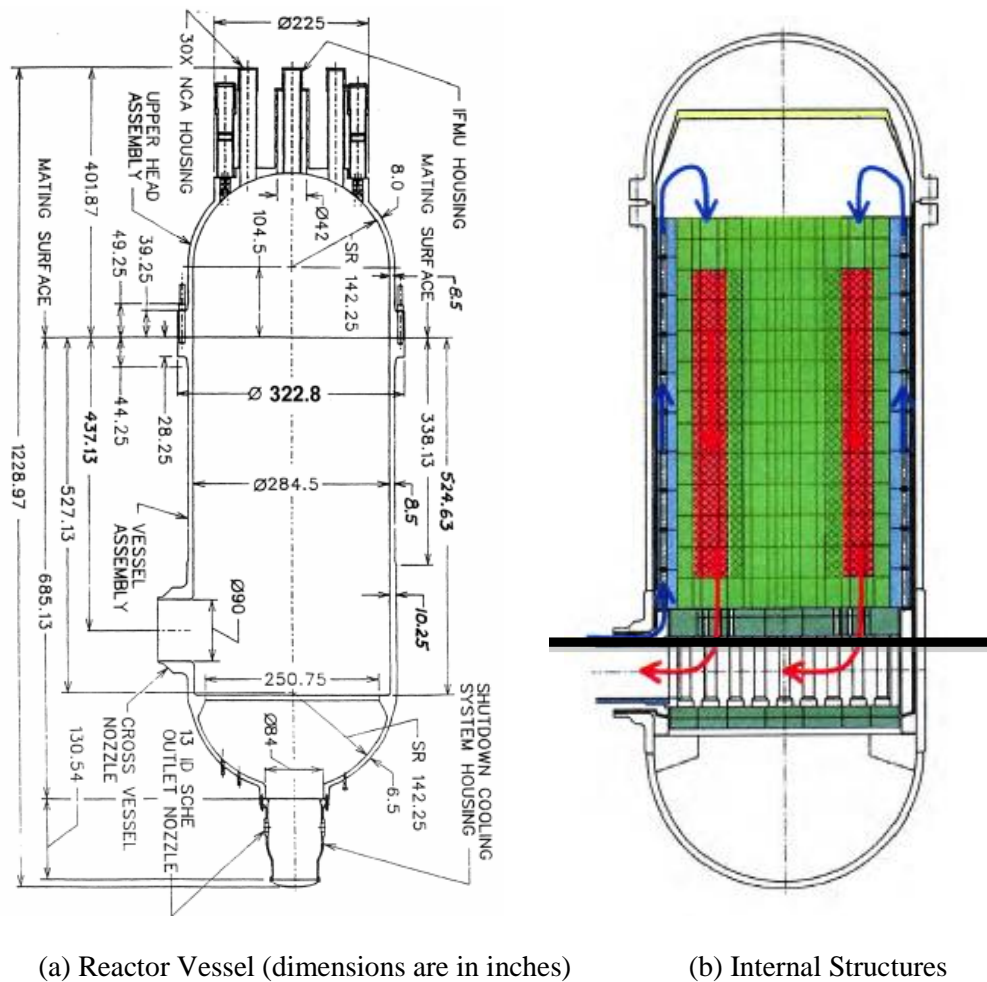


Figure A-1: GT-MHR Schematics

For the volume to be exchanged during a primary pipe break, the air in containment will displace the helium in the vessel up to the highest point of connection between the primary pipe and vessel, given by the black solid line in Figure A-1 (b). Even though tilt angles will be employed on the primary pipe for the heated helium-air facility, the orientation will always be towards the vertical upward and thus the same displacement will always occur. This volume is given by:

$$\begin{aligned}
 V_{primary} &= \pi \frac{d_{vessel}^2}{4} H \\
 &= \pi \frac{(284.5)^2}{4} (90) \\
 &= 5.72133E6 \text{ [in}^3\text{]} = 24,768 \text{ [gallons]} = 93,755 \text{ [liters]}
 \end{aligned} \tag{A-1}$$

where d_{vessel} is the diameter of the vessel, and H here is the diameter of the primary pipe.

In the standpipe case, for any tilt angle, the volume to be exchanged will be the total open volume in the vessel. This volume will include the core region for which the cross-sectional layout is given in Figure A-2 and the dimensions of a fuel block in Figure A-3.

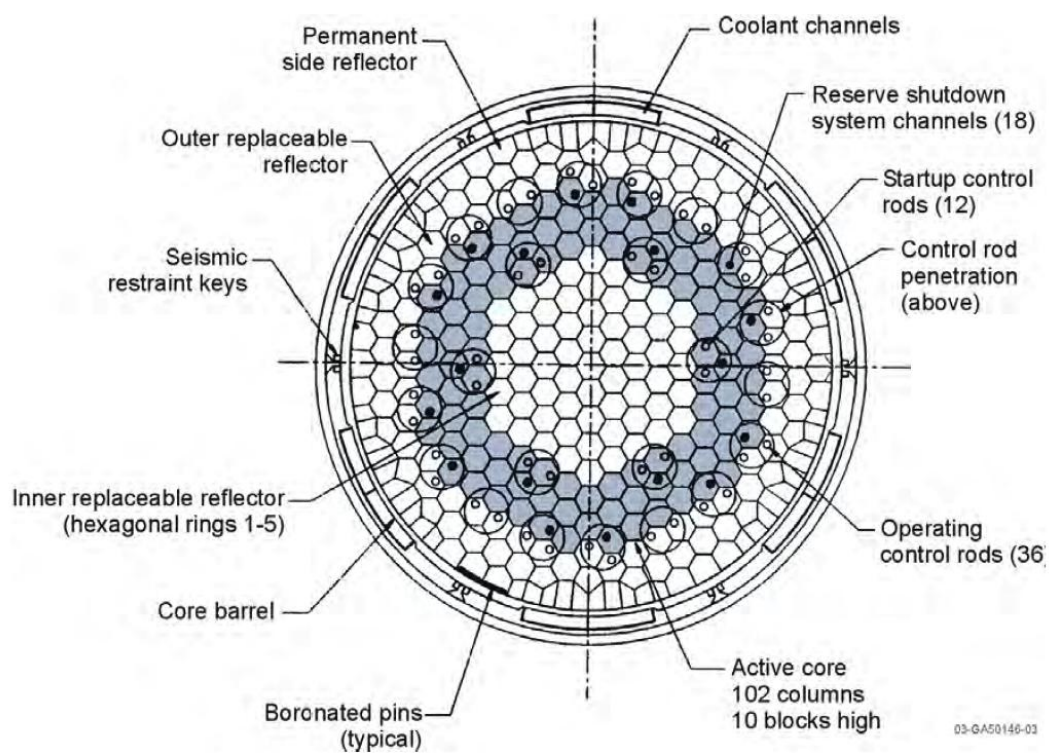


Figure A-2: Cross-sectional view of core layout

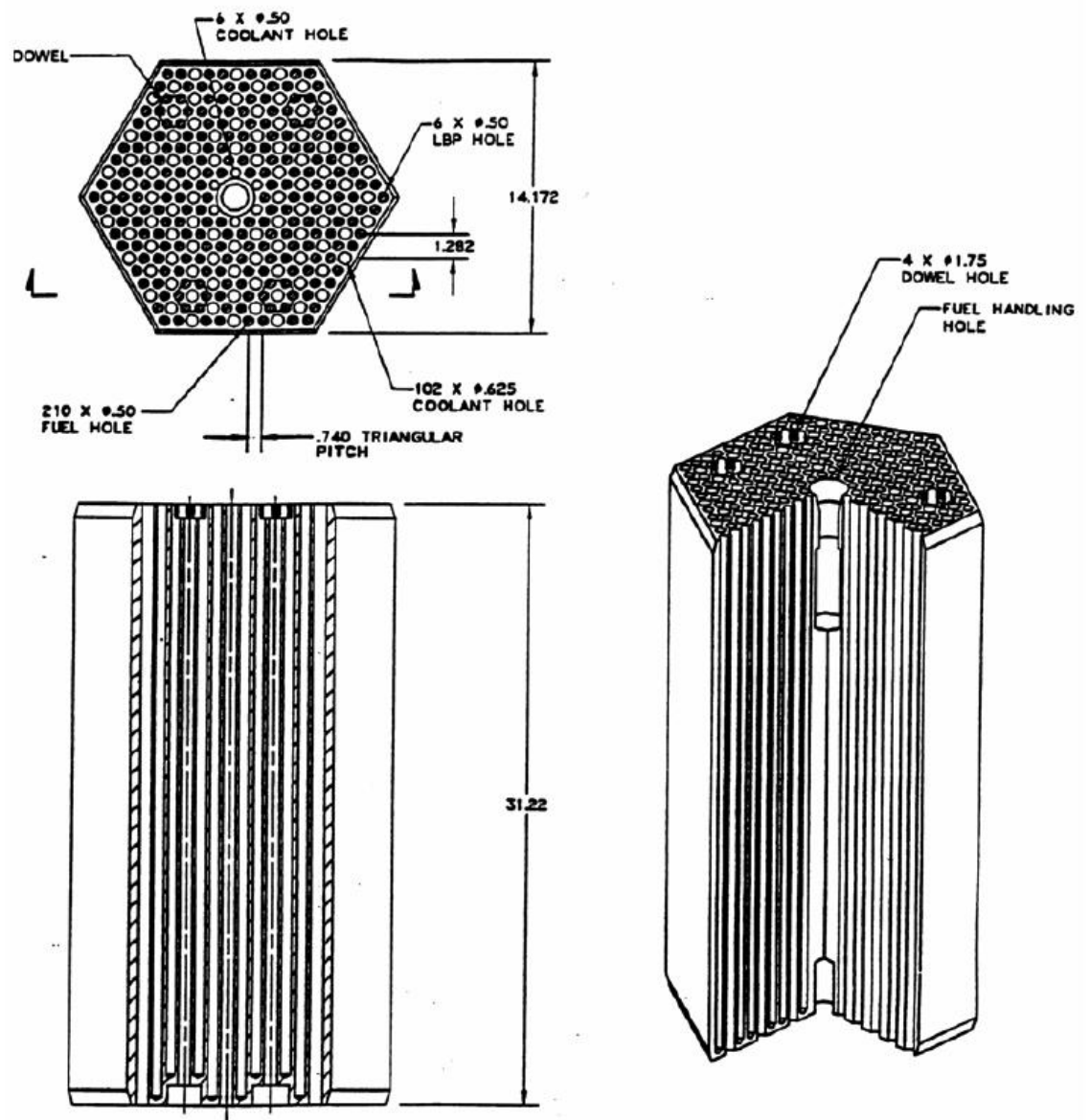


Figure A-3: Fuel Block (dimensions are in Inches)

For calculating the helium volume in the core region the following assumptions are made:

- Coolant channels are only present in the active core fuel blocks.
- The maximum diameter of the core is 22.5 feet (270 inches) and the volume between the core and vessel wall is filled with helium.
- Control rods are neglected.
- Fuel handling holes are neglected.

Then, the volume of the core region occupied by helium is given by:

$$\begin{aligned}
 V_{activecore} &= N_{fuelblocks} H \left(102\pi \frac{d_{coolant,l}^2}{4} + 6\pi \frac{d_{coolant,s}^2}{4} \right) \\
 &= 1020(31.22) \left(102\pi \frac{0.625^2}{4} + 6\pi \frac{0.5^2}{4} \right) \\
 &= 1.03403E6 \text{ [in}^3\text{]} = 4,476 \text{ [gallons]} = 16,945 \text{ [liters]}
 \end{aligned} \tag{A-2}$$

where $d_{coolant,s}$, $d_{coolant,l}$, $N_{fuelblocks}$, and H are the diameters of the smaller and larger coolant channels, number of fuel blocks in the active core, and the fuel block height respectively. The helium filling the annular gap region (with a height of 10 fuel blocks) between the vessel and core is given by:

$$\begin{aligned}
 V_{annular} &= \pi H \left(\frac{d_{vessel}^2}{4} - \frac{d_{core}^2}{4} \right) \\
 &= \pi(312.2) \left(\frac{284.5^2}{4} - \frac{270^2}{4} \right) \\
 &= 1.97148E6 \text{ [in}^3\text{]} = 8,535 \text{ [gallons]} = 32,307 \text{ [liters]}
 \end{aligned} \tag{A-3}$$

The volume of the cylindrical region above the core and the upper hemisphere is calculated by:

$$\begin{aligned}
 V_{upper} &= \pi \frac{d_{vessel}^2}{4} H + \frac{1}{2} \left(\frac{4}{3} \pi r_{hemisphere}^3 \right) \\
 &= \pi \frac{284.5^2}{4} (104.5) + \frac{1}{2} \left(\frac{4}{3} \pi (142.25)^3 \right) \\
 &= 1.26717E7 \text{ [in}^3\text{]} = 54,856 \text{ [gallons]} = 207,652 \text{ [liters]}
 \end{aligned}
 \tag{A-4}$$

Hence, the volume to be exchanged during a standpipe break is:

$$\begin{aligned}
 V_{standpipe} &= V_{primary} + V_{activecore} + V_{annular} + V_{upper} \\
 &= 24,768 + 4,476 + 8,535 + 54,856 \\
 &= 92,635 \text{ [gallons]} = 350,662 \text{ [liters]}
 \end{aligned}
 \tag{A-5}$$

Appendix B

Engineering Drawings

Vessel

Top Plate

Bottom Plate

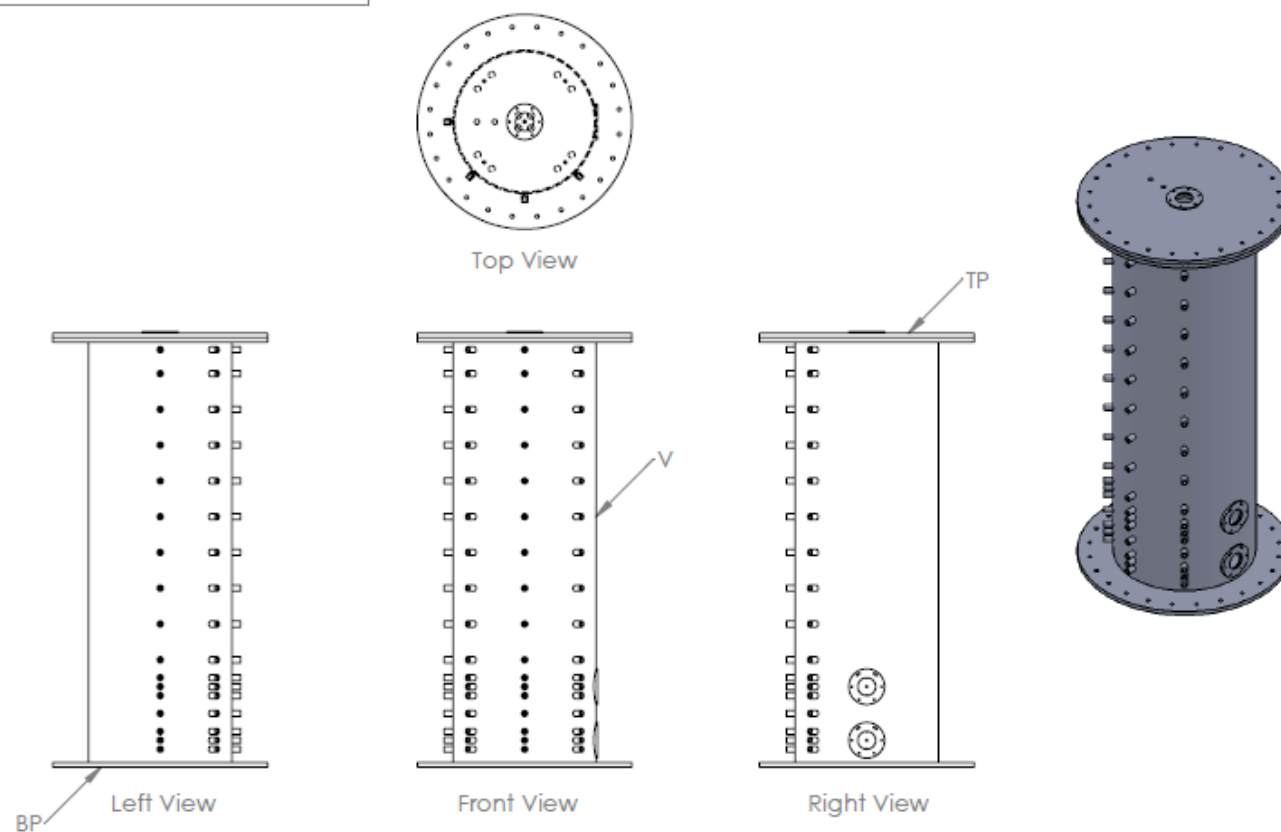
Pipe Break

SHEET 1 OF 1

SCALE: 1:24

Material: Carbon Steel
Prepared by: Jenna Baird/
Seungjin Kim
Contact: (814)865-8429

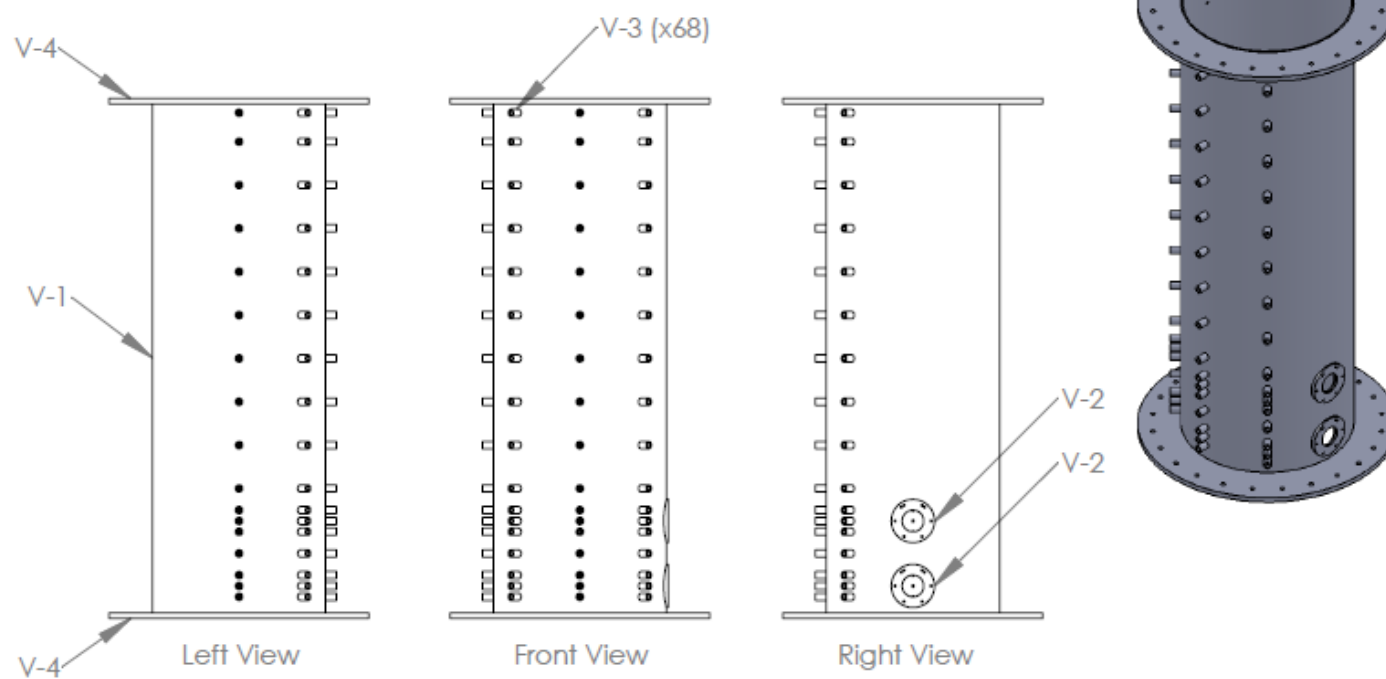
Schematic of the Final Assembly

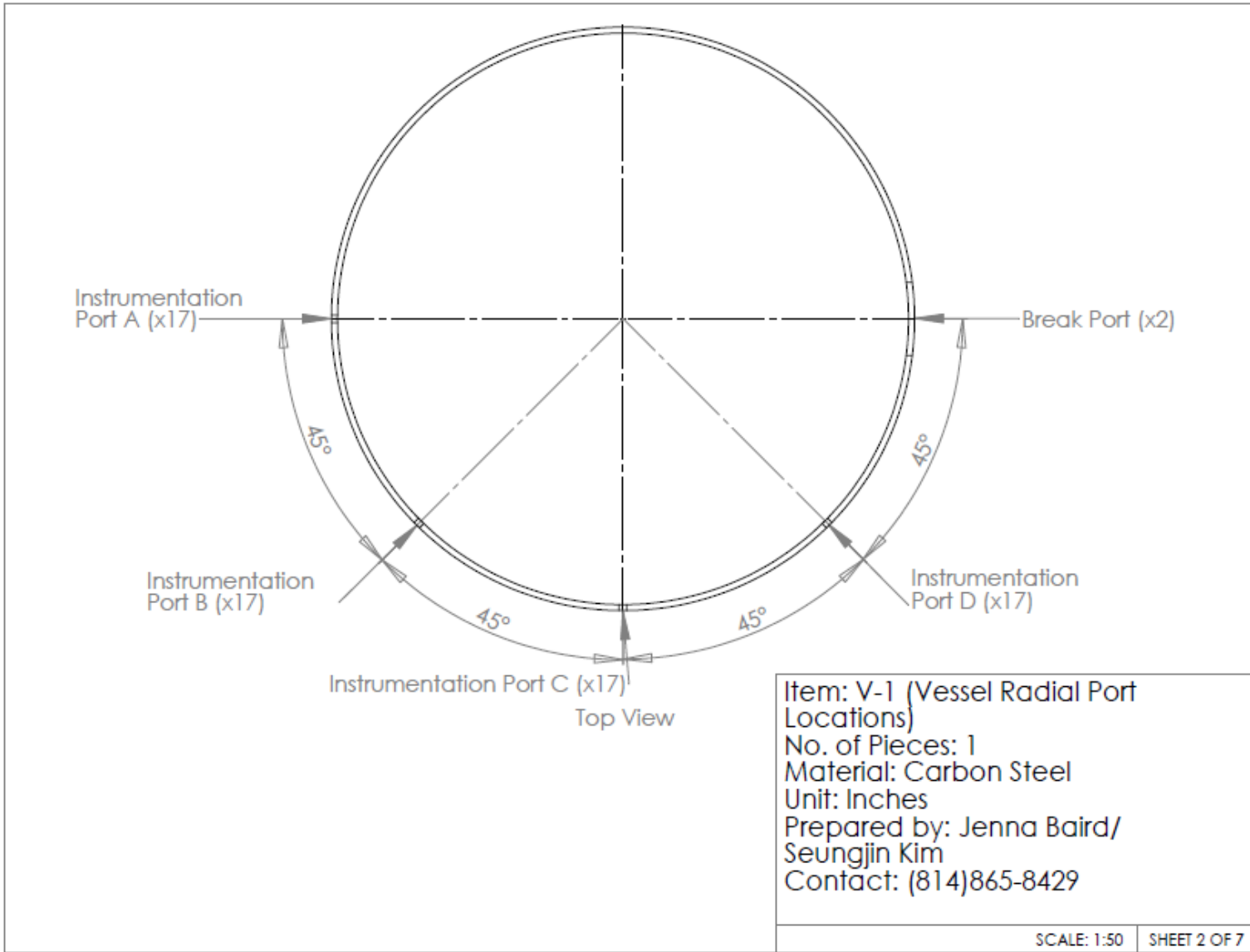


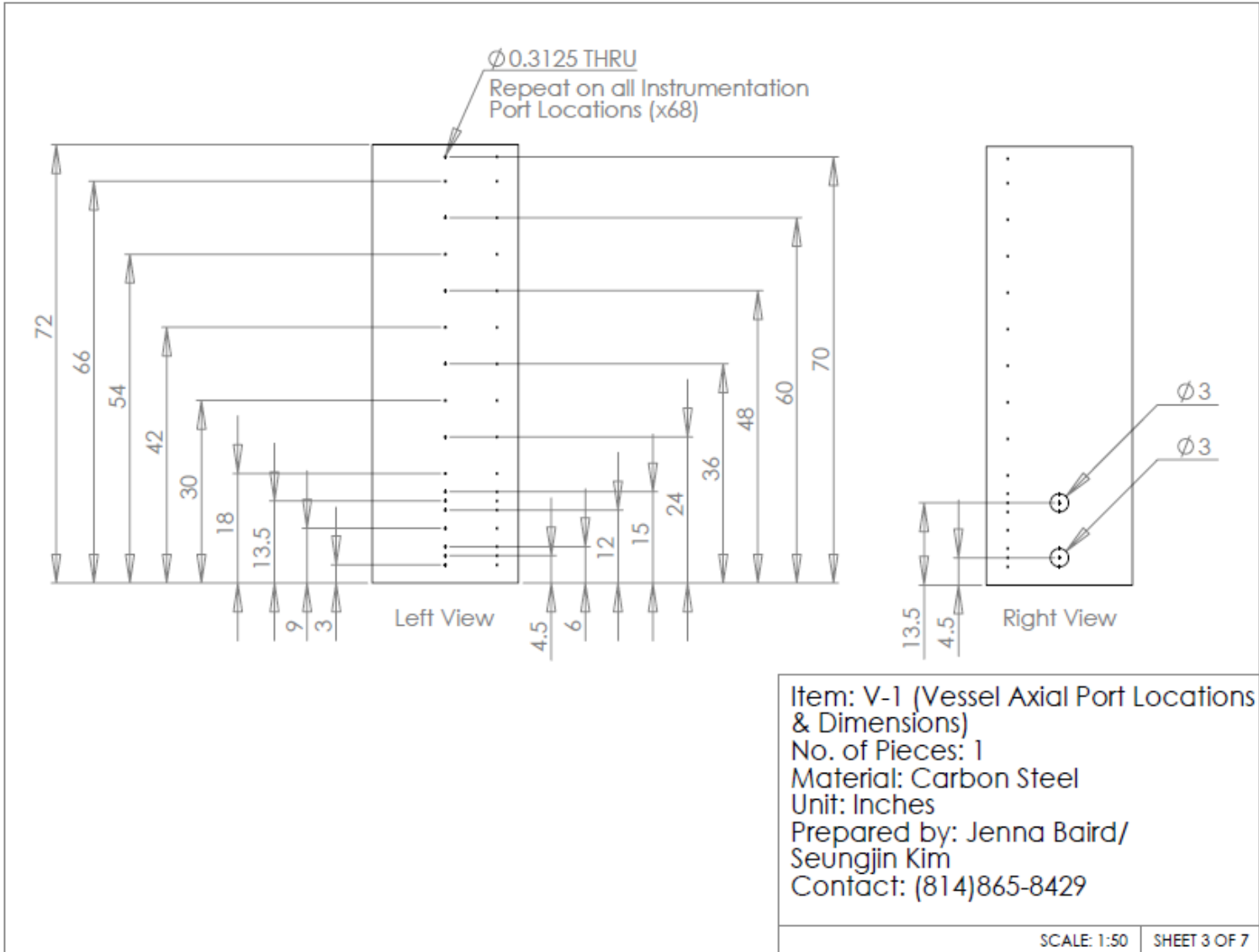
SHEET 1 OF 7 SCALE: 1:50

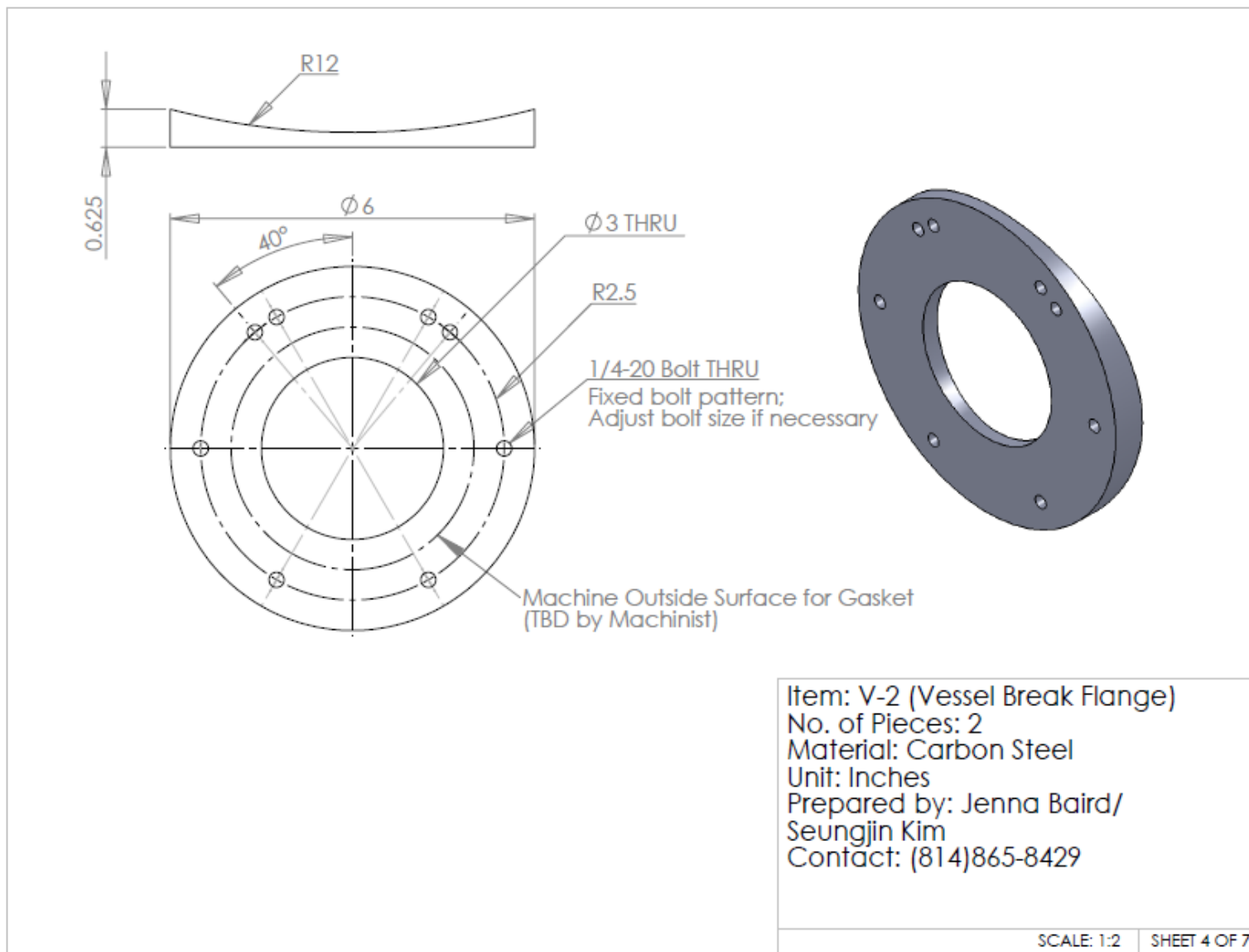
Material: Carbon Steel
Prepared by: Jenna Baird/
Seungjin Kim
Contact: (814)865-8429

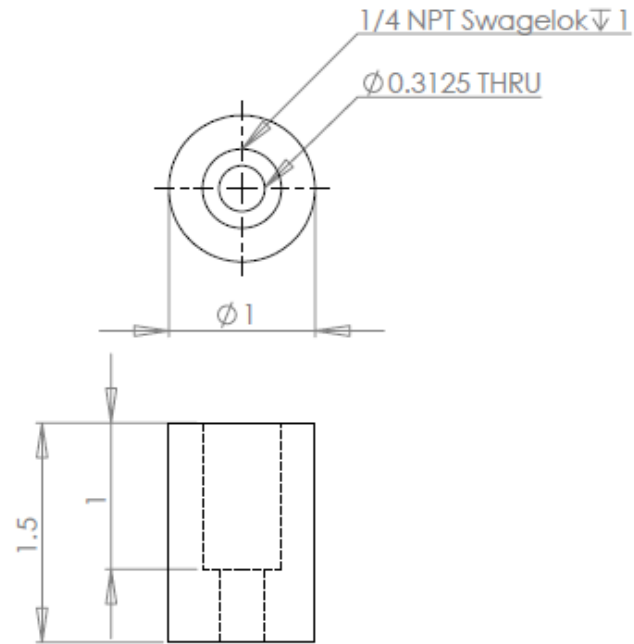
Vessel Assembly (V) V-1 - V-4



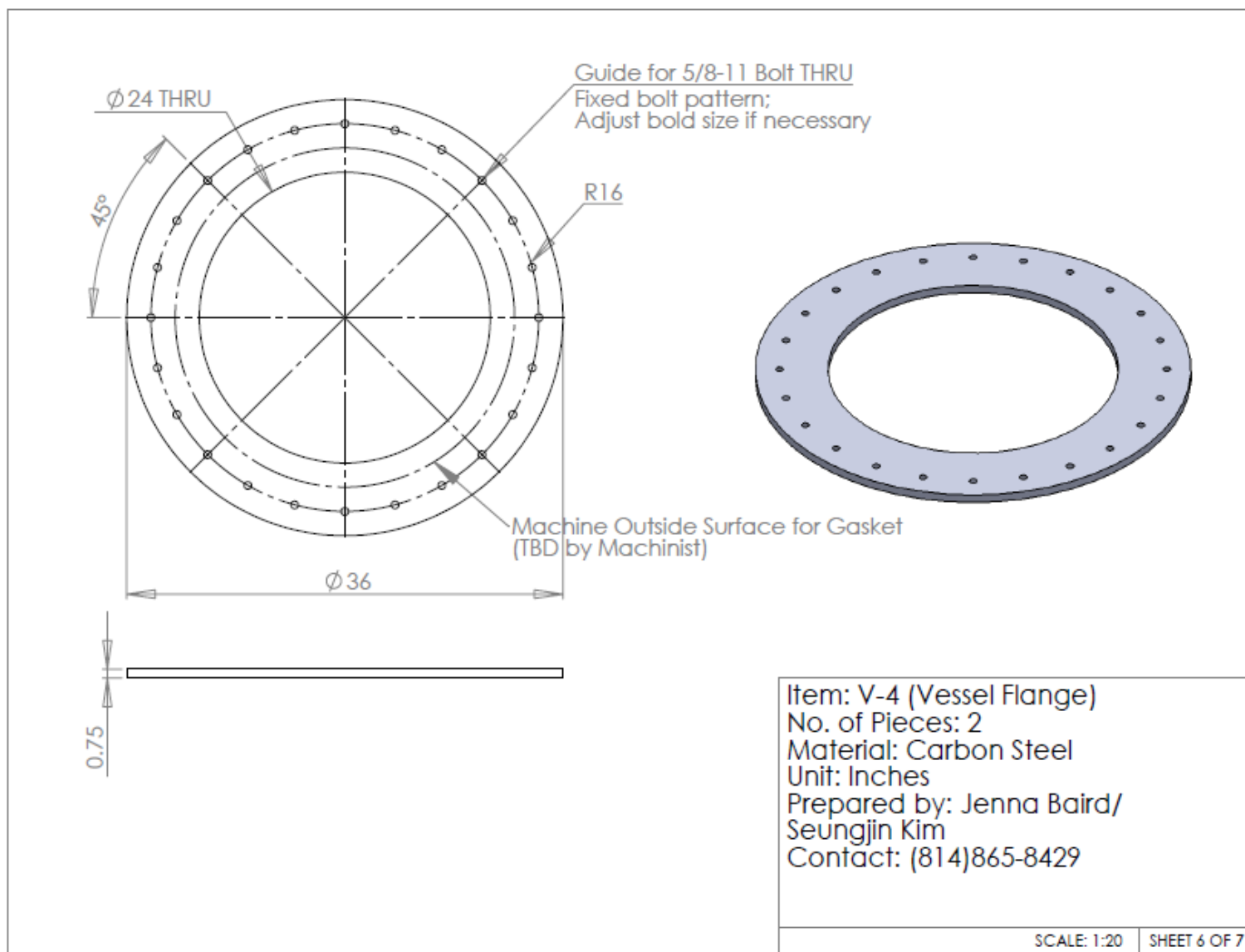








Item: V-3 (Oxygen Analyzer Plug)
 No. of Pieces: 68
 Material: Carbon Steel
 Unit: Inches
 Prepared by: Jenna Baird/
 Seungjin Kim
 Contact: (814)865-8429



SHEET 7 OF 7

SCALE: 1:50

Item: V (Vessel Weld Locations)

No. of Pieces: 1

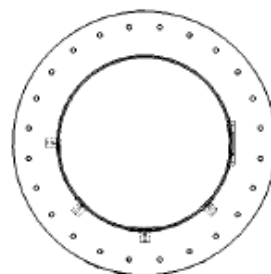
Material: Carbon Steel

Unit: Inches

Prepared by: Jenna Baird/

Seungjin Kim

Contact: (814)865-8429



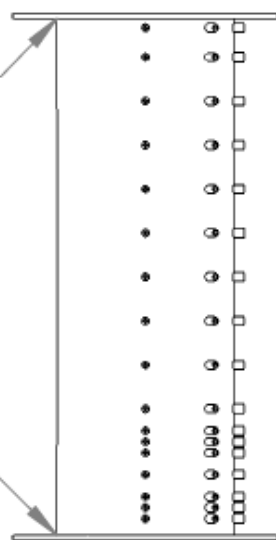
Top View

Align bolts on V-4 as shown

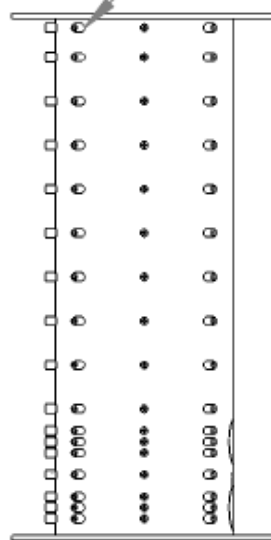
Weld V-3 to V-1
68 locations

Weld V-4 to V-1

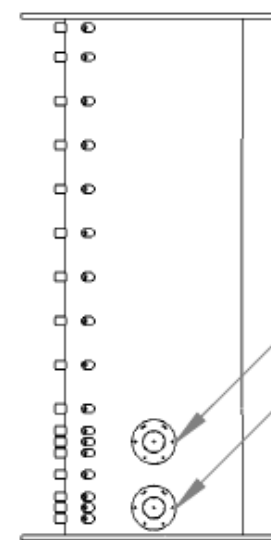
Weld V-4 to V-1



Left View



Front View



Right View

Weld V-2 to V-1

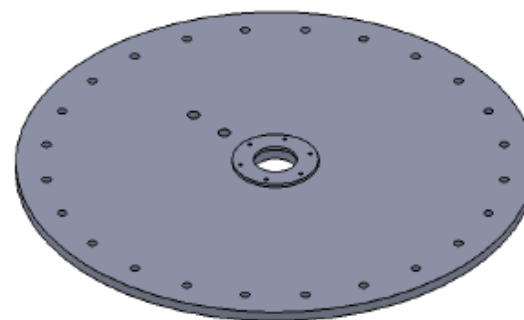
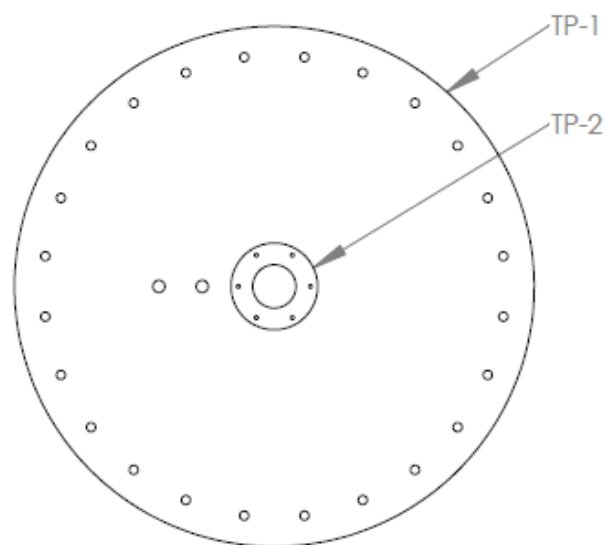
Weld V-2 to V-1

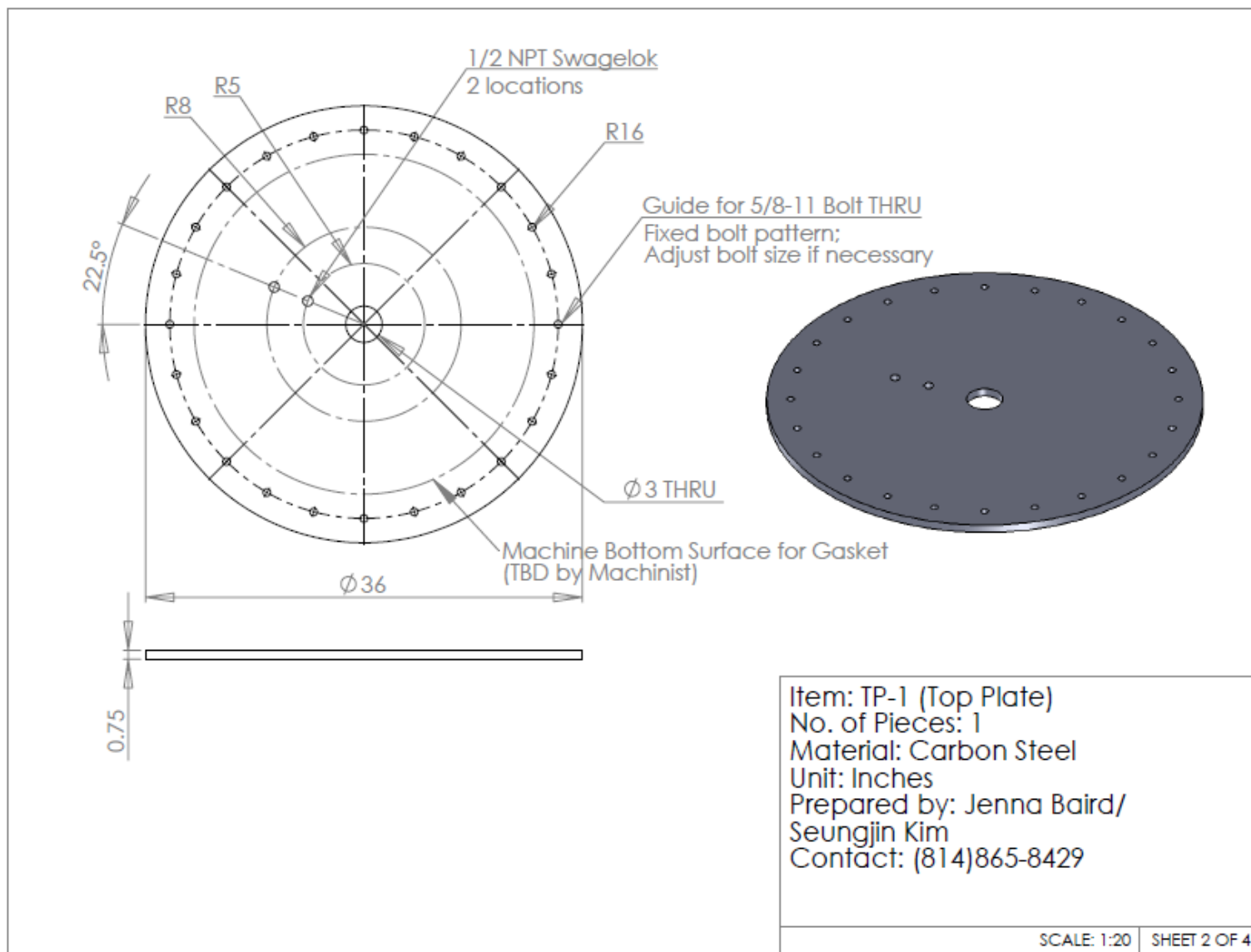
SHEET 1 OF 4

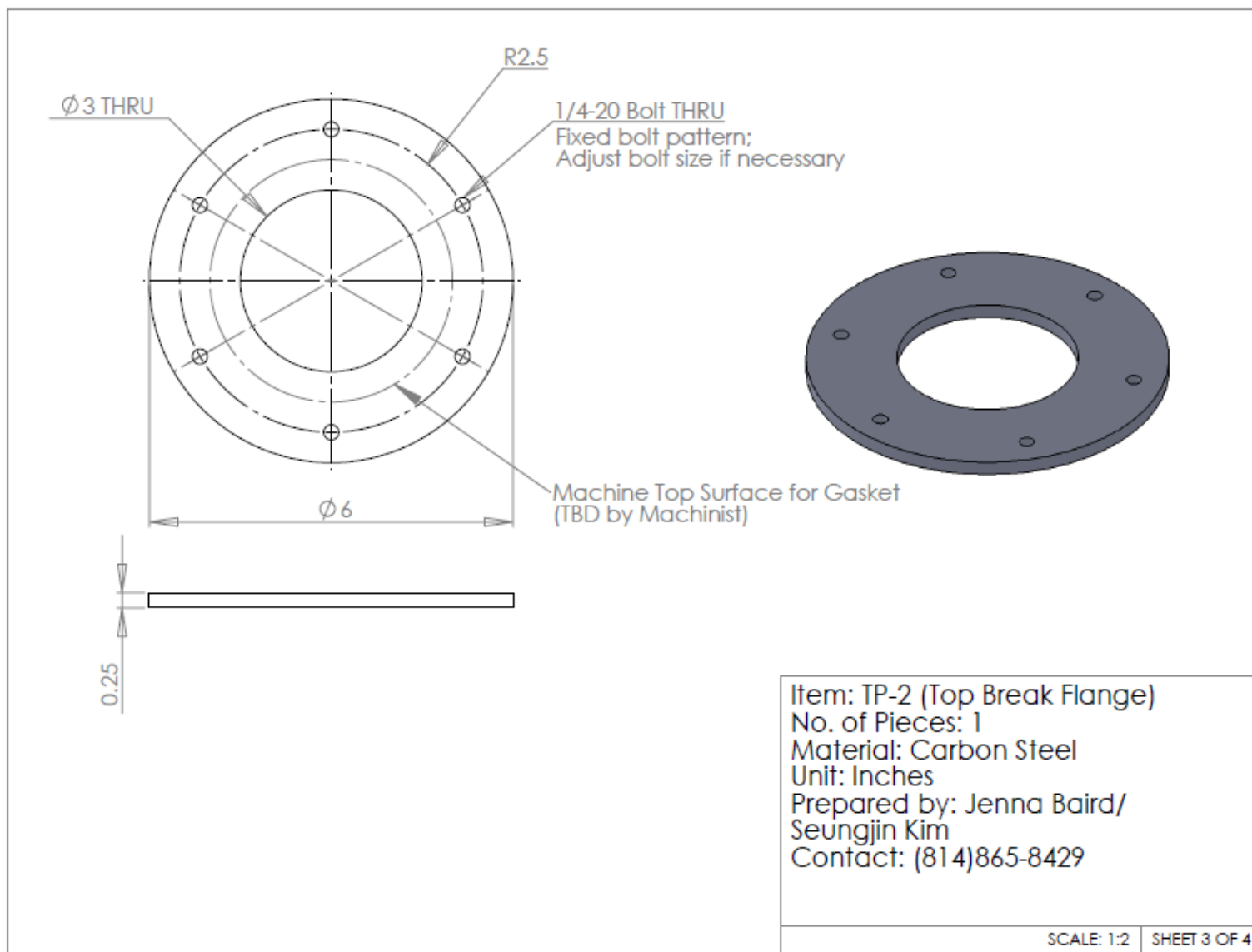
SCALE: 1:20

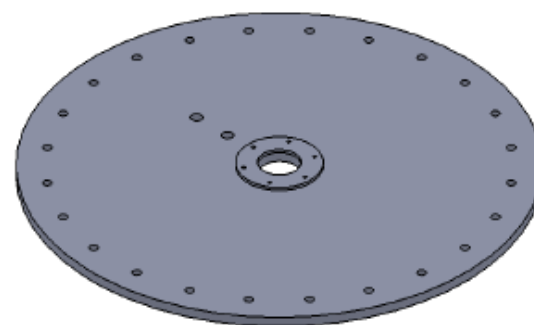
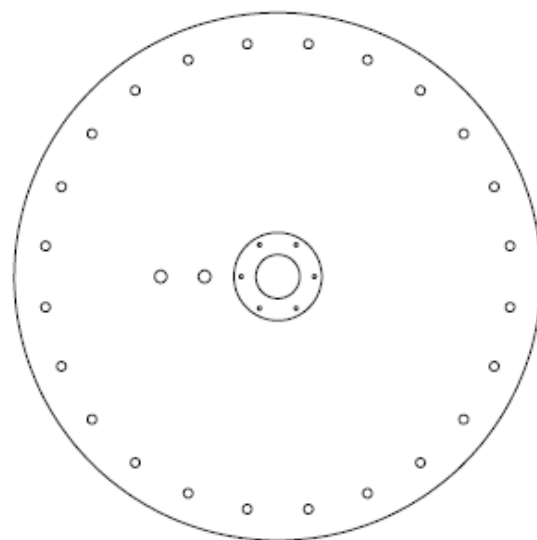
Material: Carbon Steel
Prepared by: Jenna Baird/
Seungjin Kim
Contact: (814)865-8429

Top Plate Assembly (TP) TP-1, TP-2







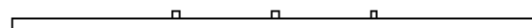
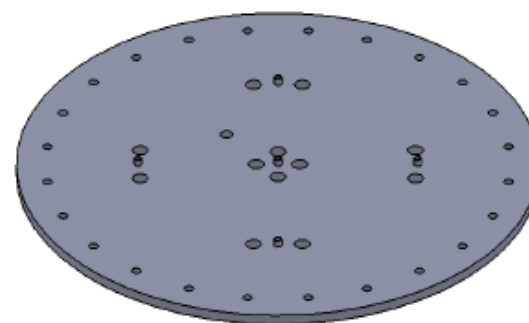
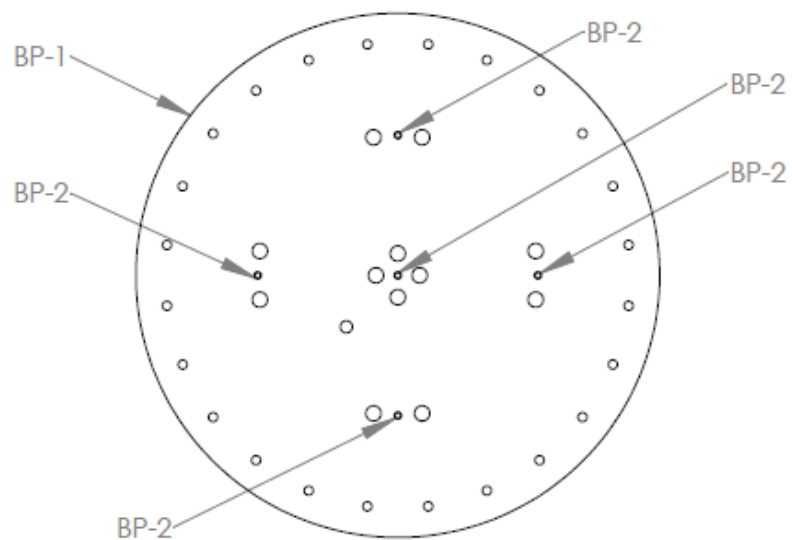


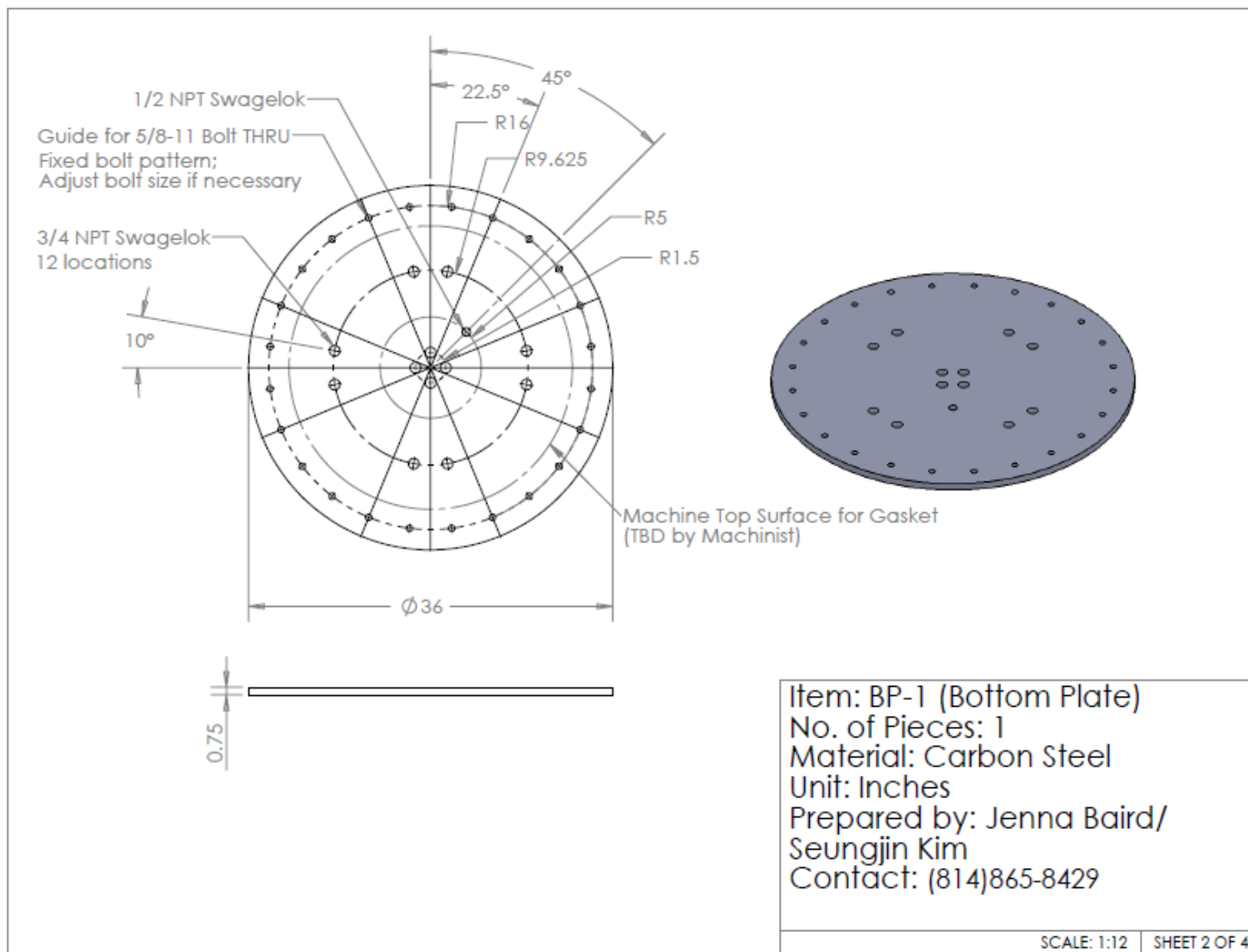
Item: TP (Top Plate Weld Locations)
No. of Pieces: 1
Material: Carbon Steel
Unit: Inches
Prepared by: Jenna Baird/
Seungjin Kim
Contact: (814)865-8429

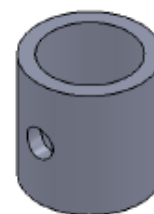
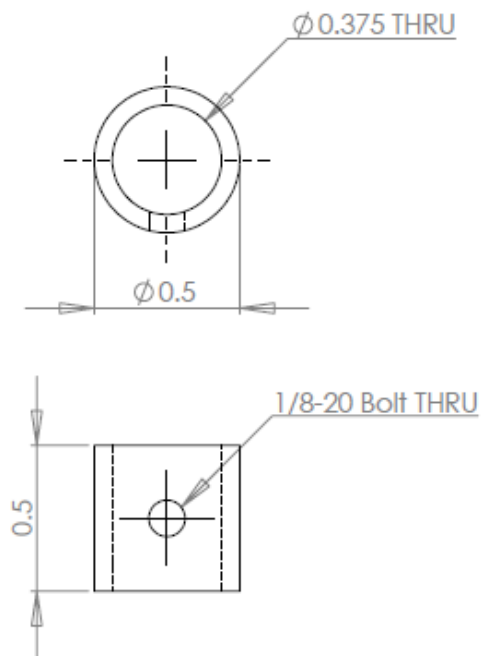
SHEET 1 OF 4 SCALE: 1:20

Material: Carbon Steel
Prepared by: Jenna Baird/
Seungjin Kim
Contact: (814)865-8429

Bottom Plate Assembly (BP) BP-1, BP-2



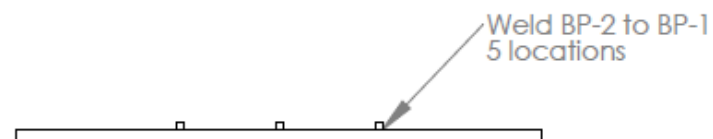
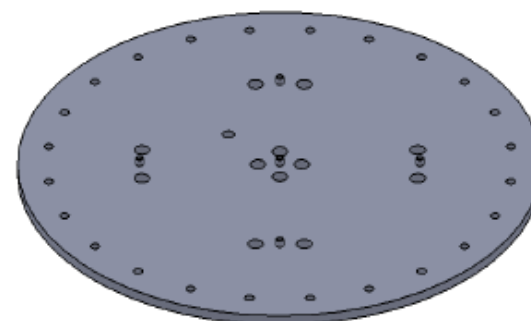
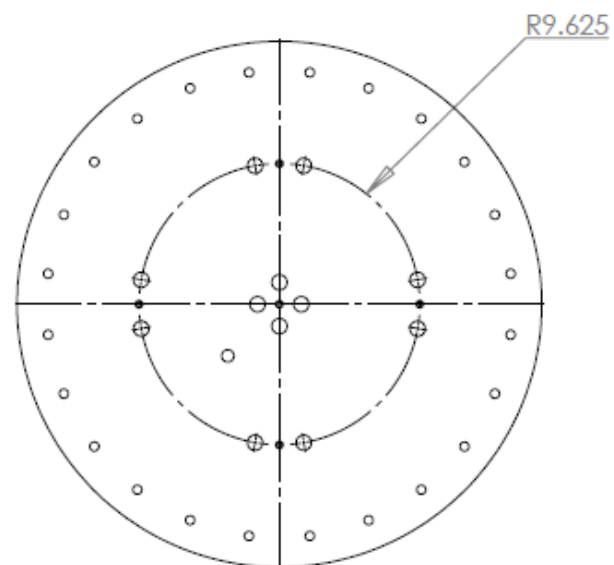




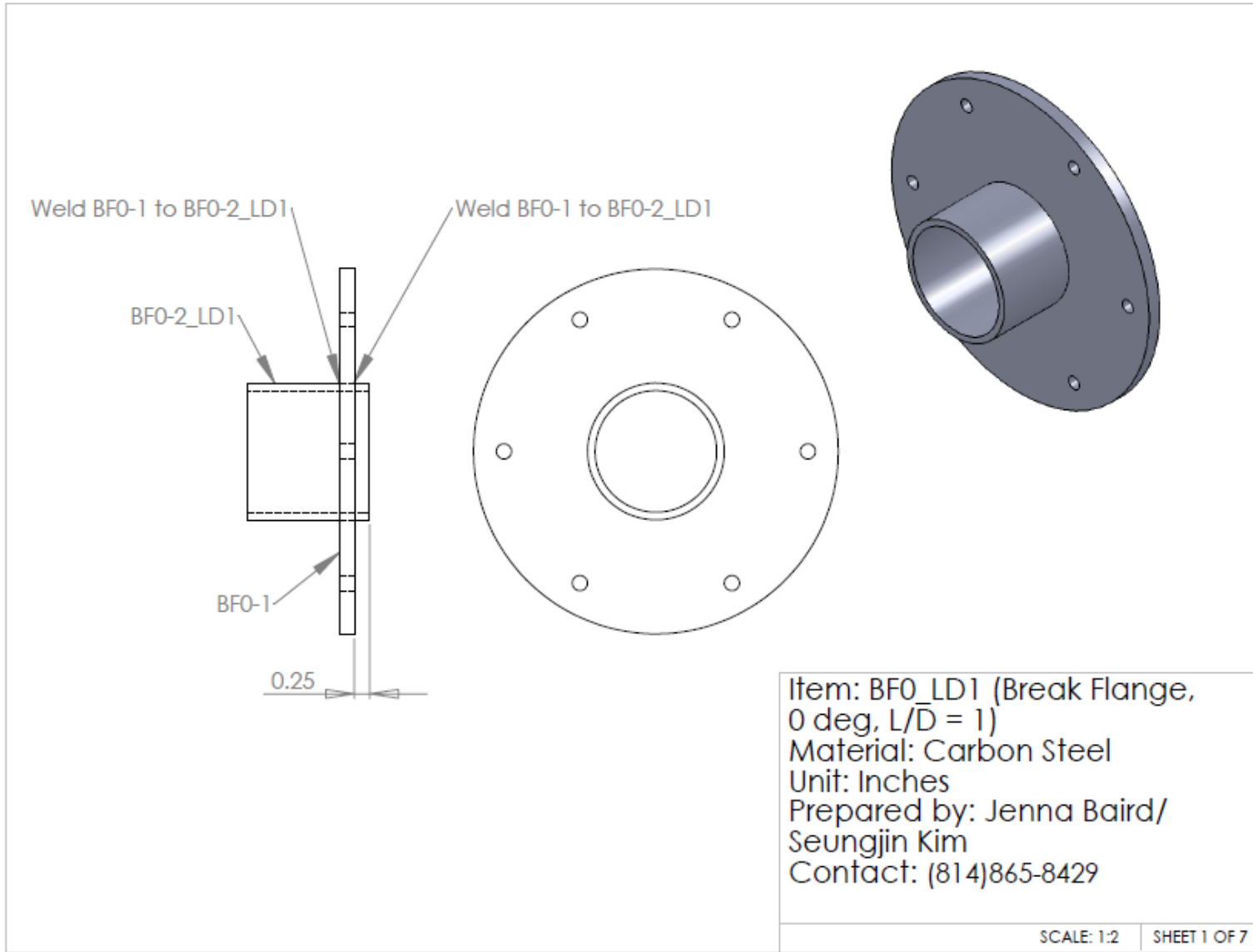
Item: BP-2 (Thermocouple Cage Rod Support)
No. of Pieces: 5
Material: Carbon Steel
Unit: Inches
Prepared by: Jenna Baird/
Seungjin Kim
Contact: (814)865-8429

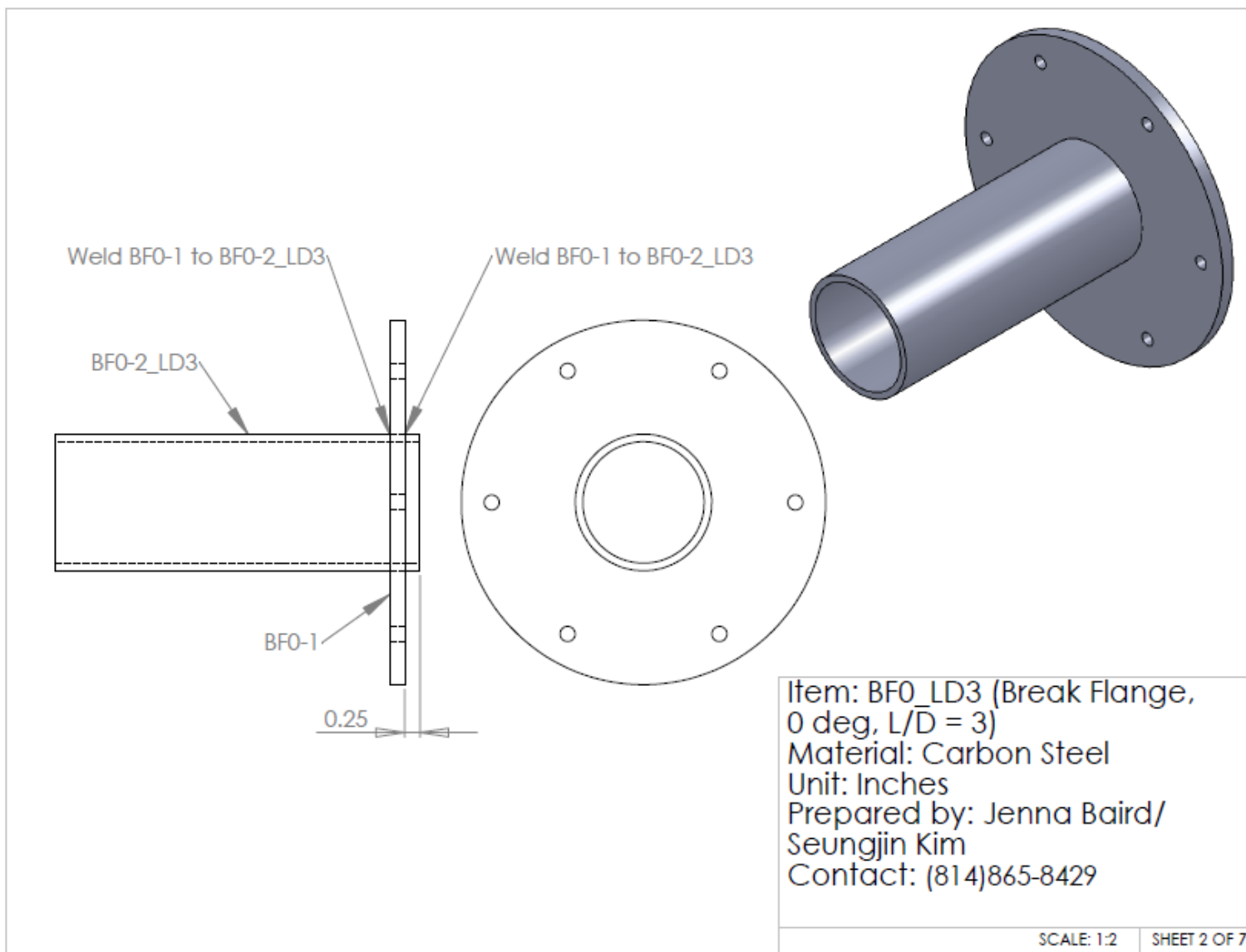
SCALE: 2:1

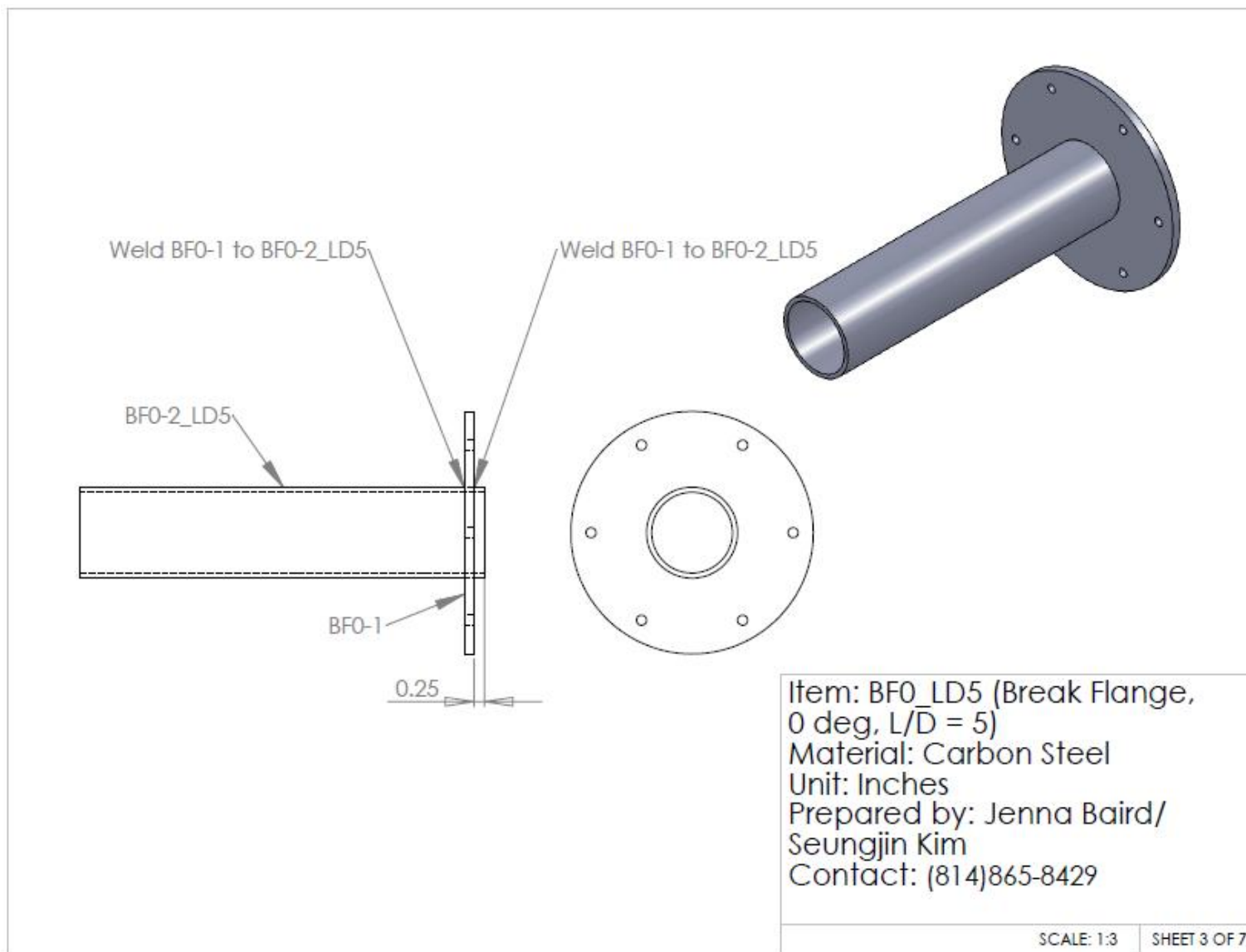
SHEET 3 OF 4

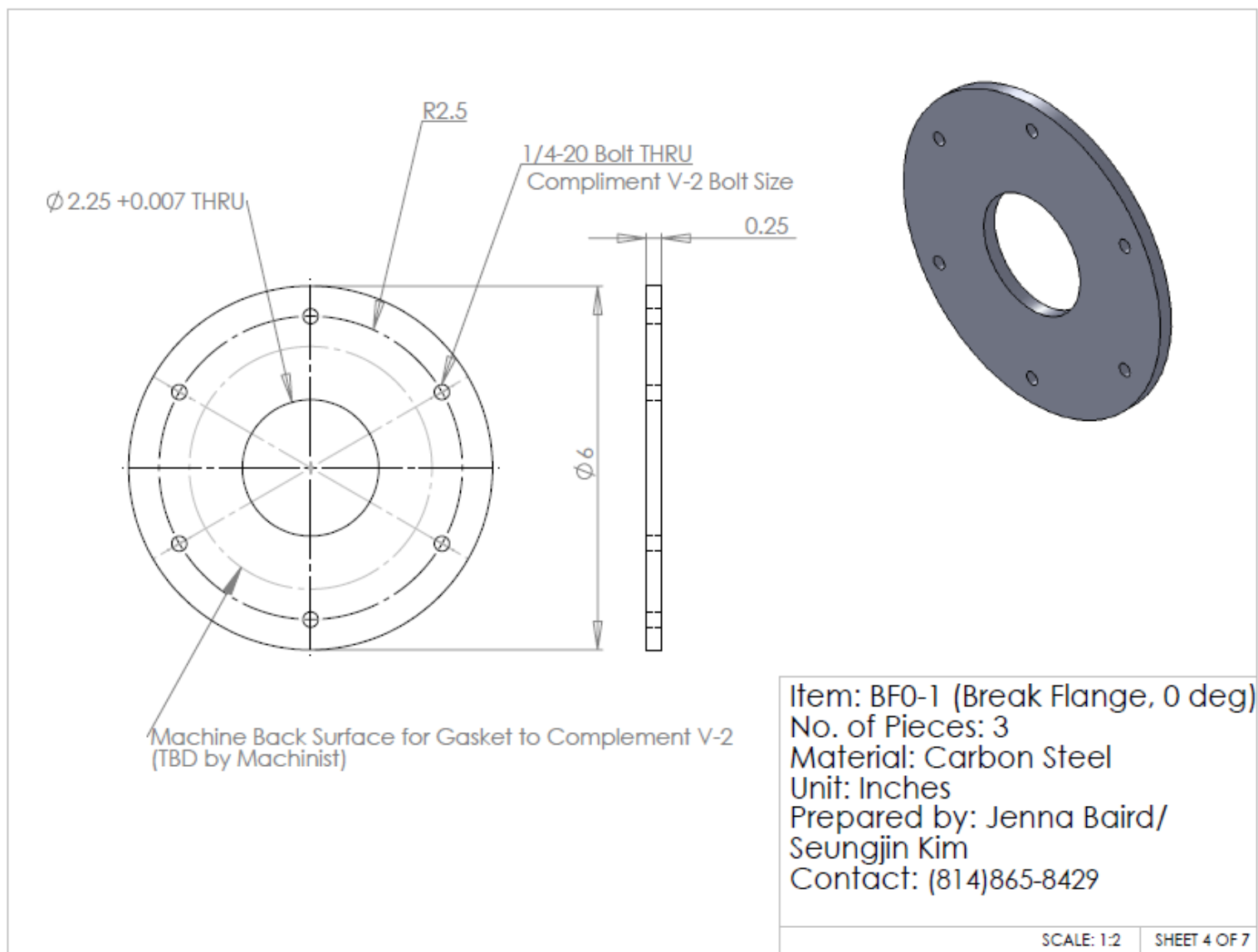


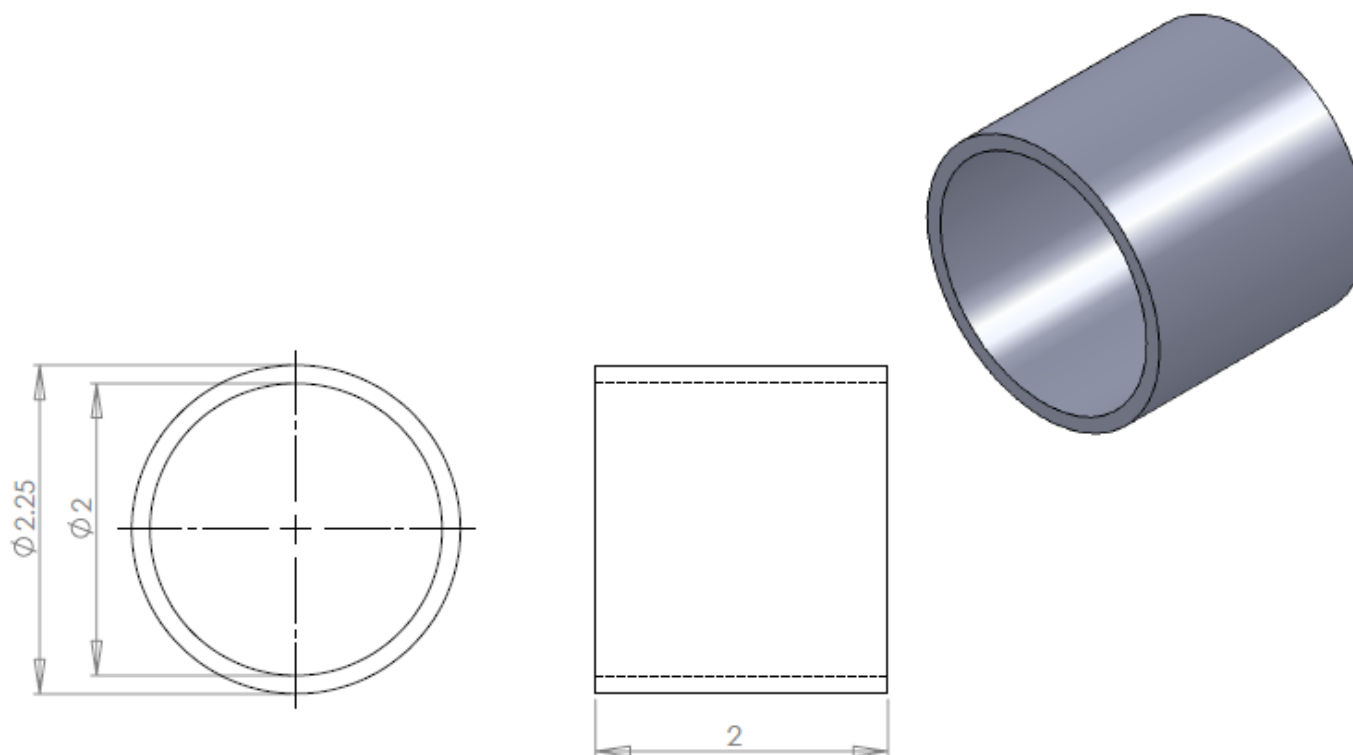
Item: BP (Bottom Plate Weld Locations)
No. of Pieces: 1
Material: Carbon Steel
Unit: Inches
Prepared by: Jenna Baird/
Seungjin Kim
Contact: (814)865-8429







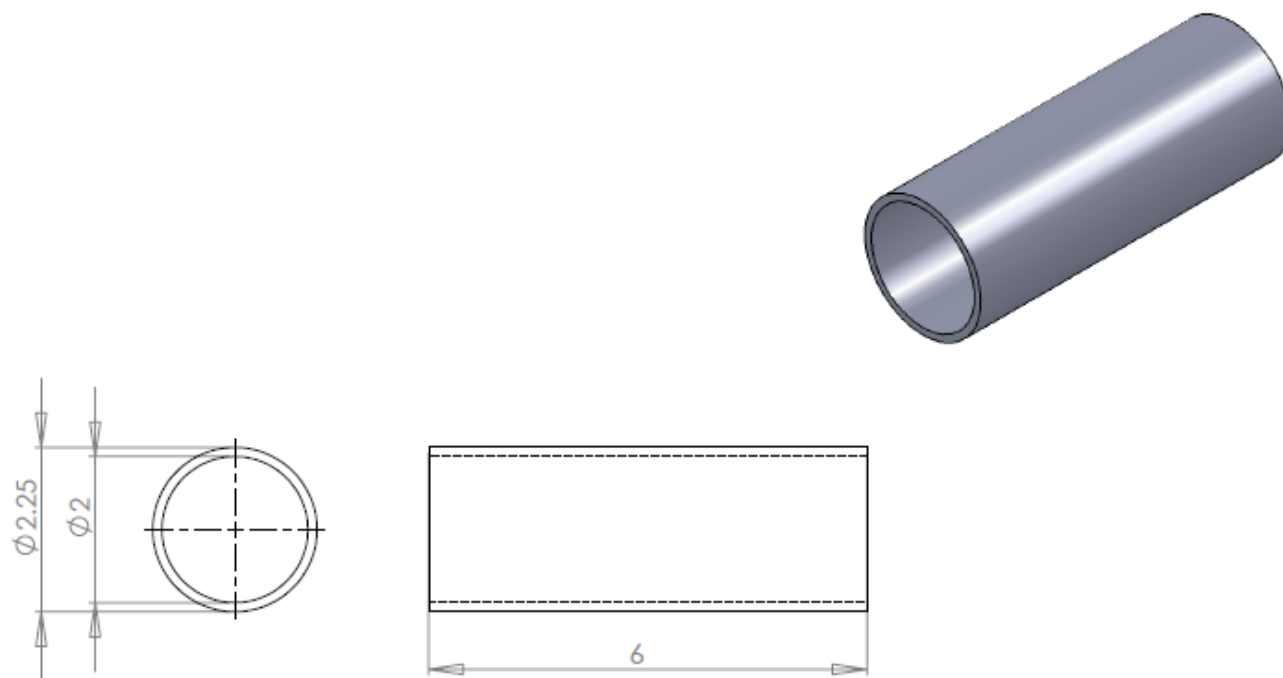




Item: BF0-2_LD1 (Break Flange
Pipe, 0 deg, L/D = 1)
No. of Pieces: 1
Material: Carbon Steel
Unit: Inches
Prepared by: Jenna Baird/
Seungjin Kim
Contact: (814)865-8429

SCALE: 1:1

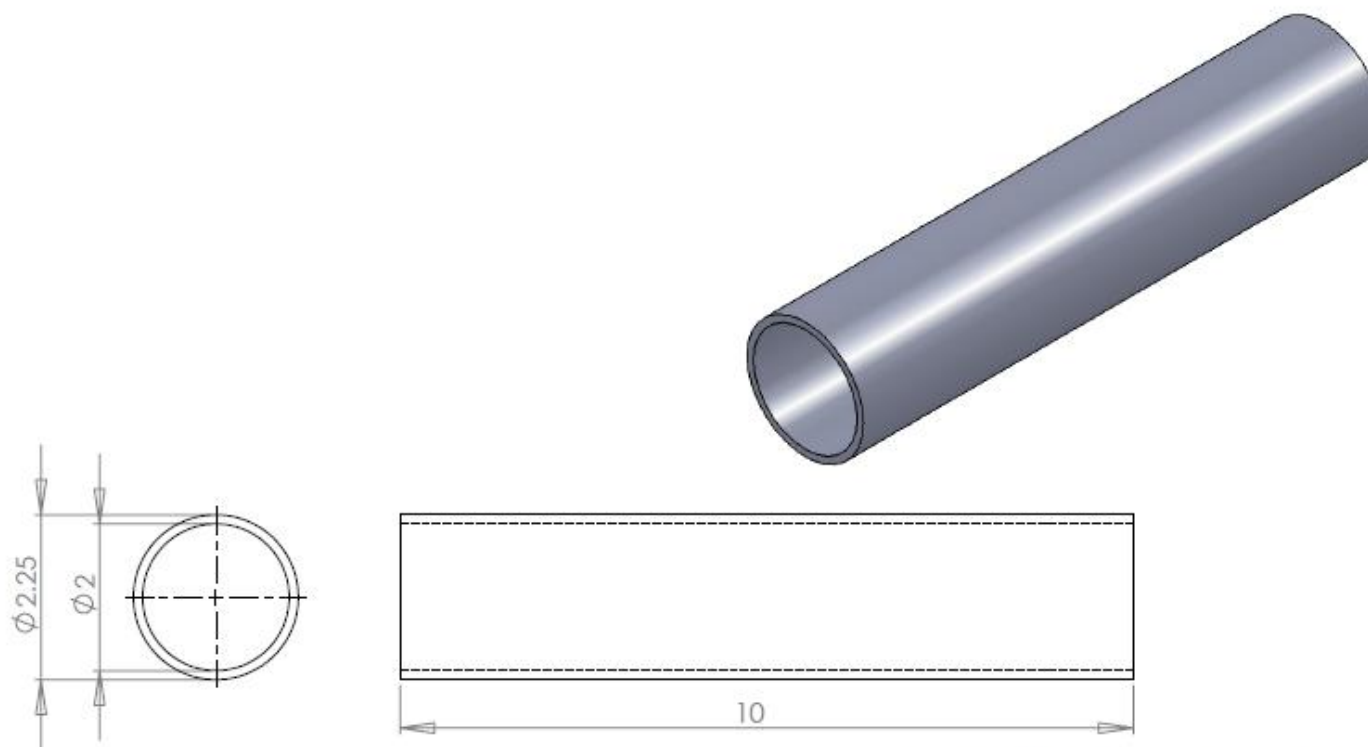
SHEET 5 OF 7



Item: BF0-2_LD3 (Break Flange
Pipe, 0 deg, L/D = 3)
No. of Pieces: 1
Material: Carbon Steel
Unit: Inches
Prepared by: Jenna Baird/
Seungjin Kim
Contact: (814)865-8429

SCALE: 1:2

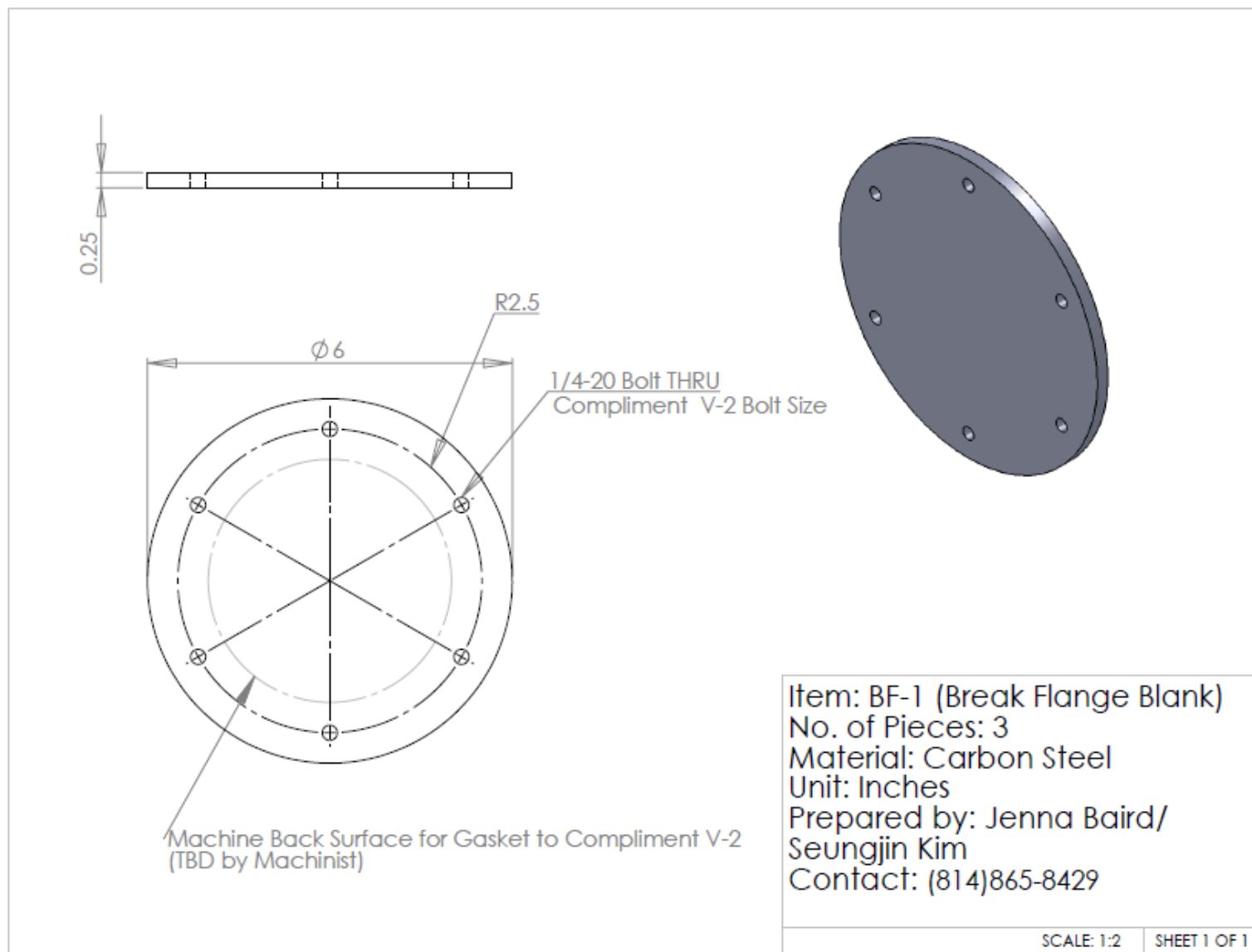
SHEET 6 OF 7

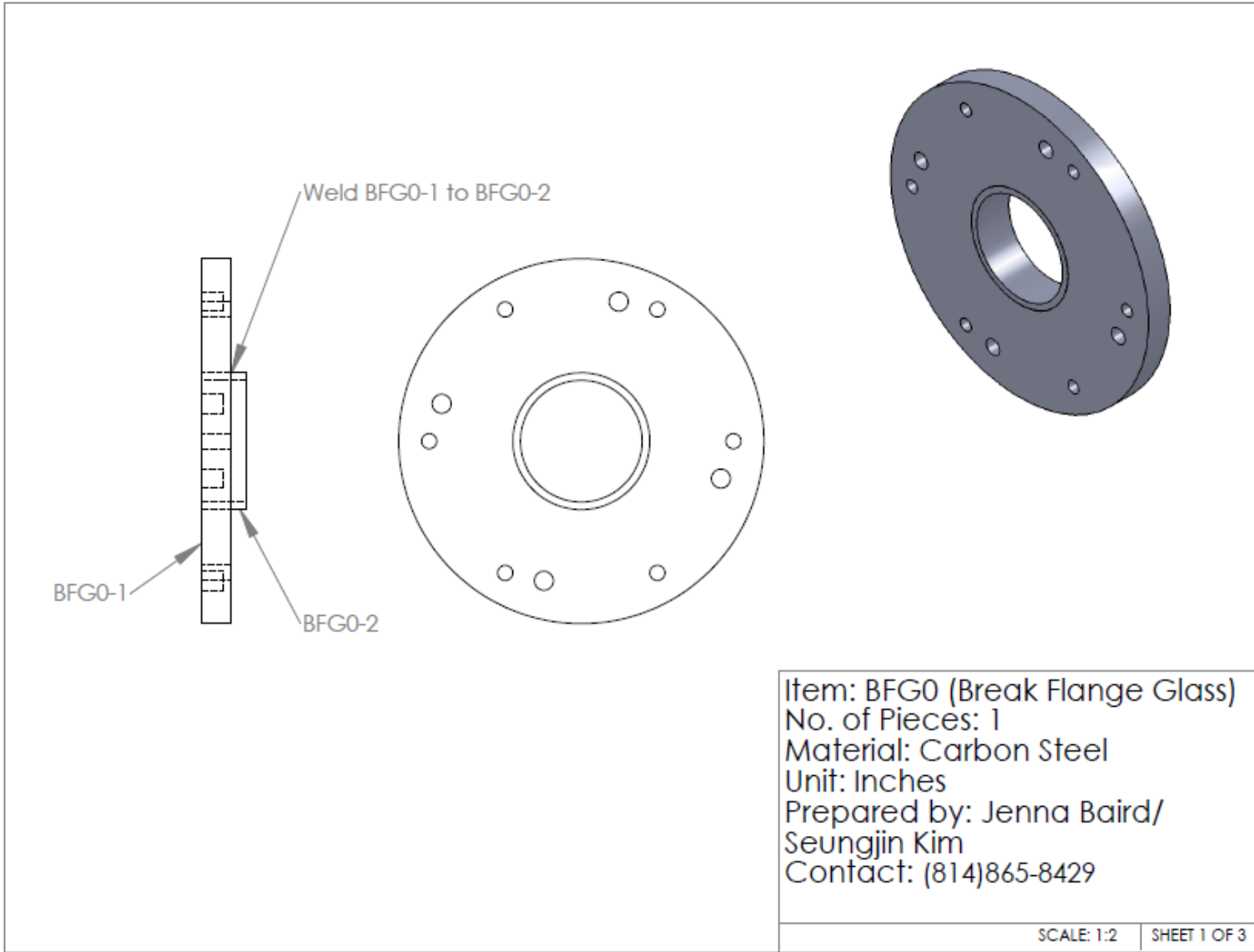


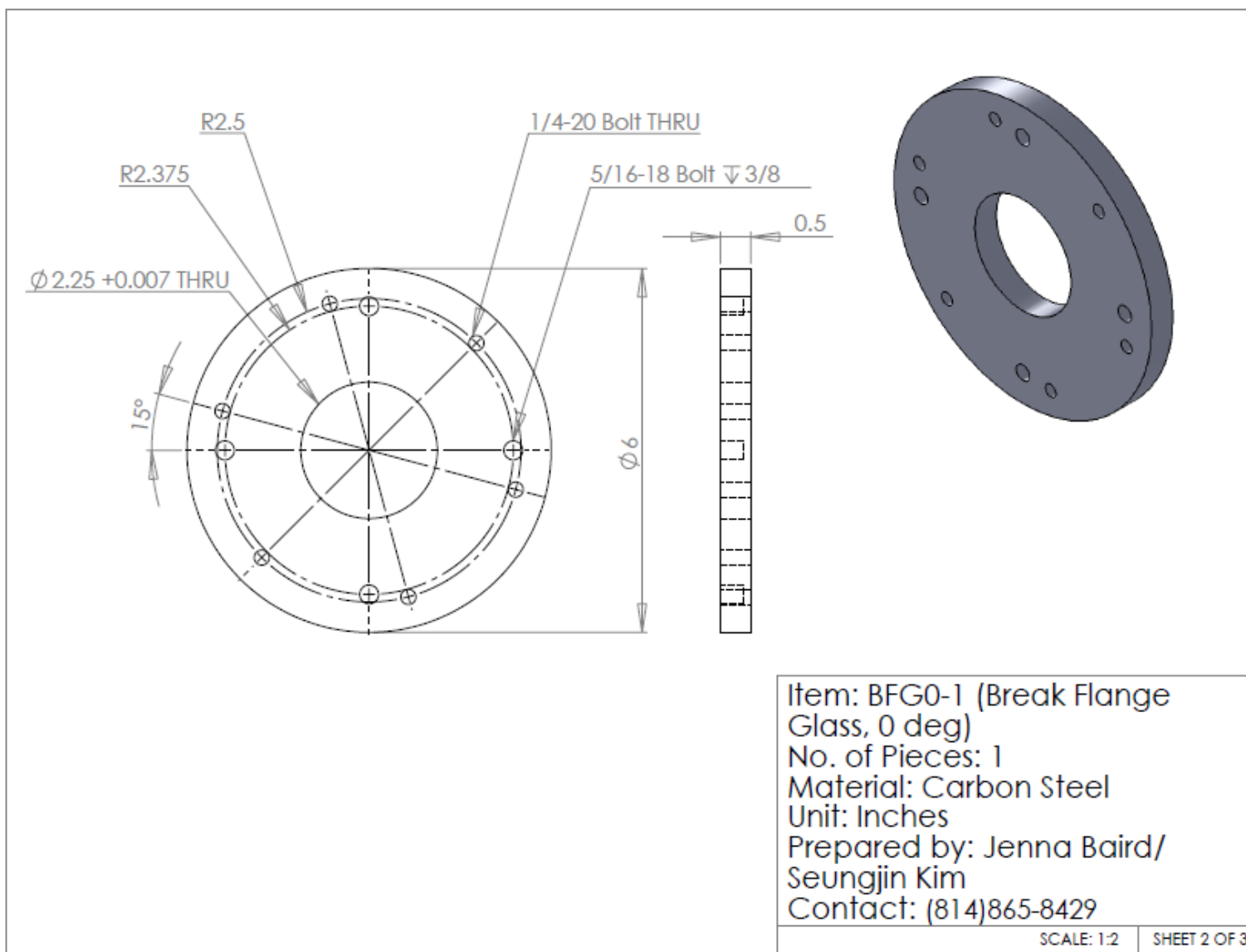
Item: BF0-2_LD5 (Break Flange
Pipe, 0 deg, L/D = 5)
No. of Pieces: 1
Material: Carbon Steel
Unit: Inches
Prepared by: Jenna Baird/
Seungjin Kim
Contact: (814)865-8429

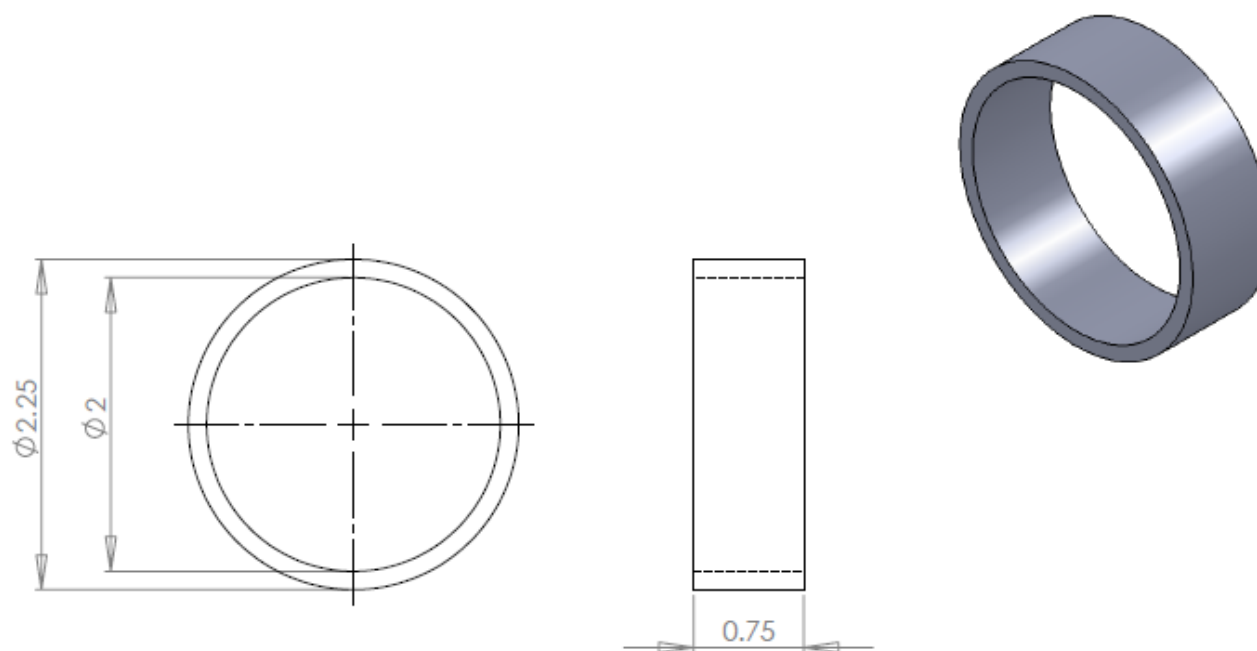
SCALE: 1:2

SHEET 7 OF 7









Item: BFG0-2 (Break Flange
Glass Pipe, 0 deg)
No. of Pieces: 1
Material: Carbon Steel
Unit: Inches
Prepared by: Jenna Baird/
Seungjin Kim
Contact: (814)865-8429

SCALE: 1:1

SHEET 3 OF 3

Appendix C**Nansulate EPX Product Data Sheet**



801 Laurel Oak Dr., Ste. 702, Naples, FL 34108
 PH (US & CAN): 800-767-3998
 PH (Internl): 1-951-324-7121
www.industrial-nanotech.com
www.nansulate.com
www.epx4.com
contact@nansulate.com

PRODUCT DATA SHEET - NANSULATE EPX - EPX4.COM

Water-Based Epoxy System

Product Characteristics

Nansulate® EPX 2-part aqueous epoxy system is a premium industrial grade protective system that provides thermal insulation, corrosion protection, chemical resistance, and fire resistance.

Nansulate® EPX contains Hydro-NM-Oxide, a material which is recorded as one of the best insulating materials available.

Nansulate® EPX has a thermal conductivity of 0.027 W/mK @ 20°C @ 1/8" (in laboratory testing). It is resistant to acids, bases and fuels, making it suitable for a variety of severe service environments. The system is also useful for low temperature applications.

This 2-part water-based epoxy system is a very low VOC product (60 grams/L) and contains no Polybrominated Diphenyl Ether (PBDE). The combination of thermal insulation and corrosion resistance make it a perfect replacement product for FBE + PU (Fusion bonded Epoxy + Polyurethane Foam), two parts of a standard pipe protection system. Nansulate® EPX can take the place of both, thus reducing material and labor costs.

Product Description

Two-part, water-based epoxy system incorporating Hydro-NM-Oxide, a product of nanotechnology. Performance temperature range: 0°F to 450°F (-18°C to 232°C).

Product Information

Color:	Blue (custom colors available upon request)
Container Sizes:	2 gallon kit, 5 gallon kit (Note: product is sold by weight, not volume)
Weight as packaged:	2-gallon kit: Part A=not less than 11.5 lbs; Part B=not less than 2.9 lbs 5-gallon kit: Part A=not less than 29.0 lbs; Part B=not less than 7.3 lbs
Weight Solids, %:	68%
Touch Dry:	3 hours
Hard Dry (return to service):	24 to 36 hours
Typical thickness range:	1/8" to 1" per coat
Theoretical coverage:	@ 1/8" - 48 s.f. per 2-gallon kit
Thermal Conductivity:	0.027 W/mK @ 20°C @ 1/8"
Chemical Resistance:	Resistant to Acids, Bases, Fuels
Tensile Strength: (ASTM D2370)	3500 psi, 24000 kpa
Abrasion Resistance:	Hard

(Industrial Nanotech, Print)

Appendix D**Air Ingress Data Collection Sheet**

Air Ingress Test #: _____

Shakedown ____ Oxygen Analyzer Measurement ____ Thermocouple Measurement ____

Pipe Break Location: _____ L/D: _____ Angle: _____

Test Conducted by: _____

Date: _____

Start Time: _____ Room Temperature: _____ Room O₂: _____

Internal Vessel Temperature: _____ Pressure: _____

Finish Time: _____ Room Temperature: _____ Room O₂: _____

Notes:

Data Recorded by: _____

Appendix E

Data Repeatability Plots with Error Bars

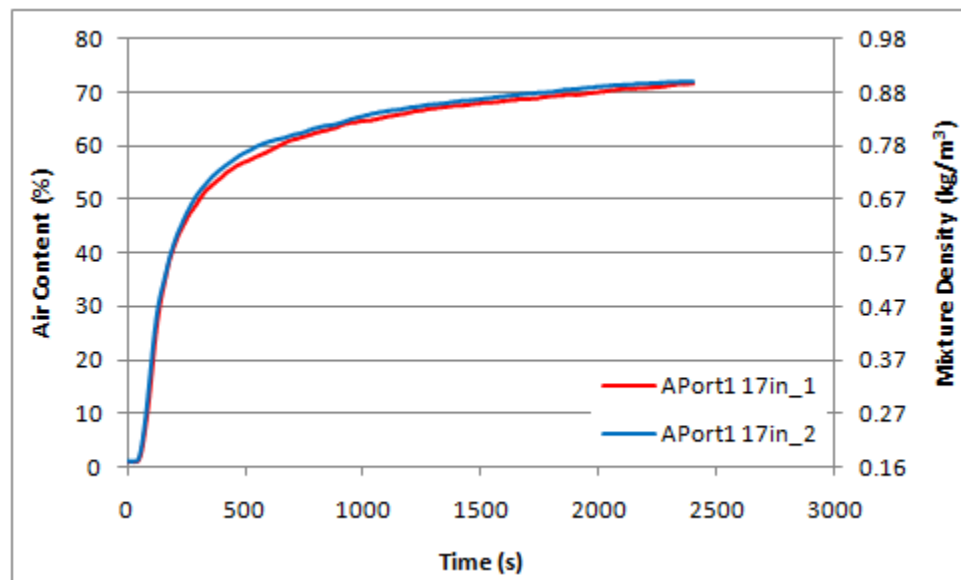


Figure E-1: Comparison of Data at APort1 17 in to Verify Repeatability

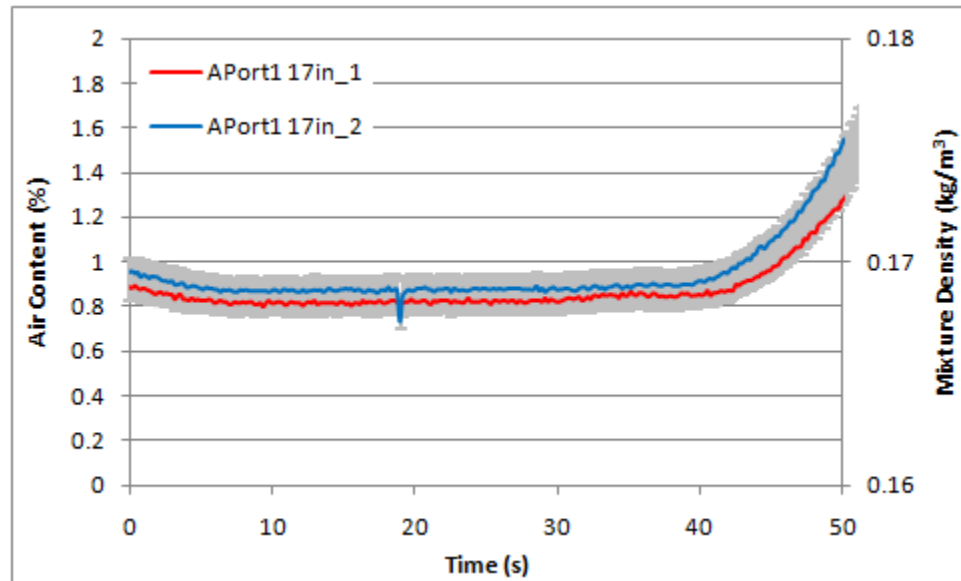


Figure E-2: Initial 50 s of APort1 17in Data (Error Bars: $\pm 10\%$)

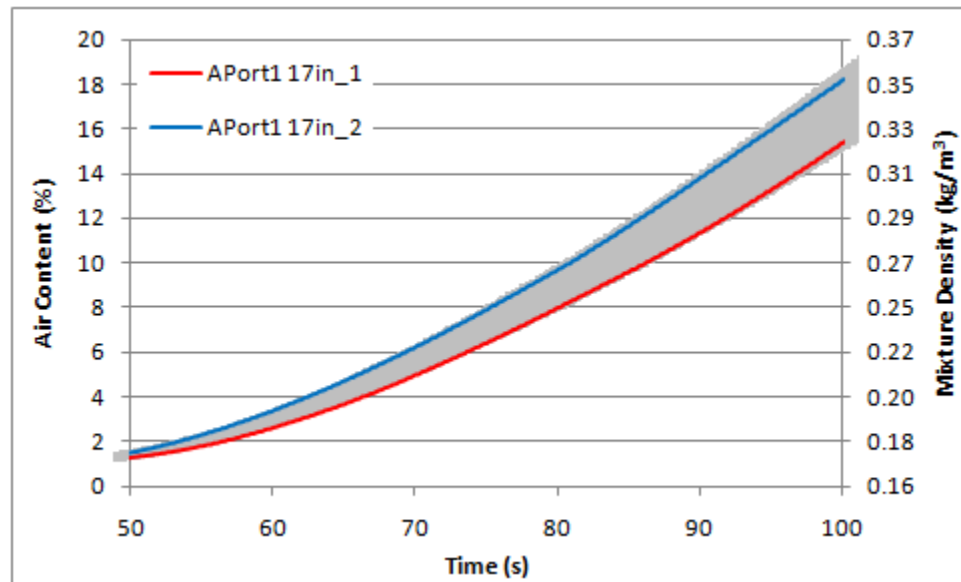


Figure E-3: Region 50 s to 100 s of APort1 17in Data (Error Bars: $\pm 10\%$)

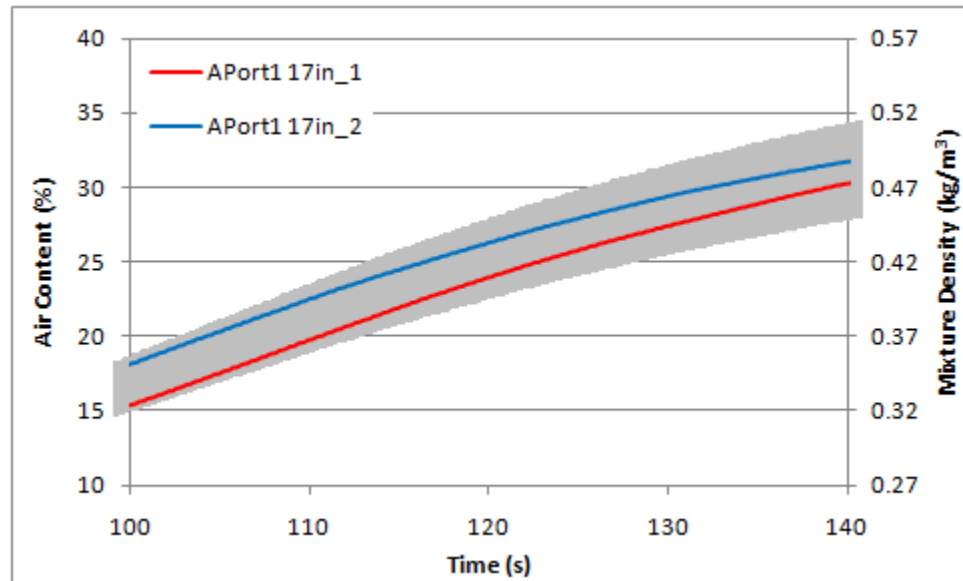


Figure E-4: Region 100 s to 140 s of APort1 17in Data (Error Bars: $\pm 10\%$)

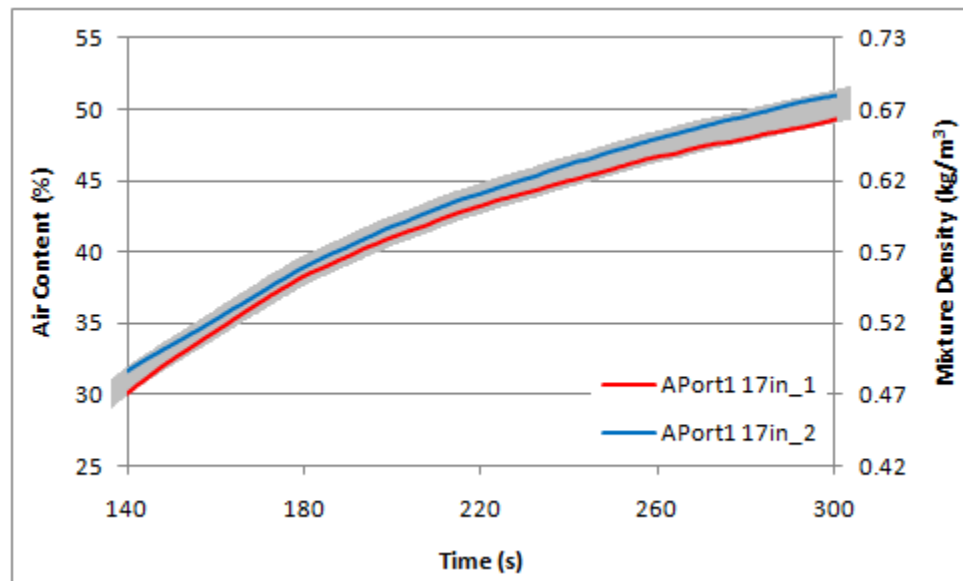


Figure E-5: Region 140 s to 300 s of APort1 17in Data (Error Bars: $\pm 2\%$)

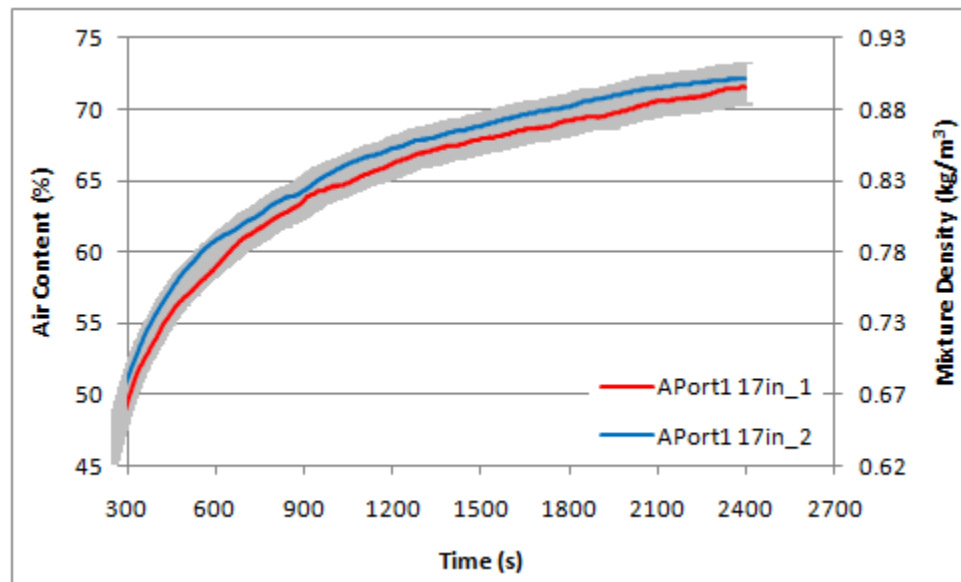


Figure E-6: Region 300 s to 2700 s of APort1 17in Data (Error Bars: $\pm 2\%$)

Appendix F

Lower Side Break Data

Local Data

Air Content vs. r/R

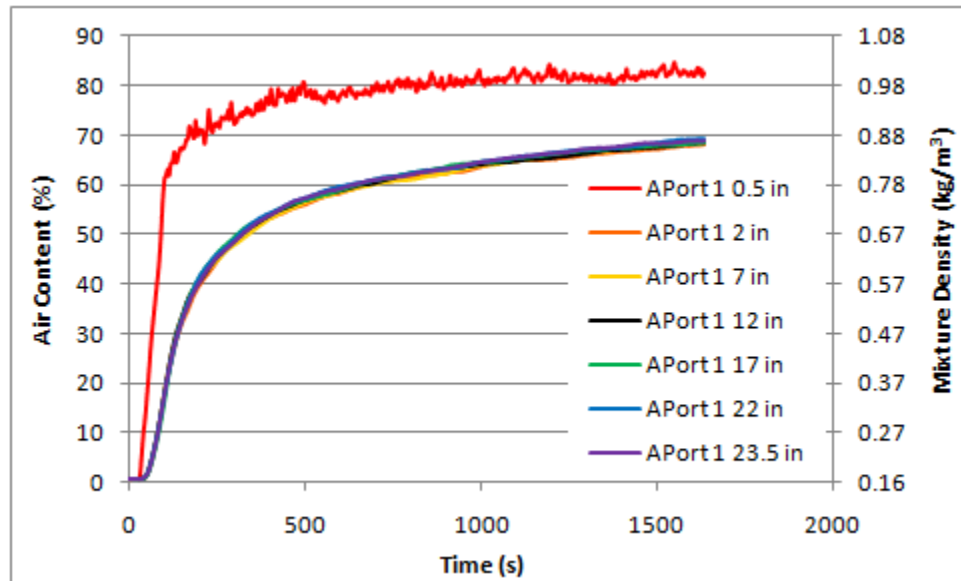


Figure F-1: Local Data for APort1 along Radial Direction

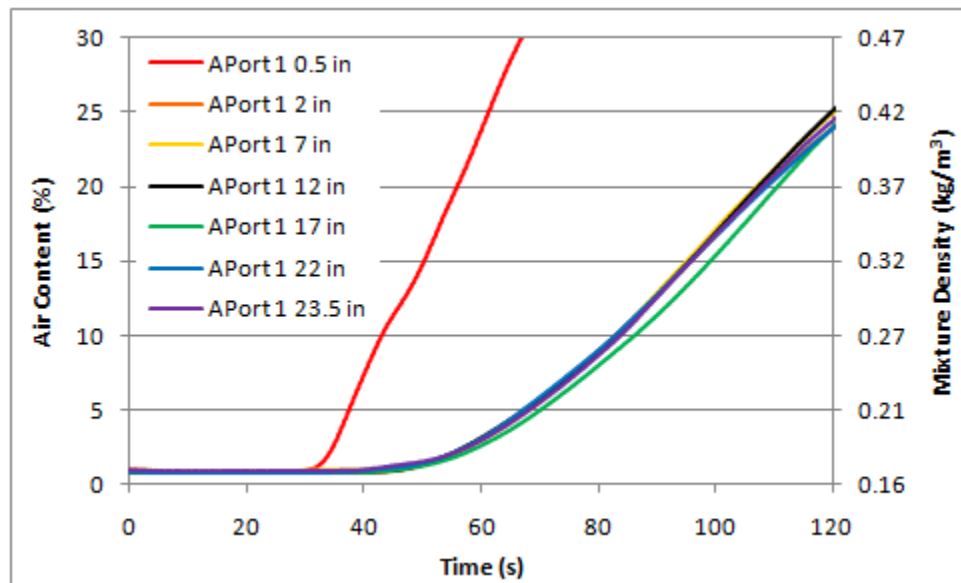


Figure F-2: Initial 120 s of Local Data for APort1 along Radial Direction

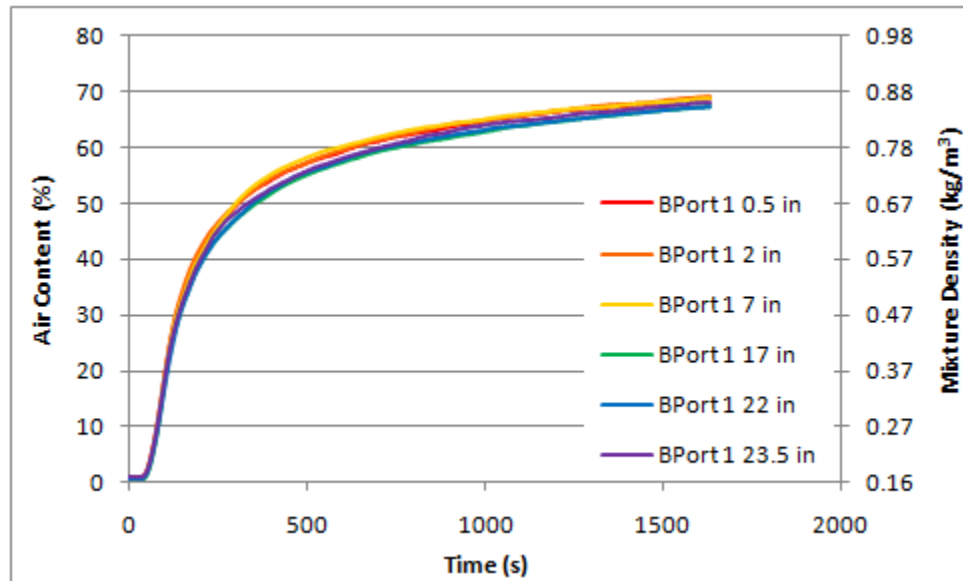


Figure F-3: Local Data for BPort1 along Radial Direction

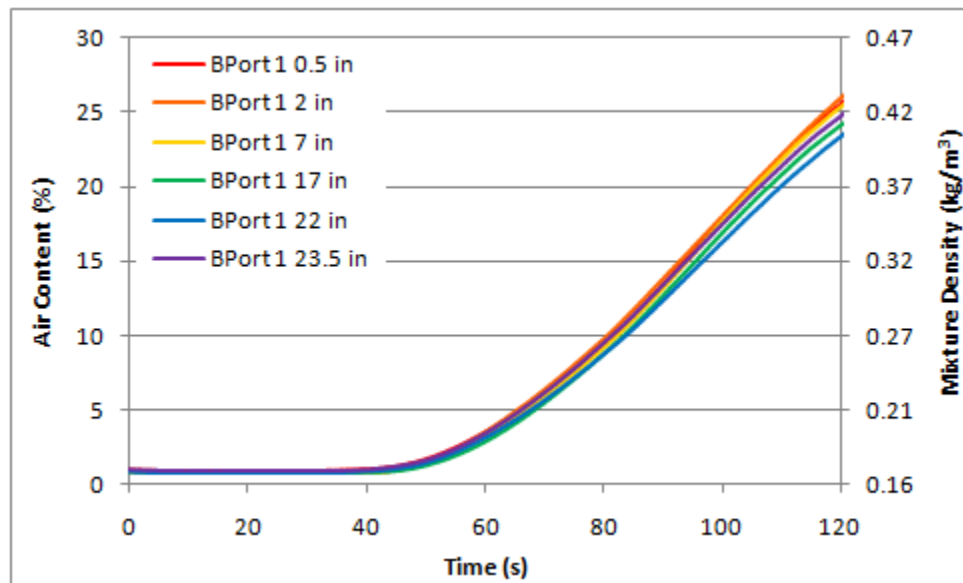


Figure F-4: Initial 120 s of Local Data for BPort1 along Radial Direction

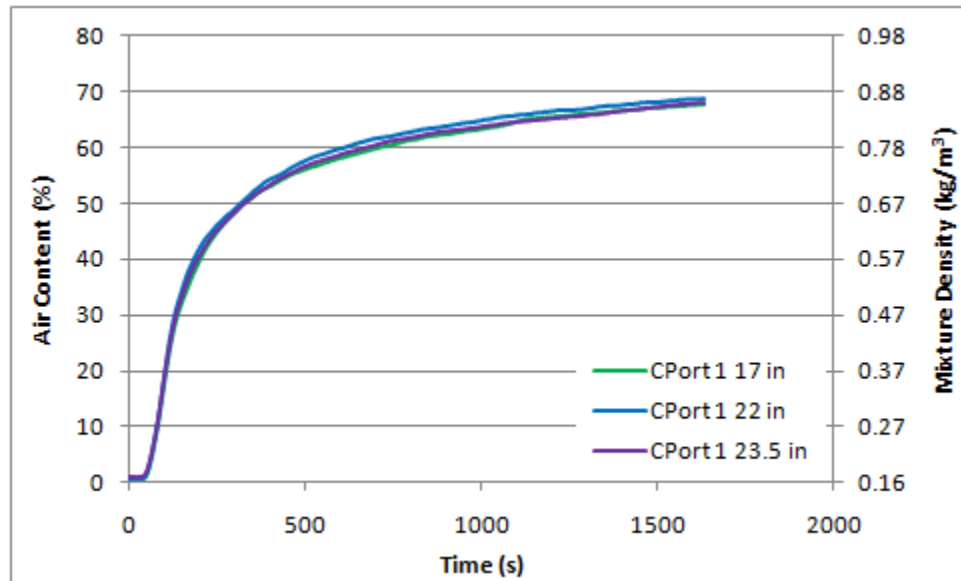


Figure F-5: Local Data for CPort1 along Radial Direction

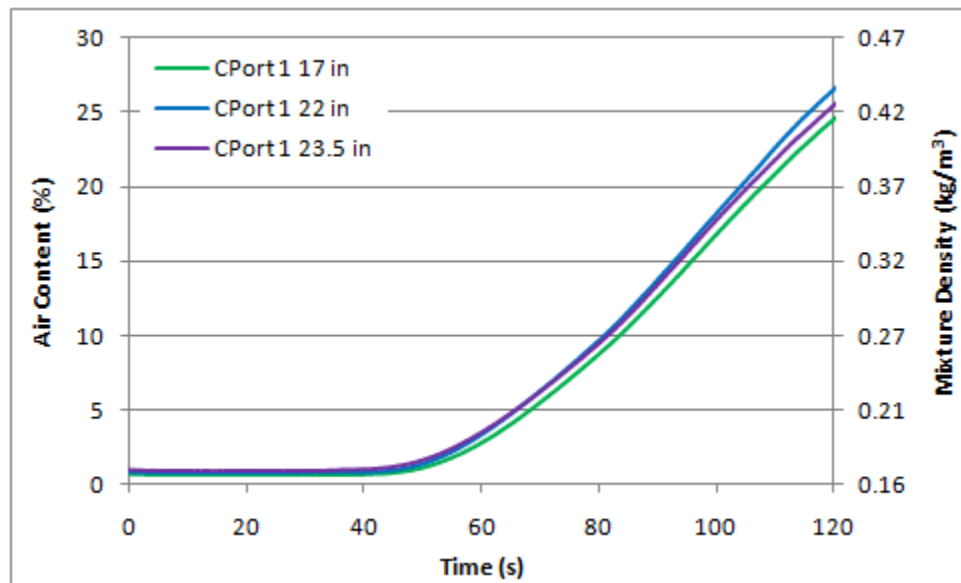


Figure F-6: Initial 120 s of Local Data for CPort1 along Radial Direction

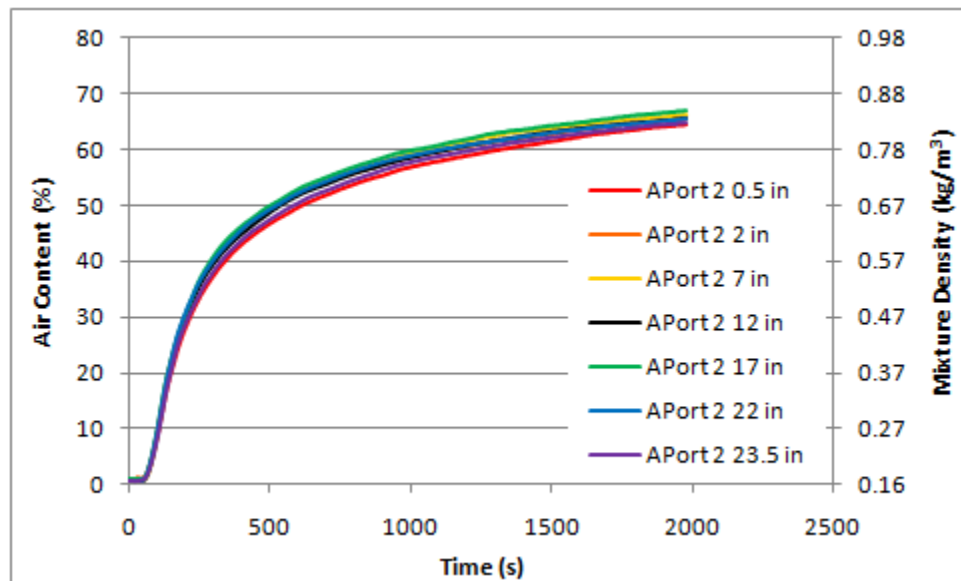


Figure F-7: Local Data for APort2 along Radial Direction

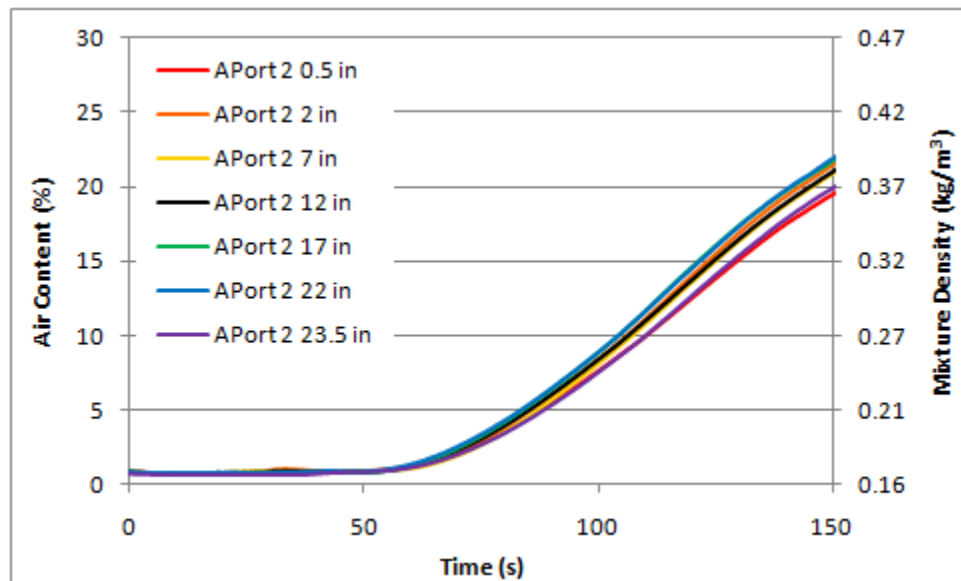


Figure F-8: Initial 150 s of Local Data for APort2 along Radial Direction

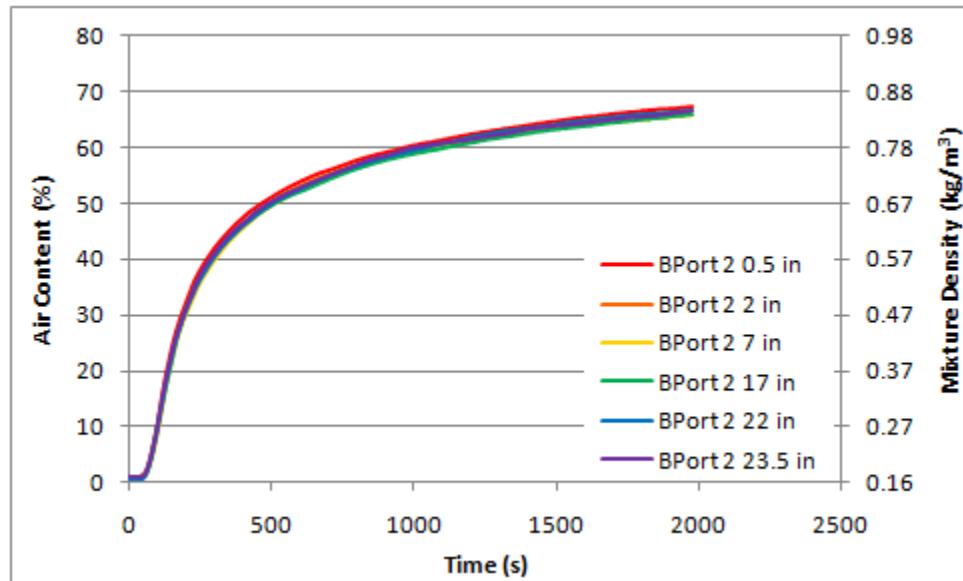


Figure F-9: Local Data for BPort2 along Radial Direction

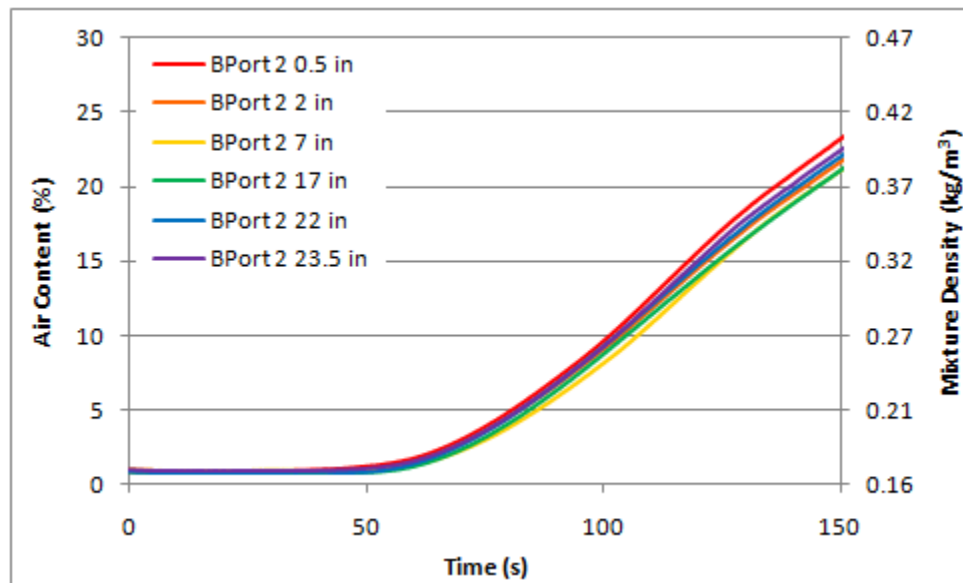


Figure F-10: Initial 150 s of Local Data for BPort2 along Radial Direction

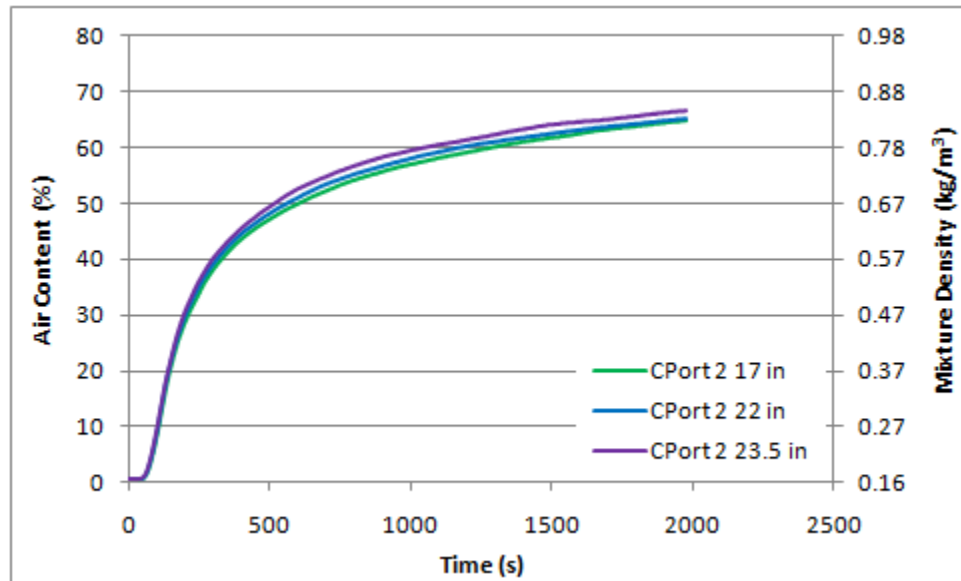


Figure F-11: Local Data for CPort2 along Radial Direction

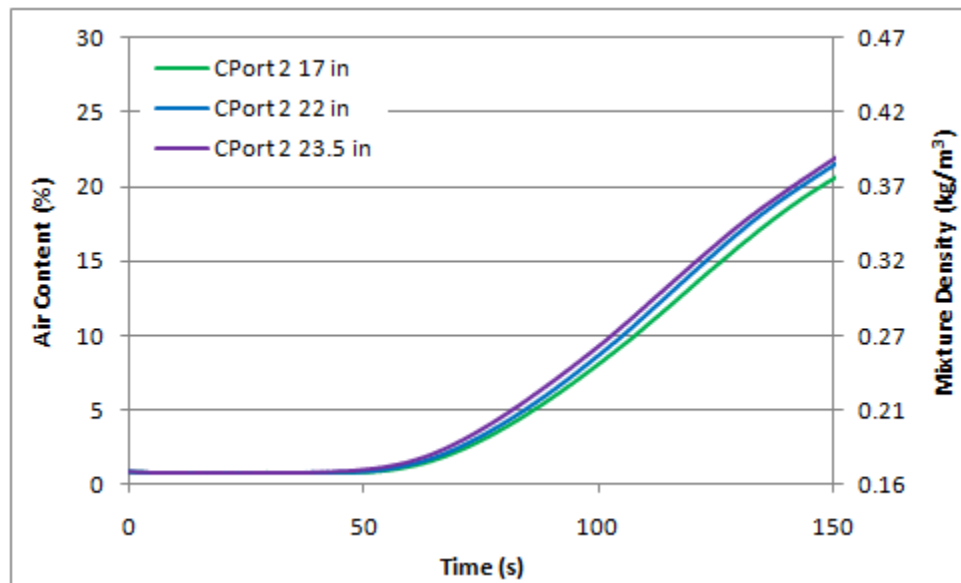


Figure F-12: Initial 150 s of Local Data for CPort2 along Radial Direction

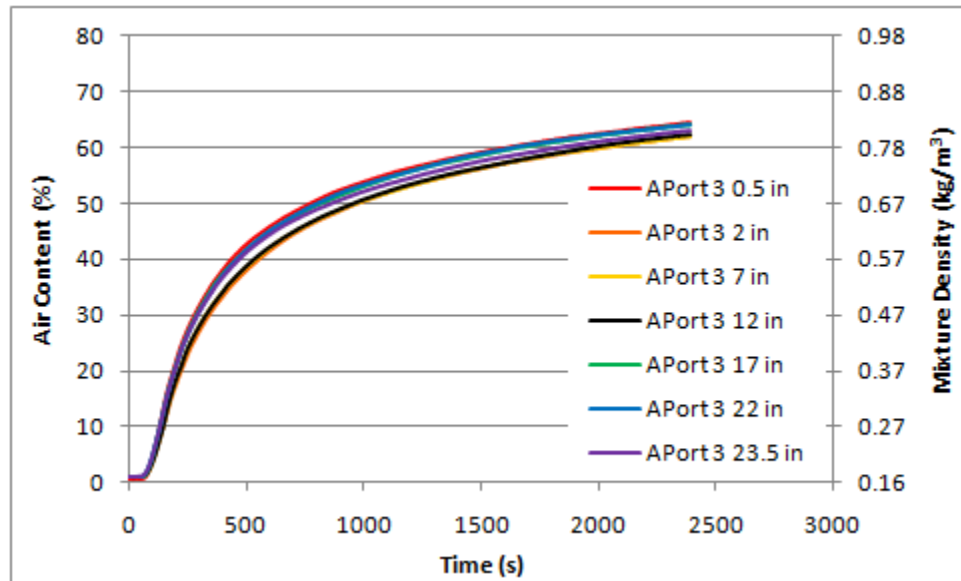


Figure F-13: Local Data for APort3 along Radial Direction

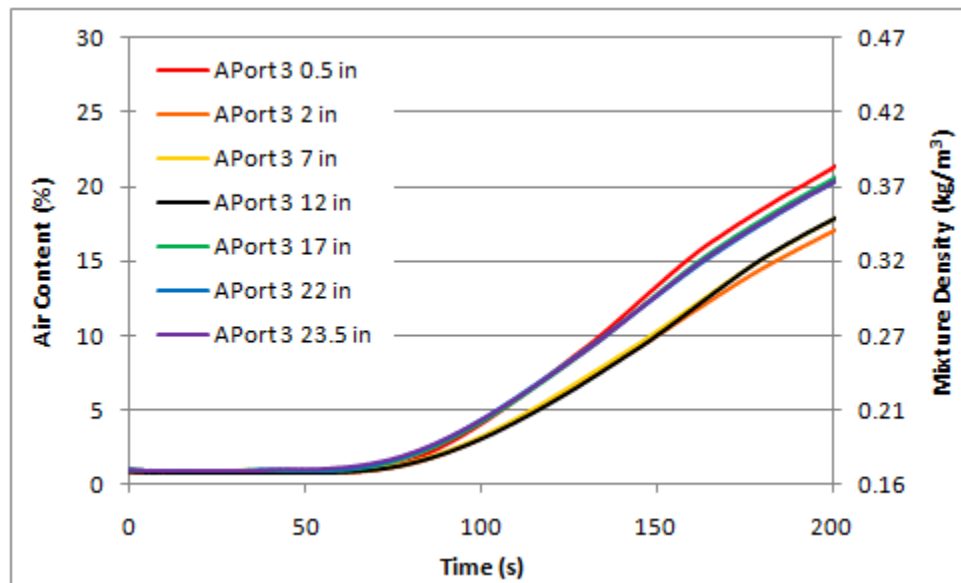


Figure F-14: Initial 200 s of Local Data for APort3 along Radial Direction

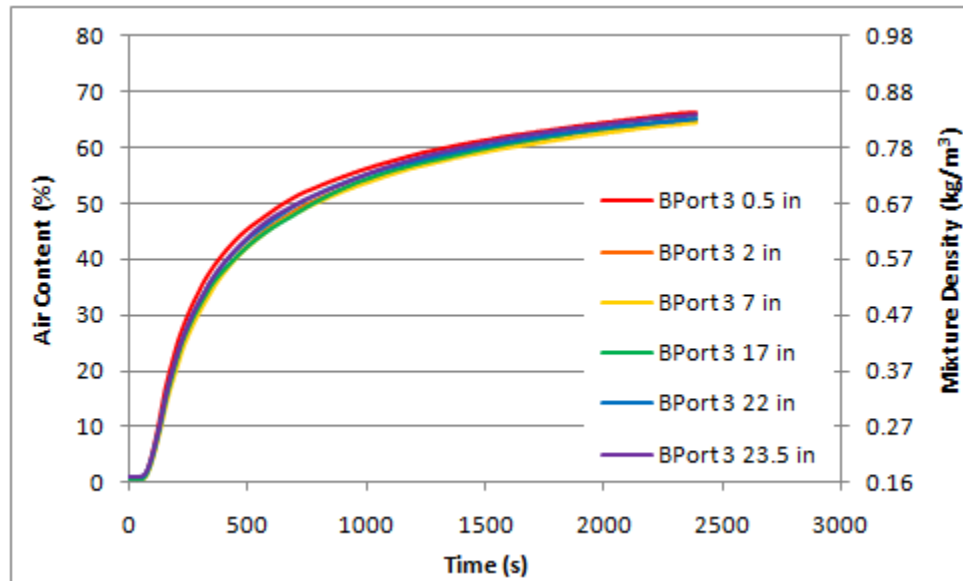


Figure F-15: Local Data for BPort3 along Radial Direction

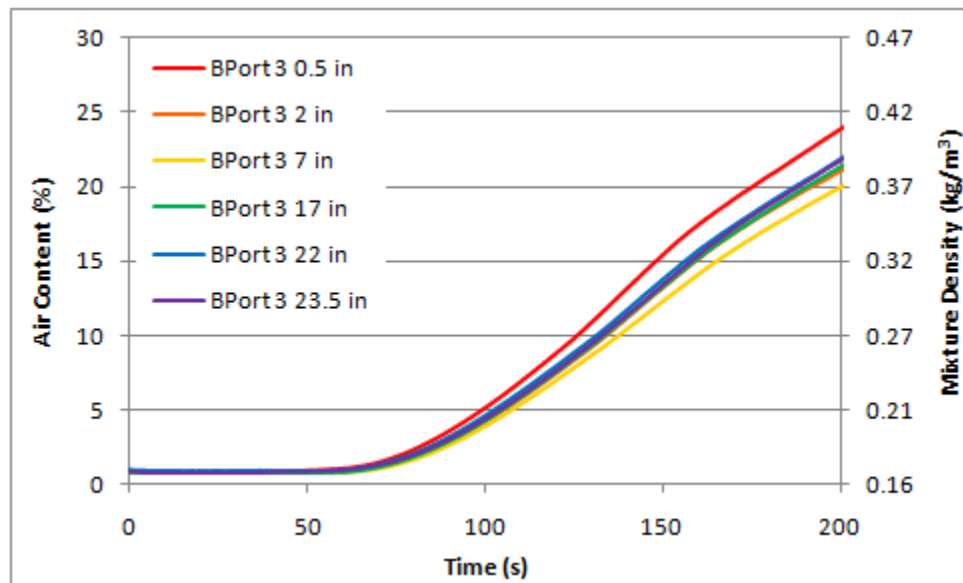


Figure F-16: Initial 200 s of Local Data for BPort3 along Radial Direction

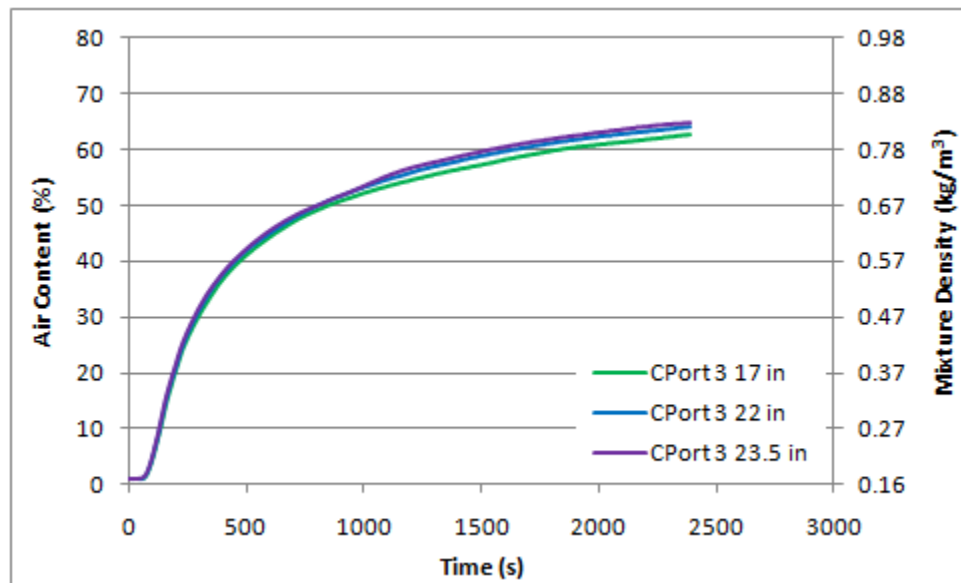


Figure F-17: Local Data for CPort3 along Radial Direction

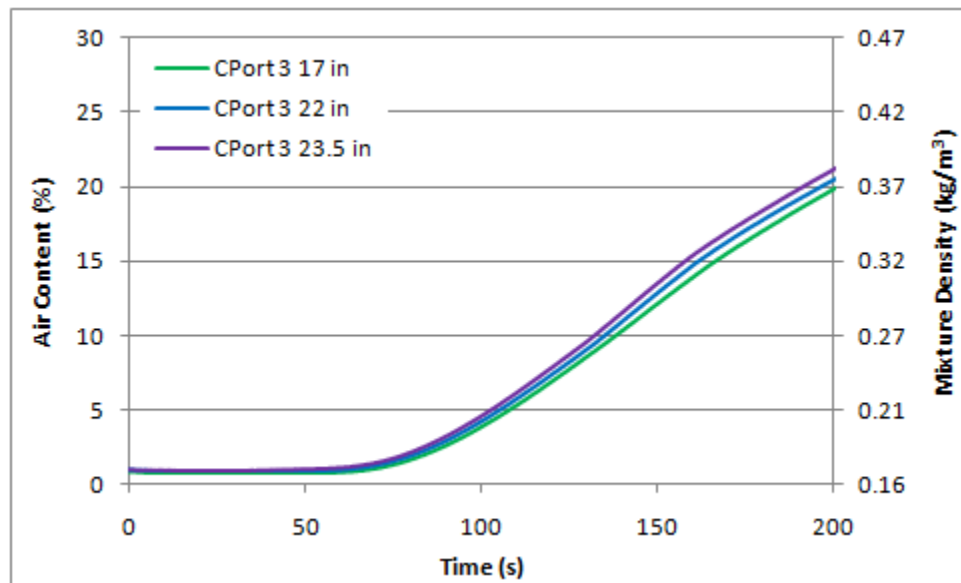


Figure F-18: Initial 200 s of Local Data for CPort3 along Radial Direction

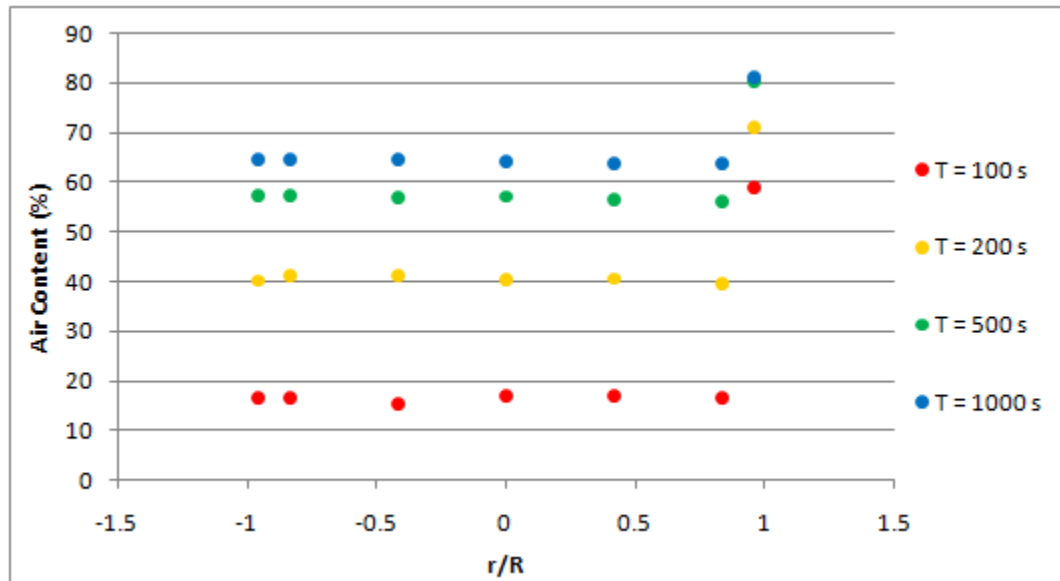


Figure F-19: Variation of Air Content along Vessel Diameter for APort1

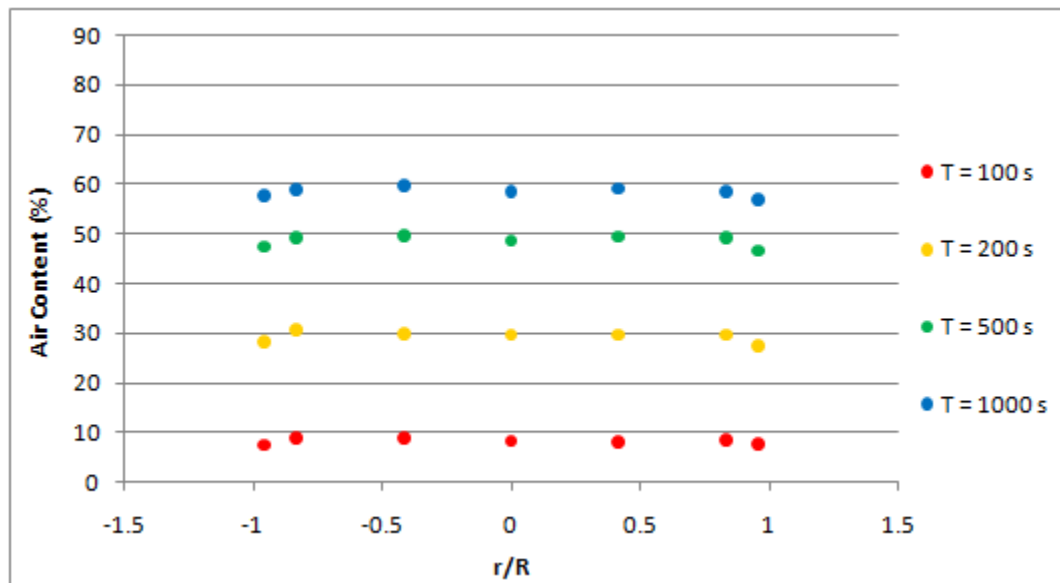


Figure F-20: Variation of Air Content along Vessel Diameter for APort2

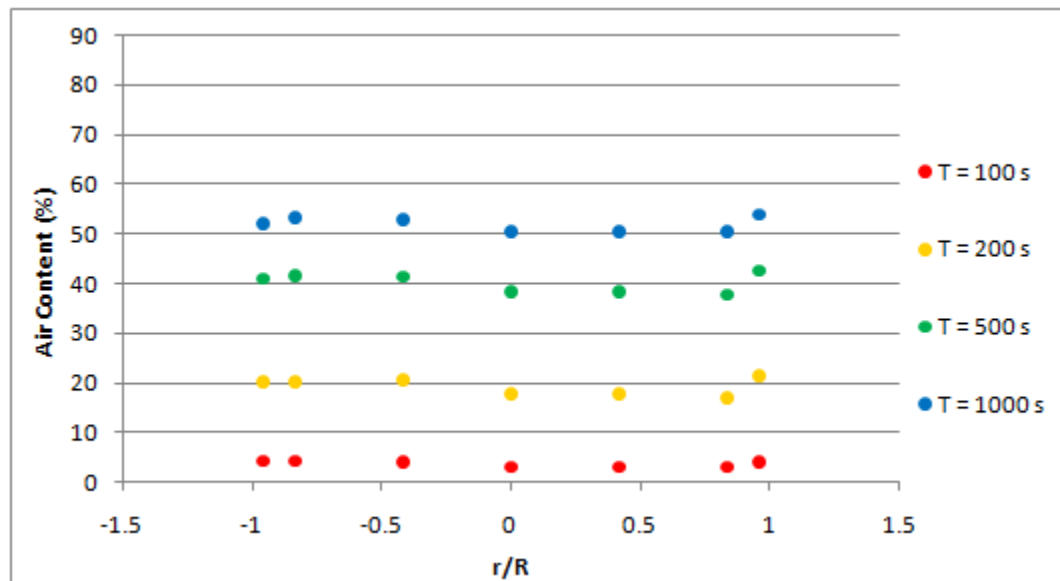


Figure F-21: Variation of Air Content along Vessel Diameter for APort3

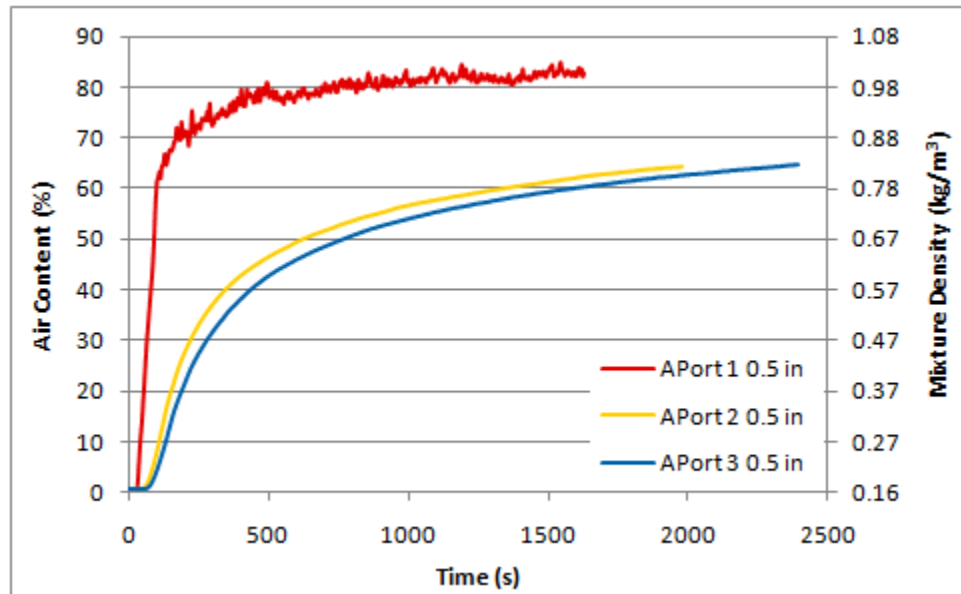


Figure F-22: Local Data for Radial Location 0.5 in along Axial Direction for APort

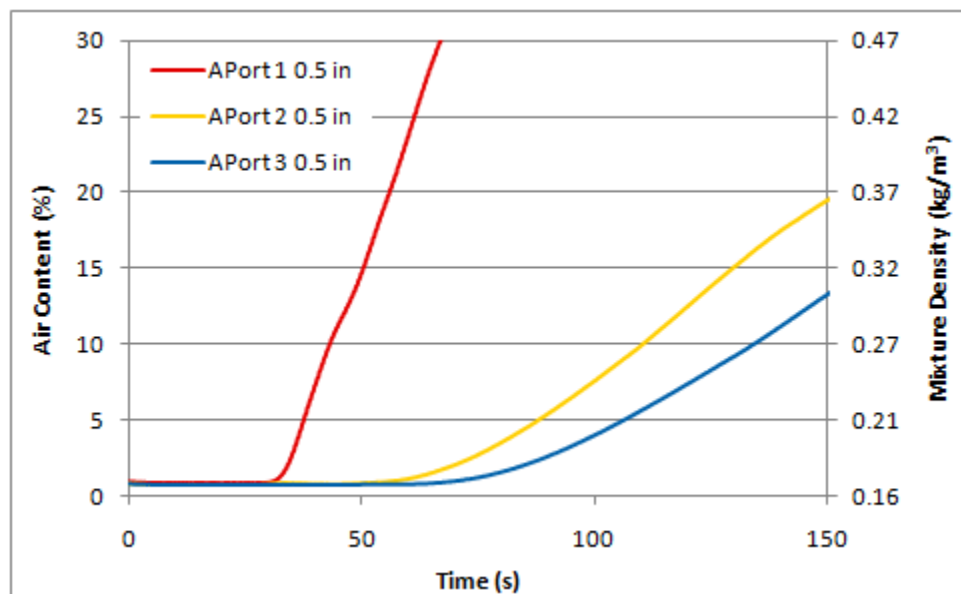


Figure F-23: Initial 150 s of Local Data for Radial Location 0.5 in along Axial Direction for

APort

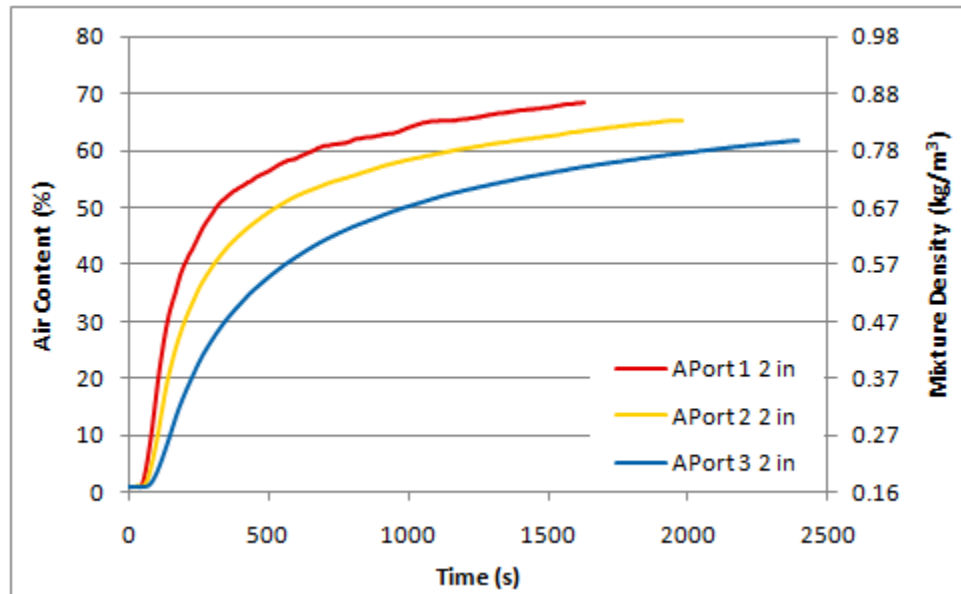


Figure F-24: Local Data for Radial Location 2 in along Axial Direction for APort

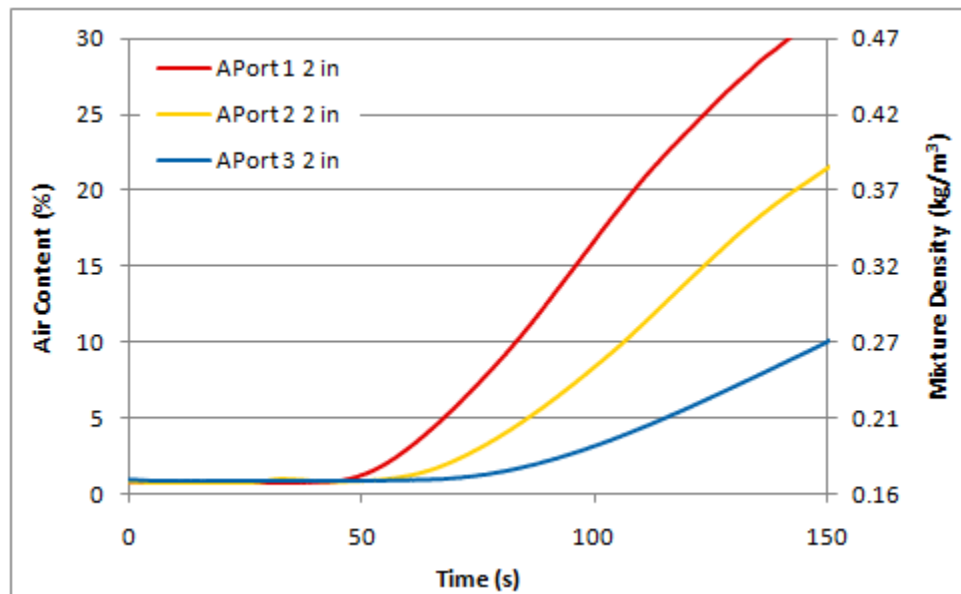


Figure F-25: Initial 150 s of Local Data for Radial Location 2 in along Axial Direction for APort

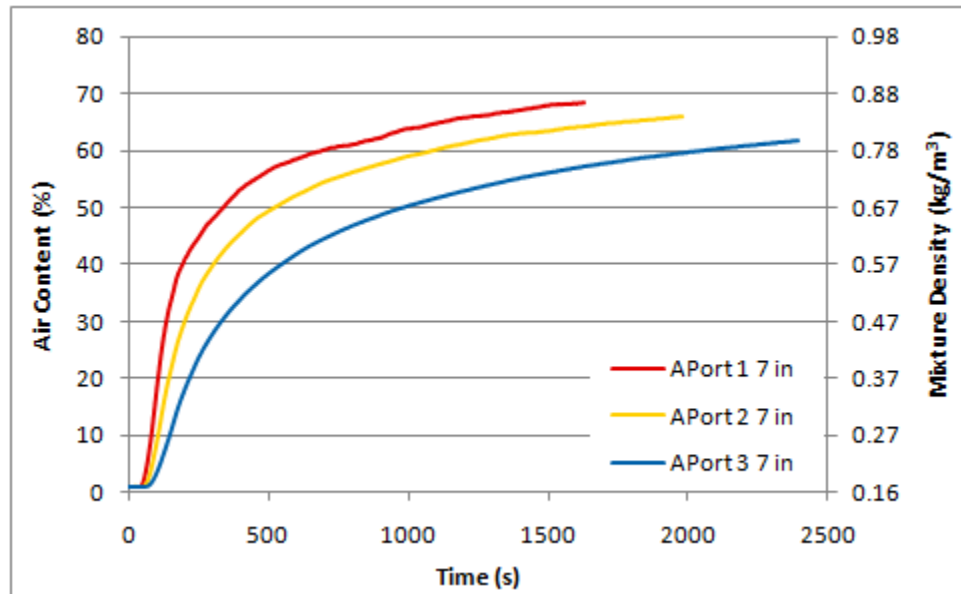


Figure F-26: Local Data for Radial Location 7 in along Axial Direction for APort

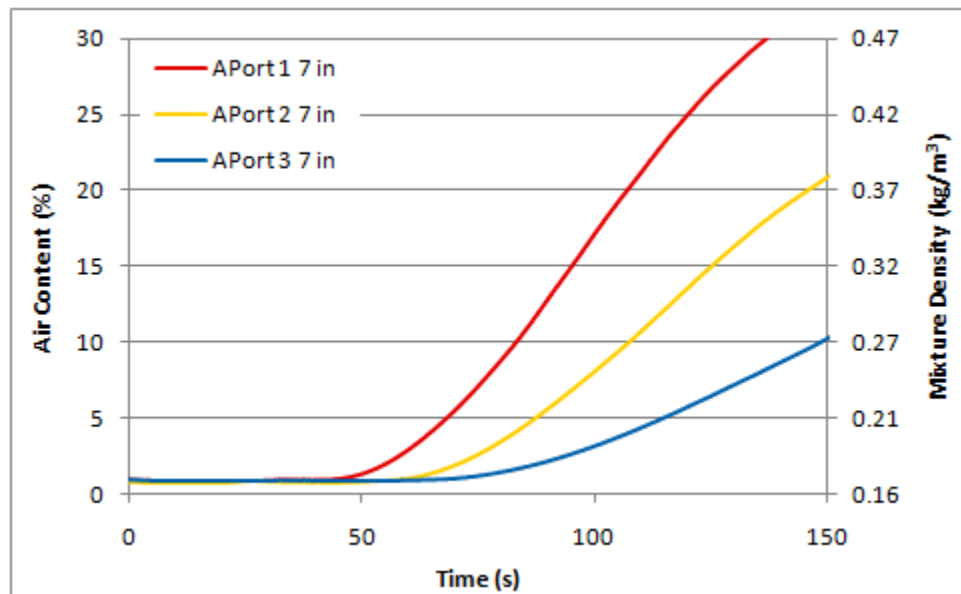


Figure F-27: Initial 150 s of Local Data for Radial Location 7 in along Axial Direction for APort

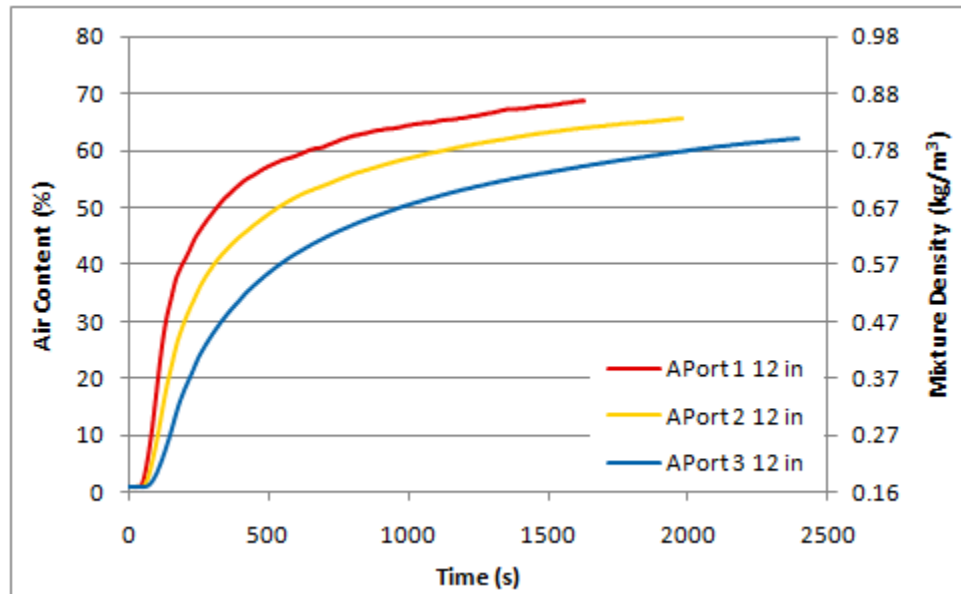


Figure F-28: Local Data for Radial Location 12 in along Axial Direction for APort

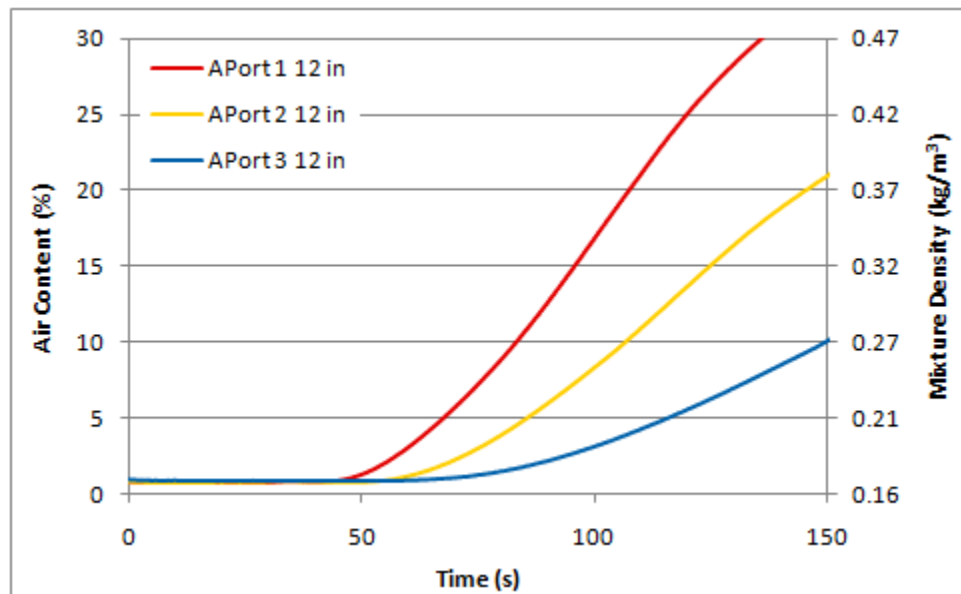


Figure F-29: Initial 150 s of Local Data for Radial Location 12 in along Axial Direction for APort

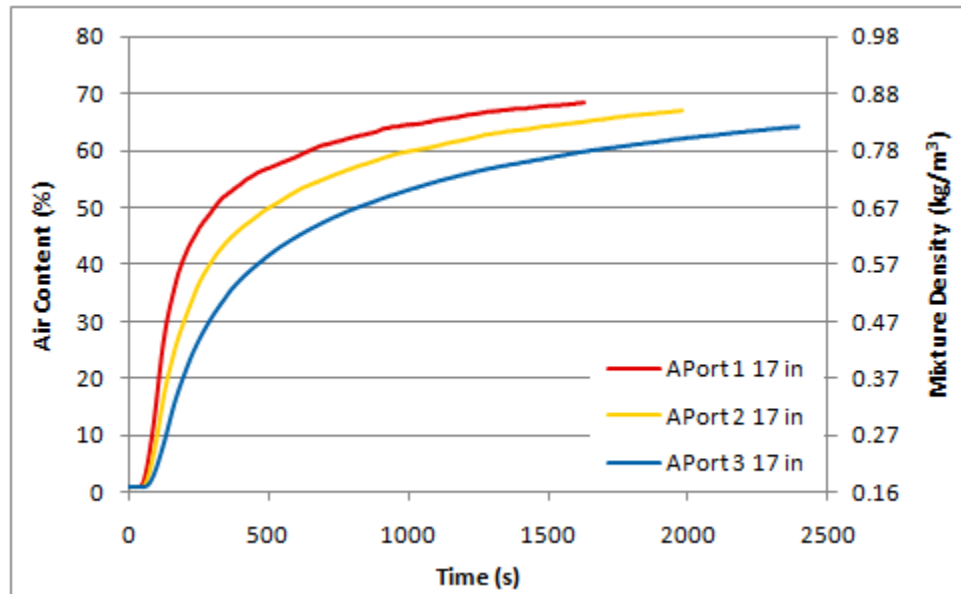


Figure F-30: Local Data for Radial Location 17 in along Axial Direction for APort

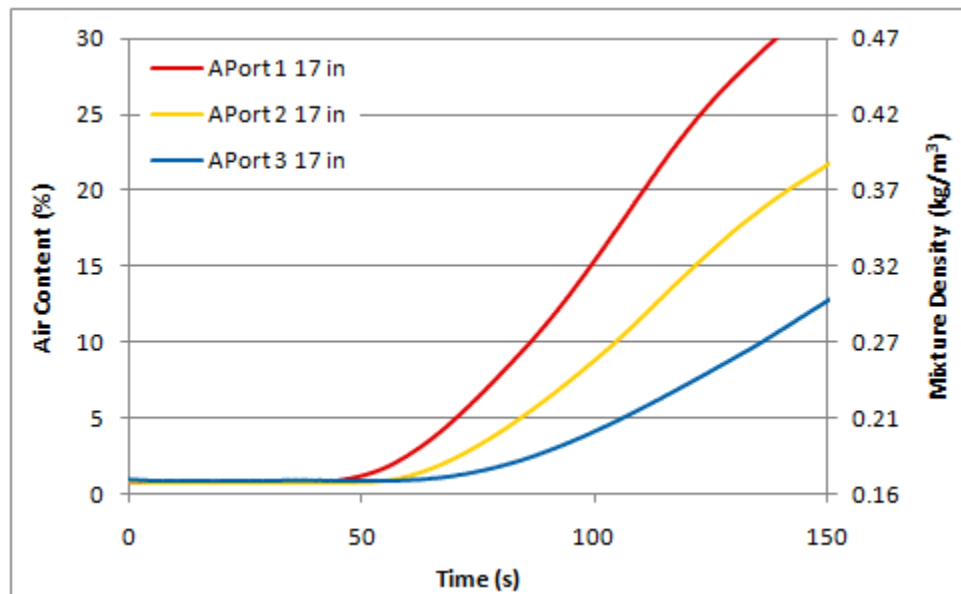


Figure F-31: Initial 150 s of Local Data for Radial Location 17 in along Axial Direction for APort

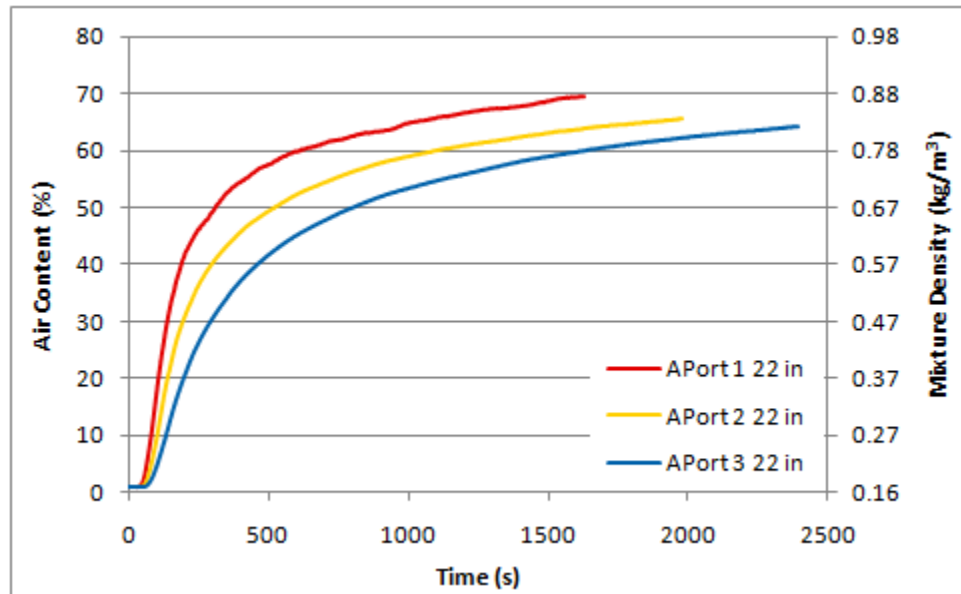


Figure F-32: Local Data for Radial Location 22 in along Axial Direction for APort

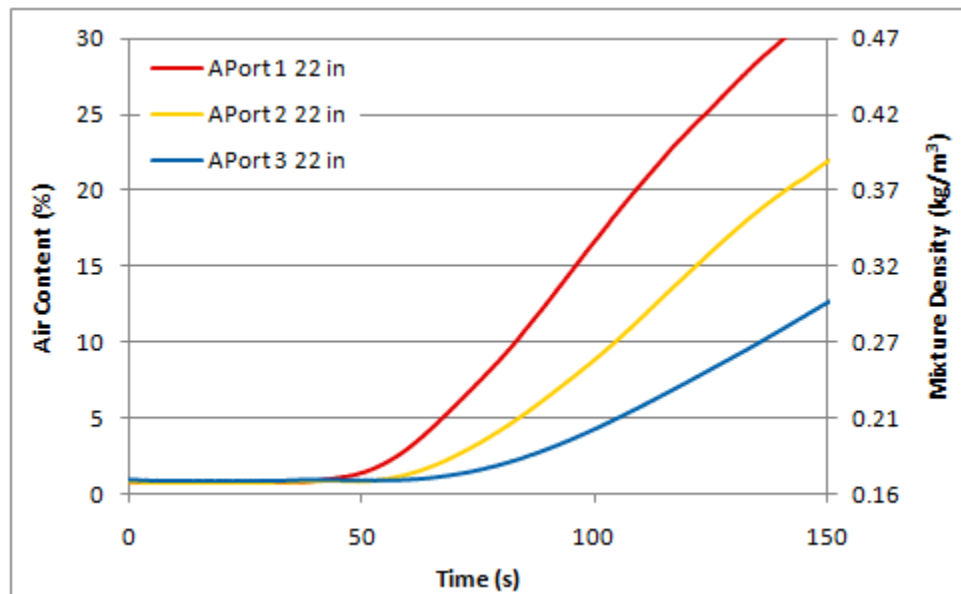


Figure F-33: Initial 150 s of Local Data for Radial Location 22 in along Axial Direction for APort

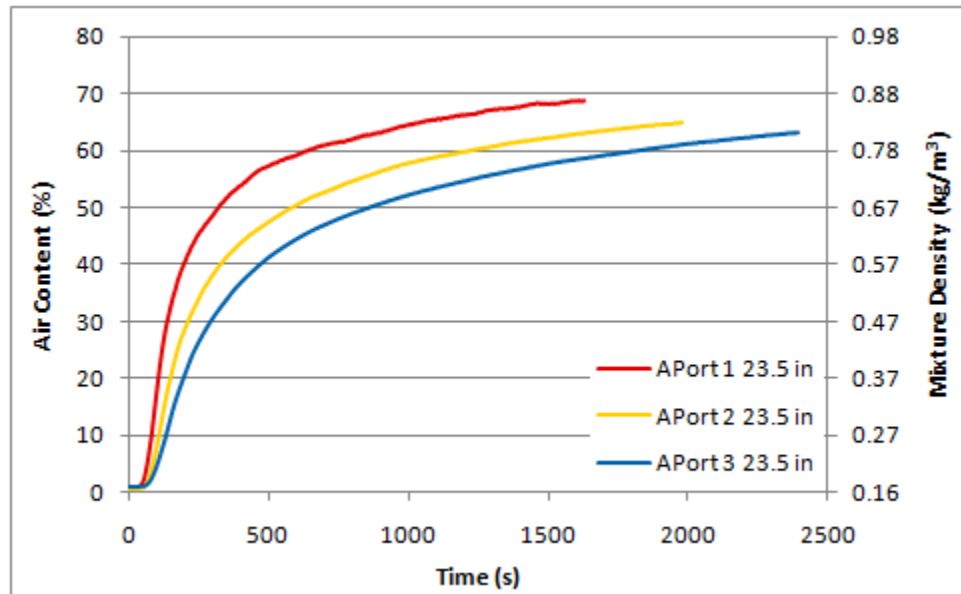


Figure F-34: Local Data for Radial Location 23.5 in along Axial Direction for APort

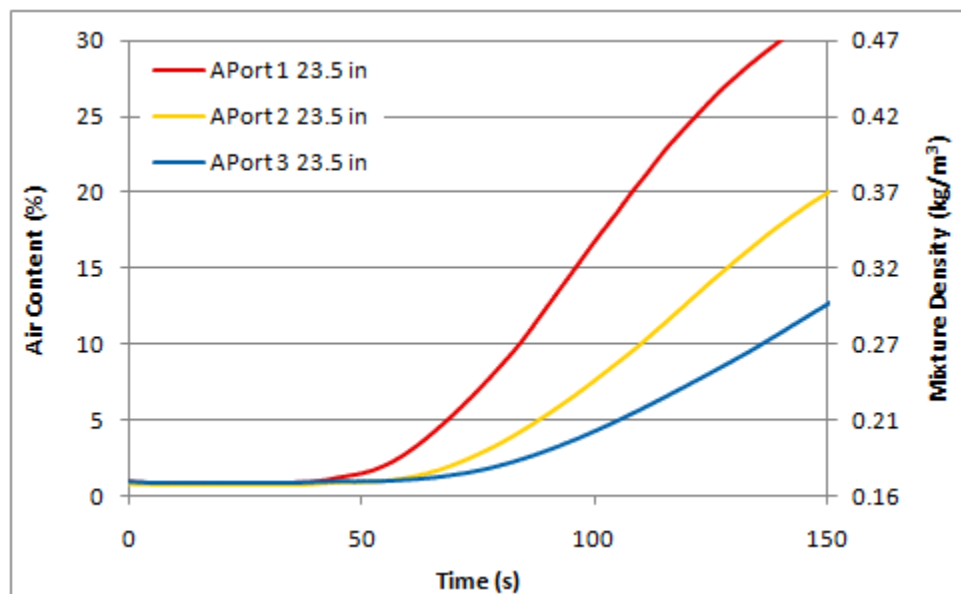


Figure F-35: Initial 150 s of Local Data for Radial Location 23.5 in along Axial Direction for

APort

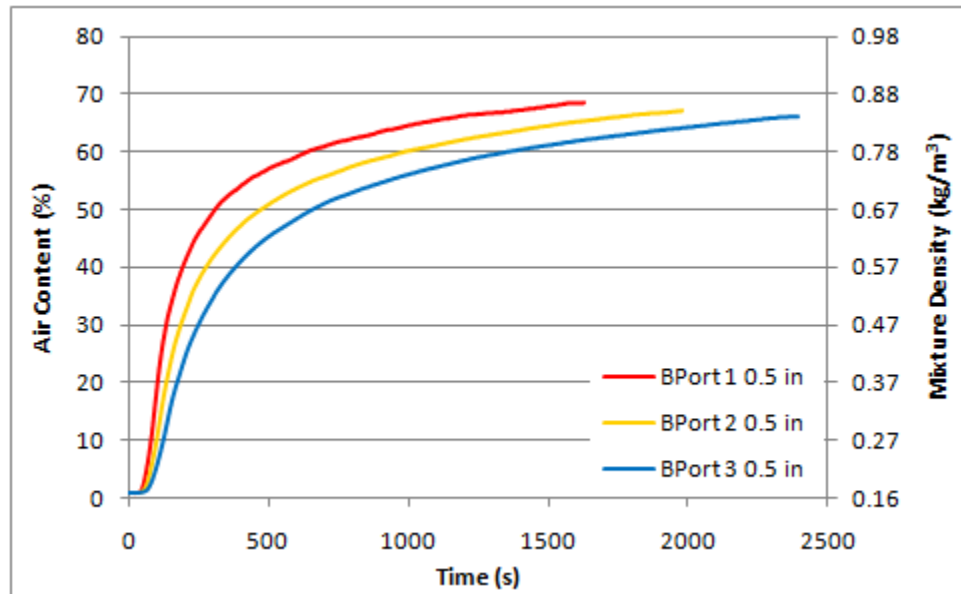


Figure F-36: Local Data for Radial Location 0.5 in along Axial Direction for BPort

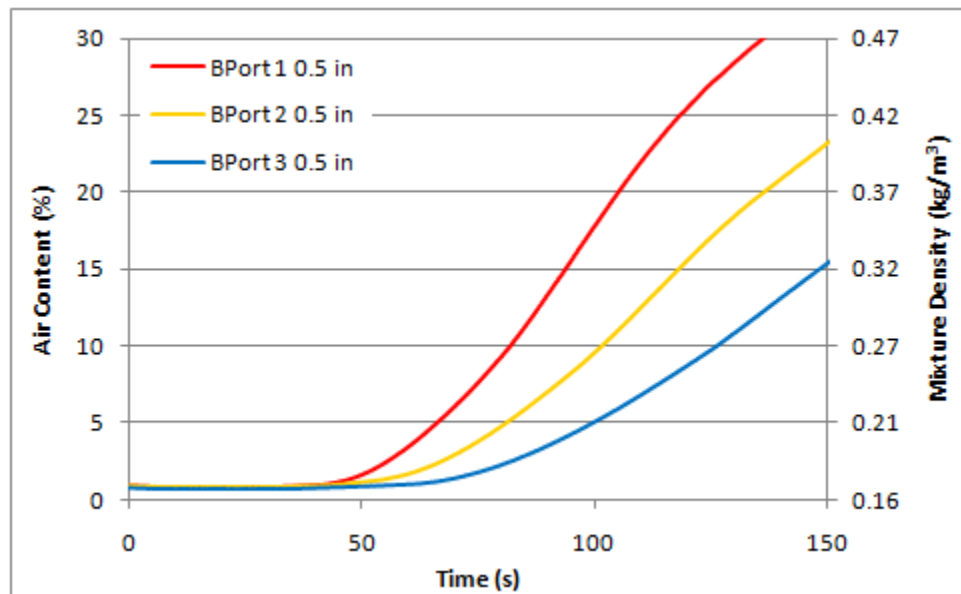


Figure F-37: Initial 150 s of Local Data for Radial Location 0.5 in along Axial Direction for

BPort

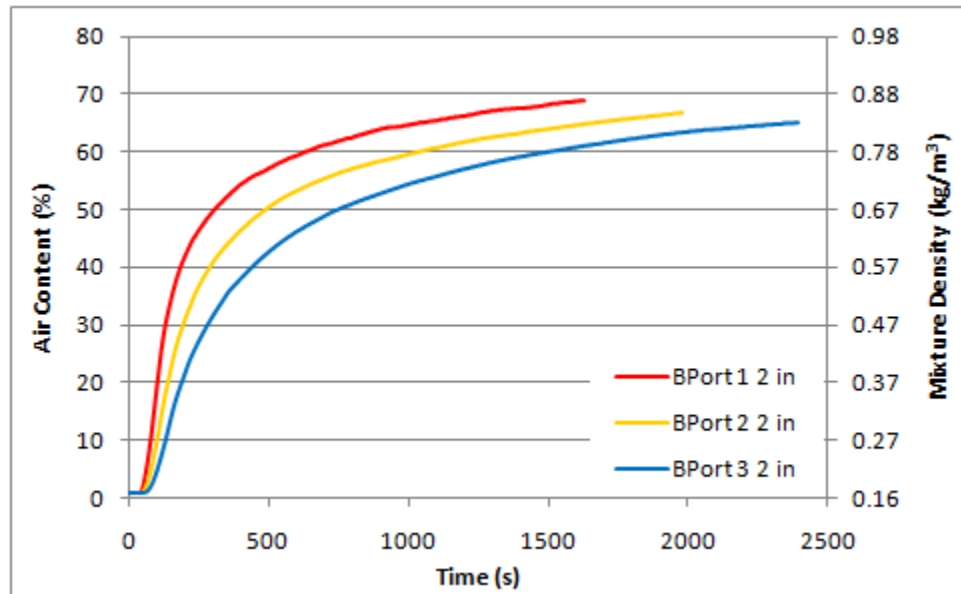


Figure F-38: Local Data for Radial Location 2 in along Axial Direction for BPort

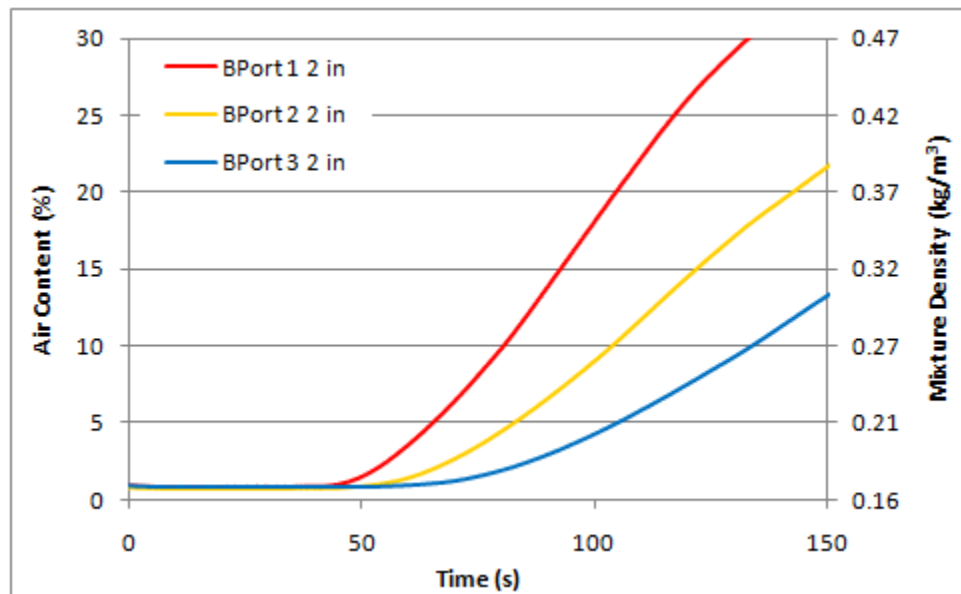


Figure F-39: Initial 150 s of Local Data for Radial Location 2 in along Axial Direction for BPort

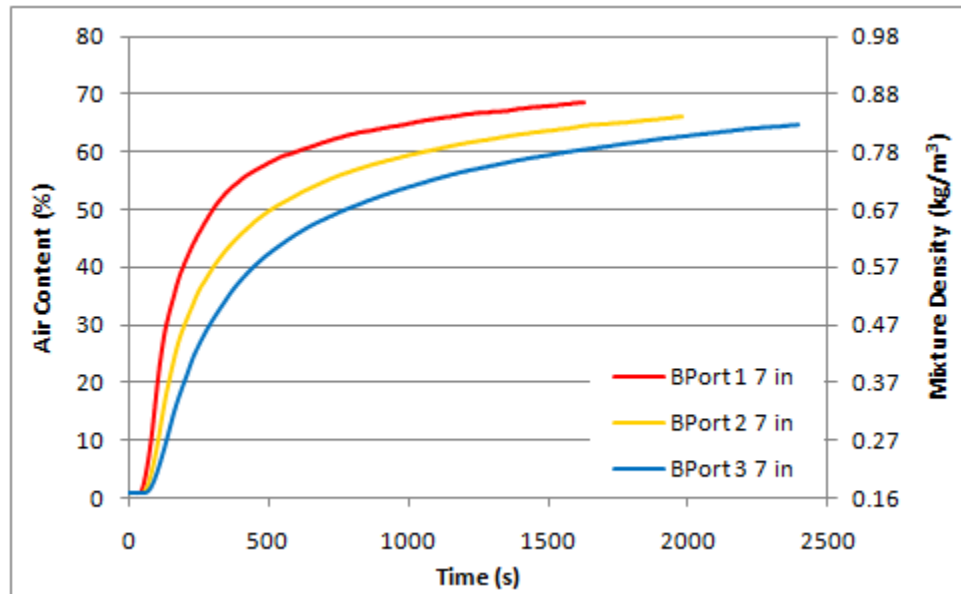


Figure F-40: Local Data for Radial Location 7 in along Axial Direction for BPort

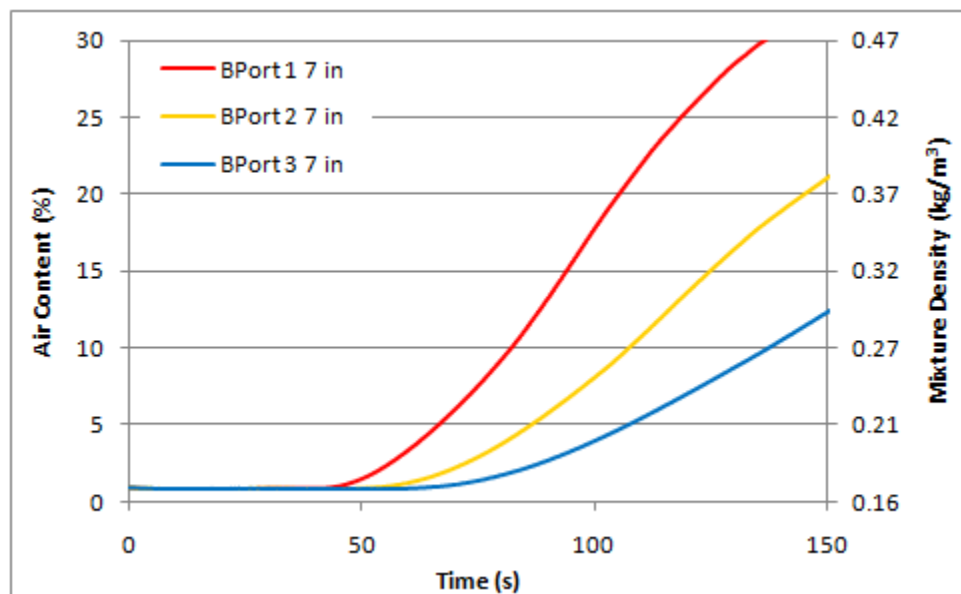


Figure F-41: Initial 150 s of Local Data for Radial Location 7 in along Axial Direction for BPort

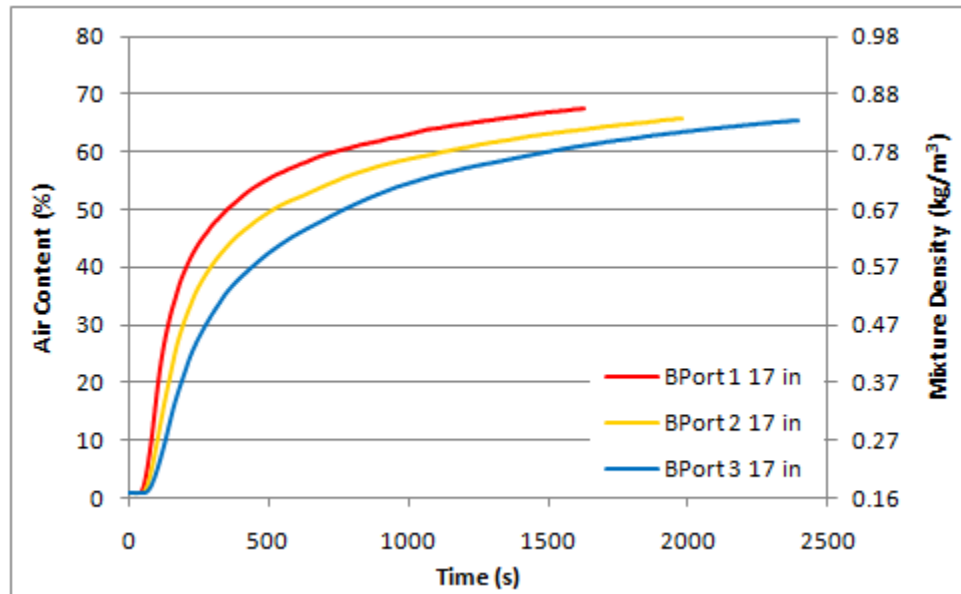


Figure F-42: Local Data for Radial Location 17 in along Axial Direction for BPort

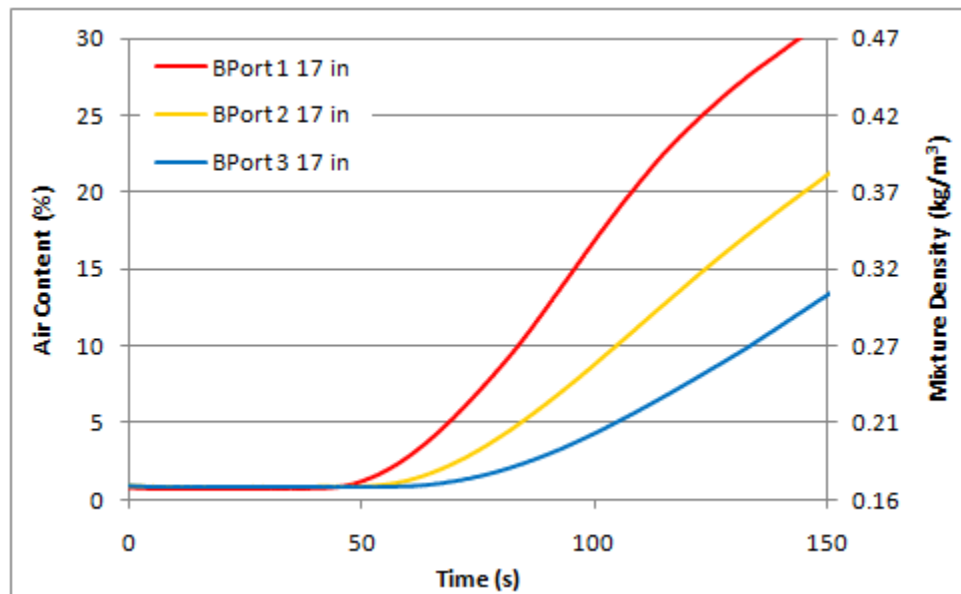


Figure F-43: Initial 150 s of Local Data for Radial Location 17 in along Axial Direction for BPort

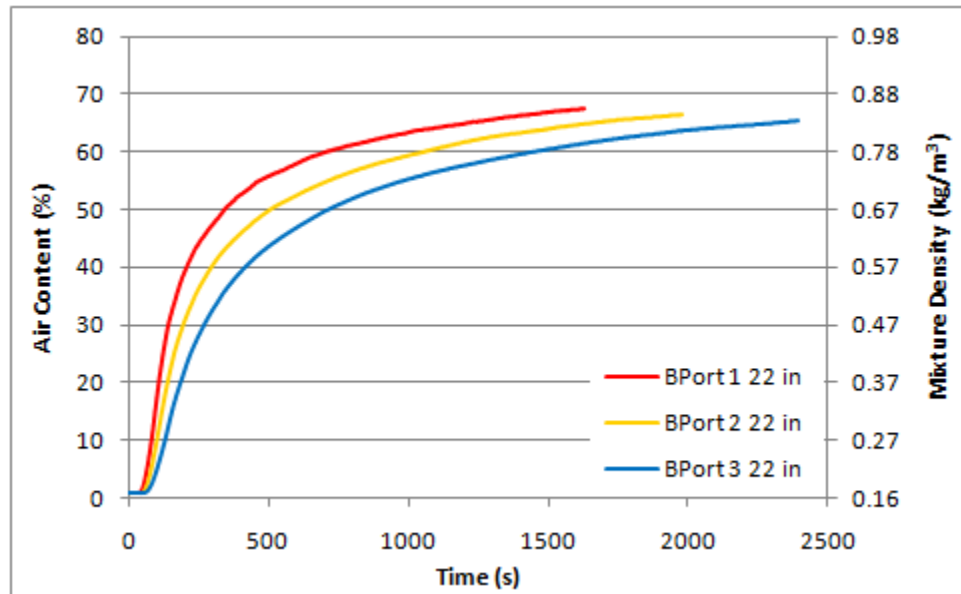


Figure F-44: Local Data for Radial Location 22 in along Axial Direction for BPort

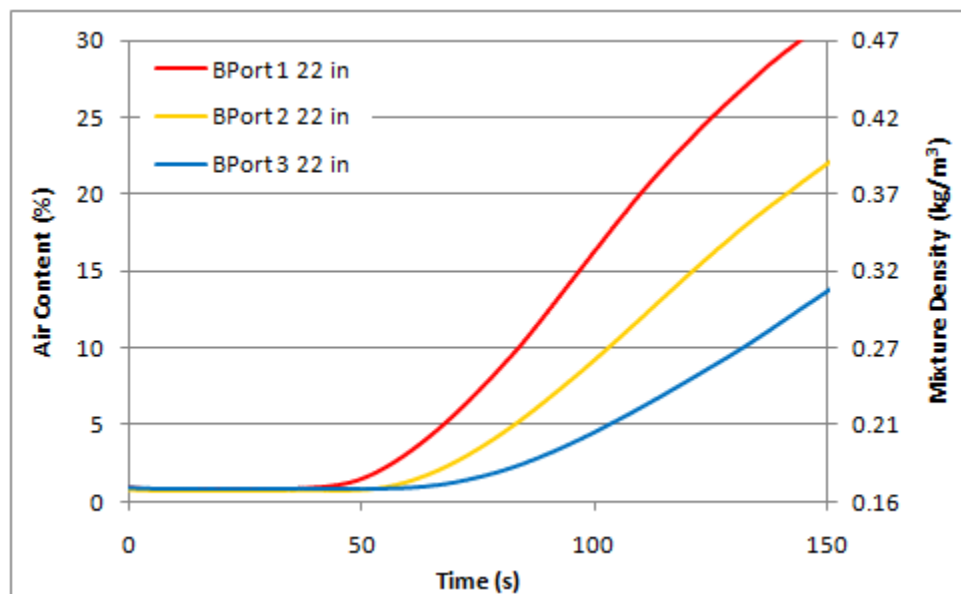


Figure F-45: Initial 150 s of Local Data for Radial Location 22 in along Axial Direction for BPort

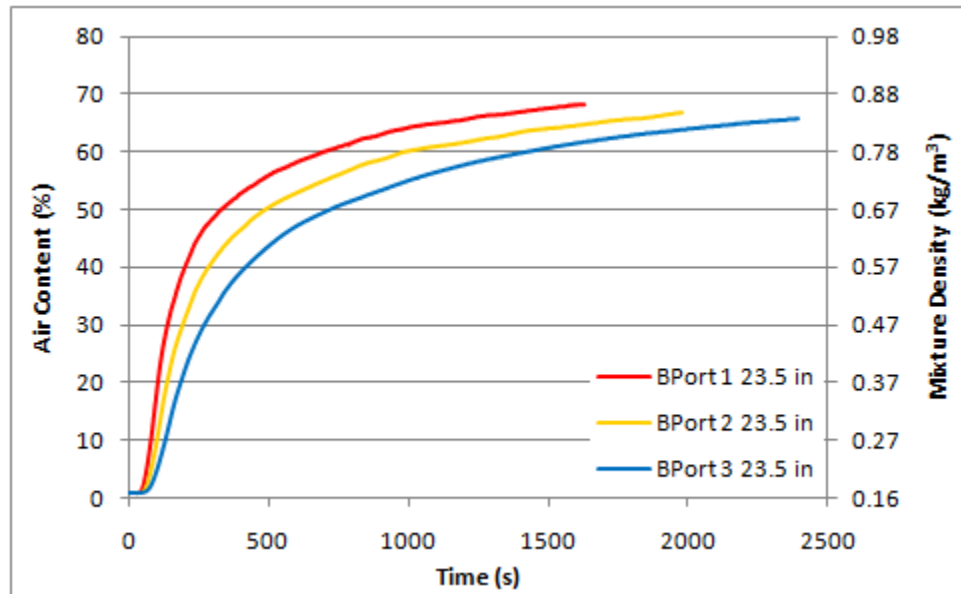


Figure F-46: Local Data for Radial Location 23.5 in along Axial Direction for BPort

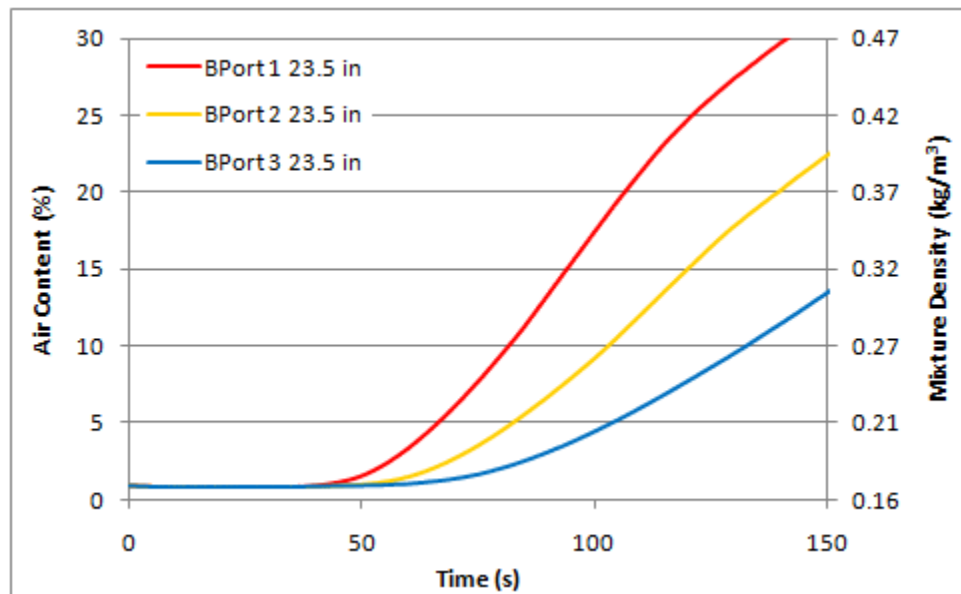


Figure F-47: Initial 150s of Local Data for Radial Location 23.5 in along Axial Direction for BPort

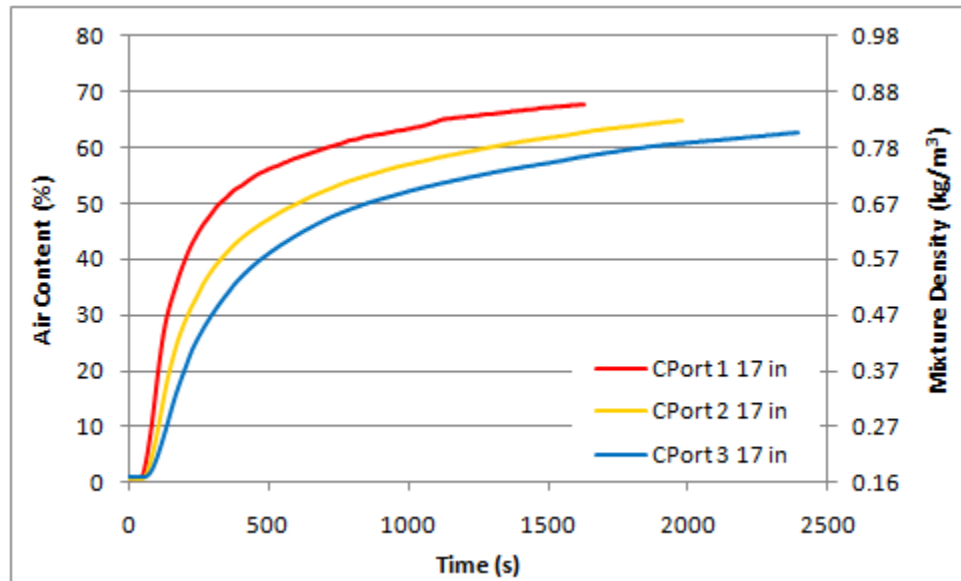


Figure F-48: Local Data for Radial Location 17 in along Axial Direction for CPort

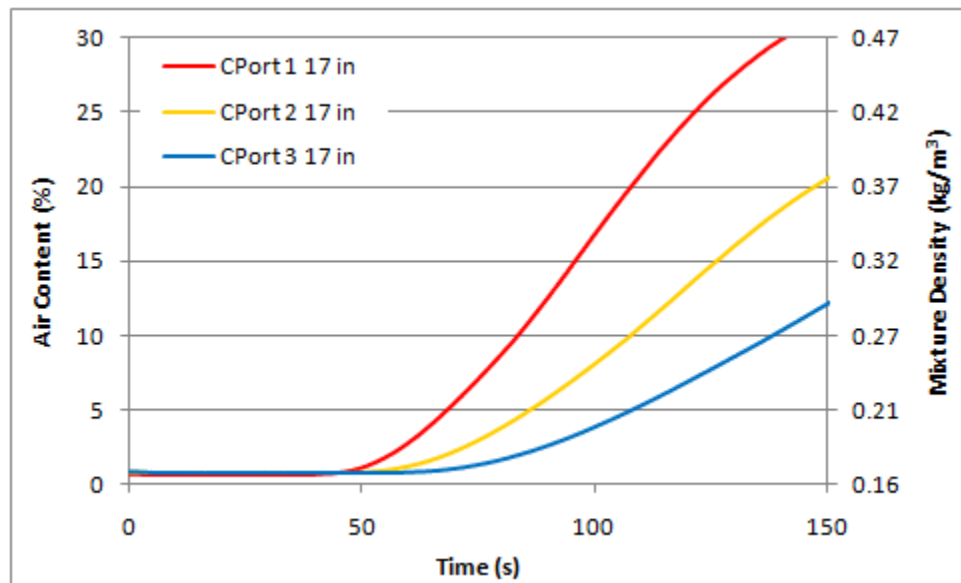


Figure F-49: Initial 150s of Local Data for Radial Location 17 in along Axial Direction for CPort

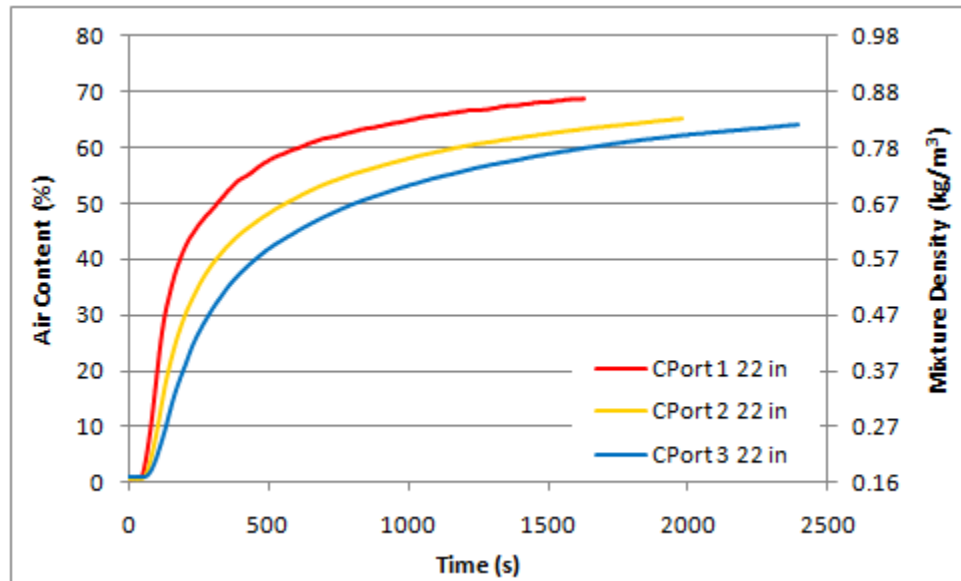


Figure F-50: Local Data for Radial Location 22 in along Axial Direction for CPort

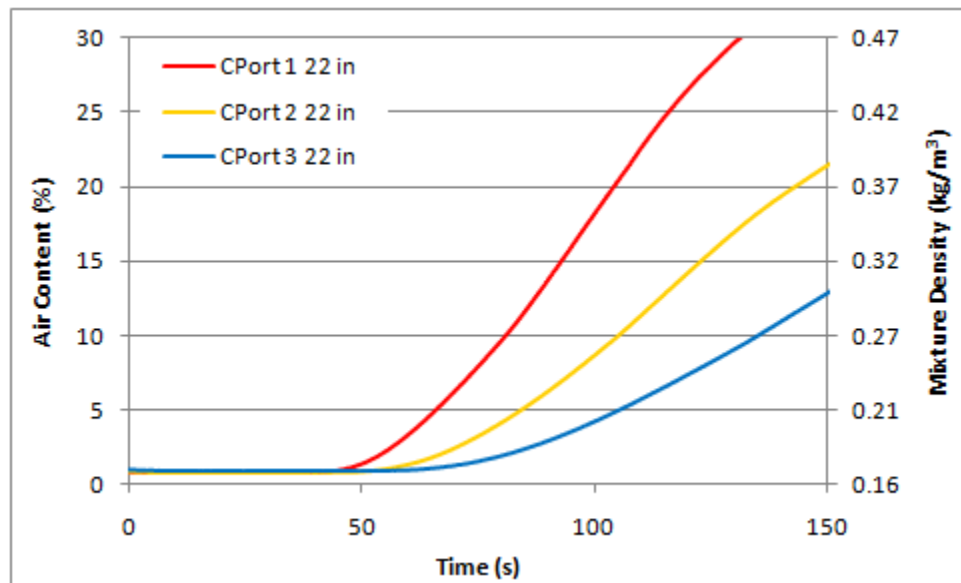


Figure F-51: Initial 150s of Local Data for Radial Location 22 in along Axial Direction for CPort

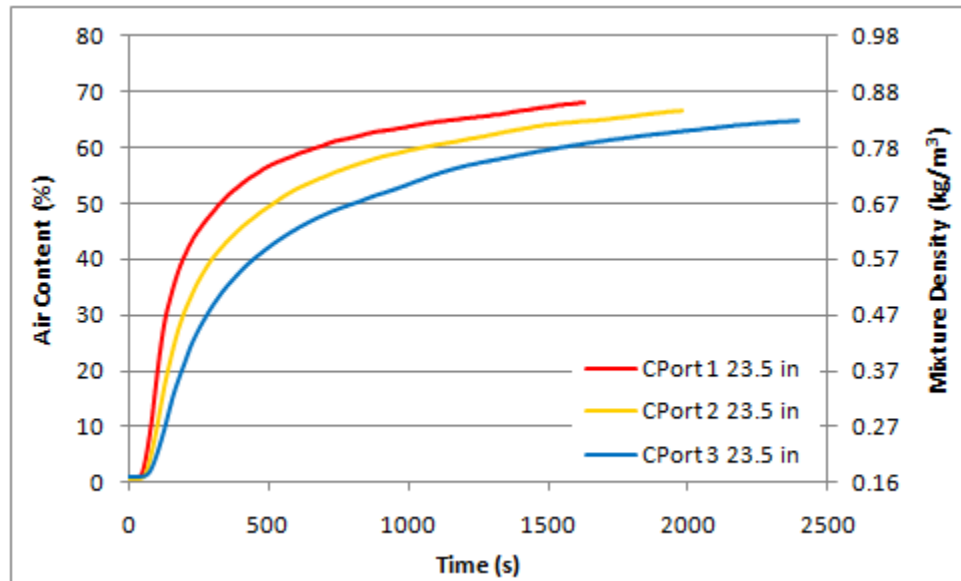


Figure F-52: Local Data for Radial Location 23.5 in along Axial Direction for CPort

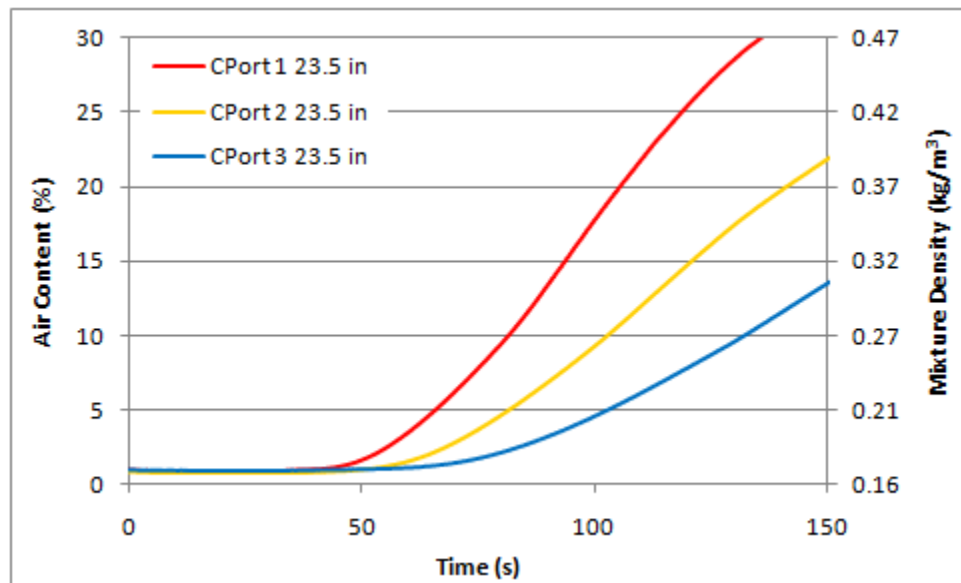


Figure F-53: Initial 150 s of Local Data for Radial Location 23.5 in along Axial Direction for
CPort

Appendix G

Lower Side Break MATLAB Plots

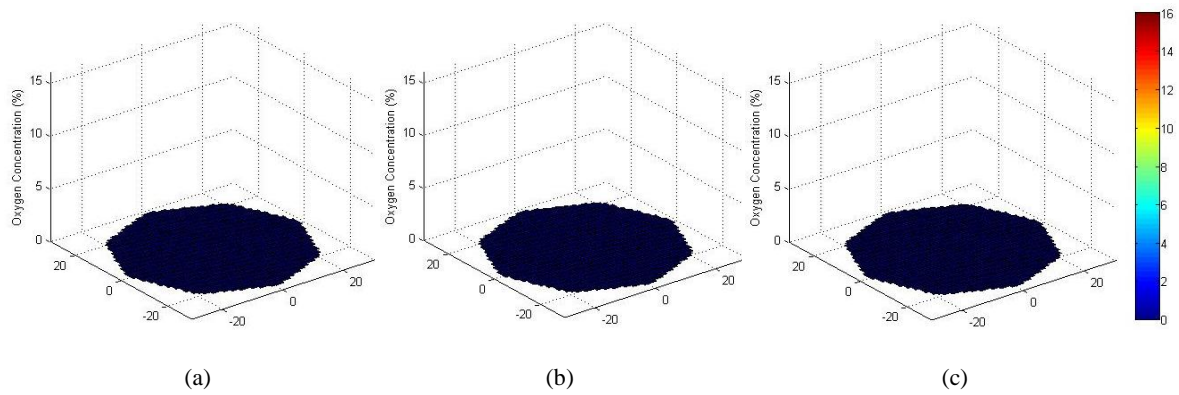


Figure G-1: Initial Oxygen Content at (a) Port1, (b) Port2, and (c) Port3

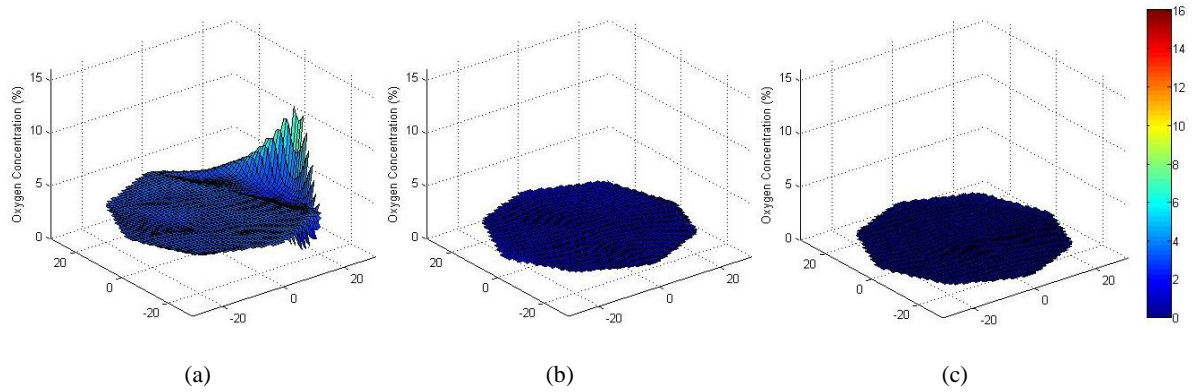


Figure G-2: Oxygen Content 100 s after Initiation at (a) Port1, (b) Port2, and (c) Port3

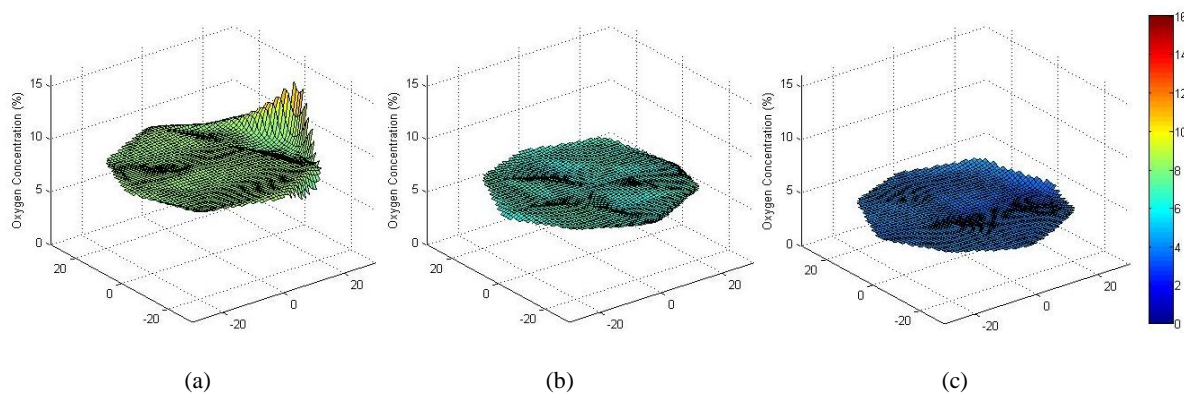


Figure G-3: Oxygen Content 200 s after Initiation at (a) Port1, (b) Port2, and (c) Port3

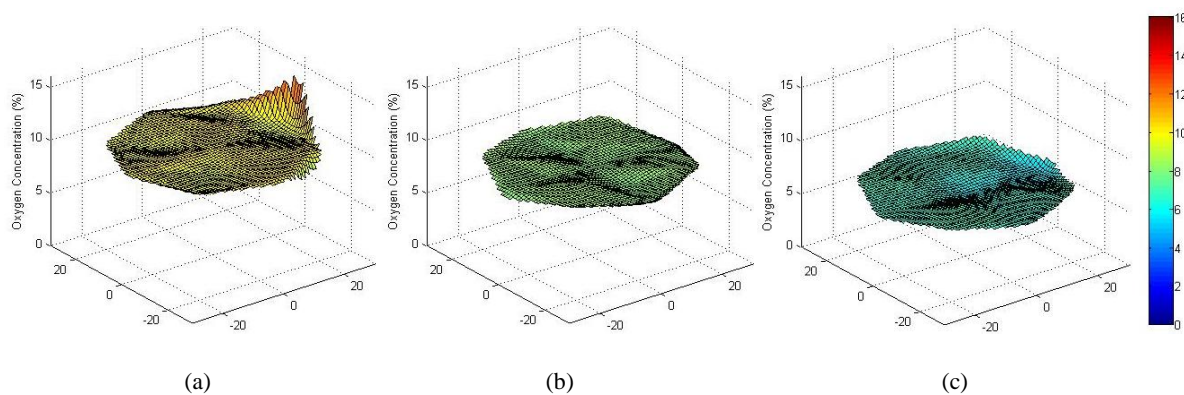


Figure G-4: Oxygen Content 300 s after Initiation at (a) Port1, (b) Port2, and (c) Port3

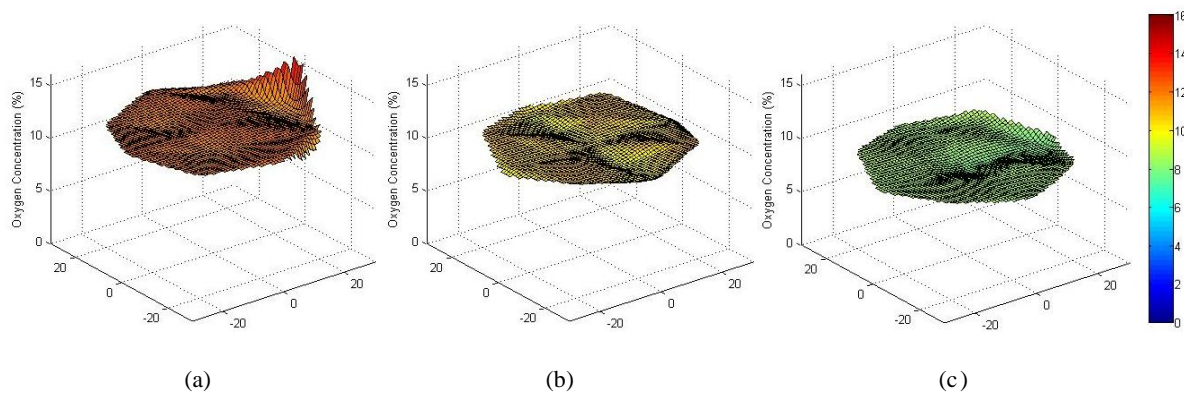


Figure G-5: Oxygen Content 500 s after Initiation at (a) Port1, (b) Port2, and (c) Port3

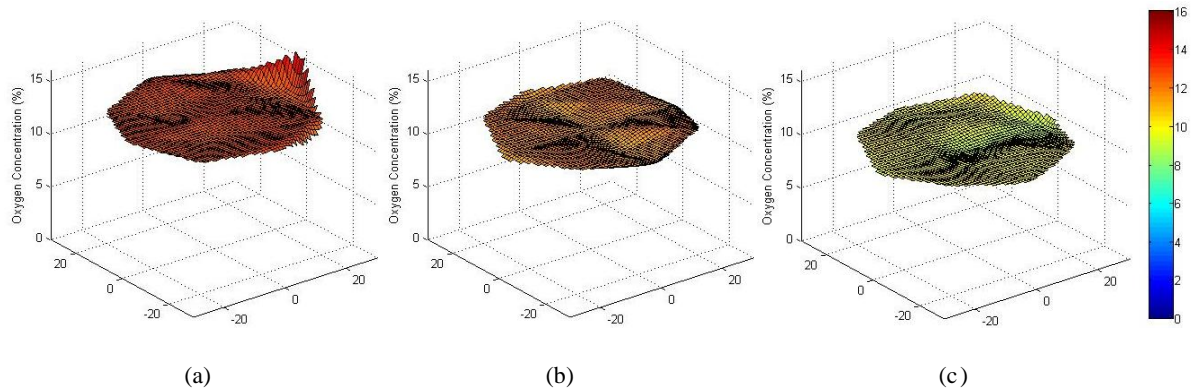


Figure G-6: Oxygen Content 700 s after Initiation at (a) Port1, (b) Port2, and (c) Port3

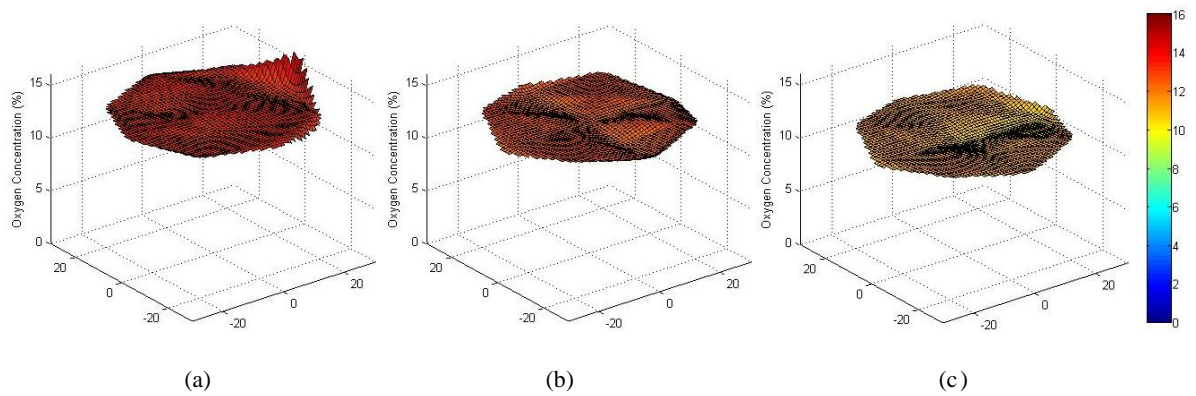


Figure G-7: Oxygen Content 1,000 s after Initiation at (a) Port1, (b) Port2, and (c) Port3

Appendix H

Higher Side Break Data

Local Data

Air Content vs. r/R

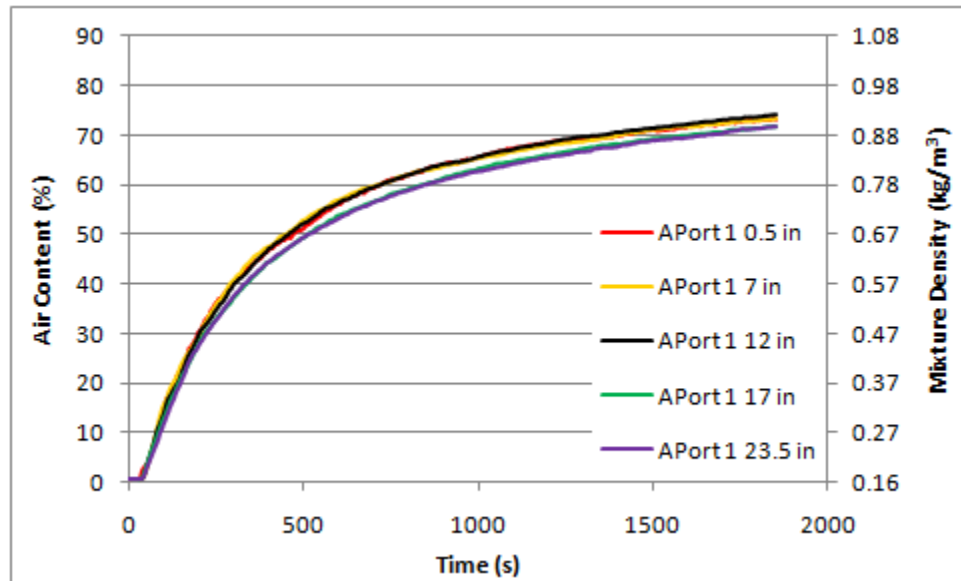


Figure H-1: Local Data for APort1 along Radial Direction

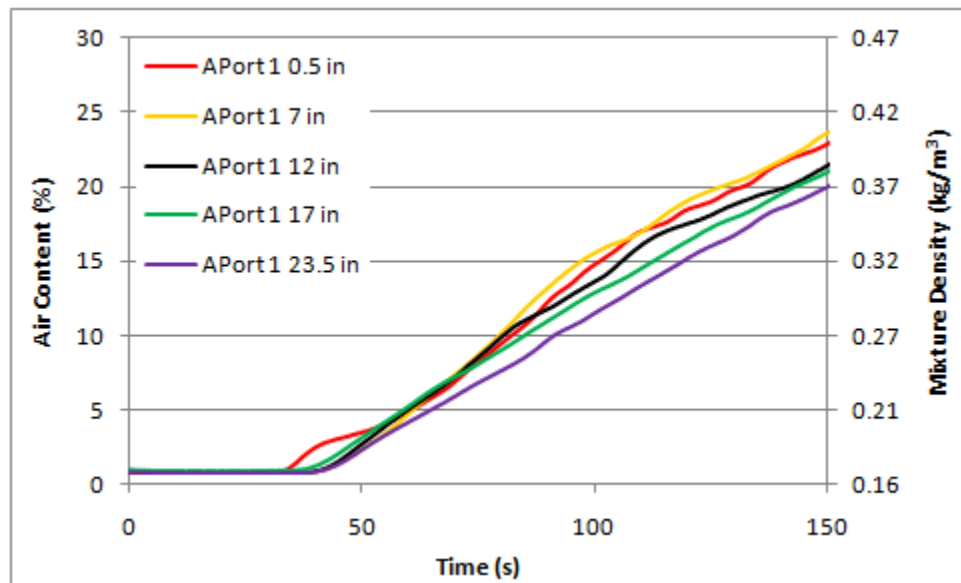


Figure H-2: Initial 150 s of Local Data for APort1 along Radial Direction

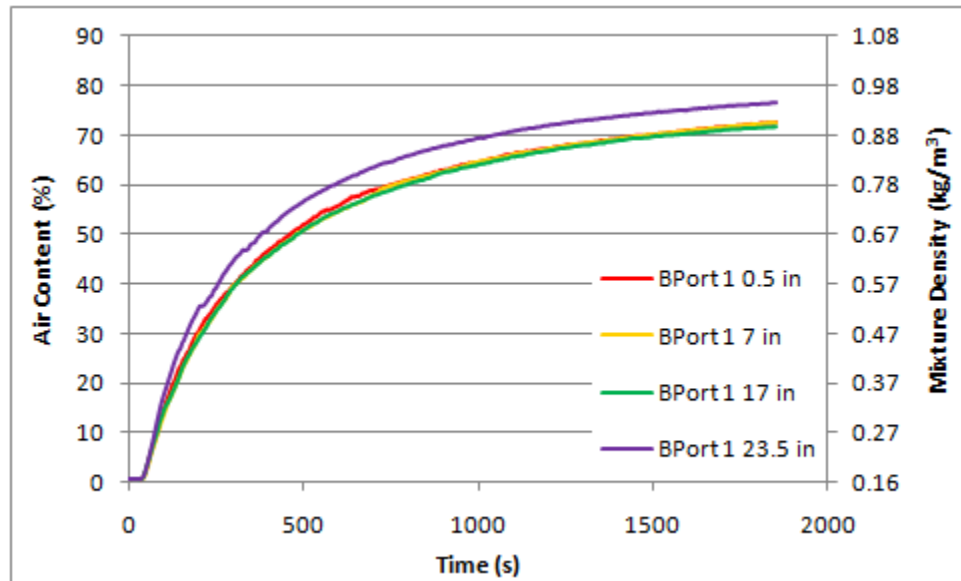


Figure H-3: Local Data for BPort1 along Radial Direction

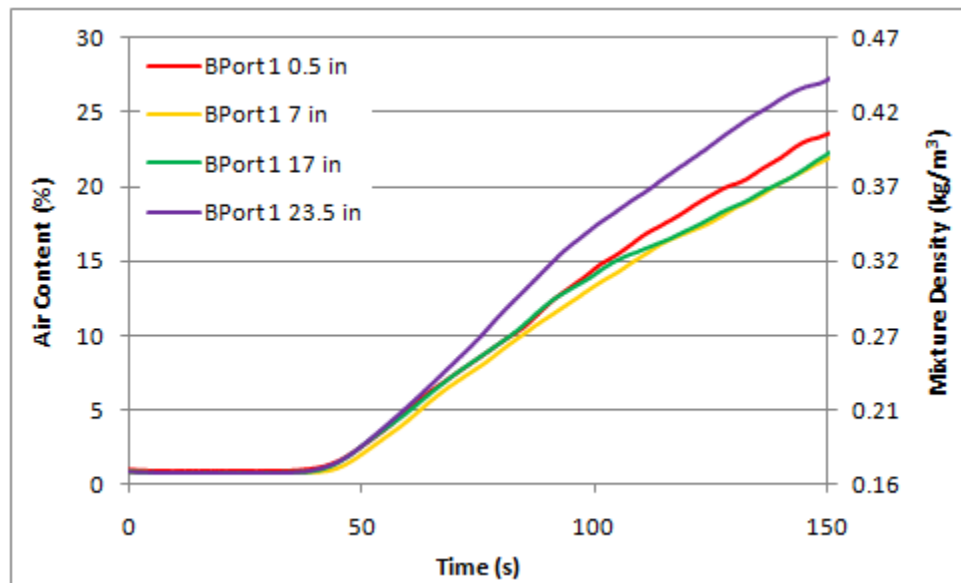


Figure H-4: Initial 150 s of Local Data for BPort1 along Radial Direction

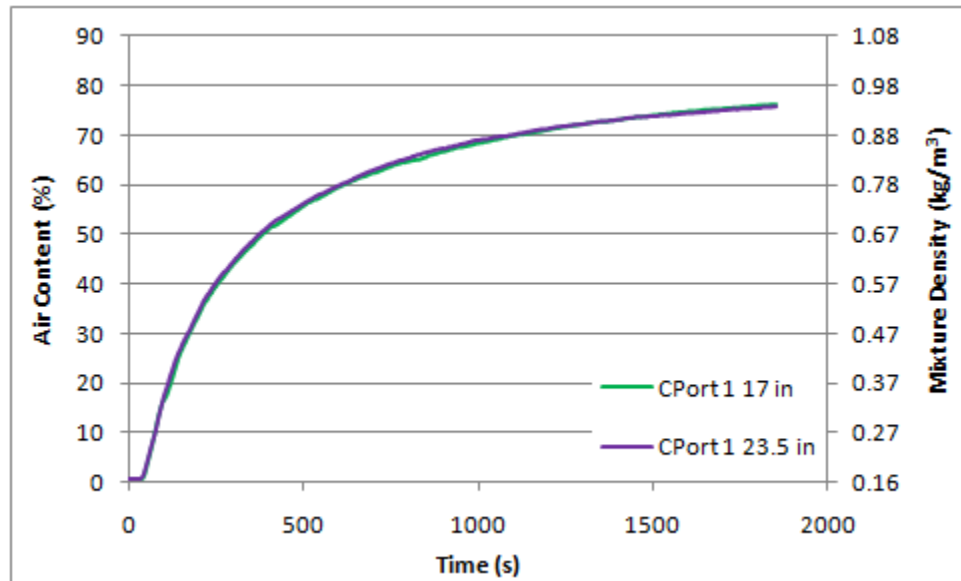


Figure H-5: Local Data for CPort1 along Radial Direction

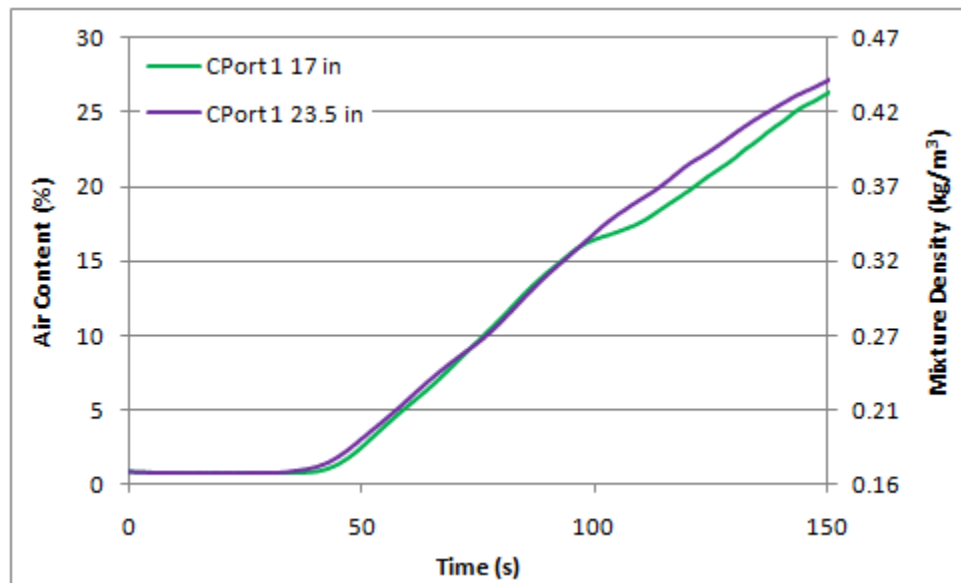


Figure H-6: Initial 150 s of Local Data for CPort1 along Radial Direction

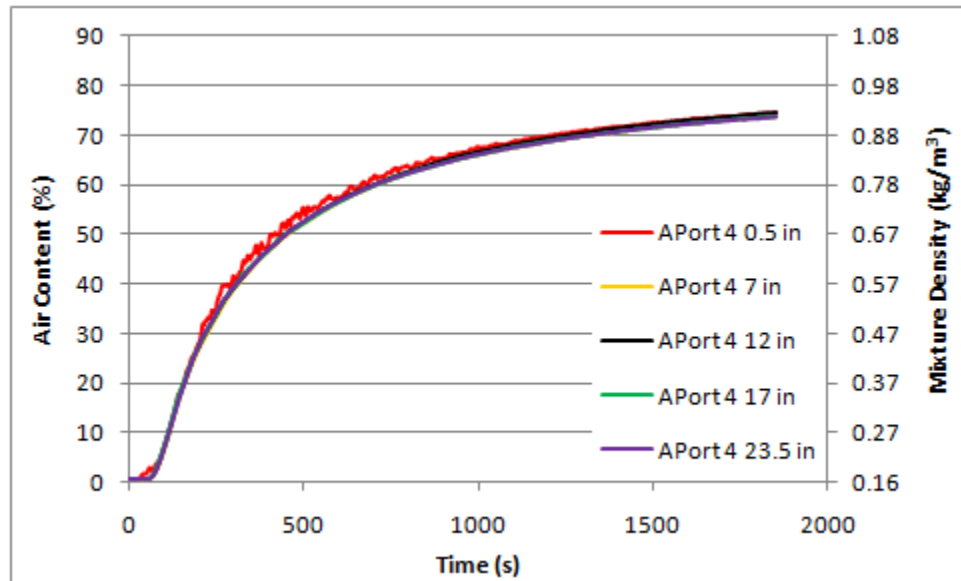


Figure H-7: Local Data for APort4 along Radial Direction

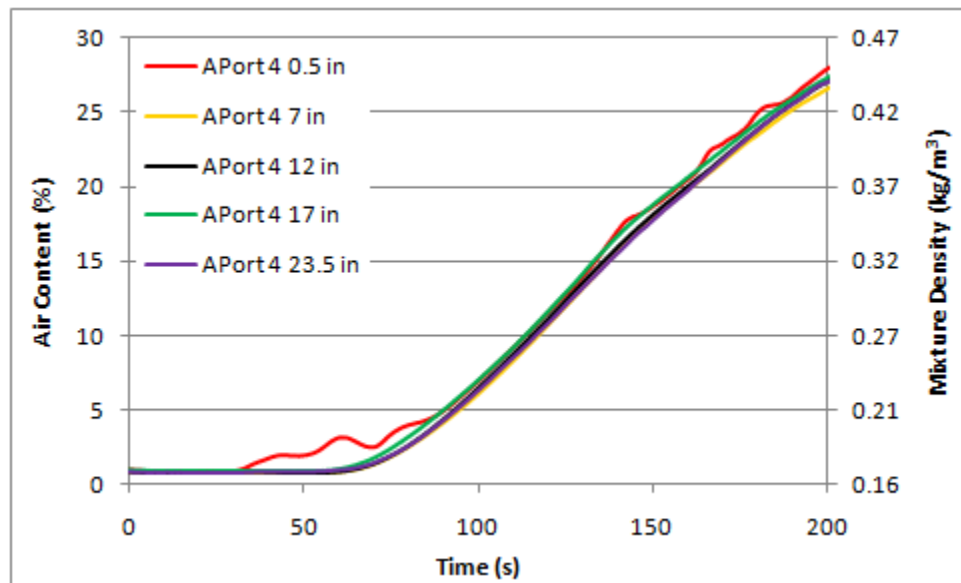


Figure H-8: Initial 200 s of Local Data for APort4 along Radial Direction

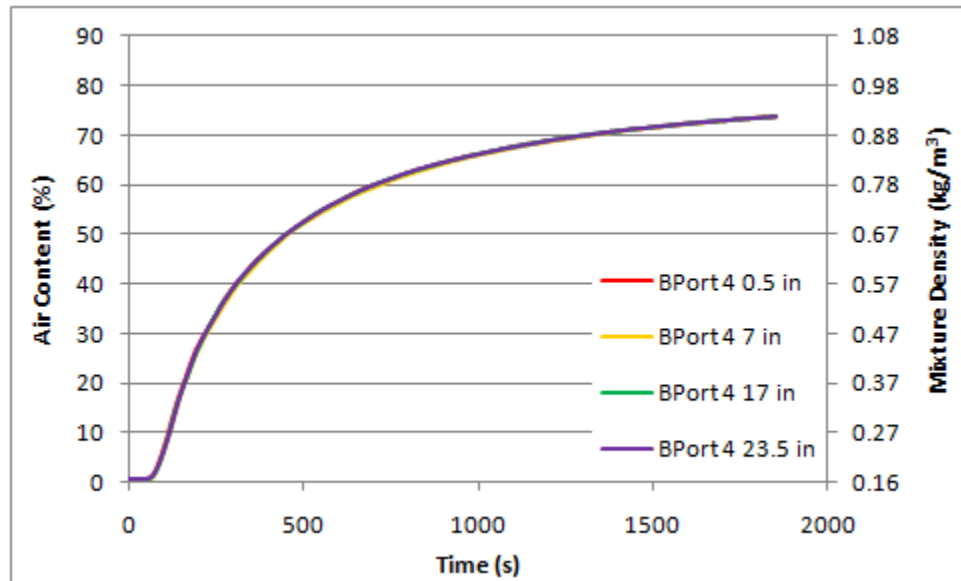


Figure H-9: Local Data for BPort4 along Radial Direction

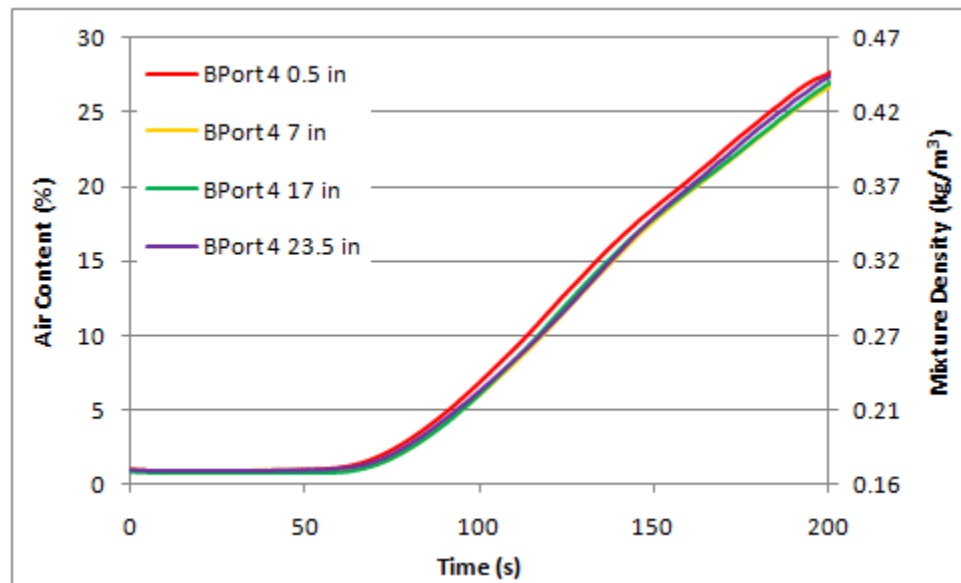


Figure H-10: Initial 200 s of Local Data for BPort4 along Radial Direction

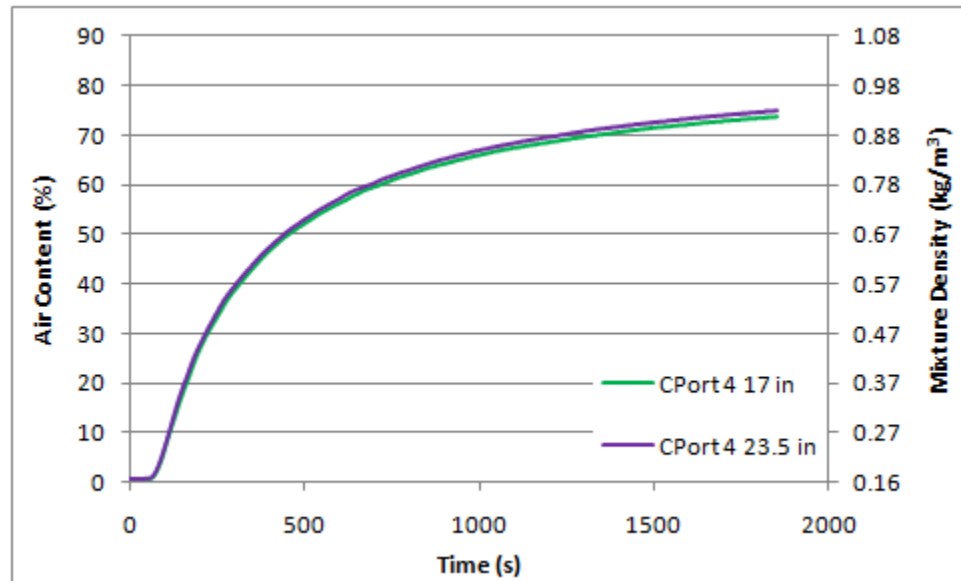


Figure H-11: Local Data for CPort4 along Radial Direction

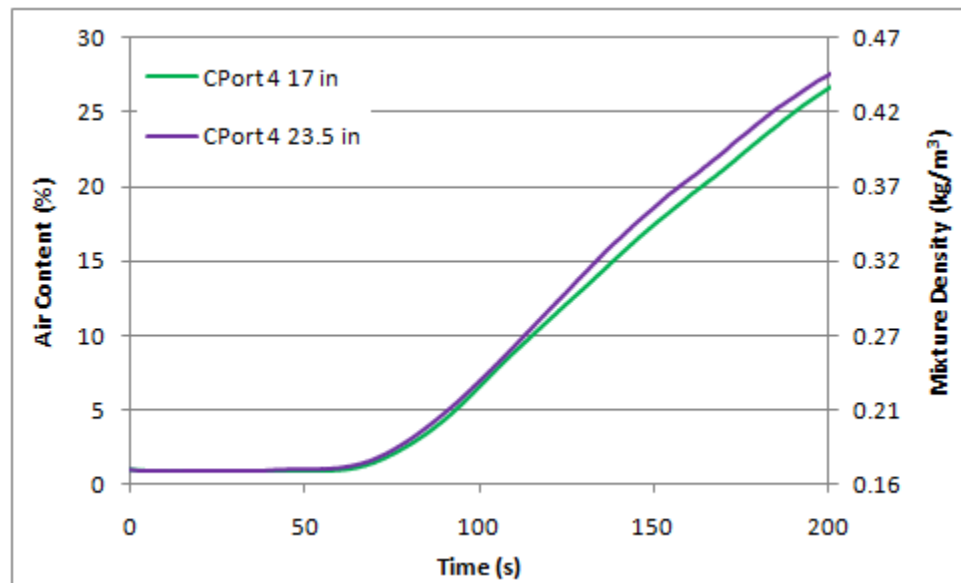


Figure H-12: Initial 200 s of Local Data for CPort4 along Radial Direction

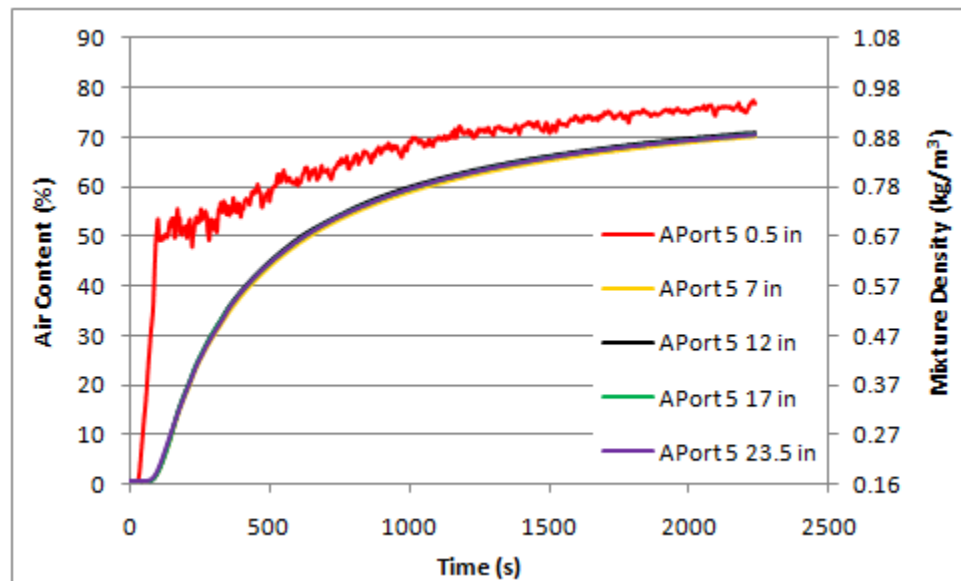


Figure H-13: Local Data for APort5 along Radial Direction

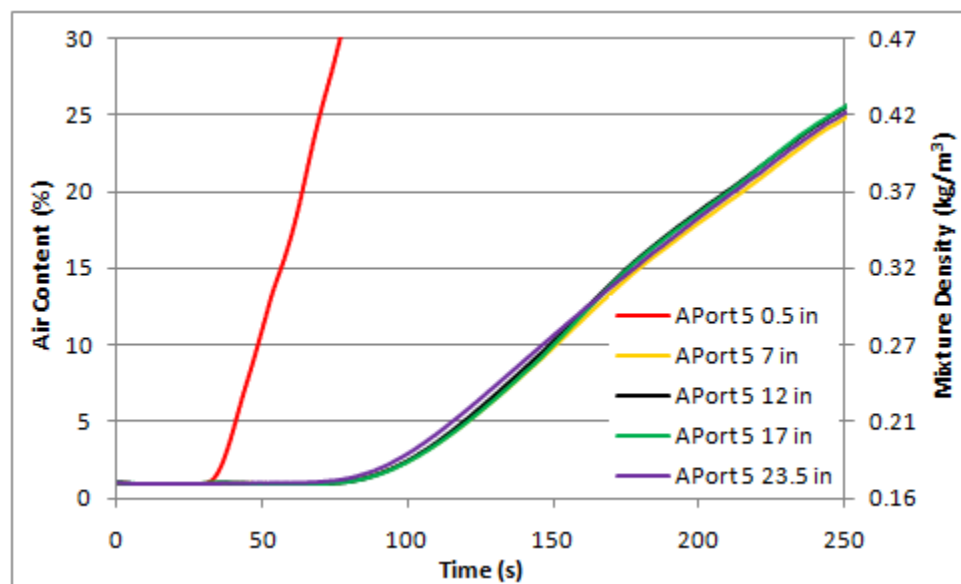


Figure H-14: Initial 250 s of Local Data for APort5 along Radial Direction

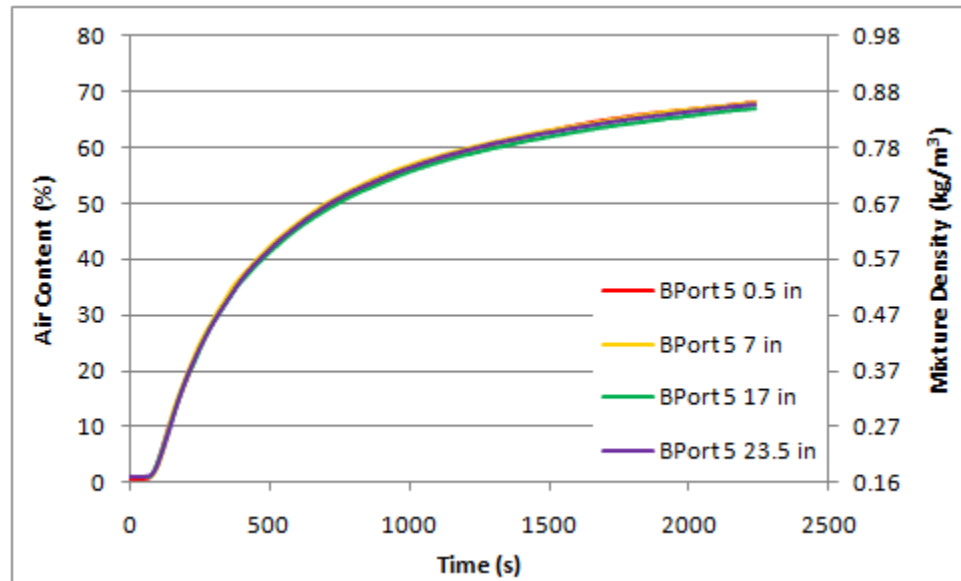


Figure H-15: Local Data for BPort5 along Radial Direction

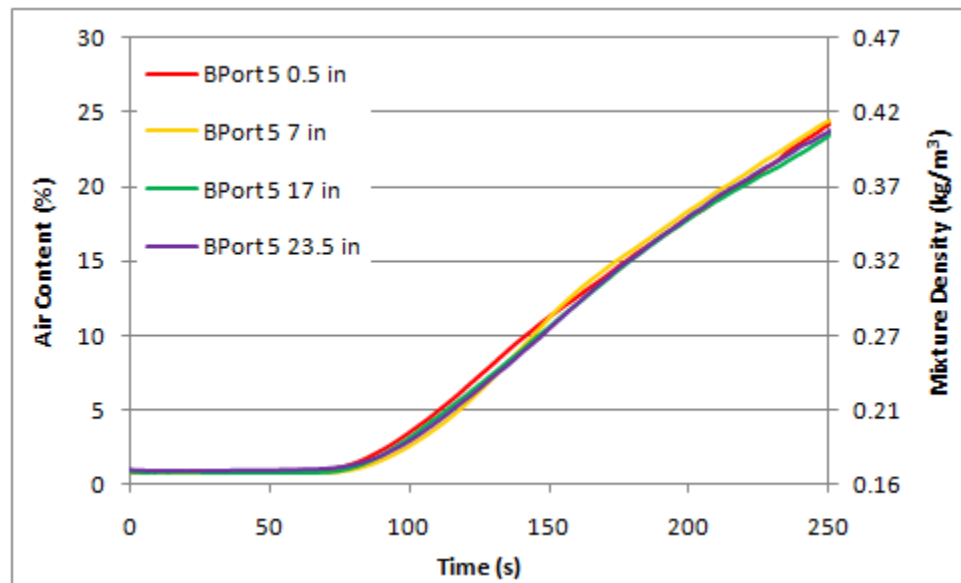


Figure H-16: Initial 250 s of Local Data for BPort5 along Radial Direction

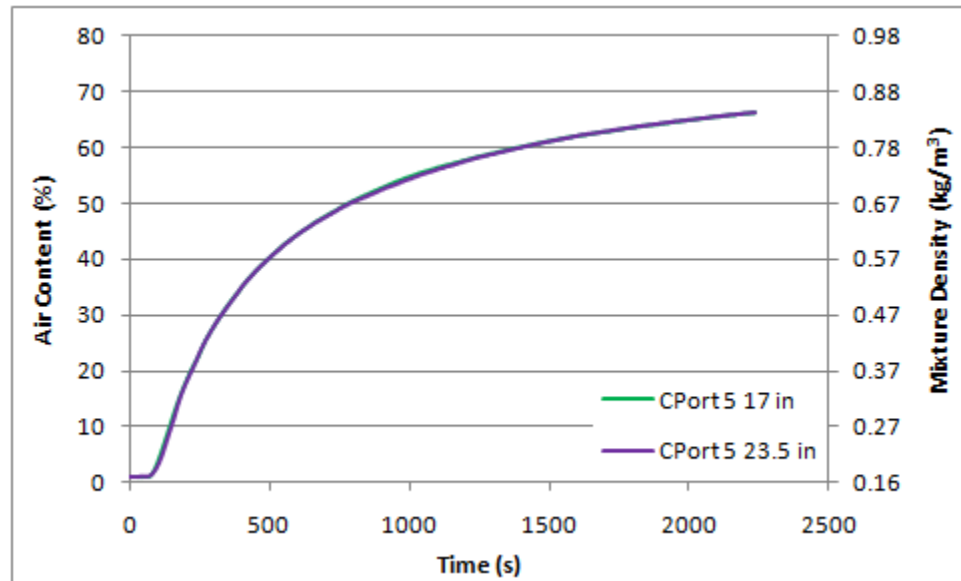


Figure H-17: Local Data for CPort5 along Radial Direction

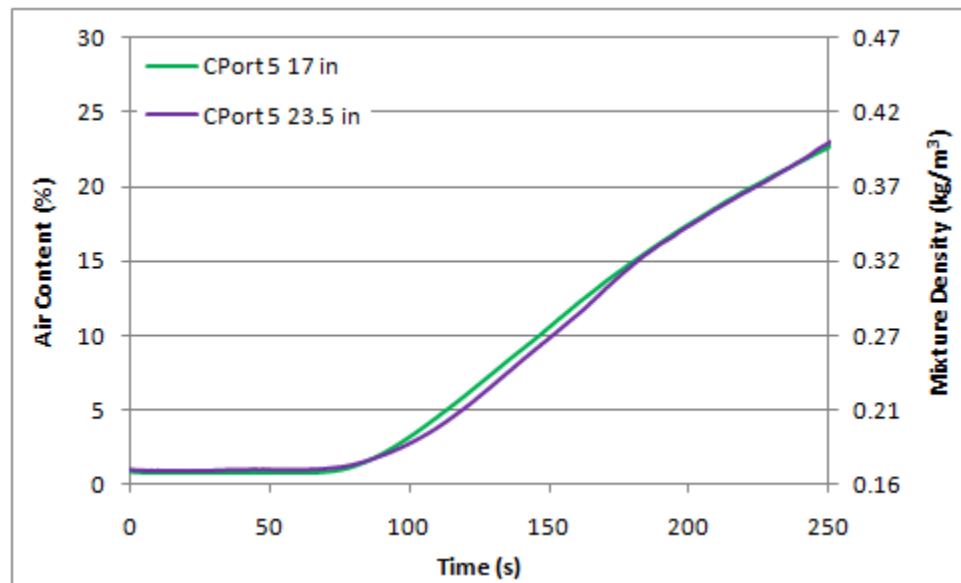


Figure H-18: Initial 250 s of Local Data for CPort5 along Radial Direction

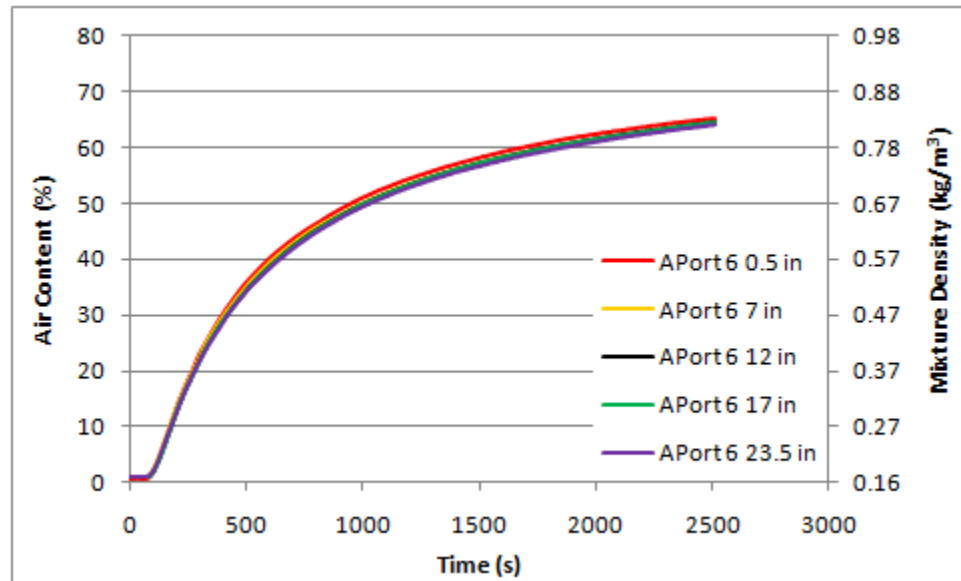


Figure H-19: Local Data for APort6 along Radial Direction

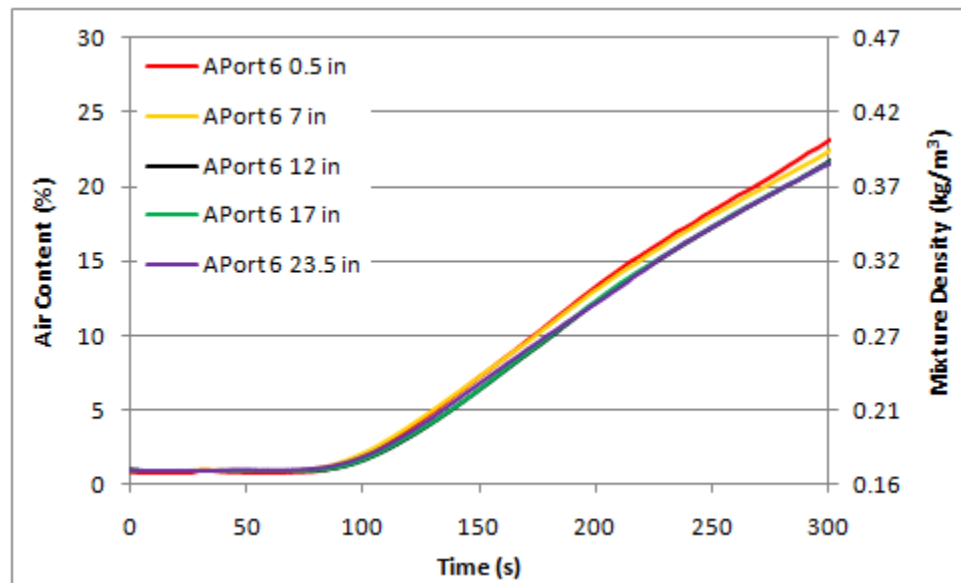


Figure H-20: Initial 300 s of Local Data for APort6 along Radial Direction

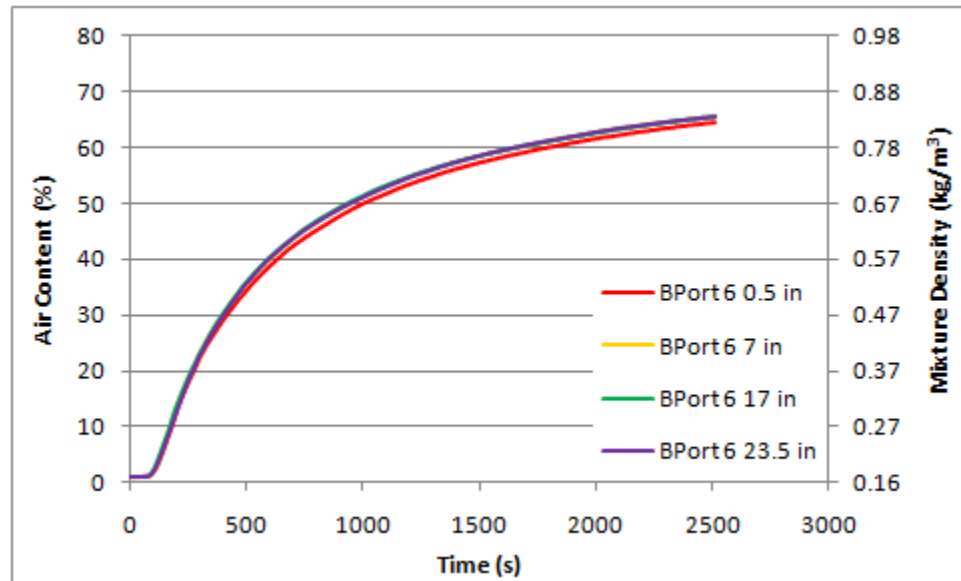


Figure H-21: Local Data for BPort6 along Radial Direction

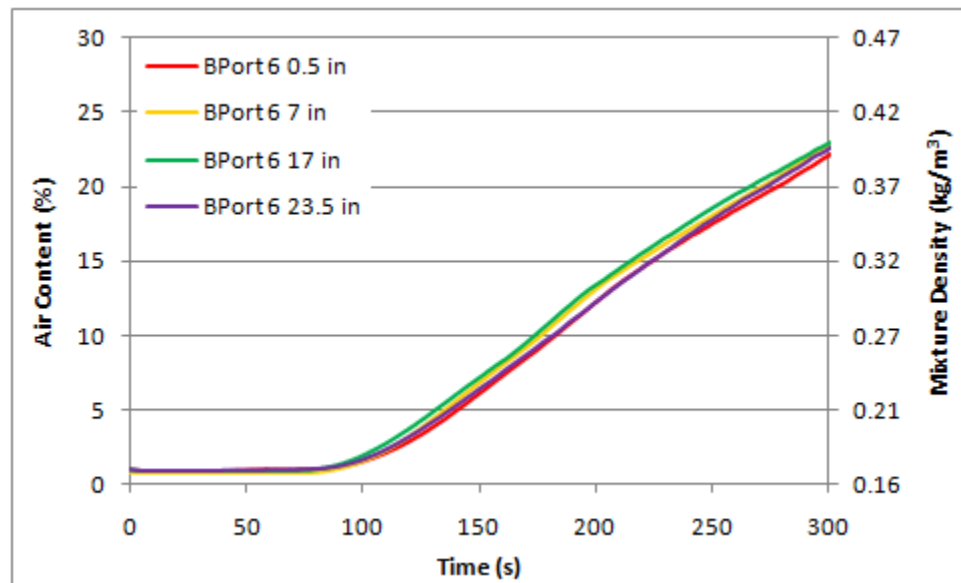


Figure H-22: Initial 300 s of Local Data for BPort6 along Radial Direction

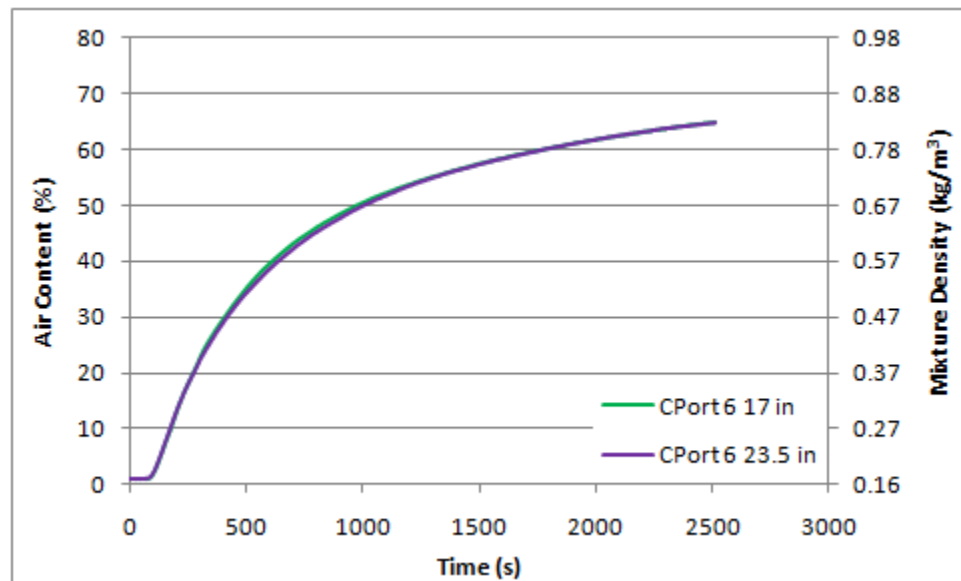


Figure H-23: Local Data for CPort6 along Radial Direction

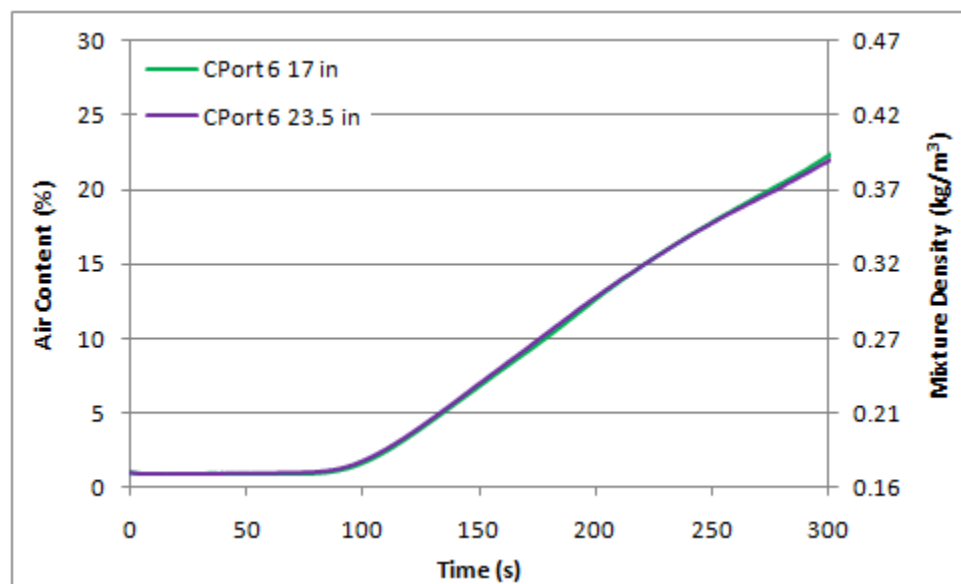


Figure H-24: Initial 300 s of Local Data for CPort6 along Radial Direction

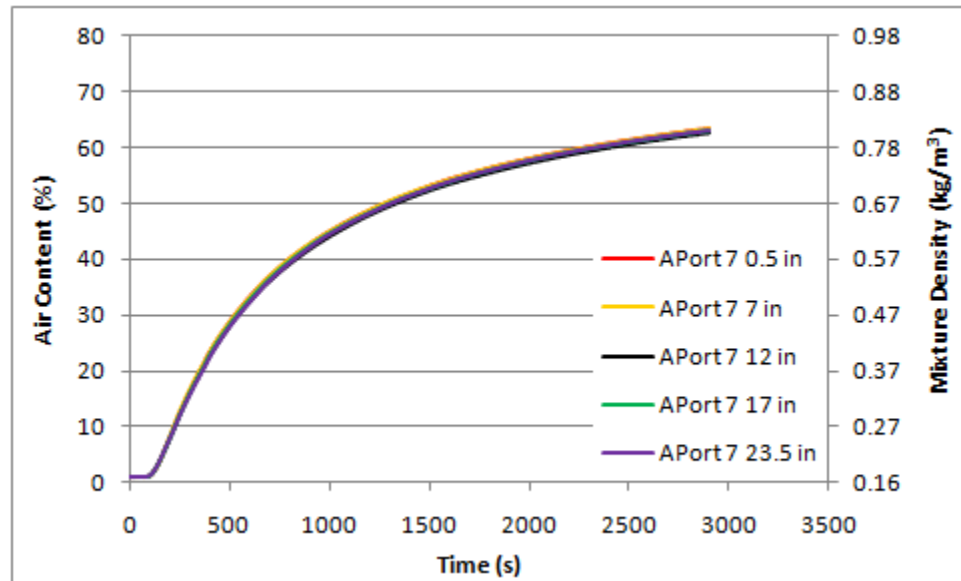


Figure H-25: Local Data for APort7 along Radial Direction

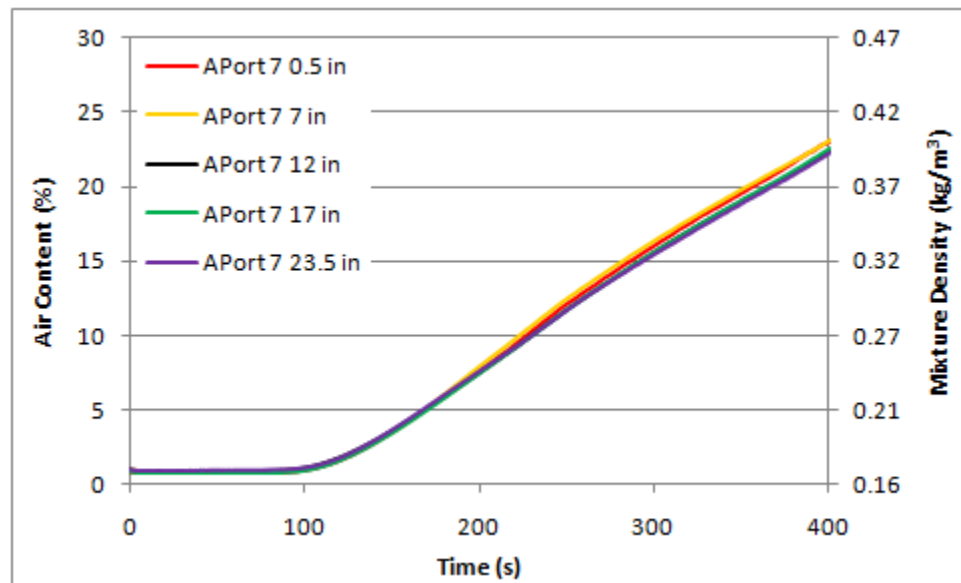


Figure H-26: Initial 400 s of Local Data for APort7 along Radial Direction

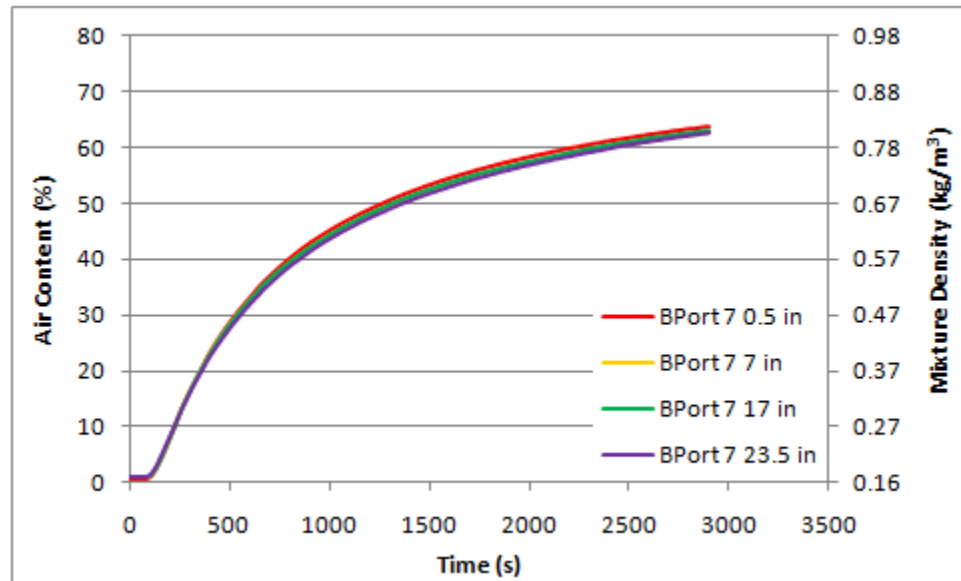


Figure H-27: Local Data for BPort7 along Radial Direction

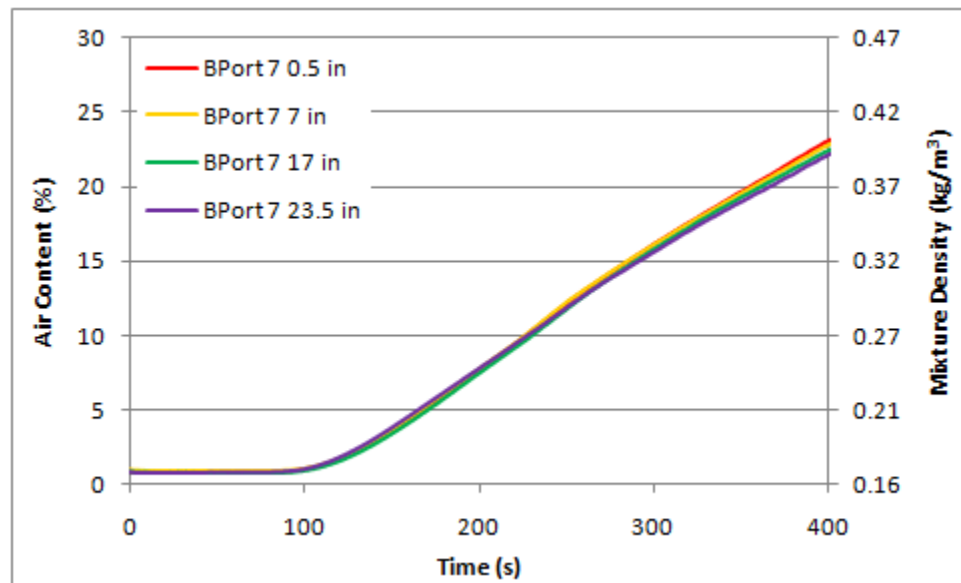


Figure H-28: Initial 400 s of Local Data for BPort7 along Radial Direction

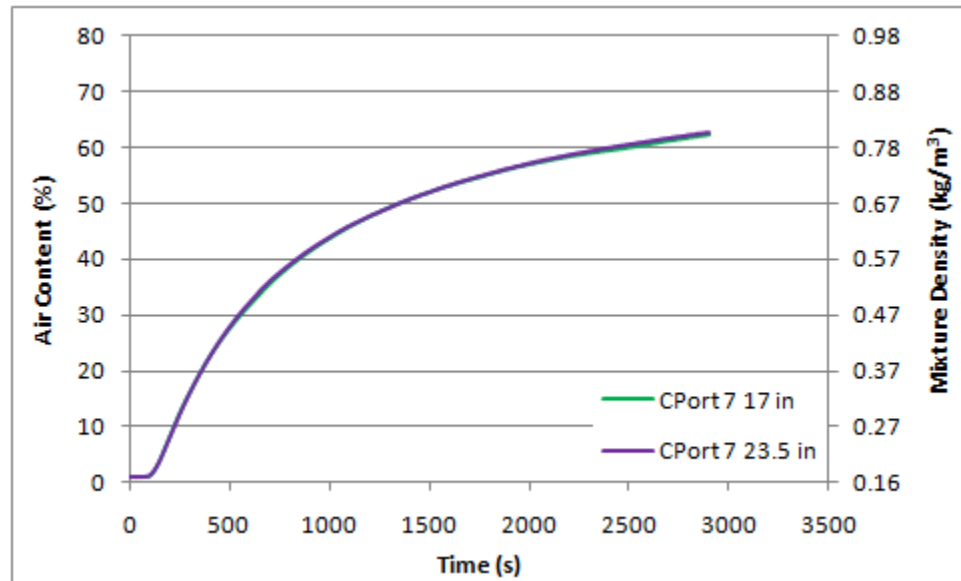


Figure H-29: Local Data for CPort7 along Radial Direction

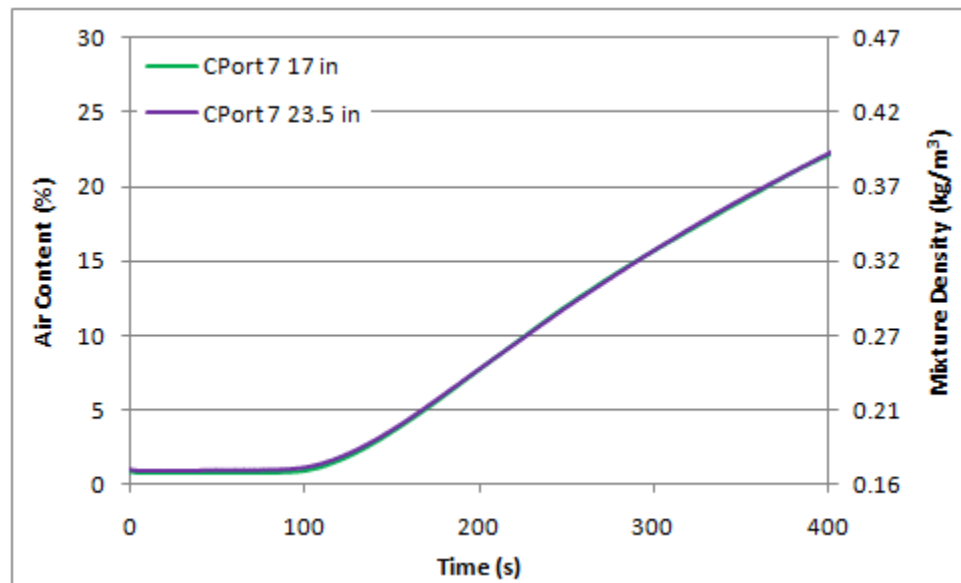


Figure H-30: Initial 400 s of Local Data for CPort7 along Radial Direction

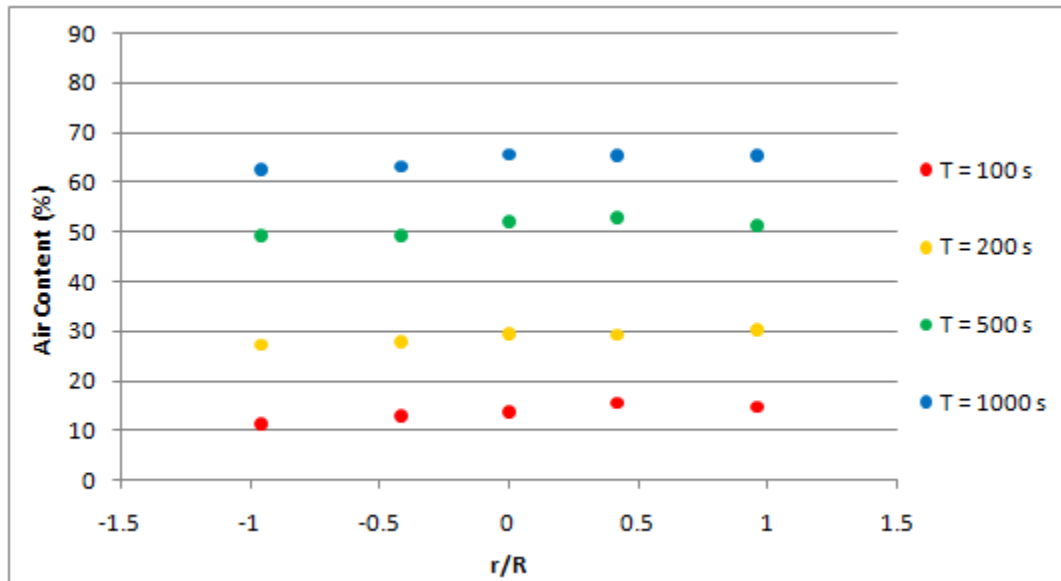


Figure H-31: Variation of Air Content along Vessel Diameter for APort1

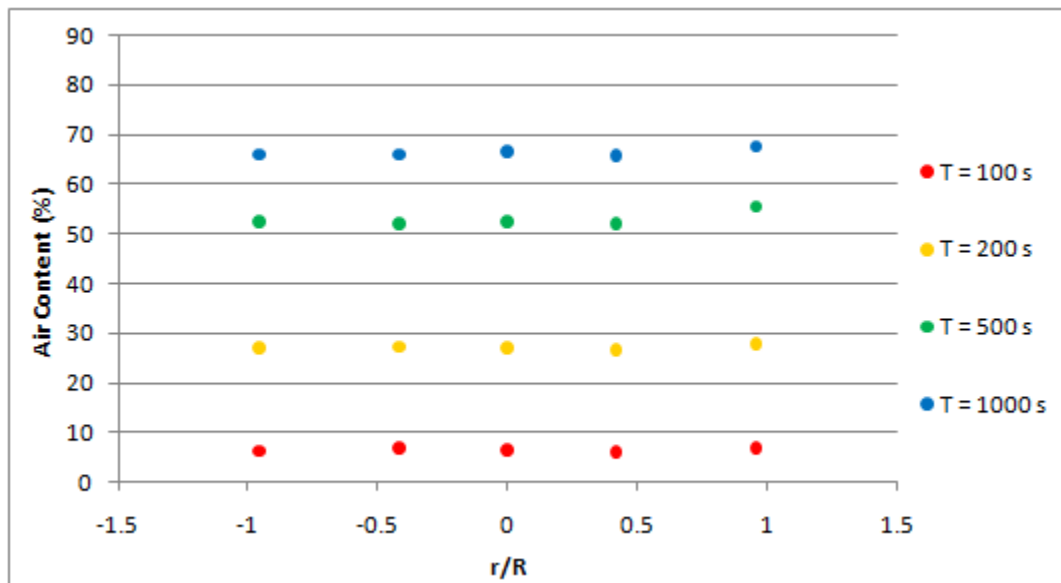


Figure H-32: Variation of Air Content along Vessel Diameter for APort4

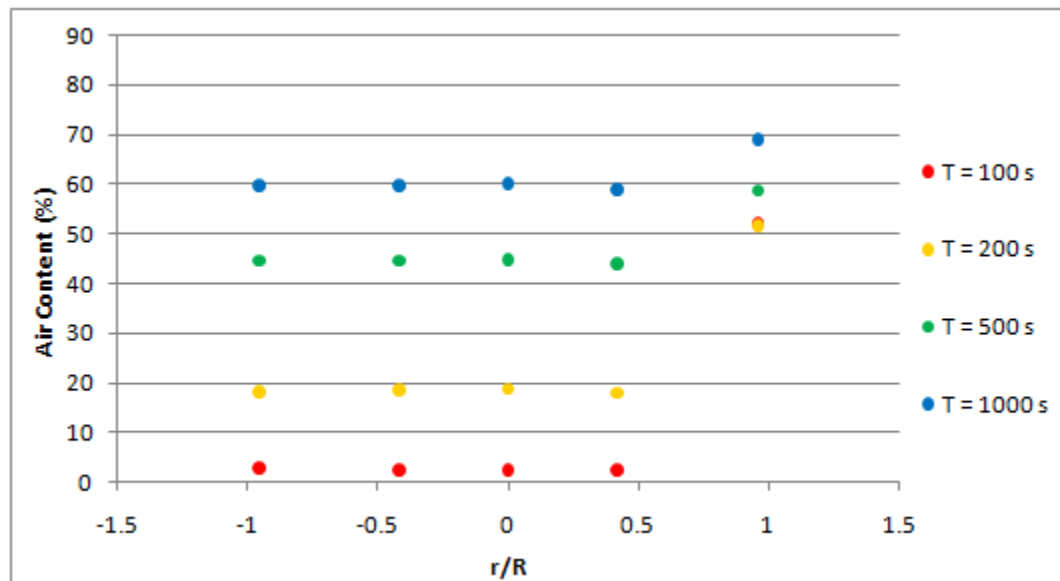


Figure H-33: Variation of Air Content along Vessel Diameter for APort5

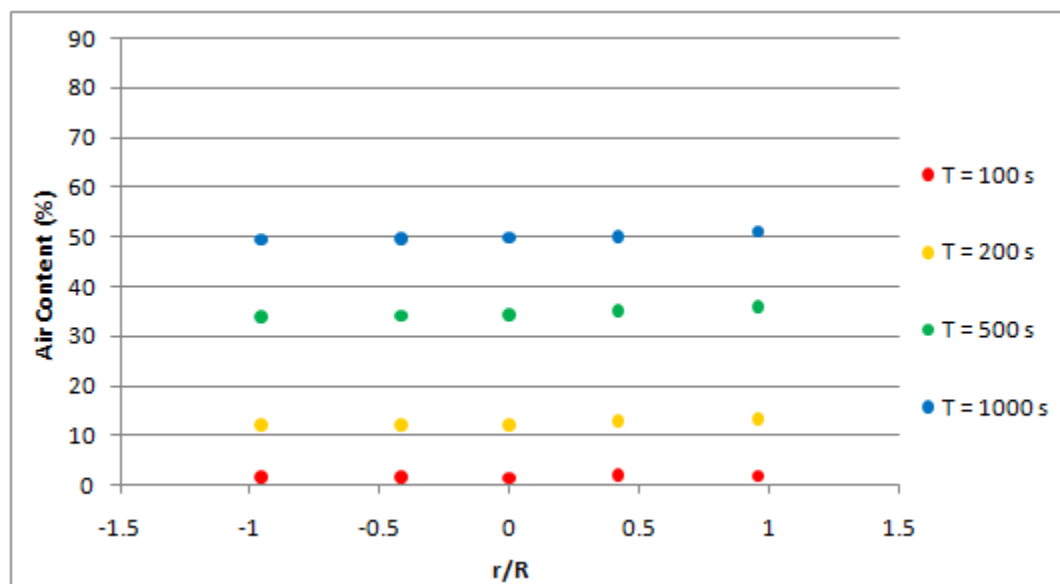


Figure H-34: Variation of Air Content along Vessel Diameter for APort6

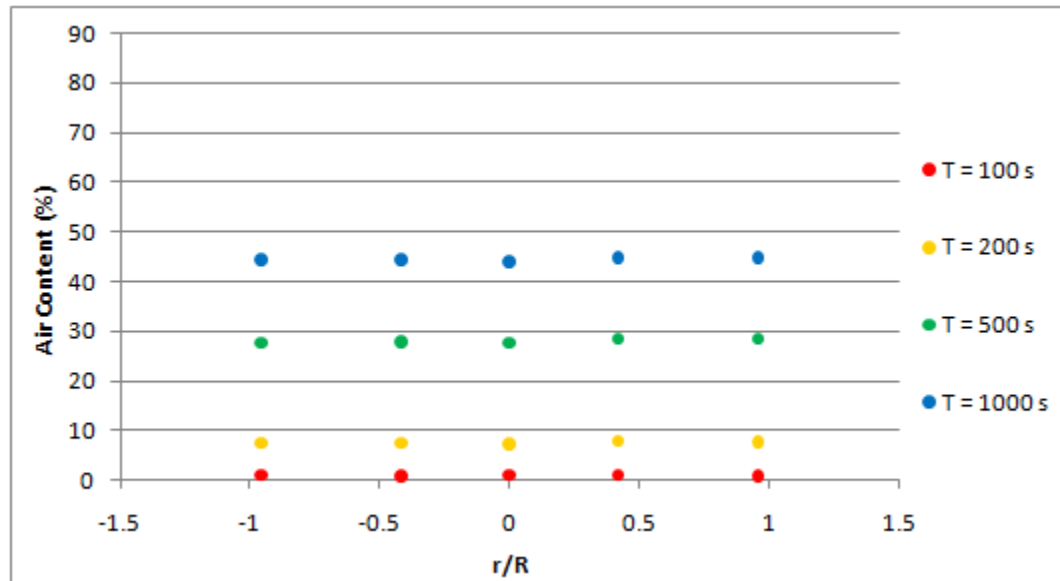


Figure H-35: Variation of Air Content along Vessel Diameter for APort7

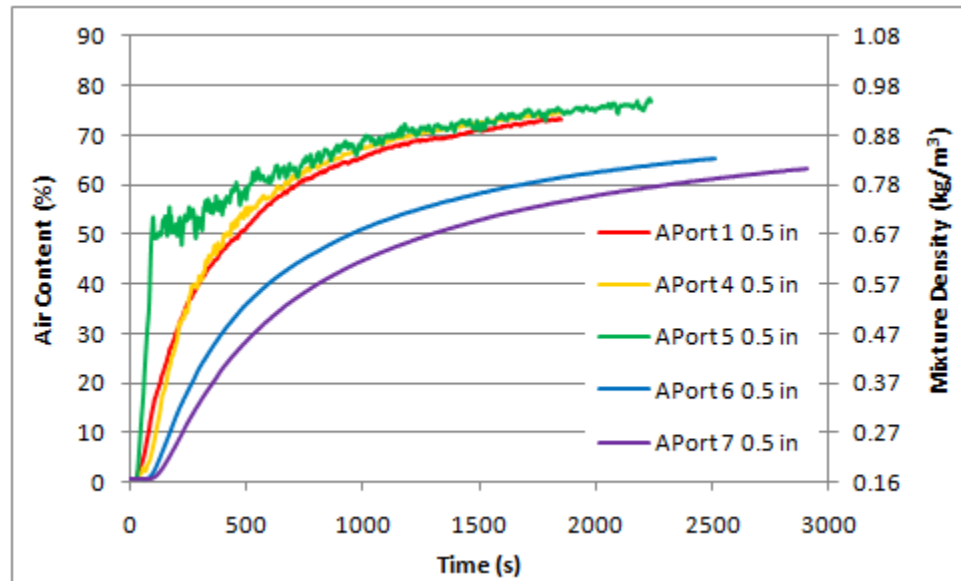


Figure H-36: Local Data for Radial Location 0.5 in along Axial Direction for APort

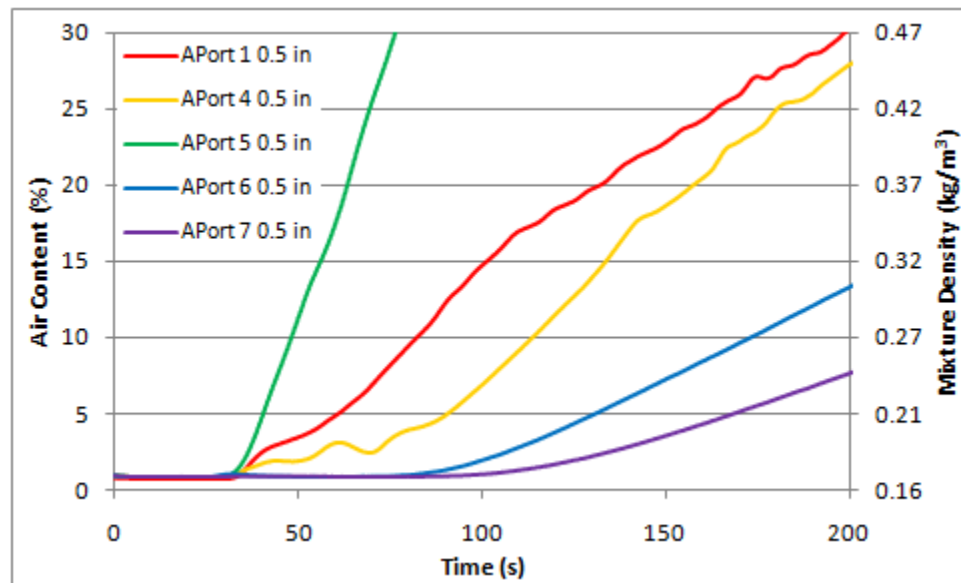


Figure H-37: Initial 200 s of Local Data for Radial Location 0.5 in along Axial Direction for
APort

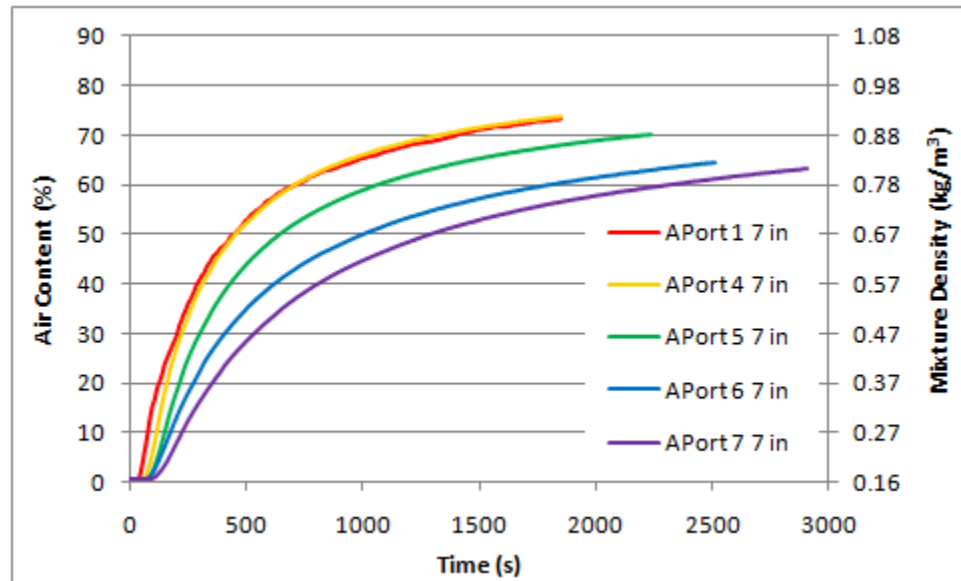


Figure H-38: Local Data for Radial Location 7 in along Axial Direction for APort

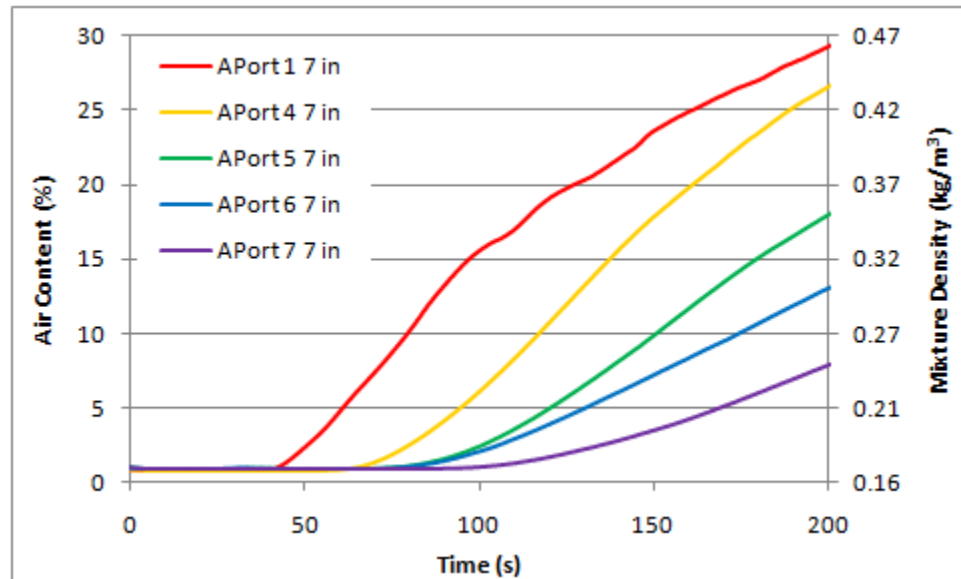


Figure H-39: Initial 200 s of Local Data for Radial Location 7 in along Axial Direction for APort

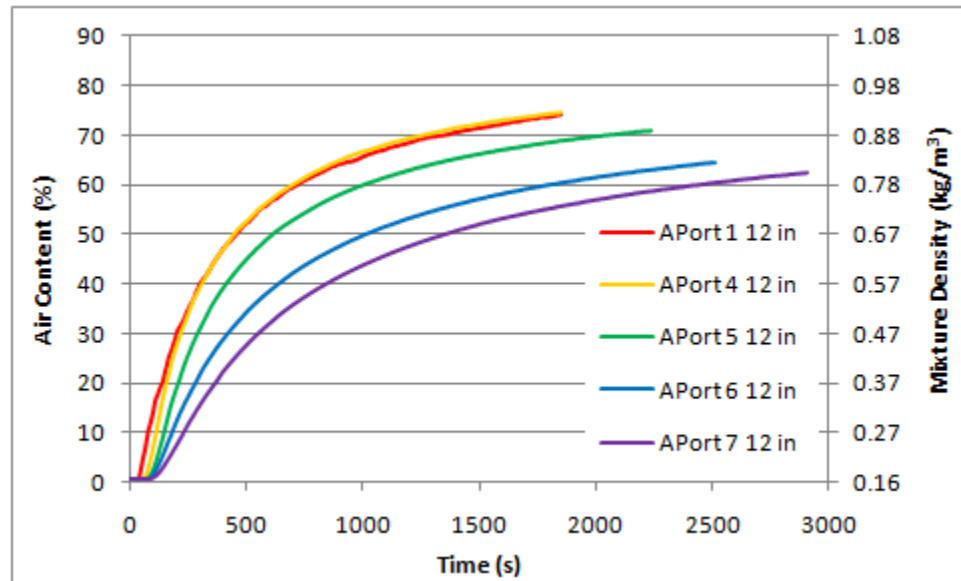


Figure H-40: Local Data for Radial Location 12 in along Axial Direction for APort

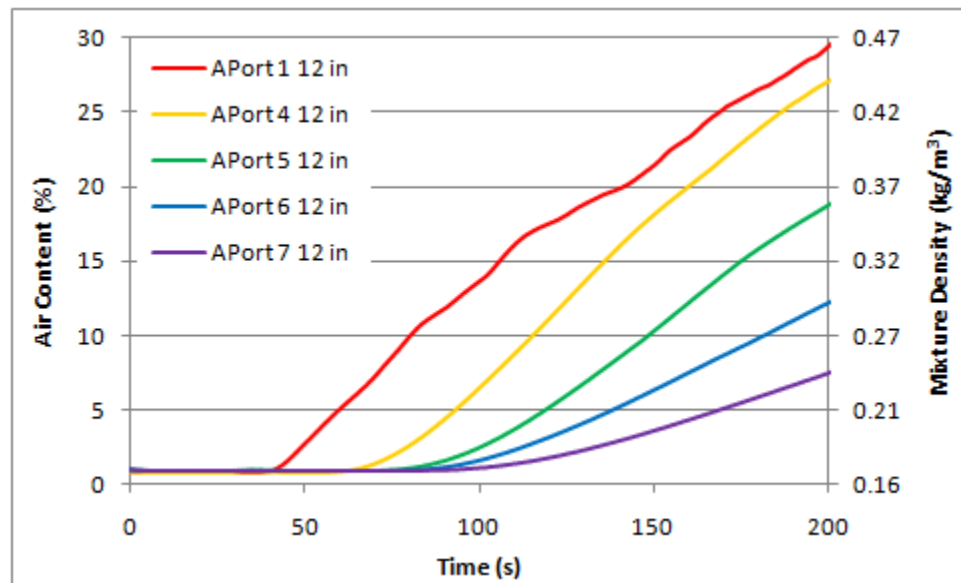


Figure H-41: Initial 200 s of Local Data for Radial Location 12 in along Axial Direction for APort

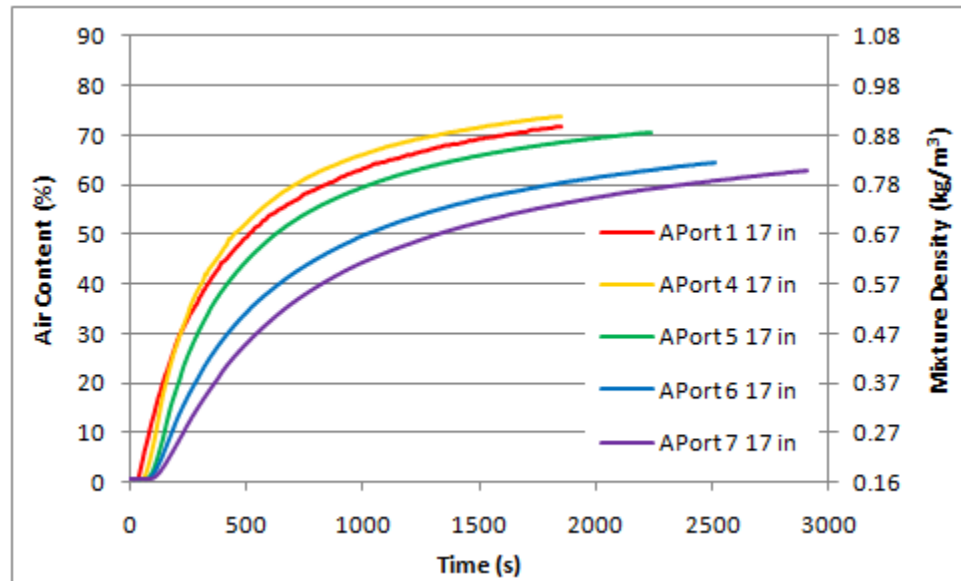


Figure H-42: Local Data for Radial Location 17 in along Axial Direction for APort

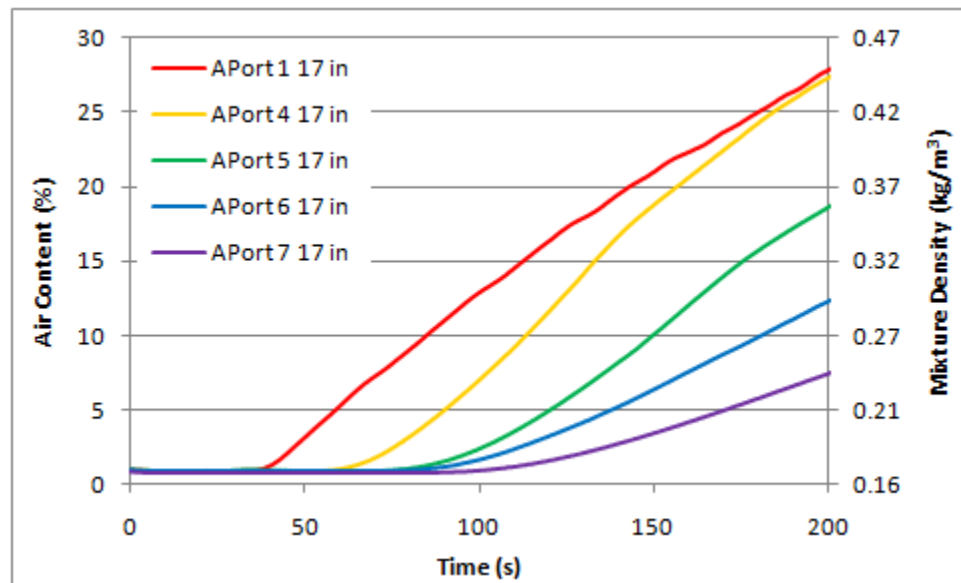


Figure H-43: Initial 200 s of Local Data for Radial Location 17 in along Axial Direction for APort

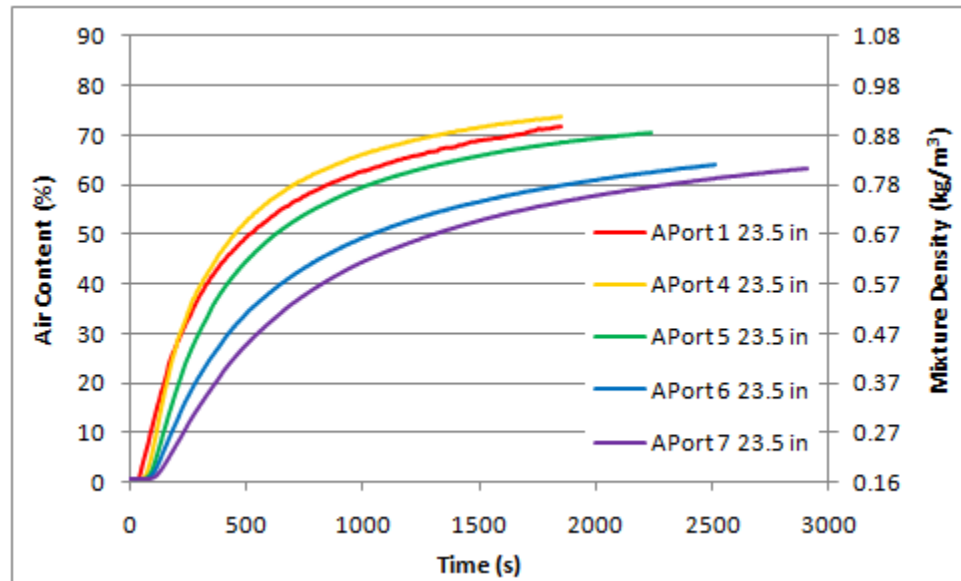


Figure H-44: Local Data for Radial Location 23.5 in along Axial Direction for APort

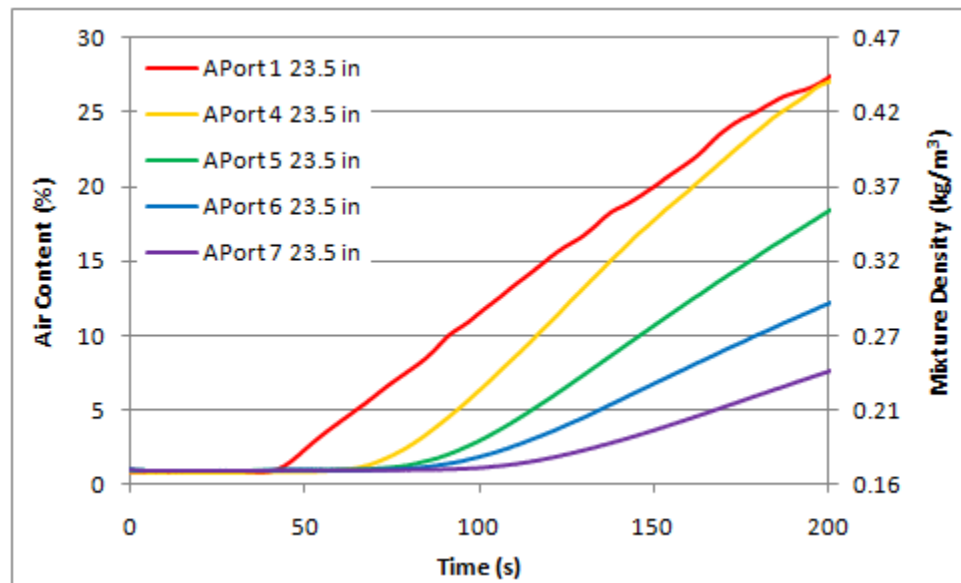


Figure H-45: Initial 200 s of Local Data for Radial Location 23.5 in along Axial Direction for APort

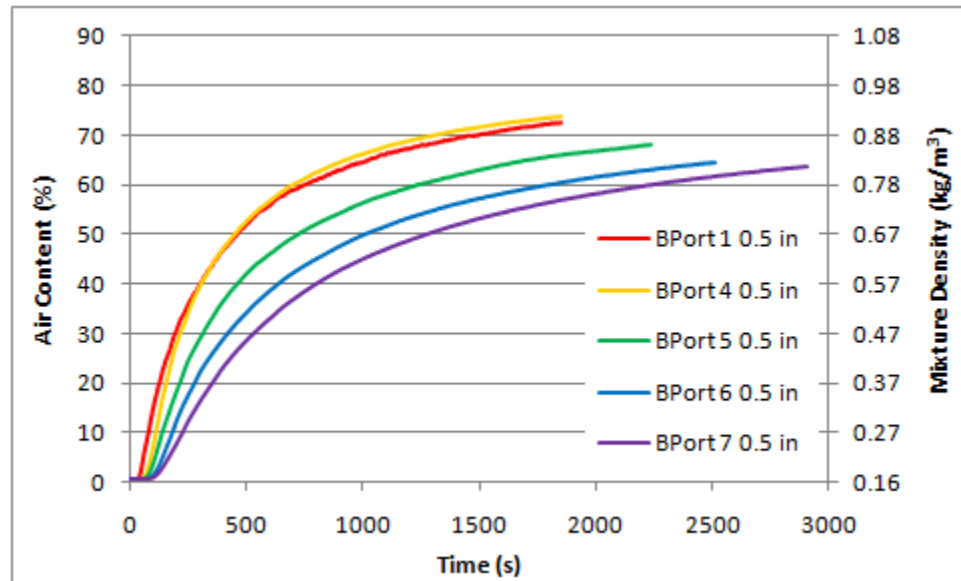


Figure H-46: Local Data for Radial Location 0.5 in along Axial Direction for BPort

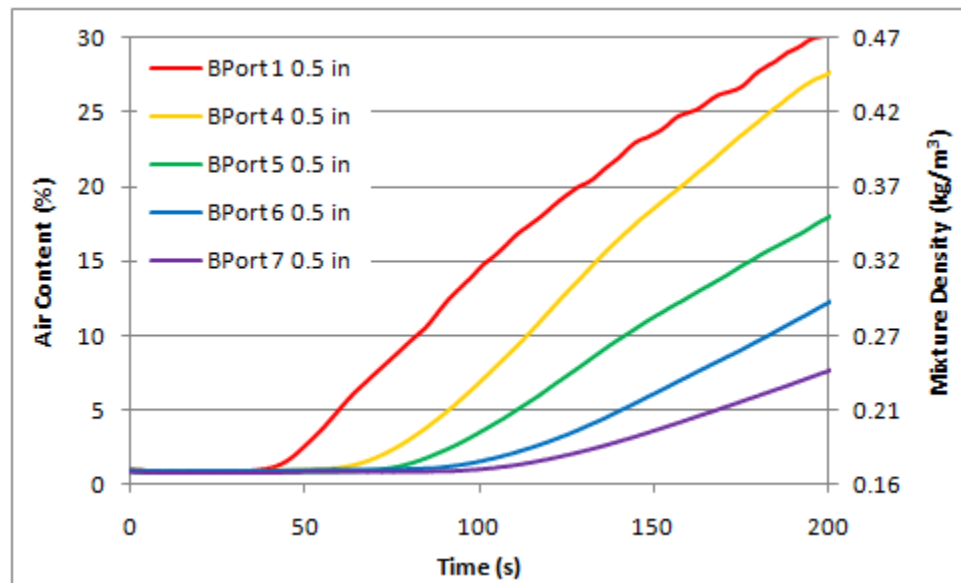


Figure H-47: Initial 200 s of Local Data for Radial Location 0.5 in along Axial Direction for BPort

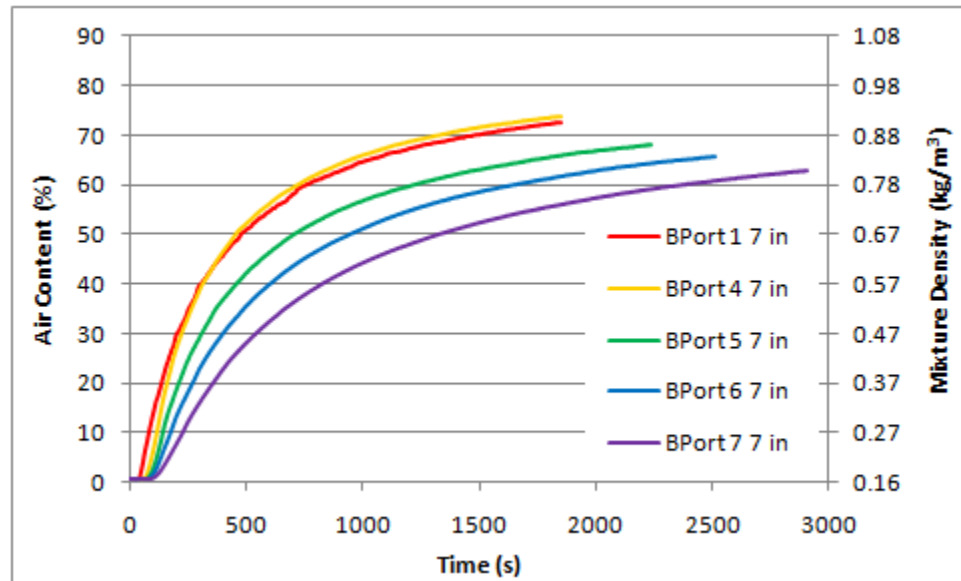


Figure H-48: Local Data for Radial Location 7 in along Axial Direction for BPort

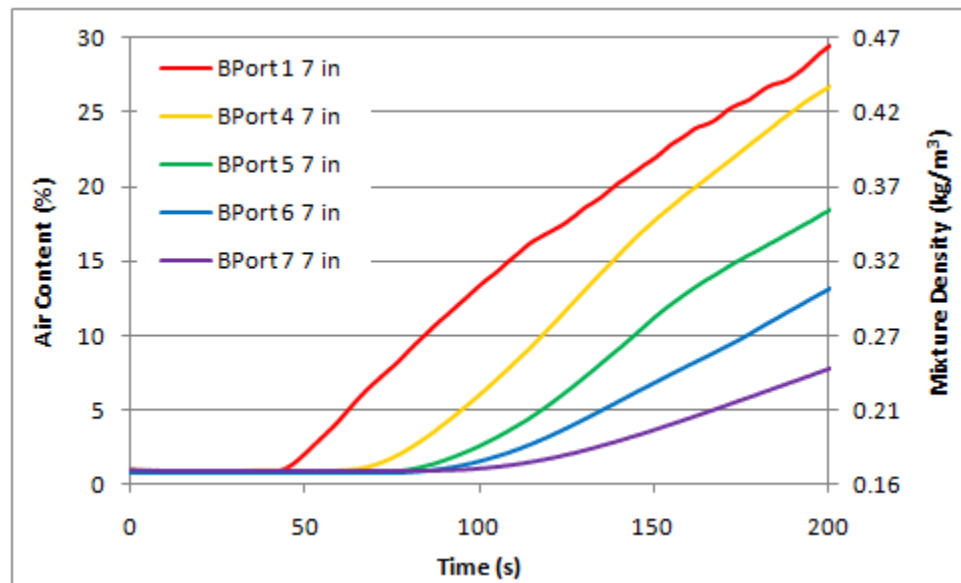


Figure H-49: Initial 200 s of Local Data for Radial Location 7 in along Axial Direction for BPort

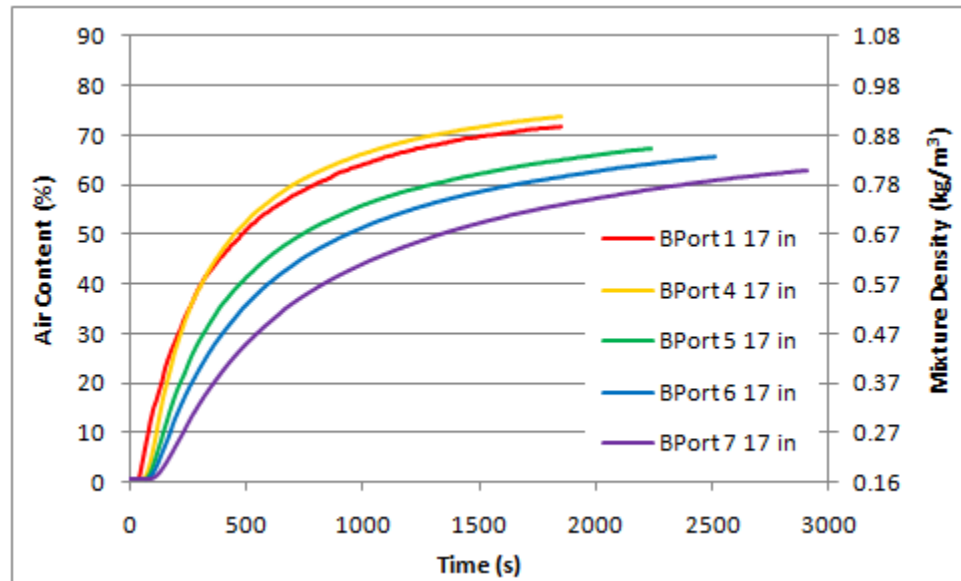


Figure H-50: Local Data for Radial Location 17 in along Axial Direction for BPort

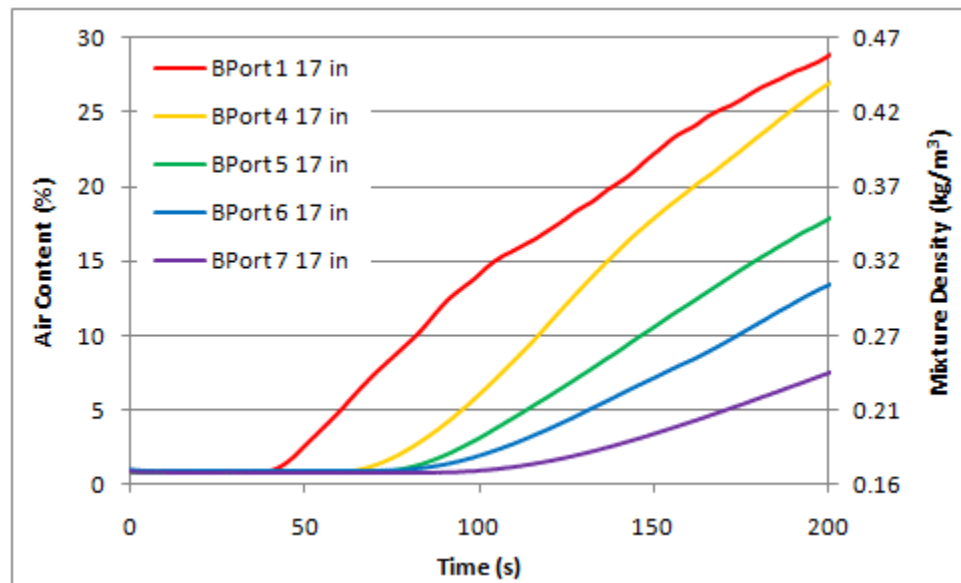


Figure H-51: Initial 200 s of Local Data for Radial Location 17 in along Axial Direction for BPort

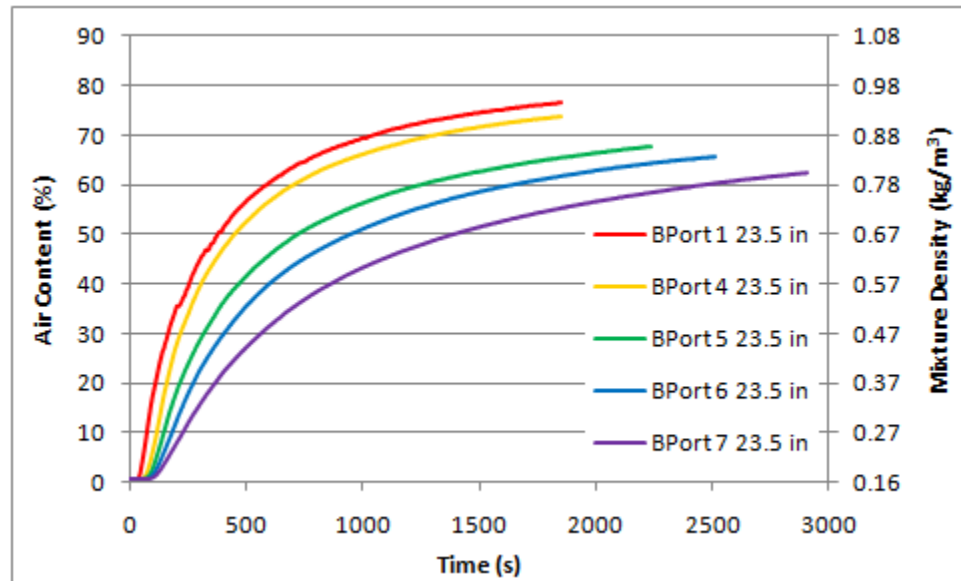


Figure H-52: Local Data for Radial Location 23.5 in along Axial Direction for BPort

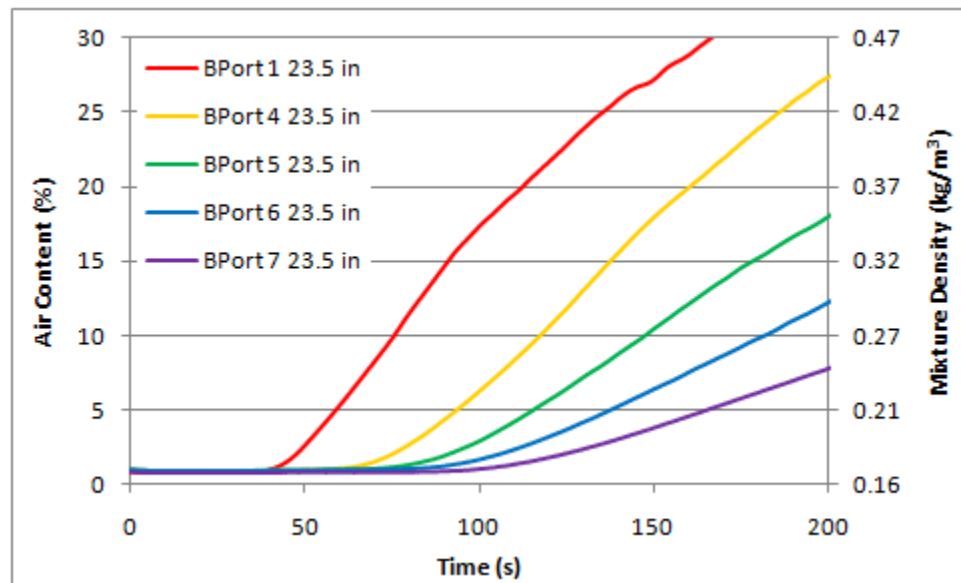


Figure H-53: Initial 200 s of Local Data for Radial Location 23.5 in along Axial Direction for
BPort

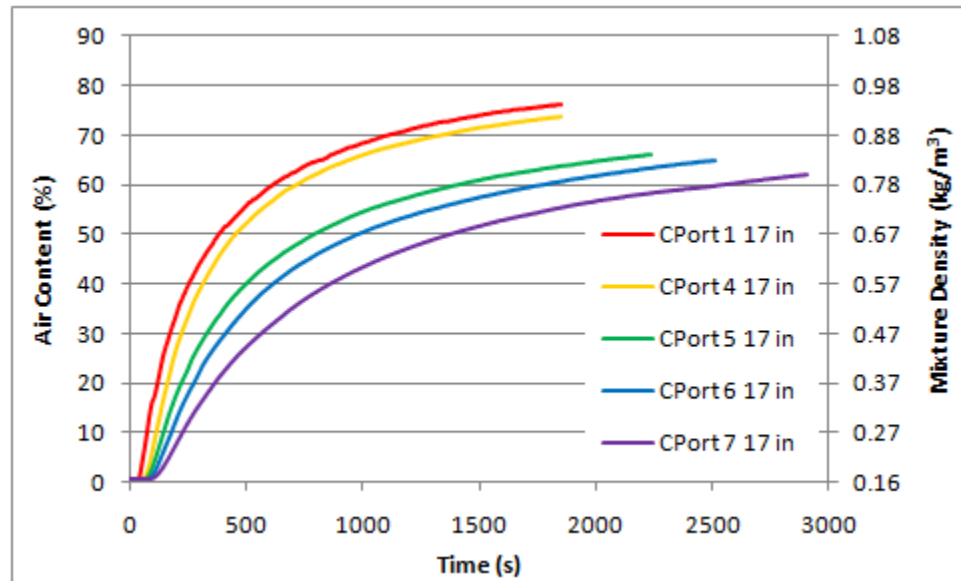


Figure H-54: Local Data for Radial Location 17 in along Axial Direction for CPort

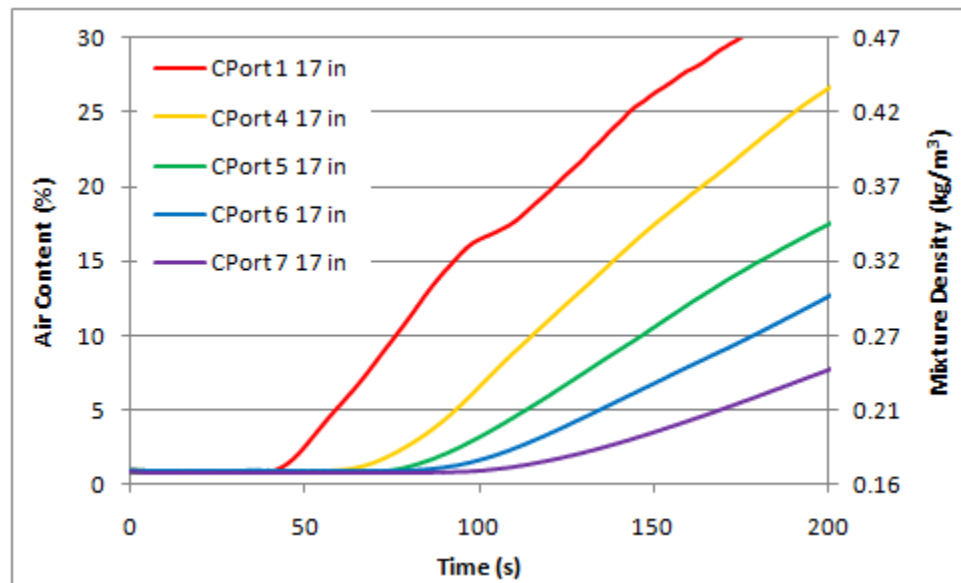


Figure H-55: Initial 200 s of Local Data for Radial Location 17 in along Axial Direction for CPort

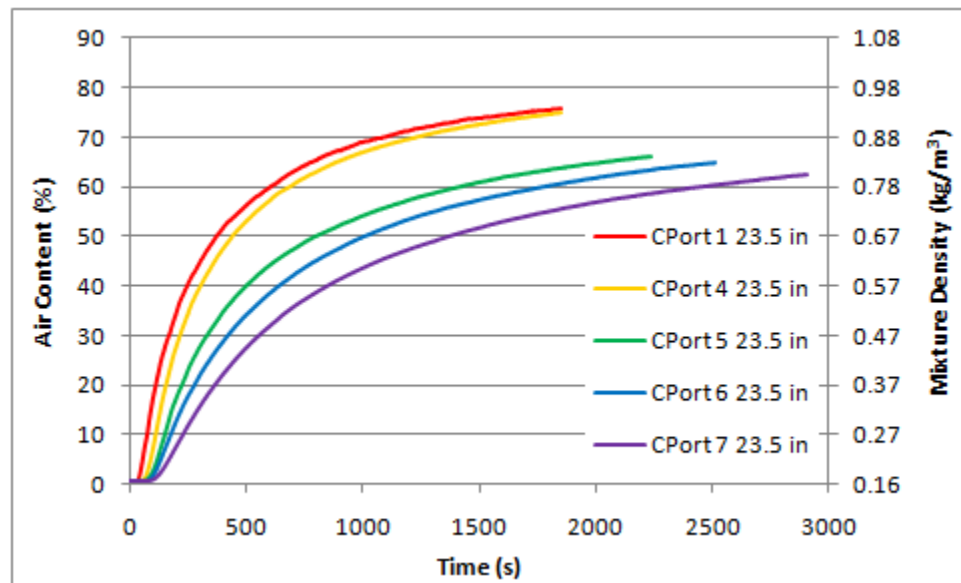


Figure H-56: Local Data for Radial Location 23.5 in along Axial Direction for CPort

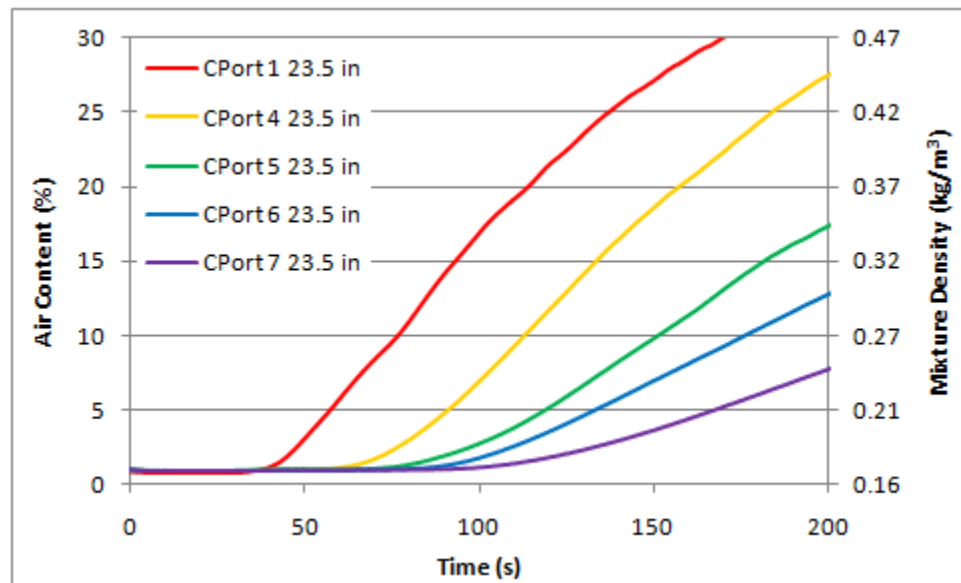


Figure H-57: Initial 200 s of Local Data for Radial Location 23.5 in along Axial Direction for CPort